Charles University
Faculty of Mathematics and Physics

DOCTORAL THESIS

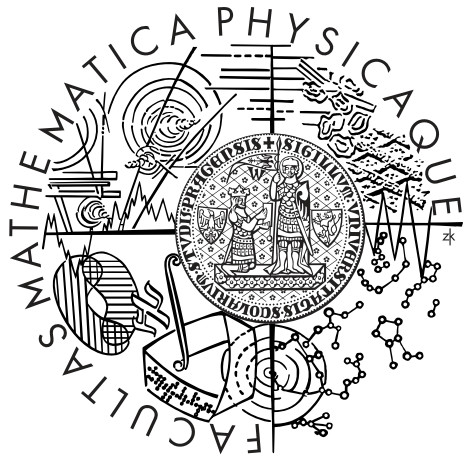

Pavel Ševeček

Simulations of asteroid collisions using a hybrid SPH/N-body approach

Astronomical Institute of Charles University

Dissertation supervisor:	doc. Mgr. Miroslav Brož, Ph.D.
Study programme:	Physics
Specialization:	Theoretical Physics, Astronomy and Astrophysics

Prague 2021

Acknowledgements

I probably would have never finished this thesis if it were not for the support and encouragement of my collaborators, friends and family. Immense thanks go to my supervisor, Miroslav Brož, for his guidance and endless patience. I thank my colleague, Josef Hanuš, for the opportunity to participate in such fascinating research. Many thanks also go to Martin Jutzi for insightful discussions about the rheological model and numerical experiments. I owe a debt of gratitude to the late Jaroslav Křivánek for motivating me to pursue a scientific career. It saddens me deeply that I am unable to tell him how much I respected him as a mentor and a friend. Of course, I am grateful to my parents and siblings for their continuous support during my studies.

Summary

Title: Simulations of asteroid collisions using a hybrid SPH/N-body approach

Author: Pavel Ševeček

Department: Astronomical Institute of Charles University

Supervisor: doc. Mgr. Miroslav Brož, Ph.D.

Abstract: Understanding asteroid collisions is a key part of Solar System science. To interpret observations of more than 100 asteroid families, various numerical simulations are used. In this work, we prefer the smoothed particle hydrodynamics (SPH), which allows a detailed description of impact mechanics, shock wave propagation, fragmentation of the target, ejection, or reaccumulation controlled by self-gravity and secondary collisions. Since the respective time scale may reach the orbital time scale, the SPH is often complemented by efficient N-body integrators and collisional handlers.

In the review part of the thesis, we describe details of numerical methods and their implementation in the new `OpenSPH` code. We also thoroughly test the code, using analytical solutions and laboratory experiments as references, and discuss its stability and convergence with respect to spatial resolution.

In the refereed papers, included in the thesis, we focus on collisions with targets of particular sizes ($D = 10$ and 100 km). We explore the dependence of outcomes on the target size, the projectile size, the impact speed, the impact angle, and most importantly, the initial spin rate. We demonstrate that rotation significantly decreases the effective strength of the targets and increases the ejected mass. We self-consistently compute the angular momentum transfer due to sub-catastrophic impacts, which determines the overall evolution of spin rates in asteroid populations.

Last but not least, we interpret the fourth largest main-belt asteroid (10) Hygiea and its collisional family. Besides the size-frequency distribution or the velocity field of fragments, we use the shape of Hygiea derived from adaptive-optics observations as a novel constraint for collisional modeling. This allowed us to not only determine the parameters of this major impact event, but to reveal impact-induced material weakening, needed to obtain consistent axial ratios.

Keywords: asteroid collisions, smoothed-particle hydrodynamics (SPH), N-body simulations, (10) Hygiea

I declare that I carried out this doctoral thesis independently, and only with the cited sources, literature and other professional sources.

I understand that my work relates to the rights and obligations under the Act No. 121/2000 Coll., the Copyright Act, as amended, in particular the fact that the Charles University has the right to conclude a license agreement on the use of this thesis as a school work pursuant to Section 60 paragraph 1 of the Copyright Act.

In ..... on ..... Signature

CONTENTS

Contents **5**

1 Preface **9**

2 SPH code for impact simulations **13**
- 2.1 Smoothed-particle discretization . . . 14
  - 2.1.1 SPH interpolant . . . 14
  - 2.1.2 Consistency conditions . . . 16
    - 2.1.2.1 Kernel constraints. . . . 16
    - 2.1.2.2 Gradient constraints. . . . 17
    - 2.1.2.3 Correction tensor. . . . 17
  - 2.1.3 Second derivatives . . . 18
  - 2.1.4 Smoothing length . . . 19
    - 2.1.4.1 Iterative algorithm. . . . 19
    - 2.1.4.2 Adaptivity. . . . 19
    - 2.1.4.3 Symmetrization. . . . 20
  - 2.1.5 Kernels and their properties . . . 20
    - 2.1.5.1 B-spline kernels. . . . 21
    - 2.1.5.2 Anisotropic kernels. . . . 22
    - 2.1.5.3 Kernel look-up tables. . . . 22
- 2.2 Lagrange equations . . . 22
  - 2.2.1 Derivation of discretized equations . . . 23
  - 2.2.2 Properties of Lagrangian-based equations . . . 24
    - 2.2.2.1 Conservation of integrals of motion. . . . 24
    - 2.2.2.2 Galilean invariance. . . . 25
    - 2.2.2.3 Regularization of the particle distribution. . . . 25
- 2.3 Equations for viscous fluids and solid bodies . . . 25
  - 2.3.1 Equation of motion and energy equation . . . 26
  - 2.3.2 Constitutive relation . . . 26
  - 2.3.3 Bulk rotation . . . 27

2.4 Density evolution . . . 28
2.4.1 Discontinuities in density . . . 28
2.4.2 Density at free surfaces . . . 29
2.4.3 Performance considerations . . . 29
2.5 Energy-conserving discretization . . . 30
2.6 Artificial terms . . . 31
2.6.1 Discontinuities in SPH discretization . . . 31
2.6.1.1 Diffusivity. . . . 32
2.6.2 Artificial viscosity . . . 33
2.6.2.1 Riemann-based viscosity. . . . 33
2.6.2.2 Standard viscosity. . . . 33
2.6.2.3 Balsara switch. . . . 34
2.6.2.4 Time-dependent viscosity. . . . 34
2.6.3 Artificial thermal conductivity . . . 35
2.6.3.1 Signal speed. . . . 35
2.6.4 Artificial stress . . . 36
2.6.4.1 Tensile instability. . . . 36
2.6.4.2 Local measure of tension. . . . 37
2.6.5 Influence of artificial terms on the solution . . . 38
2.7 Equation of state . . . 38
2.7.1 Tillotson's equation . . . 38
2.7.2 Sound speed . . . 39
2.8 Rheology . . . 40
2.8.1 Von Mises yield criterion . . . 40
2.8.2 Drucker-Prager yield criterion . . . 41
2.8.3 Acoustic fluidization . . . 42
2.8.3.1 Material weakening. . . . 42
2.8.3.2 Melosh model. . . . 43
2.8.3.3 Attenuation timescale. . . . 43
2.8.4 Fragmentation . . . 43
2.8.4.1 Weibull distribution. . . . 44
2.8.4.2 Grady-Kipp model. . . . 44
2.8.4.3 Discretization in SPH. . . . 44
2.8.4.4 Damage integration. . . . 45
2.9 Initial conditions . . . 46
2.9.1 Lattice-based distribution . . . 47
2.9.2 Parametrized spiraling . . . 48
2.9.3 Blue noise sampling . . . 49
2.9.4 Obtaining equilibrium state . . . 49
2.9.4.1 Spherically symmetric bodies. . . . 50
2.9.4.2 Poisson equation. . . . 50
2.9.4.3 Stabilization. . . . 51
2.10 Boundary conditions . . . 53
2.10.1 Ghost particles . . . 53

2.10.2 Particle freezing . . . 54
2.11 Temporal discretization . . . 55
2.11.1 Time step criteria . . . 55
2.11.2 Gravitational time step . . . 56
2.12 Self-gravitation . . . 57
2.12.1 Gravity in SPH discretization . . . 58
2.12.2 Multipole approximation . . . 60
2.12.2.1 Barnes-Hut algorithm. . . . 60
2.12.2.2 Traceless multipoles. . . . 60
2.12.2.3 Bottom-up traversal. . . . 61
2.12.2.4 Top-down traversal. . . . 61
2.12.2.5 Opening angle. . . . 61
2.12.2.6 Evaluation of acceleration. . . . 62
2.13 Implementation notes . . . 64
2.13.1 SPH solvers . . . 64
2.13.1.1 Evaluation of derivatives. . . . 64
2.13.1.2 Search radius. . . . 64
2.13.1.3 Correction tensor computation. . . . 66
2.13.1.4 Parallelization. . . . 66
2.13.2 Neighbor queries . . . 68
2.13.2.1 K-d tree. . . . 68
2.13.2.2 Spatial hash grid. . . . 69
2.14 Surface reconstruction . . . 70

3 Numerical and laboratory experiments **73**
3.1 Sod shock tube test . . . 73
3.2 Sedov-Taylor blast wave test . . . 75
3.3 Kelvin-Helmholtz instability test . . . 76
3.4 Colliding elastic bands test . . . 78
3.5 Rotating rod test . . . 79
3.6 Cliff collapse test . . . 80
3.7 Fragmentation validation test . . . 80
3.8 Convergence tests . . . 83

4 Impacts into small targets **87**
4.1 Hybrid model for family-forming events . . . 87
4.1.1 Related work . . . 88
4.2 Methods and aims . . . 89
4.2.1 Model used for simulations . . . 90
4.2.2 Numerical issues . . . 91
4.3 Major results . . . 92
4.4 Reprint . . . 95

5 Rotating targets and angular momentum transfer **115**

5.1 Collisions of rotating bodies . . . 115
5.1.1 Numerical issues . . . 116
5.1.2 Related work . . . 116
5.2 Methods and aims . . . 117
5.2.1 Extensions of the numerical model . . . 118
5.2.2 Merging parameters . . . 120
5.2.3 Code validation . . . 120
5.3 Major results . . . 122
5.3.1 SFDs of static and rotating targets . . . 122
5.3.2 Angular momentum transfer and mass loss . . . 123
5.4 Reprint . . . 125

6 Impact forming the Hygiea family **139**
6.1 Observational constraints . . . 139
6.1.1 Hygiea family . . . 140
6.1.2 Adaptive-optics observations of (10) Hygiea . . . 140
6.2 Methods and aims . . . 142
6.3 Major results . . . 143
6.3.1 Matching SFD . . . 143
6.3.2 Constraining dry friction . . . 146
6.4 Reprint . . . 148

7 Conclusions **155**
7.1 Code development . . . 155
7.2 Simulations of D = 10 km and 100 km targets . . . 155
7.3 (10) Hygiea . . . 157
7.4 Future work . . . 158

8 List of publications **159**

9 References **163**

— Chapter 1 —

PREFACE

Asteroid families are remarkable structures observed mainly in the Main Belt, but also within Martian Trojans [Christou et al., 2017], Jupiter Trojans, Hildas [Vinogradova, 2015], irregular moons [Bottke et al., 2010], or the trans-Neptunian objects [Schlichting and Sari, 2009]. Each family has been created by a large-scale collision of two asteroids (target and projectile), ejecting numerous fragments which are now spread out in space due to Keplerian shear, planetary perturbations and radiation forces [Nesvorný et al., 2015; Spoto et al., 2018]. However, we can still detect asteroids with common origin as clusters in the space of proper elements a_{p}, e_{p}, I_{p} [Knežević and Milani, 2003] and also in spectral properties, e.g. colors, albedos, or reflectance spectra [Parker et al., 2008; Usui et al., 2011; Nugent et al., 2015], as seen in Fig. 1.1. First families have been discovered by Kiyotsugu Hirayama in 1918, namely the Koronis, Eos and Themis families [Hirayama, 1918], and today more than 100 families are known [Brož et al., 2013].

Physical processes taking place during collisions of asteroids are hardly reproducible in a laboratory environment. Asteroids collide at speeds of several km/s, typically between $v \simeq 3$ and 7 km/s [Dell'Oro and Paolicchi, 1997; Dahlgren, 1998]. During impacts, material is strongly compressed, experiencing pressures of up to $P = 10^{11}$ Pa, it is melted and partly evaporated. A substantial fraction of the kinetic energy of the projectile is converted into heat. For example, the total thermal energy released during the impact that formed the Hygiea family was about $E \sim 10^{25}$ J [Vernazza et al., 2020], comparable to a detonation of 50 million Tsar bombs.

Laboratory experiments, studying break-ups of targets hit by high-speed projectiles, have to be performed on substantially smaller scales [Kadono et al., 2009; Avdellidou et al., 2016, 2017; Ogawa et al., 2021]. Targets in such experiments usually have several centimeters in size [Nakamura and Fujiwara, 1991; Morris and Burchell, 2017]. These tests provide invaluable data that constrain material properties, in particular parameters of the fragmentation model. However, these results cannot be directly compared to kilometer-sized asteroids. For asteroids with diameters of the order of $D \simeq 100$ km, experimental data would have to be extrapolated by scaling the target over six orders of magnitude. Such extrapolation cannot yield accurate predictions, mainly because the role of gravity is unconstrained by laboratory measurements. Asteroid collisions are thus commonly studied using numerical simulations.

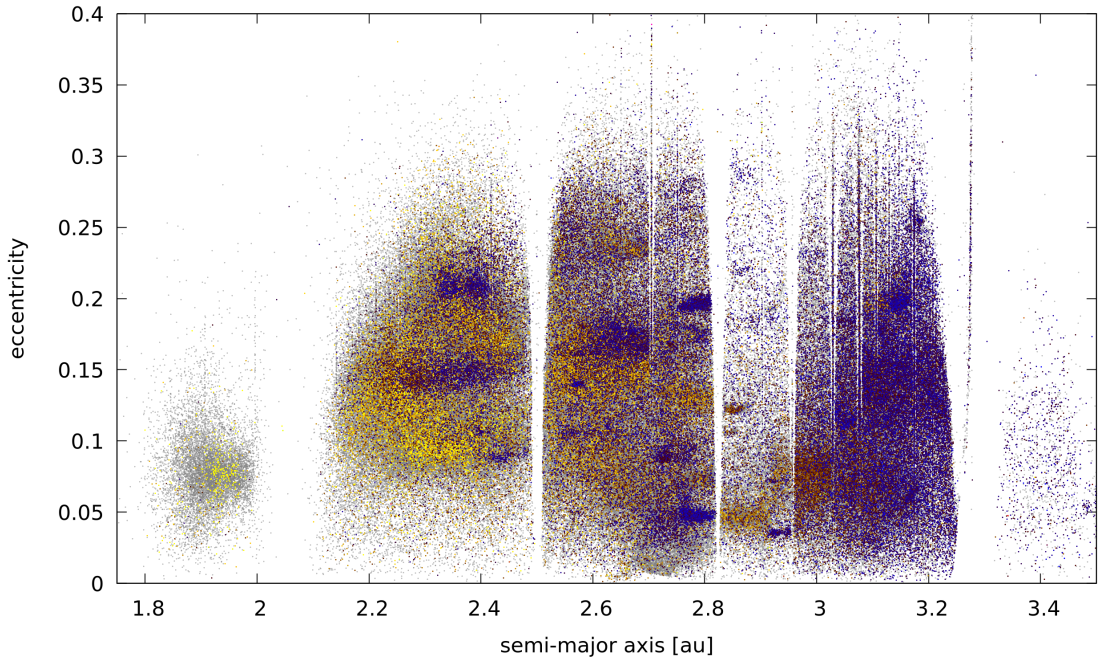

Figure 1.1: Main-belt asteroids in space of proper elements a_p, e_p. The colors correspond to albedos obtained by the WISE telescope. Data from Warner et al. [2009]; Masiero et al. [2010].

To understand the very formation of asteroid families, we have to rely on indirect observational evidence. One source of data is the families observed in the present-day Main Belt. Unfortunately, integrating orbits backward in time in order to determine the age of the family and the initial velocity field is only possible for the youngest families [Nesvorný et al., 2002; Vokrouhlický et al., 2009]. Due to the chaotic nature of the N-body problem, backward integration is not reliable for families older than few Myrs [Radović, 2017]. However, it is certainly possible to solve the problem as an inverse one: assume suitable initial conditions of the impact and integrate fragments forward in time. A synthetic family as computed by the simulation is then directly compared with the observational data [Vokrouhlický et al., 2006; Brož et al., 2013].

A key observational constraint is the size-frequency distribution (SFD). It is commonly plotted as a cumulative histogram of a number N of family members with a diameter larger than D. By matching the SFD of the synthetic and the observed family, we can estimate the impact speed, the impact angle, the size of the projectile and most importantly, the size of the parent body. A substantial fraction of the total mass may be hidden beyond the observational limit and numerical simulations help to debias this estimate.

Using ground-based observations, it is possible to measure visible (reflected) flux. Together with far-infrared (FIR), usually measured with space-based instruments, we can derive albedo and approximate diameter. Determining precise shape is more complex, though. Even the largest asteroids are small compared to a seeing-limited resolution of telescopes, and resolving disks of asteroids by more than a few pixels has until recently been beyond technological possibilities. Hence, the shapes of asteroids were mostly derived using light-curve inversion methods

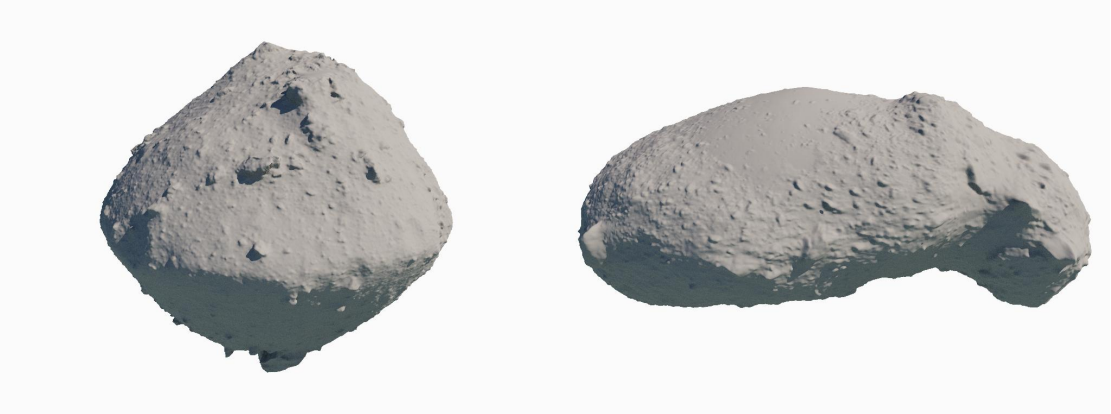

Figure 1.2: Shape models of asteroids (162173) Ryugu [Hirata et al., 2020] and (25143) Itokawa [Gaskell et al., 2008], derived from *in situ* observations. The images are not to scale; the volume-equivalent radius of Ryugu is 448 m [Watanabe et al., 2019], while for Itokawa it is 164 m [Fujiwara et al., 2006].

[Kaasalainen et al., 2001]. Only few asteroids were visited by a spacecraft during missions Galileo [Thomas et al., 1994; Meltzer, 2007], NEAR Shoemaker [Veverka et al., 1997; Russell et al., 2015], Deep Space 1 [Soderblom et al., 1999], Stardust [Hillier et al., 2011], Hayabusa [Saito et al., 2006; Demura et al., 2006], Rosetta [Russell et al., 2016], Dawn [Russell et al., 2016; Hiesinger et al., 2016], Chang'e 2 [Ji et al., 2016], New Horizons [Schenk et al., 2021], Hayabusa 2 [Watanabe et al., 2019] and OSIRIS-REx [Lauretta, 2012]. These missions successfully obtained close-up images of (1) Ceres, (4) Vesta, (21) Lutetia, (243) Ida, (253) Mathilde, (433) Eros, (951) Gaspra, (2867) Šteins (4179) Toutatis, (5535) Annefrank (9969) Braille, (25153) Itokawa, (101955) Bennu, (162173) Ryugu and (486958) Arrokoth. Using the *in situ* observations, it was possible to derive high-detail models, as shown in Fig. 1.2.

It was only the installation of a second-generation adaptive-optics instruments at ESO VLT that finally allowed us to really resolve $D \simeq 100$ km asteroids with ground-based observations. The SPHERE/ZIMPOL instrument, combined with a deconvolution algorithm, can now obtain detailed images of celestial bodies with an unprecedented angular resolution of about 3.6 mas/pixel [Schmid et al., 2017]. This corresponds to 2.6 km at the distance of 1 au. A large programme ID 199.C-0074 at the ESO VLT (152 hours) has been carried out to obtain phase-resolved images of forty large asteroids, e.g. (89) Julia [Vernazza et al., 2018], (7) Iris [Hanuš et al., 2019], (704) Interamnia [Hanuš et al., 2020], (16) Psyche [Ferrais et al., 2020], (10) Hygiea [Vernazza et al., 2020], (2) Pallas [Marsset et al., 2020], (31) Euphrosyne [Yang et al., 2020b], etc.

Adaptive-optics imagery revealed overall shapes of the asteroids as well as their major topographic features. For S-type asteroids, impact craters are a common feature and it is possible to construct the respective crater-size distribution. On the other hand, C-type asteroids exhibit smooth surfaces or shallow craters. For asteroids with an associated family, this data provides a novel insight into the collisional history of the body. We can use it as a constraint of our collisional models, together with the SFD and the velocity field of the family, and in turn, numerical simulations are then used to interpret these unique observational data.

In this thesis, I explore collisions of asteroids and formation of families using numerical methods. Due to the inherently Lagrangian nature of the problem, I use the **smoothed particle hydrodynamics (SPH)** to solve the equations of hydrodynamics, which is coupled with an efficient N-body integrator that computes gravitational interactions of bodies. I focus on disruptions of $D = 10\,\mathrm{km}$ spherical asteroids, trying to understand how the SFDs of synthetic families scale with the target size, and most importantly, what is the role of initial rotation. I also examine the asteroid Hygiea and its family, which originated in one of the most-energetic collisions in the Main belt. In this case study, I try to reconcile the surprisingly smooth and spherical surface of the asteroid with the existence of the Hygiea family.

The thesis is organized as follows. In Chapter 2, we describe the numerical model used to carry out SPH/N-body simulations, starting from a discretization of spatial derivatives to a discussion of all numerical details that had to be solved to obtain meaningful and physically accurate results. In Chapter 3, we review numerical experiments and validation tests of the `OpenSPH` code. Subsequent Chapters 4 to 6 summarize the goals and results of our selected published papers [Ševeček et al., 2017, 2019; Vernazza et al., 2020].

— Chapter ii —

SPH code for impact simulations

Numerical modeling of physical problems has a long history. Development of mesh-based methods, such as the finite element method (FEM) or the finite volume method (FVM), dates back as far as the 1940s [Hrennikoff, 1941], however, it largely took off in the 1960s and 1970s when the mainframe computers became capable of carrying out computations with more than a few thousands of degrees of freedom. These methods were applied to tackle various problems in civil engineering, primarily related to structural analysis.

On the contrary, the smoothed-particle hydrodynamics (SPH) originated in astrophysics. It was originally developed during the 1970s by Lucy [1977] for simulations of rotating protostars, and independently also by Gingold and Monaghan [1977], who coined the name of the method. Since then, it has been used in various areas of astrophysical research, such as merging of neutron stars [Rosswog et al., 2000], cosmological simulations [Stadel, 2001; Beck et al., 2015], supernovae explosions [García-Senz and Bravo, 2005; Pakmor et al., 2012], or black hole accretion [Barai et al., 2011]. The method has been adapted for simulations of solid bodies by Libersky and Petschek [1991], allowing its application in studies of asteroid collisions and formation of asteroid families [Jutzi et al., 2015]. Of course, SPH did not remain an exclusive tool for astrophysicists but also found use in automotive industry, aeronautics and computer graphics [Ihmsen et al., 2014].

An excellent review of the SPH method for self-gravitational bodies has been written by Cossins [2010] and also by Springel [2010], who further described an extension of the method for magneto-hydrodynamics or relativistic simulations. Thus, I have not tried to compile a comprehensive overview of the SPH in this thesis, instead, I focused on the application of the method for the impact simulations. As most of the simulations were performed with our newly developed code `OpenSPH`, this chapter also serves as a high-level documentation of the code. Nonetheless, many of aspects are quite universal and hopefully useful for other developers of hydrodynamical codes.

2.1 Smoothed-particle discretization

Smoothed particle hydrodynamics is a Lagrangian method. Unlike the Eulerian description, where quantities are known at fixed points in space, The SPH discretizes the continuum into a finite number of *particles* comoving with the continuum. Each particle carries a set of associated physical quantities as well as a fixed *mass* m_i. The method does not require any connectivity information of the particles; each particle interacts with other particles in its neighborhood, meaning the topology of the fluid can naturally change during the simulation. This poses an advantage over grid-based methods, where a construction and spatial adaptation of the mesh can be a challenging problem. Values of quantities at any point in space are then interpolated from particle values. The computational domain is defined implicitly by the immediate configuration of particles and thus it does not have to be *a priori* set up by the user.

Particles act as tracers, moving with the velocities of the continuum, and there is no need to explicitly handle the advection of physical quantities. Quantities are propagated together with particles, making the SPH a suitable method for simulations of extreme deformations, gravitational collapse, turbulence, convection, collision, etc.

2.1.1 SPH interpolant

To obtain the SPH interpolant for generic quantity A, we start off with identity:

$$A(\boldsymbol{r}) = \int_\Omega A(\boldsymbol{r}')\delta(\boldsymbol{r} - \boldsymbol{r}')\,\mathrm{d}\boldsymbol{r}'\,, \tag{2.1}$$

where δ denotes the Dirac delta distribution. This equation is essentially a definition of $\delta(\boldsymbol{r})$. If we however replace $\delta(\boldsymbol{r})$ with a (yet unspecified) smoothing function $W(\boldsymbol{r})$, we obtain an approximation of $A(\boldsymbol{r})$:

$$\langle A\rangle(\boldsymbol{r}) = \int_\Omega A(\boldsymbol{r}')\,W(\boldsymbol{r} - \boldsymbol{r}', h)\,\mathrm{d}\boldsymbol{r}'\,, \tag{2.2}$$

where h is a length scale, defining the amount of smoothing. As we can only know quantity values at a finite number of points in space, we need to replace the integral on the right-hand side with a sum over all particles. Therefore, we formally replace the volume element with a volume assigned to a single particle:

$$\mathrm{d}\boldsymbol{r}' = \frac{m_i}{\rho_i}\,. \tag{2.3}$$

This choice is somewhat arbitrary, any combination of quantities with dimensions of volume could be used. A standard SPH formulation uses particle masses because they are fixed during the simulation (and the total mass is therefore conserved), however different volume elements have been proposed, such as an element based on internal energy [Saitoh and Makino, 2013].

After substituting the volume element and replacing the integral with the sum over all particles, we obtain the SPH interpolant:

$$\langle A\rangle(\boldsymbol{r}) = \sum_j A_j \frac{m_j}{\rho_j} W(\boldsymbol{r} - \boldsymbol{r}_j, h_j)\,, \tag{2.4}$$

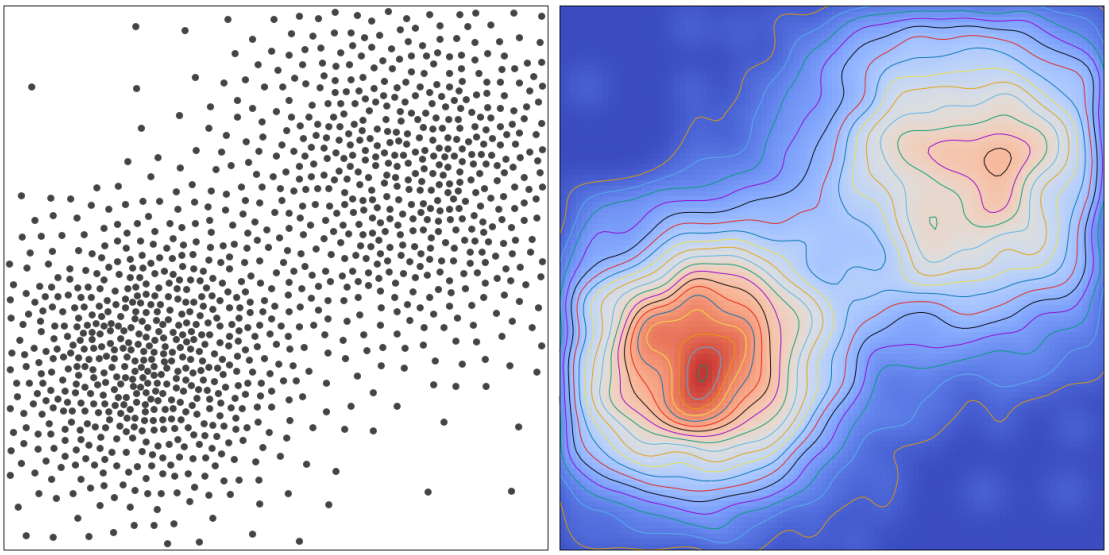

Figure 2.1: Example of a continuum density, computed from a finite set of particles irregularly distributed in space. The left panel shows individual particles, the right panel the density interpolated by Eq. 2.5 in color palette and contours.

where A_j is the quantity value of particle j, and h_j is its *smoothing length*. In the case of density, the interpolant reduces to a well-known SPH density expression:

$$\rho(\boldsymbol{r}) = \sum_j m_j W(\boldsymbol{r} - \boldsymbol{r}_j, h_j)\,. \tag{2.5}$$

Fig. 2.1 shows an example of density computed from particles using the SPH interpolant.

The interpolant (Eq. 2.4) allows us to compute quantity values at any point in the continuum from a discrete particle distribution, using the smoothing functions as weights. The function $W(\boldsymbol{r}, h)$ is called the *smoothing kernel*. It usually has compact support with a radius equal to small multiple of the smoothing length h; for example, the standard M_4 kernel (see Sec. 2.1.5) has a radius of $2h$. Thus the sum in Eq. 2.4 does not enumerate all the particles, but only those in the neighborhood of particle i. Consequently, all interpolated values drop to zero in regions with no particles.

The smoothing length h can be seen as a trade-off parameter between the discretization error and the spatial resolution. Naturally, the discretization error can be decreased by increasing the number of interacting particles, which can be achieved by increasing the smoothing lengths. However, larger radii of particles lead to stronger smoothing of quantities and to lower effective spatial resolution. If the number of neighbors is increased, it is also necessary to increase the total number of particles to maintain the resolution of the simulation.

As the kernel $W(\boldsymbol{r}, h)$ is a known function, spatial derivatives of quantities, such as gradient, can be computed by simply applying the derivative on kernel:

$$\langle \nabla A \rangle(\boldsymbol{r}) = \sum_j A_j \frac{m_j}{\rho_j} \nabla W(\boldsymbol{r} - \boldsymbol{r}_j, h_j)\,. \tag{2.6}$$

By doing so, we reduce all partial differential equations into ordinary differential equations. However, such a system of equations has a number of problems. Namely, the velocity field would not be invariant under the Galilean transformation, integrals of motion would not be generally conserved, etc. Luckily, there is considerable freedom in the discretization of spatial derivatives and it is possible to derive a modified set of equations that solves these problems, as explained in the following sections.

2.1.2 Consistency conditions

Up to this point, we did not specify the smoothing kernel and considered $W(\boldsymbol{r}, h)$ as a generic function. While there is freedom in choosing the kernel, it cannot be arbitrary and must satisfy several conditions. We use it as a function *interpolant*, hence the function $\langle A\rangle(\boldsymbol{r})$ smoothed using the kernel W must be an approximation of the original function $A(\boldsymbol{r})$ and it must approach the function $A(\boldsymbol{r})$ as the smoothing length h approaches zero. In particular, the kernel function W can be constrained in such a way that:

$$\langle A\rangle(\boldsymbol{r}) = A(\boldsymbol{r}) + \mathcal{O}(h^2)\,. \tag{2.7}$$

2.1.2.1 Kernel constraints. To obtain the conditions necessary for the property 2.7 to hold, we expand the interpolated function $\langle A\rangle(\boldsymbol{r})$ into the Taylor series, using its definition in Eq. 2.2:

$$\langle A\rangle(\boldsymbol{r}) = A(\boldsymbol{r}) \int W(\boldsymbol{r}-\boldsymbol{r}')\,\mathrm{d}\boldsymbol{r}' + \nabla A(\boldsymbol{r}) \cdot \int (\boldsymbol{r}'-\boldsymbol{r}) W(\boldsymbol{r}-\boldsymbol{r}')\,\mathrm{d}\boldsymbol{r}' + \mathcal{O}(h^2)\,. \tag{2.8}$$

It follows that the property 2.7 holds as long as the kernel function W satisfies the following *consistency conditions*:

$$\int W(\boldsymbol{r}-\boldsymbol{r}')\,\mathrm{d}\boldsymbol{r}' = 1\,, \tag{2.9}$$

$$\int (\boldsymbol{r}'-\boldsymbol{r}) W(\boldsymbol{r}-\boldsymbol{r}')\,\mathrm{d}\boldsymbol{r}' = \boldsymbol{0}\,. \tag{2.10}$$

We see that any smoothing kernel must be *normalized* — the volume integral over the kernel support must be equal to one. Condition 2.10 is fulfilled when the kernel is *symmetric*, i.e., if:

$$W(\boldsymbol{r}) = W(-\boldsymbol{r})\,. \tag{2.11}$$

Conditions 2.9 and 2.10 constrain the function $W(\boldsymbol{r})$ and do not depend on the distribution of particles. However, it is further necessary to replace the integral with a sum to obtain equations in the SPH discretization, as in Eq. 2.4. To satisfy the property 2.7 in particle discretization as well, the kernel should be further restricted in a way that necessarily depends on particle distribution. However, the kernel itself does *not* enter directly into the standard SPH equations, only its derivatives are used. Thus, it is much more important to satisfy the consistency conditions for the kernel gradient.

2.1.2.2 Gradient constraints. The gradient conditions can be obtained in a similar way as the kernel conditions above. We use the integral (continuous) definition of the interpolated gradient:

$$\langle \nabla A \rangle(\boldsymbol{r}) = \int \frac{\partial A}{\partial \boldsymbol{r}'} W(\boldsymbol{r} - \boldsymbol{r}') \, \mathrm{d}\boldsymbol{r}' = \int A(\boldsymbol{r}') \nabla W(\boldsymbol{r} - \boldsymbol{r}') \, \mathrm{d}\boldsymbol{r}' \tag{2.12}$$

and expand it into the first order in the Taylor series:

$$\langle \nabla A \rangle(\boldsymbol{r}) = A(\boldsymbol{r}) \int \nabla W(\boldsymbol{r} - \boldsymbol{r}') \, \mathrm{d}\boldsymbol{r}' + \nabla A(\boldsymbol{r}) \int (\boldsymbol{r}' - \boldsymbol{r}) \otimes \nabla W(\boldsymbol{r} - \boldsymbol{r}') \, \mathrm{d}\boldsymbol{r}' + \mathcal{O}(h^2) \,, \tag{2.13}$$

where $\otimes$ denotes the outer product.

The discretization error is of the order $\mathcal{O}(h^2)$ even for the kernel gradient, provided the following gradient consistency conditions are satisfied:

$$\int \nabla W(\boldsymbol{r} - \boldsymbol{r}') \, \mathrm{d}\boldsymbol{r}' = \boldsymbol{0} \,, \tag{2.14}$$

$$\int (\boldsymbol{r}' - \boldsymbol{r}) \otimes \nabla W(\boldsymbol{r} - \boldsymbol{r}') \, \mathrm{d}\boldsymbol{r}' = \boldsymbol{1} \,, \tag{2.15}$$

where $\boldsymbol{1}$ is the identity matrix. Unlike the kernel consistency conditions 2.9 and 2.10, these conditions do not restrict the kernel gradient any further. Condition 2.14 is satisfied for any function $W(\boldsymbol{r})$ with compact support as a consequence of the divergence theorem. Condition 2.15 holds for all normalized kernels. However, we do not deal with integrals directly in the SPH equations but rather discretize them as sums over particles, as explained above. This leads to the following consistency equations expressed in discretized form:

$$\sum_j \frac{m_j}{\rho_j} \nabla W_{ij} = \boldsymbol{0} \,, \tag{2.16}$$

$$\sum_j \frac{m_j}{\rho_j} (\boldsymbol{r}_j - \boldsymbol{r}_i) \otimes \nabla W_{ij} = \boldsymbol{1} \,. \tag{2.17}$$

As these consistency conditions depend on particle positions, we cannot satisfy them by simply modifying the kernel function $W(\boldsymbol{r})$. Generally, they hold quite poorly when using the naïve kernel discretization given by Eq. 2.6. However, we can modify the gradient discretization to satisfy both conditions identically. This leads to a different discretization with the asymptotic error still equal to $\mathcal{O}(h^2)$, and the modified gradient will reconstruct all constant and linear functions precisely. This is often referred to as the first-order consistency of the SPH discretization.

2.1.2.3 Correction tensor. To obtain such a gradient, we need to compensate for the residuals given by the left-hand sides of equations 2.16 and 2.17. Using the first condition, we can modify the gradient by subtracting the term on the left-hand side multiplied by A_i, thus resulting in the gradient:

$$\langle \nabla A \rangle(\boldsymbol{r}_i) = \sum_j \frac{m_j}{\rho_j} (A_j - A_i) \nabla W(\boldsymbol{r}_i - \boldsymbol{r}_j) \,. \tag{2.18}$$

As the gradient depends only on the differences of values A_i, it will be identically zero for *constant* functions. We can further improve the gradient using the second consistency condition.

The residual on the right-hand side of 2.17 is a tensor, which generally differs from the identity tensor. We can compensate for this error by defining a correction tensor $\boldsymbol{C}_i$ as:

$$\boldsymbol{C}_i = \left(\sum_j \frac{m_j}{\rho_j} (\boldsymbol{r}_j - \boldsymbol{r}_i) \otimes \nabla W_{ij} \right)^{-1} . \tag{2.19}$$

Finally, the adjusted gradient is given by multiplying the kernel gradient by the correction tensor:

$$\langle \nabla A \rangle (\boldsymbol{r}_i) = \sum_j \frac{m_j}{\rho_j} (A_j - A_i) \boldsymbol{C}_i \nabla W(\boldsymbol{r}_i - \boldsymbol{r}_j) . \tag{2.20}$$

Such a gradient is first-order consistent, precisely reconstructing all *linear* function in the SPH discretization. The gradient here was used as a "proxy" derivative and the same method could be carried out to discretize other spatial derivatives, such as divergence $\nabla \cdot \boldsymbol{A}$ or curl $\nabla \times \boldsymbol{A}$.

This approach could be extended to regain consistency for a second or any higher order. It is possible to compute higher kernel moments and construct a moment matrix, which could then be inverted to compute a smoothing kernel consistent up to the n-th order. Such an approach is usually called the reproducing kernel particle method [Liu and Liu, 2003]

2.1.3 Second derivatives

Many evolution equations contain second spatial derivatives of quantities. The heat diffusion equation includes the Laplacian of temperature, the Navier-Stokes equations depend on second derivatives of the velocity field, etc. We thus need to find a suitable discretization for the second derivatives in SPH.

We first derive the SPH Laplacian. It could be discretized the same way as the gradient, using Eq. 2.18 with the Laplacian of the smoothing kernel in place of the gradient:

$$\langle \nabla^2 A \rangle (\boldsymbol{r}_i) = \sum_j \frac{m_j}{\rho_j} (A_j - A_i) \nabla^2 W_{ij} . \tag{2.21}$$

Such a straightforward discretization is however highly sensitive to particle disorder, due to the second derivative of the smoothing kernel. Instead, a more robust discretization is commonly used in SPH [Brookshaw, 1985; Price, 2012]. It is based on an integral approximation of the Laplacian and it can be written as:

$$\langle \nabla^2 A \rangle (\boldsymbol{r}_i) = -2 \sum_j \frac{m_j}{\rho_j} (A_j - A_i) \frac{\boldsymbol{r}_i - \boldsymbol{r}_j}{\|\boldsymbol{r}_i - \boldsymbol{r}_j\|^2} \cdot \nabla W_{ij} . \tag{2.22}$$

Compared to Eq. 2.21, it uses kernel gradient instead of the Laplacian and results in a more stable derivative. The difference is of order $\mathcal{O}(h^2)$, similarly to other modifications of the discretized derivatives.

Eq.2.22 can be also applied to vector quantities $\boldsymbol{A}$. Another frequently used second derivative of a vector quantity is the gradient of divergence $\nabla(\nabla \cdot \boldsymbol{A})$. The derivation of the SPH discretization

is more complex, see Español and Revenga [2003]. Using notation $\boldsymbol{A}_{ij} = \boldsymbol{A}_i - \boldsymbol{A}_j$ and $\boldsymbol{r}_{ij} = \boldsymbol{r}_i - \boldsymbol{r}_j$, the SPH version of the derivative can be expressed as [Price, 2012]:

$$\langle \nabla(\nabla \cdot \boldsymbol{A}) \rangle (\boldsymbol{r}_i) = -2 \sum_j \frac{m_j}{\rho_j} \left[(D+2)(\boldsymbol{A}_{ij} \cdot \boldsymbol{r}_{ij}) \boldsymbol{r}_{ij} - \boldsymbol{A}_{ij} \|\boldsymbol{r}_{ij}\|^2 \right] \frac{\boldsymbol{r}_{ij}}{\|\boldsymbol{r}_{ij}\|^4} \cdot \nabla W_{ij} \,, \tag{2.23}$$

where D is the number of spatial dimensions.

2.1.4 Smoothing length

The smoothing lengths h_j define the spatial resolution of the simulation. It is a quantity similar to the voxel size in grid-based methods. Each particle can generally have a different smoothing length.

The values of smoothing lengths are usually assigned so that the number of neighboring particles is approximately the same for all particles, thus spatially homogenizing the discretization error. This is achieved by using the following definition:

$$h_i = \eta \sqrt[D]{\frac{m_i}{\rho_i}} \,, \tag{2.24}$$

where η is a dimensionless constant, typically around 1.5, and D is the number of spatial dimensions. As the factor under the root represents the volume of particle i, the smoothing length h_i defined this way can be interpreted as an effective radius of the particle. However, the actual radius of the particle influence can be significantly larger, even infinite.

2.1.4.1 Iterative algorithm. The definition 2.24 of smoothing length h_i is unfortunately circular: it depends on density ρ_i, given by Eq. 2.5, which in turn depends on smoothing lengths of particles in the kernel support, including the i-th particle itself. Luckily, this is not a big obstacle. We can find a self-consistent solution using an iterative method. We first choose an initial guess of smoothing lengths, use it to compute the particle densities, subsequently use the densities to correct the smoothing lengths, and so on. The iterations are performed until the required precision has been reached; the sequence is typically quickly converging, so more than five iterations are rarely needed.

2.1.4.2 Adaptivity. As smoothing lengths do not change significantly between the time steps, it is often better to link the change of h_i with the change of density ρ_i rather than recompute h_i using the iterative approach every time step. This leads to a continuity equation for smoothing lengths, derived by taking a temporal derivative of Eq. 2.24:

$$\frac{\mathrm{d}h_i}{\mathrm{d}t} = -\frac{h_i}{D\rho_i} \frac{\mathrm{d}\rho_i}{\mathrm{d}t} \,. \tag{2.25}$$

This evolution equation handles adaptation of the spatial resolution during the simulation. Whenever density increases, the smoothing length is decreased to increase the spatial resolution. On the other hand, the particles naturally expand in low-density regions.

Eq. 2.25 is used if the density is evolved using the continuity equation; Eq. 2.24 is then only used to set up the initial conditions. When the summed density is used instead, the "integral" form given by Eq. 2.24 should be used for self-consistency. Density evolution is discussed in detail in Sec. 2.4.

2.1.4.3 Symmetrization. In order to satisfy the law of action and reaction and conserve the total momentum during the simulation (see Sec. 2.2), the kernel gradient needs to be antisymmetric with respect to the particle indices i and j, i.e. $\nabla W(\boldsymbol{r}_{ij}, h_i)$ must be equal to $-\nabla W(\boldsymbol{r}_{ji}, h_j)$. This is generally not true when particles have different smoothing lengths. To correct it, symmetrized smoothing lengths $\bar{h}_{ij}$ are used instead:

$$\bar{h}_{ij} = \frac{1}{2}(h_i + h_j)\,. \tag{2.26}$$

Alternatively, the smoothing kernel W itself can be symmetrized as:

$$\bar{W_{ij}} = \frac{1}{2}\left(W_{ij}(h_i) + W_{ij}(h_j)\right)\,. \tag{2.27}$$

Both approaches ensure the kernel gradient ∇W_{ij} is antisymmetric. We have used Eq. 2.26 in all simulations.

2.1.5 Kernels and their properties

The kernel is usually defined as a two-parameter function, $W = W(\boldsymbol{r}, h)$; here $\boldsymbol{r}$ is a generic position vector and h is the smoothing length. In practice, $\boldsymbol{r}$ is replaced by a difference of particle positions $\boldsymbol{r}_i - \boldsymbol{r}_j$. While the SPH discretization allows for quite generic smoothing kernels in theory, commonly used functions have a gaussian-like shape. This is a consequence of requirements, some of which were outlined in previous sections. We made the following observations:

- Kernel must be *normalized*, the volumetric integral of the kernel is thus:

$$\int_\Omega W(\boldsymbol{r}, h)\,\mathrm{d}\boldsymbol{r} = 1\,. \tag{2.28}$$

- Kernel must be an approximation of the Dirac δ-distribution, the function $W(\boldsymbol{r}, h)$ must approach $\delta(\boldsymbol{r})$ as the smoothing length h decreases to zero. In other words, the SPH interpolant $\langle A\rangle(\boldsymbol{r})$, defined by the integral approximation of function $A(\boldsymbol{r})$ by Eq. 2.2, must fulfill:

$$\lim_{h\to 0}\int_\Omega A(\boldsymbol{r}')\,W(\boldsymbol{r}-\boldsymbol{r}', h)\,\mathrm{d}\boldsymbol{r}' = A(\boldsymbol{r})\,. \tag{2.29}$$

- Kernel must be a symmetric function with respect to the position vector, thus:

$$W(\boldsymbol{r}) = W(-\boldsymbol{r})\,. \tag{2.30}$$

However, there is a number of additional requirements, arising from the stability analysis of the method [Swegle et al., 1995], physical considerations or simply practical reasons.

- Kernel should be a *smooth* function. As the kernel function enters into discretized equations as a gradient, a divergence, or a higher-order derivative, the minimum practical smoothness of the kernel is C^2, i.e. continuous up to the second derivative.

- Ideal kernel is a monotonically *decreasing* function. While this is not necessary to discretize the equations, the kernel value must decrease as interacting particles recede to ensure the stability of the method. Furthermore, it makes sense from the physical standpoint that the influence of the particle decreases at larger distances.
- Kernel has to be a strictly *non-negative* function. This property distinguishes SPH from other kernel-based methods, where kernels with negative values (such as Catmull-Rom kernel) can be conveniently used to achieve higher-order accuracy. In SPH, however, kernel values are directly linked to the bulk density of the material, hence the kernel must be non-negative everywhere to avoid unphysical negative densities in the simulation.
- The support of the kernel should be compact, i.e. there exists a number $\eta > 0$ so that:

$$\|\boldsymbol{r}\| > \eta h \longrightarrow W(\boldsymbol{r}, h) = 0\,. \tag{2.31}$$

  This requirement is only necessary for optimal performance of the code. A small value of η can significantly reduce the number of particle interactions that need to be calculated. For commonly used kernels, the value is in interval $2 \leq \eta \leq 4$. Importantly, using a kernel with twice the support radius means the number of neighbors increases roughly eight times in three-dimensional simulations, which is a considerable performance penalty.

2.1.5.1 B-spline kernels. We see that the gaussian function $g(\|\boldsymbol{r}\|/h)$ satisfies all the conditions except for the last one — gaussian has infinite support. For this reason, a widely used family of kernels are the polynomial B-spline kernels [Rosswog, 2009; Cossins, 2010; Price, 2012]. These functions are piece-wise polynomial approximations of the gaussian, but unlike the gaussian, they have compact support. Kernel M_n of the order $(n-1)$ is defined using the Fourier transform [Schoenberg, 1946]:

$$\mathrm{M}_n(r, h) = \frac{1}{2\pi} \int_{-\infty}^{\infty} \left(\frac{\sin(\omega h/2)}{\omega h/2} \right)^n \cos \omega r \, \mathrm{d}\omega\,. \tag{2.32}$$

The kernel used by a majority of SPH codes is a cubic B-spline M_4:

$$\mathrm{M}_4(r, h) = \frac{\sigma}{h^d} \begin{cases} \frac{1}{4}(2-q)^3 - (1-q)^3\,, & 0 \leq q < 1\,, \\ \frac{1}{4}(2-q)^3\,, & 1 \leq q < 2\,, \\ 0 & \text{otherwise,} \end{cases} \tag{2.33}$$

where $q = r/h$ and $\sigma = 2/3, 10/(7\pi), 1/\pi$ in $1, 2, 3$ dimensions, respectively. It is a C^2 function, the second derivative of which is a piece-wise linear function. The kernel support has radius $2h$.

For larger kernel support and thus more precise interpolation, one can use the fourth-order kernel M_5:

$$\mathrm{M}_5(r, h) = \frac{\sigma}{h^d} \begin{cases} (\frac{5}{2}-q)^4 - 5(\frac{3}{2}-q)^4 + 10(\frac{1}{2}-q)^4\,, & 0 \leq q < \frac{1}{2}\,, \\ (\frac{5}{2}-q)^4 - 5(\frac{2}{2}-q)^4\,, & \frac{1}{2} \leq q \leq \frac{3}{2}\,, \\ (\frac{5}{2}-q)^4\,, & \frac{3}{2} \leq q < \frac{5}{2}\,, \\ 0 & \text{otherwise,} \end{cases} \tag{2.34}$$

where $\sigma = 1/24, 96/(1199\pi), 1/(20\pi)$ in $1, 2, 3$ dimensions, respectively. Similarly, higher-order kernels can be constructed. The higher the order, the larger the kernel support and the closer the function approaches the gaussian.

Many additional kernels with various properties can be found in the literature, such as the Wendland functions [Wendland, 1995], the core triangle kernel [Read et al., 2010], the modified M_4 kernel with non-zero central gradient [Thomas and Couchman, 1992] or the linear quartic kernel [Valcke et al., 2010]. They differ in interpolation accuracy, stability properties, etc.

Standard SPH kernels only depend on the ratio $q = \boldsymbol{r}/h$ rather than on each variable separately. Kernel functions can be thus written as:

$$W(\boldsymbol{r}, h) = \frac{1}{h^D} w\left(\frac{\|\boldsymbol{r}\|}{h}\right), \tag{2.35}$$

where $w(q)$ is a function of the dimensionless parameter q and D is the number of spatial dimensions. In this form, the kernels are *isotropic* functions as they depend only on the magnitude $\|\boldsymbol{r}\|$.

2.1.5.2 Anisotropic kernels. While this is the most common form of kernel functions, it might be worthwhile to consider anisotropic kernels, especially for inherently anisotropic problems, such as linear shock wave propagation. This is a core of the adaptive smoothed particle hydrodynamics [Owen et al., 1998], or ASPH, where the smoothing lengths h are replaced by the symmetric anisotropy tensors $\boldsymbol{G}$. The kernel function then has a more general form:

$$W(\boldsymbol{r}, \boldsymbol{G}) = |\det \boldsymbol{G}| \cdot w(\|\boldsymbol{G}\boldsymbol{r}\|), \tag{2.36}$$

This form reduces to the isotropic function for $\boldsymbol{G} = h^{-1}\mathbf{1}$.

2.1.5.3 Kernel look-up tables. In high-performance SPH codes, values of the kernel function and its derivatives are usually tabulated. For given q, the code reads the two closest values from a look-up table and computes the kernel value using a linear interpolation. Additional optimization can be made by using q^2 rather than q as the key of the look-up table, thus avoiding the expensive square root during kernel evaluation. Similarly, the tabulated values of kernel gradients are divided by q, the gradient is then computed from the look-up table (lut) as:

$$\nabla W(\boldsymbol{r}, h) = \frac{\boldsymbol{r}}{h^{D+2}} \operatorname{lut}\left(\frac{\|\boldsymbol{r}\|^2}{h^2}\right). \tag{2.37}$$

2.2 Lagrange equations

There is considerable freedom in choosing the SPH discretization. We can adopt gradients that constrain local discretization errors; however, constraining *global* errors is more complex, as it cannot be determined by discretization of a single term in the set of equations. To ensure that the total energy is conserved in SPH formalism, the equation of motion has to be consistent with the energy equation; changing one implies the other has to be modified as well.

2.2.1 Derivation of discretized equations

Unlike the local error minimization, it is not immediately obvious how the set of equations should be derived in order to conserve the integrals of motion. To obtain a set of *conservative* SPH equations, we follow a different strategy than previously. Rather than starting from the gradient and deriving the equations "from-bottom-to-top", we start by specifying the Lagrangian $\mathscr{L}$ of the system and derive the equations "from-top-to-bottom", using the Lagrange equations:

$$\frac{\mathrm{d}}{\mathrm{d}t}\left(\frac{\partial \mathscr{L}}{\partial \boldsymbol{v}_i}\right) = \frac{\partial \mathscr{L}}{\partial \boldsymbol{r}_i}\,. \tag{2.38}$$

For simplicity, we assume a fluid-like material and neglect the self-gravitation and external potential forces; the derived equations can be generalized to account for material strength (see Sec. 2.3) and gravitation (see Sec. 2.12).

The Lagrangian can be naturally defined as a difference of the kinetic and the internal energies of all particles:

$$\mathscr{L} = \sum_j \left(\frac{1}{2} m_j \boldsymbol{v}_j^2 - m_j u_j\right)\,. \tag{2.39}$$

The left-hand side of Eq. 2.38 can be evaluated by assuming the internal energy u_j does not depend on particle velocities $\boldsymbol{v}_i$. Hence:

$$\frac{\mathrm{d}}{\mathrm{d}t}\left(\frac{\partial \mathscr{L}}{\partial \boldsymbol{v}_i}\right) = m_i \frac{\mathrm{d}\boldsymbol{v}_i}{\mathrm{d}t}\,. \tag{2.40}$$

The derivative of the Lagrangian with respect to particle positions $\boldsymbol{r}_i$ can be found by taking into account the first law of thermodynamics. In intensive quantities, it can be written as:

$$\mathrm{d}u_j = T_j \mathrm{d}s_j + \frac{P_j}{\rho_j^2}\mathrm{d}\rho_j\,, \tag{2.41}$$

where T_j is the temperature and s_j is the specific entropy of the j-th particle. The Lagrangian derivative is thus:

$$\frac{\partial \mathscr{L}}{\partial \boldsymbol{r}_i} = -\sum_j m_j \left(T_j \frac{\partial s_j}{\partial \boldsymbol{r}_i} + \frac{P_j}{\rho_j^2}\frac{\partial \rho_j}{\partial \boldsymbol{r}_i}\right)\,. \tag{2.42}$$

By further assuming an *adiabatic* process, $\mathrm{d}s_j = 0$, the only remaining unknown term in the equation of motion is the derivative of density ρ_j at the position of particle j with respect to the position $\boldsymbol{r}_i$ of particle i. This is finally where the SPH density discretization 2.5 comes into play. As positions $\boldsymbol{r}_j$ are independent coordinates of the configuration space, the gradient can be written as:

$$\frac{\partial \rho_j}{\partial \boldsymbol{r}_i} = \sum_k m_k \frac{\partial W_{jk}}{\partial \boldsymbol{r}_i} = \sum_k m_k (\delta_{ji} - \delta_{ki}) \nabla W_{jk}\,. \tag{2.43}$$

By plugging the derived gradient back into Eq. 2.38, we obtain the equation of motion for the i-th particle:

$$\boxed{\frac{\mathrm{d}\boldsymbol{v}_i}{\mathrm{d}t} = \sum_j m_j \left(\frac{P_i}{\rho_i^2} + \frac{P_j}{\rho_j^2}\right)\nabla W_{ij}\,.} \tag{2.44}$$

The continuity equation can be determined analogously, by computing the temporal derivative of density from equation 2.5. Using the chain rule, we find:

$$\boxed{\frac{\mathrm{d}\rho_j}{\mathrm{d}t} = \sum_k m_k \frac{\mathrm{d}W_{jk}}{\mathrm{d}t} = \sum_k m_k (\boldsymbol{v}_j - \boldsymbol{v}_k) \cdot \nabla W_{jk} \,.} \tag{2.45}$$

The remaining equation is the energy equation, which can now be easily written down by taking the temporal derivative of Eq. 2.41:

$$\frac{\mathrm{d}u_j}{\mathrm{d}t} = \frac{P_j}{\rho_j^2} \frac{\mathrm{d}\rho_j}{\mathrm{d}t} \,. \tag{2.46}$$

Using the previous result for density derivative, we find:

$$\boxed{\frac{\mathrm{d}u_i}{\mathrm{d}t} = \frac{P_i}{\rho_i^2} \sum_j m_j (\boldsymbol{v}_i - \boldsymbol{v}_j) \cdot \nabla W_{ij} \,.} \tag{2.47}$$

2.2.2 Properties of Lagrangian-based equations

The continuity equation, the equation of motion and the energy equation (together with the equation of state) form a closed set of first-order differential equations. We immediately see that the derived set of equations has several desirable properties.

2.2.2.1 Conservation of integrals of motion. When using the derived set of equations, the total linear momentum, total angular momentum as well as total energy are conserved during the simulation [Rosswog, 2009; Price, 2012]. This is undoubtedly a great strength of the SPH. The conservative property arises from a suitable symmetrization of the equation of motion 2.44 in indices i and j. As the kernel gradient is an antisymmetric function (i.e. changes its direction when indices i and j are swapped), the force exerted by particle i on particle j has the same magnitude but opposite direction than the force exerted by particle j on particle i, thus satisfying the principle of action and reaction. To verify the linear momentum is indeed conserved, we can write down the temporal derivative of the total momentum vector $\boldsymbol{p}$:

$$\frac{\mathrm{d}\boldsymbol{p}}{\mathrm{d}t} = \sum_i m_i \frac{\mathrm{d}\boldsymbol{v}_i}{\mathrm{d}t} = \sum_i \sum_j m_i m_j \left(\frac{P_i}{\rho_i^2} + \frac{P_j}{\rho_j^2} \right) \nabla W_{ij} = \boldsymbol{0} \,, \tag{2.48}$$

where the last equality stems from summing over a product of a symmetric and antisymmetric term. Therefore, the total momentum $\boldsymbol{p}$ must be constant. A similar argument can be made for the total angular momentum. Finally, the conservation of total energy comes from the consistent discretization of the energy equation. It can be confirmed by taking a derivative of the Hamiltonian H:

$$\frac{\mathrm{d}H}{\mathrm{d}t} = \sum_i \left(m_i \boldsymbol{v}_i \cdot \frac{\mathrm{d}\boldsymbol{v}_i}{\mathrm{d}t} + m_i \frac{\mathrm{d}u_i}{\mathrm{d}t} \right) \tag{2.49}$$

and by plugging in Eqs. 2.44 and 2.47. We obtain:

$$\frac{\mathrm{d}H}{\mathrm{d}t} = -\sum_{i,j} m_i m_j \left(\frac{P_i}{\rho_i^2} \boldsymbol{v}_j + \frac{P_j}{\rho_j^2} \boldsymbol{v}_i \right) \cdot \nabla W_{ij} = 0 \,, \tag{2.50}$$

where we utilized the antisymmetry of ∇W_{ij} as before.

2.2.2.2 Galilean invariance. The SPH equations have the same outcome regardless of the selected inertial reference frame. This can be readily seen from Eq. 2.45 and Eq. 2.47. As both equations depend only on velocity differences $\boldsymbol{v}_i - \boldsymbol{v}_j$, adding a constant velocity to all particles does not change the derivatives of quantities. It also implies that when the body moves with a constant velocity, i.e. all particles have the same velocity vector, its density and specific energy remain constant. The Galilean invariance is a big advantage of SPH over grid-based Eulerian methods, where the solution generally depends on (and it may be highly sensitive to) the velocity of the continuum with respect to the computational grid [Wadsley et al., 2008; Robertson et al., 2010].

2.2.2.3 Regularization of the particle distribution. Unlike the velocity field, the pressure gradient in the equation of motion 2.44 is symmetrized using a *sum* of particle pressures rather than their difference. As explained previously, such a symmetrization is necessary to conserve integrals of motion. Consequently, in case all particles have the same pressure value, the computed pressure gradient is generally *not* exactly zero. While this seems like an undesirable feature of the discretization, it actually improves the interpolation properties of the kernel in a long run. Pressure gradients emerge due to particle disorder and they act as repelling forces, pushing particles away from each other. The gradient will disappear if the neighboring particles are symmetrically and uniformly distributed around the reference particle, making it an ideal state for the evaluation of SPH derivatives. Mathematically, this is expressed by the consistency conditions 2.16 and 2.17. Although correcting pressure gradient by a constant factor (similarly as the velocity field in Eq. 2.45) would identically satisfy the condition 2.16 — regardless of particle distribution — condition 2.17 and higher moments would not be generally satisfied. By using the derived symmetrization of pressure gradient, the particles will be automatically driven towards a configuration that meets the consistency conditions [Price, 2012]. This is a significant advantage over other possible SPH discretizations, where some *ad hoc* regularization term has to be added in order to provide an analogous mechanism [Dilts, 1999].

2.3 Equations for viscous fluids and solid bodies

In simulations of ideal fluids, the forces inside the medium are determined by pressure gradients only. However, fluids with non-negligible viscosity, granular materials with internal friction or solid bodies with material strength require a more general treatment, as the internal forces are specified by the stress tensor $\boldsymbol{\sigma}$ rather than the scalar pressure P.

2.3.1 Equation of motion and energy equation

In the SPH formalism, this means we have to assign a symmetric stress tensor $\boldsymbol{\sigma}_i$ to each particle. It is useful to split the tensor into an isotropic part, given by the pressure P_i, and a deviatoric stress tensor $\boldsymbol{S}_i$:

$$\boldsymbol{\sigma}_i = \boldsymbol{S}_i - P_i \mathbf{1} \,. \tag{2.51}$$

As the internal forces result from the stress divergence instead of pressure gradient, the equation of motion can be obtained by generalizing Eq. 2.44, replacing the particle pressures with stress tensors:

$$\frac{\mathrm{d}\boldsymbol{v}_i}{\mathrm{d}t} = -\sum_j m_j \left(\frac{\boldsymbol{\sigma}_i}{\rho_i^2} + \frac{\boldsymbol{\sigma}_j}{\rho_j^2} \right) \cdot \nabla W_{ij} \,. \tag{2.52}$$

Due to the symmetrical form of the bracketed term, the action–reaction principle still holds, implying the total linear momentum is still conserved in this discretization. However, the direction of the force vector between two particles i and j is generally different than the relative position $\boldsymbol{r}_i - \boldsymbol{r}_j$. As a consequence, the total angular momentum is no longer conserved. This issue is addressed in Sec. 2.3.3.

Likewise, the energy equation needs to be supplemented by a viscous heating term. If we define the velocity divergence as:

$$\nabla \cdot \boldsymbol{v}_i = \sum_j m_j (\boldsymbol{v}_j - \boldsymbol{v}_i) \cdot \nabla W_{ij} \tag{2.53}$$

and the strain rate as a symmetrized velocity gradient:

$$\dot{\boldsymbol{\epsilon}}_i = \frac{1}{2} \sum_j m_j \big((\boldsymbol{v}_j - \boldsymbol{v}_i) \otimes \nabla W_{ij} + \nabla W_{ij} \otimes (\boldsymbol{v}_j - \boldsymbol{v}_i) \big) \,, \tag{2.54}$$

we can write down the energy equation as:

$$\frac{\mathrm{d}u_i}{\mathrm{d}t} = -\frac{P_i}{\rho_i} \nabla \cdot \boldsymbol{v}_i + \frac{1}{\rho_i} \boldsymbol{S}_i \,:\, \dot{\boldsymbol{\epsilon}}_i \,, \tag{2.55}$$

where $\boldsymbol{S}_i \,:\, \dot{\boldsymbol{\epsilon}}_i = \sum_{\alpha,\beta} S_i^{\alpha\beta} \dot{\epsilon}_i^{\alpha\beta}$ is the double-dot product.

2.3.2 Constitutive relation

Since we added a new independent quantity — the deviatoric stress $\boldsymbol{S}_i$ — we have to add a corresponding equation to close the set. The equation determining the stress tensor is different for fluids and solids. In fluids, the stress tensor represents the viscosity and it thus depends on the velocity gradient $\nabla \boldsymbol{v}_i$. In the Navier-Stokes equations, the dependence is linear and it can be written as [Landau and Lifshitz, 1987]:

$$\boldsymbol{S}_i = 2\mu_\mathrm{d} \left(\dot{\boldsymbol{\epsilon}}_i - \frac{\mathbf{1}}{3} \nabla \cdot \boldsymbol{v}_i \right) \,, \tag{2.56}$$

where μ_d is the dynamic viscosity of the fluid.

For solid bodies, the stress is an outcome of the material strength. It depends on the displacement of the material from its reference configuration rather than its velocity field. To avoid storing the reference configuration of particles, we can use the strain rate $\dot{\boldsymbol{\epsilon}}_i$ in place of the strain $\boldsymbol{\epsilon}_i$ and define an evolution equation for the deviatoric stress $\boldsymbol{S}_i$. The most simple stress-strain dependence is linear, as described by Hooke's law, hence we have a linear dependence between the stress derivative and the strain rate:

$$\frac{\mathrm{d}\boldsymbol{S}_i}{\mathrm{d}t} = 2\mu\left(\dot{\boldsymbol{\epsilon}}_i - \frac{\mathbf{1}}{3}\nabla\cdot\boldsymbol{v}_i\right), \tag{2.57}$$

where μ is the shear modulus of the material. The right-hand side of this equation is the same as in Eq. 2.56, only the material constant differs. For fluids, the deviatoric stress tensor $\boldsymbol{S}_i$ can be computed directly from the state of the simulation, for solids, however, the stress tensor has to be integrated in time from the specified initial conditions.

2.3.3 Bulk rotation

In simulations with viscosity or material strength, the total angular momentum is not generally conserved. This creates problems especially in simulations with rotation, such as in viscous circumstellar disks or rotating solid bodies. If left untreated, the spin rate of rotating bodies would decrease over time until the bodies stop completely, which would prohibit long-term simulations.

The issue stems from the discretization of velocity gradient 2.54 and divergence 2.53. As described in Sec. 2.1.2, these spatial derivatives are zero-order consistent, ensuring that constant velocities remain constant after discretization, but more complex flows are inevitably inaccurate due to discretization errors. It works quite well for translational motion, but even a rotation with a constant spin rate gives rise to unphysical velocity gradients. The rotation of a body is misinterpreted as its deformation due to imprecise discretization. These deformations in turn induce stresses inside the body, creating forces that act in the direction opposite to the rotation, gradually slowing down the body and losing its angular momentum.

This inconsistency can be corrected by making the velocity gradient first-order consistent. We introduce the correction tensor $\boldsymbol{C}$ as [Schäfer et al., 2016]:

$$\boldsymbol{C}_i = \left(\sum_j \frac{m_j}{\rho_j}(\boldsymbol{r}_j - \boldsymbol{r}_i)\otimes\nabla W_{ij}\right)^{-1}. \tag{2.58}$$

In case the bracketed matrix is not invertible, the Moore-Penrose pseudo-inverse [Penrose, 1955] is used instead. Using the correction tensor, we obtain the following corrected continuity equation:

$$\frac{\mathrm{d}\rho_i}{\mathrm{d}t} = \sum_j m_j(\boldsymbol{v}_i - \boldsymbol{v}_j)\cdot\boldsymbol{C}_i\nabla W_{ij}\,. \tag{2.59}$$

The corrected equation of motion can be found similarly, taking into account the symmetrization of interacting particles:

$$\frac{\mathrm{d}\boldsymbol{v}_i}{\mathrm{d}t} = -\sum_j m_j\left(\frac{\boldsymbol{\sigma}_i}{\rho_i^2}\cdot\boldsymbol{C}_i\nabla W_{ij} + \frac{\boldsymbol{\sigma}_j}{\rho_j^2}\cdot\boldsymbol{C}_j\nabla W_{ij}\right). \tag{2.60}$$

Lastly, the energy equation has to be corrected as well, using the correction tensor for the kernel gradient in both the velocity divergence and the strain rate.

The first-order consistency significantly increases the discretization accuracy. Although the total angular momentum is still not conserved exactly, the correction tensor greatly improves the conservation and allows for solid bodies rotating with a constant spin rate. We verify this on a simple test simulation in Sec. 3.5.

2.4 Density evolution

There are two different approaches to evolving the density in SPH simulations. These are usually called the *direct summation* and the *continuity equation*. The former uses Eq. 2.5 to compute the density from immediate positions, masses and smoothing lengths of particles, while the latter treats the density as an independent quantity, which is evolved using the first-order differential equation 2.45. There are pros and cons to both approaches, so one must choose the approach that fits better to the problem being solved.

The conceptual difference of the direct sum and the continuity equation can be seen if we write the density using the integral SPH interpolant rather than the sum. The discretized interpolant reads:

$$\langle\rho\rangle(\boldsymbol{r}) = \int \rho(\boldsymbol{r}')\, W(\boldsymbol{r}-\boldsymbol{r}')\, \mathrm{d}\boldsymbol{r}' \,. \tag{2.61}$$

The continuity equation is a differential equation and thus requires all quantities to be differentiable, while the directly summed density is essentially a solution of an integral equation and it has no such requirements. The density field computed using Eq. 2.61 allows for non-differentiable or even discontinuous density $\rho(\boldsymbol{r}')$.

2.4.1 Discontinuities in density

Since the continuity equation 2.45 has been derived by computing the temporal derivative of 2.5, both formulations yield identical results (neglecting the error caused by discretization for the moment) if the assumptions are satisfied, in particular if the density and the velocity are continuous and smooth quantities. However, the solutions will differ if the discontinuities are present. It can be shown by computing the temporal derivative of the continuity equation:

$$\int \left(\frac{\partial \rho}{\partial t} + \nabla \cdot (\rho \boldsymbol{v}) \right) W(\boldsymbol{r}-\boldsymbol{r}')\, \mathrm{d}\boldsymbol{r}' = 0 \,. \tag{2.62}$$

After rearranging the terms and going from integral form to particle discretization, we get [Price, 2008]:

$$\sum_j m_j (\boldsymbol{v}_i - \boldsymbol{v}_j) \cdot \nabla W_{ij} = \frac{\mathrm{d}}{\mathrm{d}t} \sum_j m_j W_{ij} + \oint \rho \boldsymbol{v} W(\boldsymbol{r}_i - \boldsymbol{r}') \cdot \mathrm{d}\boldsymbol{\Gamma}' \,. \tag{2.63}$$

The left-hand side is the continuity equation 2.45, while the right-hand side is the temporal derivative of the directly summed density 2.5 *plus* an extra surface term. Provided the kernel $W(\boldsymbol{r})$ has finite support, this term would disappear if both the density ρ and velocity $\boldsymbol{v}$ were

differentiable. In presence of discontinuities, however, the term is generally non-zero and it is missing in the density solution based on the continuity equation. For this reason, the direct summation is more robust and preferred if strong shocks are expected in the simulation [Price, 2008].

2.4.2 Density at free surfaces

Unfortunately, the direct summation is not the "magic wand", it has problems of its own. Namely, it has troubles reconstructing the density field at free surfaces of bodies and material interfaces [Reinhardt and Stadel, 2017; Emsenhuber et al., 2018]. The problem is rooted in the isotropy of the smoothing kernel W. The kernel support is incomplete at free surfaces, as neighbors occupy only half of the space and thus the evaluated density will be only about *half* of the material density, creating an artificial low-density "atmosphere" near the surface. There are ways to mitigate the problem, such as using ghost particles to fill the empty half of the kernel or the corrective SPH density discretization [Liu and Liu, 2003]:

$$\rho_i = \frac{\sum_j m_j W_{ij}}{\sum_j \frac{m_j}{\rho_j} W_{ij}} \,. \tag{2.64}$$

In this equation, the SPH density estimate is divided by a factor representing the completeness of the kernel support. It is an implicit equation, the density ρ_i is present on both the left-hand side and the right-hand side of Eq. 2.64, and it needs to be computed by an iterative method. It does not necessarily imply an additional overhead, though; if the smoothing length is computed using Eq. 2.24, a self-consistent iterative solution is necessary anyway, so the corrective SPH approach only modifies the expression for density evaluation.

The continuity equation 2.45 has no issues at surfaces because the density only changes when the body is compressed or expanded, otherwise it keeps the material density assigned by the initial conditions. Such a fine control of density is especially important for weakly-compressible materials, i.e. solids or liquids, where even a minor density difference may lead to a large pressure gradient.

On the other hand, the evolved density is not constrained in any way and may get arbitrarily low in a divergent flow. The density often appears in the denominator of the SPH equations, therefore tiny values of density make the numerical scheme severely unstable. To avoid instabilities, we set the minimal value of density to the implicit minimal value of summed density, using 2.5 for an isolated particle with no neighbors:

$$\rho_{\min} = \min_i m_i W(\mathbf{0}, h_i) \,. \tag{2.65}$$

2.4.3 Performance considerations

Finally, the direct sum contrasts with the evolution equation from the implementation point of view. As the density appears on the right-hand side of the equation of motion and other evolution equations, it is necessary to first compute the density using Eq. 2.5 and then use the updated density to evaluate the pressure gradient and other SPH derivatives. Consequently, the

direct sum approach requires *at least two* loops over all particle pairs in each time step. On the other hand, the continuity equation is simply another evolution equation to be evaluated and requires no special handling. Unless other modifications of the standard SPH scheme are used, only a single loop over particle pairs is required if the continuity equation is used and it thus usually outperforms the direct sum approach.

2.5 Energy-conserving discretization

For simulations with ideal gas or other inviscid fluids, the total energy is conserved, as discussed in Sec. 2.2. However, the conservation of energy is no longer guaranteed if there are forces due to viscosity or internal friction, although the change of the total energy is often small and does not pose any problem.

In some cases, such as weak cratering impacts, we found that the energy growth can be prohibitive. To mitigate the issue, we implemented an alternative way to evolve the internal energy, using a compatibly-differenced scheme [Owen, 2014]. Instead of computing the energy derivative, the energy change is computed directly from particle pair-wise accelerations $\boldsymbol{a}_{ij}$ and half-step velocities $\bar{\boldsymbol{v}}_i = \boldsymbol{v}_i + \frac{1}{2}\boldsymbol{a}_i \Delta t$, using the equation:

$$\Delta u_i = \sum_j f_{ij} (\bar{\boldsymbol{v}}_j - \bar{\boldsymbol{v}}_i) \cdot \boldsymbol{a}_{ij} \Delta t \,, \tag{2.66}$$

where Δt is the current time step and f_{ij} the energy partitioning factors. They can be chosen arbitrarily, provided they fulfill the constraint $f_{ij} + f_{ji} = 1$. With this form of the SPH, the total energy can be conserved to machine precision, at a cost of performance overhead.

There is a freedom in the choice of factors f_{ij}, the total energy is conserved regardless of factor definition. However, they have to be chosen so that the simulation behaves physically. Namely, the second law of thermodynamics should be satisfied, i.e. the heat should flow from hotter particles to colder particles. Frontiere et al. [2017] suggested physically-motivated definition of the factors f_{ij}, using specific entropies s_i of particles:

$$f_{ij} = \begin{cases} \dfrac{s_{\min}}{s_{\min} + s_{\max}} \,, & \Delta u_{ij}(s_i - s_j) \geq 0 \,, \\ \dfrac{s_{\max}}{s_{\min} + s_{\max}} \,, & \Delta u_{ij}(s_i - s_j) < 0 \,, \end{cases} \tag{2.67}$$

where $s_{\min} = \min(s_i, s_j)$ and $s_{\max} = \max(s_i, s_j)$. Such a definition is quite simple and suitable for studies of adiabatic problems, however, the specific entropies s_i are not always known. They can be easily computed for the equation of state of ideal gas:

$$s_i = \frac{P_i}{\rho_i^\gamma} \,, \tag{2.68}$$

where γ is the adiabatic index. Unfortunately, there is no straightforward way to obtain s_i in simulations involving solid materials, as Tillotson's equation of state 2.102 only defines the relationship $P = P(\rho, u)$; there is no closed-form formula for entropy s_i, just as no formula exists for temperature T_i.

In the general case, we use *ad hoc* partitioning factors f_{ij} introduced by Owen [2014]. They are constructed to mimic the behavior of Eq. 2.67, but using particle energies only. First, we define the smoothly variation diminishing factor f_{ij}^{sm} as:

$$f_{ij}^{\text{sm}} = \frac{1}{2}\left(1 + \frac{u_{ji}\,\text{sgn}(\Delta E_{ij})}{|u_{ji}| + \frac{1}{1+|u_{ji}|}}\right), \tag{2.69}$$

where $\Delta E_{ij} = m_i \Delta u_{ij}/f_{ij}$. Second, a strictly monotonic variation diminishing factor f_{ij}^{mono} is defined. Given $A = \Delta E_{ij}/u_{ji}$ and $B = A/m_i$ if $A \geq 0$ and $B = A/m_j$ otherwise, we define:

$$f_{ij}^{\text{mono}} = \begin{cases} \max(0, \text{sgn}(B)), & |B| \leq 1, \\ \dfrac{m_i}{\Delta E_{ij}}\left(\dfrac{\Delta E_{ij} + m_i u_i + m_j u_j}{m_i + m_j} - u_i\right), & |B| > 1. \end{cases} \tag{2.70}$$

Finally, the partitioning factors f_{ij} are computed by a linear interpolation as:

$$f_{ij} = (1-\chi) f_{ij}^{\text{sm}} + \chi f_{ij}^{\text{mono}}, \tag{2.71}$$

using the weight χ given by:

$$\chi = \frac{|u_j - u_i|}{|u_i| + |u_j| + \epsilon}, \tag{2.72}$$

where ϵ is a small number to avoid numerical instabilities.

2.6 Artificial terms

The SPH interpolant 2.4 can reasonably approximate the original function only if the function is sufficiently smooth. If the function contains steep spikes or oscillations, the discretization error introduced by smoothing the function with the kernel may be significant. The problem is even more serious for discontinuous functions, as the continuum in SPH description is continuous by construction and thus cannot accurately represent discontinuities.

2.6.1 Discontinuities in SPH discretization

Unfortunately, discontinuities are quite common in the astrophysical context. They appear on the fronts of shock waves, at the interfaces of different materials, etc. The standard formulation of SPH cannot properly handle these discontinuities, because the assumption of differentiability was used to derive the set of evolution equations. If no such assumption was made, the discontinuities would manifest as additional surface terms in the equations [Colagrossi et al., 2009], similarly to the integrated density in Sec. 2.4. We can show that by expressing the SPH gradient of a generic quantity A:

$$\langle \nabla A \rangle(\boldsymbol{r}) = \int \frac{\partial}{\partial \boldsymbol{r}'}\big(A(\boldsymbol{r}')\,W(\boldsymbol{r}-\boldsymbol{r}')\big)\,\mathrm{d}\boldsymbol{r}' + \int A(\boldsymbol{r}')\,\nabla W(\boldsymbol{r}-\boldsymbol{r}')\,\mathrm{d}\boldsymbol{r}', \tag{2.73}$$

where we utilized the fact that $\nabla W(-\boldsymbol{r}) = -\nabla W(\boldsymbol{r})$. This leads to the identity:

$$\langle \nabla A \rangle(\boldsymbol{r}) = \oint A(\boldsymbol{r}') W(\boldsymbol{r} - \boldsymbol{r}') \, \mathrm{d}\boldsymbol{\Gamma}' + \int A(\boldsymbol{r}') \nabla W(\boldsymbol{r} - \boldsymbol{r}') \, \mathrm{d}\boldsymbol{r}' \,. \tag{2.74}$$

The first term in the equation disappears as long as the function $A(\boldsymbol{r})$ is continuous and has bound support. In the presence of a discontinuity, however, the surface terms generally remain and they are neglected in the standard SPH formulation.

Computing a surface integral in the SPH discretization is rather complex (albeit surely possible), as smoothed particles are volumetric objects by nature with no topological information specifying the connectivity to other particles. Hence, there is no straightforward way to obtain the surface element for a given particle, or even determine whether the particle lies on the surface (cf. Sec. 2.14).

We can avoid the troubles by getting rid of the discontinuities in the first place. A possible solution is to add a discontinuity-capturing term to the evolution equation of the discontinuous state quantities [Price, 2008]. Such a term smooths the step in quantity over several particles, getting rid of the discontinuity and allowing the SPH to handle the discontinuity naturally.

2.6.1.1 Diffusivity. Considering the discontinuity-capturing term is purely numerical, the smoothing effect can be achieved arbitrarily. Specifically, it does not need to be a smoothing or diffusion term introduced by some physical process; it can be problem-independent and simply appear as another term on the right-hand side of the evolution equation. Nevertheless, it is common to base the diffusion term for quantity A on the Laplacian $\nabla^2 A$, which is inspired by the diffusion equation. The diffusion term can be written as:

$$\left(\frac{\mathrm{d}A_i}{\mathrm{d}t}\right)_{\mathrm{dif}} = \eta \nabla^2 A_i \,, \tag{2.75}$$

where η is as-of-yet unspecified diffusivity factor. Unlike the physical terms, the numerical diffusion has to be *dependent* on spatial resolution and it shall converge to zero when the resolution approaches infinity. Consequently, we set the diffusivity η proportional to the spacing of particles:

$$\eta = \frac{1}{2} \alpha w_{ij} \|\boldsymbol{r}_i - \boldsymbol{r}_j\| \,, \tag{2.76}$$

where the dimensionless constant α determines the magnitude of the smoothing and w_{ij} is the signal speed. As explained below, the signal speed must be carefully selected for each quantity.

Using Eq. 2.22 to discretize the Laplacian in the SPH, we finally obtain a generic expression for the diffusion term:

$$\left(\frac{\mathrm{d}A_i}{\mathrm{d}t}\right)_{\mathrm{dif}} = \sum_j \alpha w_{ij} \frac{m_j}{\rho_j} (A_i - A_j) \, \hat{\boldsymbol{r}}_{ij} \cdot \nabla W_{ij} \,, \tag{2.77}$$

where $\hat{\boldsymbol{r}}_{ij} = (\boldsymbol{r}_i - \boldsymbol{r}_j)/\|\boldsymbol{r}_i - \boldsymbol{r}_j\|$. The density ρ_j in the denominator is often symmetrized, i.e. replaced by $\overline{\rho}_{ij} = (\rho_i + \rho_j)/2$, to make the whole smoothing term symmetric with respect to particles i and j.

2.6.2 Artificial viscosity

Historically, the first equation that was modified to properly handle shocks was the equation of motion [Monaghan, 1989]. An SPH formulation with no smoothing terms leads to obvious issues when shock waves are involved, such as particle interpenetration and unphysical oscillations in the pressure field after the shock wave passes. To resolve these problems, we add a numerical term into the equation of motion called the artificial viscosity.

2.6.2.1 Riemann-based viscosity. There is a number of possible approaches to construct a numerical viscosity term. A straightforward way is to use the diffusion term 2.77 derived above, with velocities $\boldsymbol{v}$ in place of the generic quantity A. This leads to the artificial viscosity initially introduced by Monaghan [1997]:

$$\left(\frac{\mathrm{d}\boldsymbol{v}_i}{\mathrm{d}t}\right)_{\mathrm{av}} = \sum_j \alpha w_{ij} \frac{m_j}{\overline{\rho}_{ij}} (\boldsymbol{v}_i - \boldsymbol{v}_j) \cdot \hat{\boldsymbol{r}}_{ij} \nabla W_{ij} \,. \tag{2.78}$$

The numerical viscosity is only needed to resolve the shock fronts, it is undesirable to increase the viscosity in divergent flows. Therefore, the viscosity term is set to zero if $(\boldsymbol{v}_i - \boldsymbol{v}_j) \cdot \hat{\boldsymbol{r}}_{ij} > 0$.

The signal speed is estimated using the exact solution of Riemann problem:

$$w_{ij} = c_i + c_j - 3(\boldsymbol{v}_i - \boldsymbol{v}_j) \cdot \hat{\boldsymbol{r}}_{ij} \,, \tag{2.79}$$

where c_i is the sound speed of particle i. For a consistent and conservative formulation, a corresponding term has to be added into the energy equation:

$$\left(\frac{\mathrm{d}u_i}{\mathrm{d}t}\right)_{\mathrm{av}} = \sum_j \left(-\frac{\alpha w_{ij}}{2} \frac{m_j}{\overline{\rho}_{ij}} (\boldsymbol{v}_{ij} \cdot \hat{\boldsymbol{r}}_{ij})^2 \right) \hat{\boldsymbol{r}}_{ij} \cdot \nabla W_{ij} \,. \tag{2.80}$$

2.6.2.2 Standard viscosity. Although Eq. 2.78 is naturally based on the general form for the diffusion operator, it is common to use a different, somewhat *ad hoc* numerical viscosity in SPH codes [Monaghan, 1989, 1992; Benz and Asphaug, 1994; Cossins, 2010; Price, 2012]. This viscosity modifies the equation of motion as:

$$\frac{\mathrm{d}\boldsymbol{v}_i}{\mathrm{d}t} = -\sum_j m_j \left(\frac{P_i}{\rho_i^2} + \frac{P_j}{\rho_j^2} + \Pi_{ij} \right) \nabla W_{ij} \,. \tag{2.81}$$

As the term Π_{ij} needs to be "active" on the shock front and small (or ideally zero) elsewhere, it is based on the velocity divergence $\nabla \cdot \boldsymbol{v}$, which is non-zero only at the shock front in the case of incompressible flow. To reduce the sensitivity to particle disorder, the velocity divergence is approximated as:

$$(\nabla \cdot \boldsymbol{v})_i = \sum_j \frac{(\boldsymbol{v}_i - \boldsymbol{v}_j) \cdot (\boldsymbol{r}_i - \boldsymbol{r}_j)}{\|\boldsymbol{r}_i - \boldsymbol{r}_j\|^2 + \epsilon h^2} \,. \tag{2.82}$$

Since the viscosity term Π_{ij} is a pair-wise interaction, given by the state of particles i and j, we define a pair-wise velocity divergence as:

$$\mu_{ij} = \frac{h(\boldsymbol{v}_i - \boldsymbol{v}_j) \cdot (\boldsymbol{r}_i - \boldsymbol{r}_j)}{\|\boldsymbol{r}_i - \boldsymbol{r}_j\|^2 + \epsilon h^2} \,. \tag{2.83}$$

The term Π_{ij} contains a combination of linear and quadratic function of μ_{ij}. The viscosity proportional to μ_{ij}^2 was suggested by VonNeumann and Richtmyer [1950]:

$$\Pi_{ij}^{\mathrm{NR}} = \frac{\beta \mu_{ij}^2}{\overline{\rho}_{ij}}\,, \tag{2.84}$$

where β is a dimensionless constant with value typically in the interval $\beta = 0.3 \div 3$. As it is quadratic in velocity, it prevents interpenetration of particles moving at high Mach numbers, hence it is better suited to handle strong shocks compared to 2.78.

To stabilize the simulation in presence of weak shocks and to damp any unphysical oscillations in the pressure field, an artificial viscosity linear in μ_{ij} is also added [Landshoff, 1955; Lattanzio et al., 1985]:

$$\Pi_{ij}^{\mathrm{L}} = -\frac{\alpha \overline{c}_{ij} \mu_{ij}}{\overline{\rho}_{ij}}\,, \tag{2.85}$$

where $\overline{c}_{ij} = (c_i + c_j)/2$ is the symmetrized sound speed, α is a dimensionless constant, usually set up as $\beta = 2\alpha$. In the case of a divergent flow, $\mu_{ij} > 0$, the viscosity Π_{ij} is set to zero.

Seeing that the linear and quadratic terms have different purposes and nicely complement each other, most codes use a sum of both terms [Monaghan, 1989]:

$$\Pi_{ij} = \frac{-\alpha \overline{c}_{ij} \mu_{ij} + \beta \mu_{ij}^2}{\overline{\rho}_{ij}}\,. \tag{2.86}$$

2.6.2.3 Balsara switch. Although the artificial viscosity is essential for handling of discontinuities in the SPH, the added viscosity may have undesirable effects. The problem stems from the fact that Eq. 2.86 adds the viscosity to *all* the particles with non-zero velocity divergence and not only the particles close to the shock front. As a consequence, the term substantially increases the viscosity in shear motion. A rather simple yet efficient solution is to use the vorticity $\nabla \times \boldsymbol{v}$ as an indicator of shear motion and introduce the Balsara switch [Balsara, 1995]:

$$f_i = \frac{\left\| \langle \nabla \cdot \boldsymbol{v}_i \rangle \right\|}{\left\| \langle \nabla \cdot \boldsymbol{v}_i \rangle \right\| + \left\| \langle \nabla \times \boldsymbol{v}_i \rangle \right\| + \epsilon_2 c_i / h}\,. \tag{2.87}$$

The factors f_i are equal to 1 in pure convergent flow and 0 in pure shear flow. They are thus used as multipliers of μ_{ij} (2.83):

$$\mu_{ij} = \frac{h(\boldsymbol{v}_i - \boldsymbol{v}_j) \cdot (\boldsymbol{r}_i - \boldsymbol{r}_j)}{\|\boldsymbol{r}_i - \boldsymbol{r}_j\|^2 + \epsilon h^2} \frac{f_i + f_j}{2}\,. \tag{2.88}$$

2.6.2.4 Time-dependent viscosity. While these are the standard terms used in majority of SPH codes, there are more involved approaches to artificial viscosity, which may be useful in certain situations. For example, Morris and Monaghan [1997] introduced an artificial viscosity with coefficients α_i and β_i generally different for each particle. These coefficients are also time-dependent, governed by an evolution equation that increases the artificial viscosity at the front of the shock wave, but attenuates the viscosity once the shock wave passes:

$$\frac{\mathrm{d}\alpha_i}{\mathrm{d}t} = -\frac{\alpha_i - \alpha_{\min}}{\tau} + \max\left[-(\alpha_{\max} - \alpha_i) \nabla \cdot \boldsymbol{v}_i, 0\right]\,, \tag{2.89}$$

where $\tau = h/(\epsilon_2 c_s)$ is a decay timescale, $\epsilon_2 = 0.1$ to 0.2, $\alpha_{\max} \simeq 1.5$, $\alpha_{\min} \simeq 0.05$ [Rosswog et al., 2000]. For a more detailed description and additional modifications of the artificial viscosity, see Dolag et al. [2005] or Cullen and Dehnen [2010].

2.6.3 Artificial thermal conductivity

While the artificial viscosity treats problems caused by discontinuities in the velocity field, the issues arising from ignoring the discontinuity terms in evolution equations are not exclusive to the equation of motion. Generally, an artificial smoothing term should be added for *every* time-dependent quantity [Monaghan, 1997; Price, 2008]. In particular, the discontinuities in the specific energy and consequently in the pressure lead to issues when mixing of different materials is involved. It has been demonstrated that the standard SPH formulation cannot reproduce the mixing of fluids in the Kelvin-Helmholtz instability [Valcke et al., 2010]. The lack of smoothing term effectively acts as a numerical surface tension at interfaces and keeps the entropy of the fluid constant, which prevents the mixing of fluids [Valdarnini, 2012].

Problems caused by pressure discontinuities can be mitigated by introducing an artificial thermal conductivity. We thus add an extra numerical term into the energy equation, using the generic diffusivity term 2.77 as a template [Price, 2008]:

$$\left(\frac{\mathrm{d}u_i}{\mathrm{d}t}\right)_{\mathrm{dif}} = \sum_j \frac{m_j}{\overline{\rho}_{ij}} \alpha_u w_u (u_i - u_j)\, \hat{\boldsymbol{r}}_{ij} \cdot \nabla W_{ij}\,, \tag{2.90}$$

where $\overline{\rho}_{ij} = (\rho_i + \rho_j)/2$ is the symmetrized density, $\alpha_u = 1.5$ is a dimensionless constant controlling the conductivity, w_u is the signal speed (to be defined) and $\hat{\boldsymbol{r}}_{ij} = (\boldsymbol{r}_i - \boldsymbol{r}_j)/\|\boldsymbol{r}_i - \boldsymbol{r}_j\|$. Importantly, the term is not used instead of the artificial viscosity term 2.80 but rather as an additional term in the energy equation.

2.6.3.1 Signal speed. Price [2008] suggested using a signal speed:

$$w_u = \sqrt{\frac{|P_i - P_j|}{\overline{\rho}_{ij}}}\,. \tag{2.91}$$

Since the signal speed w_u depends on the difference of particle pressures, it smooths the internal energy in the presence of a pressure discontinuity or a steep pressure profile, ensuring pressure equilibration and allowing fluids to properly mix.

In the pressure equilibrium, the artificial conduction disappears and it does not affect the solution any longer. However, the pressure equilibrium does not necessarily imply a hydrostatic equilibrium, and similarly, a body in a hydrostatic equilibrium does not necessarily have zero pressure gradients everywhere. In simulations involving forces other than the pressure gradient, such as friction, material strength, self-gravity or any external potential, the signal speed 2.91 would trigger an artificial thermal diffusion even if the body is in the hydrostatic equilibrium, and as such it is not usable [Valcke et al., 2010]. An alternative signal speed, which is independent of pressure and thus viable for simulations involving the gravity and other forces, has been suggested by Valdarnini [2012]:

$$w_u = |(\boldsymbol{v}_i - \boldsymbol{v}_j) \cdot \hat{\boldsymbol{r}}_{ij}|\,. \tag{2.92}$$

The artificial thermal conductivity is only needed to handle shocks and it is generally undesirable elsewhere. It is possible to add a dissipation switch, similar to the artificial viscosity switch 2.89 introduced by Morris and Monaghan [1997].

2.6.4 Artificial stress

The artificial terms discussed above are necessary to capture and properly resolve the discontinuities in the SPH numerical scheme. They ensure smoothing of physical quantities over (at least) several particles, however, they do not guarantee the stability of the numerical scheme during the simulation. By stability, we mean the conditions under which the particles drift back to their initial positions upon minor displacements.

2.6.4.1 Tensile instability. As mentioned by Swegle et al. [1994], the standard SPH discretization is generally stable upon compression (i.e. for positive pressure values), but it shows instabilities in tension when the pressure values are negative. The instability leads to a clustering of particles and a formation of clumps, instead of stretching the particle configuration. The issue appears in simulations with the stress tensor, e.g. when solid bodies with material strength are used.

The instability is related to the sign of the stress σ and the second derivative W'' of the smoothing kernel. Swegle et al. [1995] showed that instability occurs if:

$$\sigma \cdot W''(\boldsymbol{r}_{ij}) > 0\,. \tag{2.93}$$

The condition does *not* depend on the spatial resolution and it has no parameters which could be modified to avoid it. The scheme cannot be stabilized by the artificial viscosity or other terms discussed in previous sections; if the second kernel derivative has the same sign as the stress, the numerical scheme is *always* unstable. For the typically used SPH kernels and the usual number of neighbors within the kernel support, the condition is satisfied for negative stress σ, i.e. in tension. This effect is coined the *tensile* instability [Monaghan, 2000].

On the other hand, if there is a significantly higher number of neighbors, the particles are close to each other (relative to the kernel support) and the second derivative $W''(\boldsymbol{r}_{ij})$ changes sign, causing the scheme to become unstable in compression. This is called the *pairing* instability [Price, 2012; Dehnen and Aly, 2012] and leads to a spontaneous formation of particle pairs or small clusters of particles, even if no stress tensor is used. The pairing instability can be mitigated by keeping the number of neighbors under a certain limit. It is also easy to recognize in simulations, as there is usually no physical reason for particles to form clusters in gas or fluid simulations.

The tensile instability is more involved, though. First, there is no straightforward way to mitigate it. Second, the issue may be subtle in simulations of solid bodies, as it results in (numerical) fragmentation, which may be quite similar to fracture of the material due to the growth of cracks (see Sec. 2.8.4). This makes the instability difficult to recognize, therefore it is important to resolve the issue to ensure any fracture appearing in the simulation is physical rather than numerical, especially in simulations where the fragmentation plays a significant role.

The tensile instability can be suppressed by adding an extra numerical term, called the artificial stress [Monaghan, 2000; Gray, 2001]. Is modifies the equation of motion as:

$$\frac{\mathrm{d}\boldsymbol{v}_i}{\mathrm{d}t} = \sum_j m_j \left(\frac{\boldsymbol{\sigma}_i}{\rho_i^2} + \frac{\boldsymbol{\sigma}_j}{\rho_j^2} + \Pi_{ij}\mathbf{1} + \boldsymbol{\zeta}_{ij} \right) \cdot \nabla W_{ij} \,. \tag{2.94}$$

The symmetric tensor $\boldsymbol{\zeta}_{ij}$ is defined as:

$$\boldsymbol{\zeta}_{ij} = \big(\boldsymbol{R}_i + \boldsymbol{R}_j\big) \left(\frac{W(\boldsymbol{r}_i - \boldsymbol{r}_j)}{W(\langle \Delta r \rangle)} \right)^n \,, \tag{2.95}$$

where $\langle \Delta r \rangle$ is the mean particle spacing, $n = 4$ is a fixed constant and $\boldsymbol{R}_i$ are tensors computed for each particle, as explained below. The mean particle spacing is proportional to the smoothing lengths, so the term $W(\langle \Delta r \rangle)$ can be considered a constant in the simulation and it can be computed only once at the beginning of the simulation.

2.6.4.2 Local measure of tension. Tensors $\boldsymbol{R}_i$ are set in proportion to the physical stress terms in the equation of motion, although they are activated in tension only. In compression, they are set to zero; the artificial stress is not needed and the term may undesirably alter the physical stress. It is similar to setting the artificial viscosity to zero in divergent flows where $\nabla \cdot \boldsymbol{v} > 0$. In one dimension, the term R_i can be computed as:

$$R_i = \begin{cases} -\epsilon \sigma_i / \rho_i^2 \,, & \sigma_i \geq 0 \,, \\ 0 \,, & \sigma_i < 0 \,, \end{cases} \tag{2.96}$$

where $\epsilon \simeq 0.04$ is a small number determining the magnitude of the artificial stress. The decomposition of compression and tension is more complex in three dimensions, because the stresses $\boldsymbol{\sigma}_i$ are symmetric tensors. The tensor needs to be decomposed into its principal axes using the eigendecomposition. As the tensor $\boldsymbol{\sigma}_i$ is real and symmetric, we can use the identity:

$$\boldsymbol{\sigma} = \boldsymbol{U} \mathrm{diag}(\sigma^A, \sigma^B, \sigma^C) \boldsymbol{U}^\mathsf{T} \,, \tag{2.97}$$

where $\sigma^A, \sigma^B, \sigma^C$ are eigenvalues of the tensor. We then construct the part of the stress tensor $\boldsymbol{\sigma}$ containing the tension by taking the positive parts of the eigenvalues:

$$\boldsymbol{\sigma}^+ = \boldsymbol{U} \mathrm{diag}\left(\max(\sigma^A, 0), \max(\sigma^B, 0), \max(\sigma^C, 0) \right) \boldsymbol{U}^\mathsf{T} \,. \tag{2.98}$$

Finally, the artificial stress terms $\boldsymbol{R}_i$ are computed using the same formula as in one dimension, only the modified stress $\boldsymbol{\sigma}^+$ is used in place of $\boldsymbol{\sigma}$:

$$\boldsymbol{R}_i = -\epsilon \frac{\boldsymbol{\sigma}_i^+}{\rho_i^2} \,. \tag{2.99}$$

Alternatively, the tensile instability can be removed by keeping the particle neighborhood fixed during the simulation [Peer et al., 2017]. When particles always interact with the same set of neighbors, it allows to handle extreme deformations of elastic materials without instability issues. However, it keeps the topology of the simulated continuum locked as well, making it difficult to couple the solid body physics with a fragmentation model.

2.6.5 Influence of artificial terms on the solution

Adding *ad hoc* diffusion terms into our SPH equations raises a question about the validity of the resulting solution. After all, there are terms in the discretized equations with no corresponding terms in the continuous equations, from which the discretization was derived. One might expect that the artificial terms negatively affect the simulation and consequently, the computed result is not an accurate solution to the original problem anymore.

Luckily, this is not the case. As demonstrated in Sec. 2.1.2, the discretization error is of order $\mathcal{O}(h^2)$, and any changes to the spatial derivatives lead to "equally good" discretization, provided the magnitude of these changes is also $\mathcal{O}(h^2)$. Similarly, adding artificial terms to equations does not make them less accurate, as long as their magnitude is $\mathcal{O}(h^2)$. In other words, the numerical terms *do* affect the solution, but the introduced difference is of the same order as the discretization errors. The influence of the numerical terms decreases as the spatial resolution is increased, similarly to the discretization errors. In the limiting case of infinite resolution, the numerical terms would disappear completely and we would once again regain the original continuous equations.

This $\mathcal{O}(h^2)$ margin is a blessing and a curse for the SPH method. On one hand, the flexibility allows us to construct a conserving numerical scheme that properly handles shock waves, rotating solid bodies, etc. Naïve discretization would have none of these properties. On the other hand, it is not immediately obvious which scheme is the most appropriate for the given problem. Even though all discretizations yield the same result in the limit of infinite number of particles, one always works with a finite number of particles, where the various numerical schemes differ — in some cases significantly. Using a wrong scheme may result in unacceptable results (cf. Fig. 3.6). Therefore, it is essential to compare the results of the SPH code with an analytical solution, where such a solution exists, or with laboratory experiments.

2.7 Equation of state

Equations of hydrodynamics describe the temporal evolution of *any* continuum. The same conservation equations hold for ideal gas, water or other viscous fluids, solids or granular materials. To close the set of equations and provide the numerical model with the physical properties specific for the given material, we need to add the equation of state (EoS).

The equation of state determines the relationship between the pressure P, the density ρ and the specific internal energy u (or other set of independent state quantities), usually as a function $P = P(\rho, u)$. In collision simulations, we are generally interested in state equations of solid materials. For this purpose, a number of equations have been formulated, such as the Mie-Grüneisen or the Murnaghan equation. However, these equations are rather simplistic and do not capture important processes that take place during asteroid impacts.

2.7.1 Tillotson's equation

The equation state commonly used in impact simulations has been first described by Tillotson [1962]. It was developed for hyper-velocity impacts and takes into account the melting and vaporization of the material at high temperatures. It defines the pressure $P(\rho, u)$ separately for

two phases of the material — condensed (cold) phase and expanded (hot) phase. The appropriate phase is selected according to the specific internal energy u. If it is lower than the energy u_{iv} of incipient vaporization, the condensed phase is used:

$$P_{\mathrm{c}} = A\mu + B\mu^2 + \left(a + \frac{b}{\frac{u}{u_0\eta^2} + 1}\right)\rho u\,, \tag{2.100}$$

where A, B, a, b, u_0 are Tillotson's parameters of the condensed material, $\eta = \rho/\rho_0$ and $\mu = \eta - 1$. In case the specific energy u exceeds the energy u_{cv} of complete vaporization and material is expanded ($\rho/\rho_0 \leq 1$), the material is in the expanded phase and the equation of state follows the law:

$$P_{\mathrm{e}} = a\rho u + \left(\frac{b\rho}{\frac{1}{u_0\eta^2} + \frac{1}{u}} + A\mu e^{-\beta(\rho_0/\rho - 1)}\right) e^{-\alpha(\rho_0/\rho - 1)^2}\,, \tag{2.101}$$

where α, β are Tillotson's material parameters of the expanded phase.

If the specific energy $u > u_{\mathrm{iv}}$ and the material started to evaporate, but it has not yet evaporated completely ($u < u_{\mathrm{cv}}$), the pressure is given by a linear interpolation between pressures of both phases [Asphaug, 1993]:

$$P = \frac{(u - u_{\mathrm{iv}})P_{\mathrm{e}} + (u_{\mathrm{cv}} - u)P_{\mathrm{c}}}{u_{\mathrm{cv}} - u_{\mathrm{iv}}}\,. \tag{2.102}$$

Although we used Tillotson's equation of state exclusively in our work, there are certainly more detailed and physically accurate equations for hyper-velocity simulations, such as the ANEOS [Thompson and Lauson, 1974; Melosh, 2000] or SESAME equation [Bennett et al., 1978; McHardy, 2018]. However, these equations are no longer closed-form like Tillotson's equation, the values need to be tabulated and then interpolated during the simulation.

2.7.2 Sound speed

The equation of state is further used for computing the sound speed c. Even though the sound speed does not explicitly appear in hydrodynamic equations, it is often used in artificial terms, such as artificial viscosity (Eq. 2.86) or artificial conductivity (Eq. 2.90). The sound speed is also needed to determine the time step, making it essential for the stability of the numerical scheme. We derive the sound speed by taking the derivative of Tillotson's equation 2.102, as in Kegerreis et al. [2019]:

$$c^2 = \left(\frac{\partial P}{\partial \rho}\right)_s\,. \tag{2.103}$$

Using $\mathrm{d}u = T\mathrm{d}s - (P/\rho^2)\mathrm{d}\rho$, we obtain the sound speed c_c and c_e of the condensed and the expanded phases, respectively:

$$c_\mathrm{c}^2 = \frac{P_\mathrm{c}}{\rho}\left(1 + a + \frac{b}{\omega}\right) + \frac{b(\omega-1)}{\omega^2}\left(2\mu - \frac{P_\mathrm{c}}{\rho}\right) + \frac{1}{\rho}\left(A + B(\eta^2 - 1)\right), \tag{2.104}$$

$$c_\mathrm{e}^2 = \frac{P_\mathrm{e}}{\rho}\left(1 + a + \frac{b}{\omega}e^{-\alpha\nu^2}\right) + \left[\frac{b\rho u}{\omega^2\eta^2}\left(\frac{1}{u_0\rho}\left(2u - \frac{P_\mathrm{e}}{\rho}\right) + \frac{2\alpha\nu\omega}{\rho_0}\right) + \right.$$
$$\left. + \frac{A}{\rho_0}\left(1 + \frac{\mu}{\eta^2}(\beta + 2\alpha\nu - \eta)\right)e^{-\beta\nu}\right]e^{-\alpha\nu^2}, \tag{2.105}$$

where $\nu = 1/\eta - 1$ and $\omega = u/(u_0\eta^2) + 1$. In case the specific energy u lies between u_iv and u_cv, the squares of sound speeds c_c^2 and c_e^2 are linearly interpolated similarly as before:

$$c^2 = \frac{(u - u_\mathrm{iv})c_\mathrm{e}^2 + (u_\mathrm{cv} - u)c_\mathrm{c}^2}{u_\mathrm{cv} - u_\mathrm{iv}}. \tag{2.106}$$

Unfortunately, Tillotson's equation is an *incomplete* equation state. It only provides the pressure function $P(\rho, u)$, there is no straightforward way to compute the temperature $T(\rho, u)$. However, we can at least obtain a reasonable estimate using:

$$T = \frac{u}{c_p}, \tag{2.107}$$

where c_p is the specific heat capacity at constant pressure.

2.8 Rheology

When Hooke's law is used as the constitutive equation, the material behaves as a perfectly elastic solid. Such material is useful for validation tests of the numerical model, but its applicability to real-world situations is significantly limited, as it only applies at low stresses and small deformations. During impacts and other high-energy processes, it is essential to consider more complex rheology and take into account plasticity and material failure.

2.8.1 Von Mises yield criterion

A simple rheology model that includes material weakening at large stresses and plastic deformations was described by von Mises [1913]. It has been extensively used in the first hydrocodes studying asteroid impacts [Benz and Asphaug, 1994; Benz and Asphaug, 1995]. The model has a single material parameter, called the plasticity limit Y_0, which determines the transition point between elastic and plastic deformations. Once the magnitude of the stress exceeds the plasticity limit, it is reduced to this limit and therefore any subsequent deformation only increases the strain while keeping the stress constant.

The magnitude of the stress is determined by its second invariant $\mathcal{J}_2 = \sqrt{\boldsymbol{S} : \boldsymbol{S}}$. Mathematically, the reduction factor f of the stress for an intact (undamaged) rock is given by:

$$f = \min\left(\frac{Y_0}{\sqrt{\frac{3}{2}\boldsymbol{S} : \boldsymbol{S}}}, 1\right) \tag{2.108}$$

Any equation using the stress tensor $\boldsymbol{S}$ should then use the reduced stress tensor $f\boldsymbol{S}$ instead to manifest the plasticity; this approach is often called the radial return method [Jutzi et al., 2015].

The model can be easily generalized to include weakening of the material shear strength with increasing temperature. Instead of using a constant plasticity limit Y_0, we assume it depends on the internal energy u. The simplest (but viable) functional dependence is a linear relationship:

$$Y_0(u) = Y_0 \max\left(1 - \frac{u}{u_{\text{melt}}}, 0\right), \tag{2.109}$$

where u_{melt} is the melting specific internal energy. Naturally, zero yield strength is used whenever the internal energy u is larger than the melt energy u_{melt}.

It is also possible to directly incorporate a fragmentation model into the von Mises criterion. Assuming the relative weakening due to material failure is described by the scalar damage D (see Sec. 2.8.4), the yield strength can be modified to include the damage as:

$$Y = (1 - D)Y_0\,. \tag{2.110}$$

An important consequence of such a description is that fully damaged material has no shear strength and behaves as ideal fluid. Von Mises material is thus viable for simulating metallic bodies, but it fails when applied to granular materials due to the absence of dry friction.

2.8.2 Drucker-Prager yield criterion

A more general rheology, suitable for simulations involving bodies of granular material, is based on Drucker-Prager model [Collins et al., 2004; Jutzi et al., 2015]. It defines the yield strength of an intact (undamaged) rock and yield strength of a fully damaged rock separately. For undamaged material, the yield strength Y_{i} is given by:

$$Y_{\text{i}} = Y_0 + \frac{\mu_{\text{i}} P}{1 + \mu_{\text{i}} P/(Y_{\text{M}} - Y_0)}\,, \tag{2.111}$$

where Y_0 is the cohesion (shear strength at zero pressure), μ_i is the (dimensionless) coefficient of internal friction and Y_M is the von Mises plasticity limit. Although pressure can be negative due to tension, we limit the pressure to positive values in this equation to avoid possible division by zero.

The yield strength of a completely damaged rock is considerably simpler:

$$Y_{\text{d}} = \mu_{\text{d}} P\,, \tag{2.112}$$

where μ_{d} is the (dimensionless) coefficient of dry friction.

Whenever the material damage D lies between zero and one (i.e. partially damaged material), the yield strength Y is given by a linear interpolation:

$$Y = Y_{\text{i}}(1 - D) + Y_{\text{d}} D\,. \tag{2.113}$$

The temperature dependence can also be implemented similarly as in the von Mises criterion.

The Drucker-Prager rheology differs from the von Mises rheology in several key aspects. First, the yield strength is pressure-dependent — it increases with larger pressure. The rock has non-zero strength even at zero pressure, as given by its cohesion Y_0, but the strength substantially increases when the overburden pressure is applied. This is a characteristic property of granular material, essential for realistic simulations. Second, even a completely damaged rock has non-zero strength, proportional to the overburden pressure. The coefficient μ_d of dry friction relates to the angle of repose θ as $\tan\theta \simeq \mu_\mathrm{d}$. Thus, the damaged rock under constant gravity forms a slope with angle θ, unlike the von Mises material, which would eventually form a flat plane or surface corresponding to equipotentials (similarly to fluids).

2.8.3 Acoustic fluidization

The Drucker-Prager model gives viable predictions when applied to granular materials and it can successfully reproduce the end result of a gravity-induced collapse, thus it is a frequently used model in rock mechanics [Holsapple, 2009]. However, the model cannot explain the complex structures observed in craters created by high-energy impacts, neither the terrestrial ones (e.g. Chicxulub or Puchezh-Katunki) nor craters on Moon and other solar system bodies (e.g. Rheasilvia crater on Vesta). The numerical experiments only match the observations well when applied to small craters. These so-called simple craters are bowl-shaped depressions encircled by elevated rims. With increasing impact energy, craters start to transition from simple to complex. Observed complex craters have additional topographical features, namely the central peak and occasionally multiple rings. This simple-to-complex transition depends on the surface gravity; on the Moon it appears for crater diameters $D \approx 15\,\mathrm{km}$ [Melosh and Ivanov, 1999].

2.8.3.1 Material weakening. The rheological model needs to be generalized in order to explain these features of complex craters. It requires such rheology that allows the central peak to form shortly after the impact, while also preserving the peak for millions of years afterwards. The key observation is that the central peak naturally forms when the transient crater collapses, provided the material behaves as a viscous fluid rather than a granular rock.

A number of physical processes explaining this material weakening have been proposed. Such a process has to temporarily reduce the strength of the material upon impact in order to form the central peak, but quickly restore the strength after the impact to prevent the peak from collapsing. A commonly used model explaining this behavior is acoustic fluidization.

The acoustic fluidization model attributes the transient weakening of the material to the discrete structure of the surface rock. The model assumes that the rock is not a seamless continuum, but rather it consists of blocks separated by layers of matrix material. This assumption seems to be supported by observations; indeed, deep drilling into terrestrial impact craters showed rock blocks with sizes between 50 and 200 meters [Ivanov et al., 1996]. Upon the impact, the strong acoustic vibrations created by the shock wave allow blocks to move with much lower resistance than the material strength would imply, behaving similarly to fluid. However, this effect is only temporary as the acoustic oscillations are attenuated or travel away, and the material strength is restored, preserving the topographical features of the crater. Such a model has been successfully employed to explain geological structures in the San Andreas fault [Melosh, 1996], Chicxulub crater [Riller et al., 2018] or craters on Ganymede [Bray et al., 2014].

2.8.3.2 Melosh model. First proposed by Melosh [1996], the degree of fluidization is described by the vibrational energy E_{vib}. It is a state quantity interpreted as a vibrational acoustic energy per unit volume and its time evolution is determined by the differential equation [Melosh, 1996; Hay et al., 2014]:

$$\frac{\mathrm{d}E_{\text{vib}}}{\mathrm{d}t} = \frac{\xi}{4}\nabla^2 E_{\text{vib}} - \frac{c_p}{\lambda Q}E_{\text{vib}} + e\boldsymbol{\sigma} : \dot{\boldsymbol{\epsilon}}\,. \tag{2.114}$$

The first term on the right-hand side describes scattering, ξ being the scattering diffusivity. The second term converts the acoustic energy into heat. Here c_p is the wave speed, λ is the characteristic wavelength of oscillations and Q is the quality factor determining the fraction of acoustic energy converted to heat per oscillation cycle. Finally, the last term is the (re)generation term, specifying the amount of vibrational energy generated during material flow, e being the dimensionless regeneration efficiency.

In the special case when $\xi = e = 0$, the solution to the Eq. 2.114 is a simple exponential decay. This simplification of the acoustic fluidization model is usually called the block model [Hay et al., 2014].

Acoustic vibrations of blocks imply the local pressure is lower than the ambient overburden pressure and thus the yield strength of the material is decreased as well. The rheology of the damaged material is modified to the Bingham-like form [Silber et al., 2017]:

$$Y_d = \mu(P - P_{\text{vib}}) + \eta_{\text{lim}}\rho\dot{\epsilon}\,, \tag{2.115}$$

where P_{vib} is the vibrational pressure, calculated from the vibrational energy as $P_{\text{vib}} = \sqrt{2\rho c_s^2 E_{\text{vib}}}$, and η_{lim} is the effective viscosity of fluidized material.

2.8.3.3 Attenuation timescale. Acoustic fluidization introduces a number of free parameters which are generally difficult to constrain. In the simplest case of the block model, it requires the attenuation timescale T_{dec} and the initial vibrational pressure P_{vib}. It is difficult to determine this parameter *a priori* and it has to be selected to fit observational constraints. However, Ivanov [2019] plotted the optimal decay timescale T_{dec} against the crater diameter D for a number of studied cases and found the points are correlated, providing an empirical formula for the decay timescale:

$$[T_{\text{dec}}]_{\text{s}} = 1.2\,[D]_{\text{km}}\,. \tag{2.116}$$

While the optimal value of T_{dec} can still differ significantly, the formula provides a good initial estimate.

2.8.4 Fragmentation

Besides plasticity, another characteristic behavior of solid materials is a failure under deformation. When the strain ϵ in the body exceeds a certain activation threshold ϵ_{act}, a crack appears and starts to grow. At this point, the deviation from Hooke's law is significant; the stress in the body is relieved and it is no longer increased when increasing the strain. The cracks then develop until the body is fragmented and dispersed.

Cracks originate from flaws in the rock structure. Flaw sizes range from nanometer-sized dislocations up to macroscopic cavities [Lawn and Wilshaw, 1975]. However, even flaws $\sim 1\,\text{m}$

in size are still about 10^3 times smaller than the resolution limit of our simulations and it is thus impossible to capture the growth of individual cracks in the continuum. Instead, a statistical treatment of crack growth is used.

2.8.4.1 Weibull distribution. Generally, the notion of a single activation threshold ϵ_{act} is far too simplistic to properly simulate real materials. The activation threshold is different for each flaw and it can differ by many orders of magnitude. For brittle solids, the Weibull distribution [Weibull, 1939] is commonly used to describe the number of flaws in unit volume whose activation threshold is lower than ϵ. It follows the power law:

$$N(\epsilon) = k\epsilon^m \,, \tag{2.117}$$

where k and m are the Weibull coefficients, specific for given material.

2.8.4.2 Grady-Kipp model. The activation and growth of cracks were described by Grady and Kipp [1980]. The Grady-Kipp model introduces a scalar state quantity called damage D. It represents the degree of fragmentation, with $D = 0$ being an intact, elastic material and $D = 1$ being fully fractured material. Damaged material exhibits reduced strength in tension, modifying the pressure P and the deviatoric stress tensor $\boldsymbol{S}$ as[1]:

$$P^\star = \begin{cases} P \,, & P \geq 0 \,, \\ (1-D)P \,, & P < 0 \,, \end{cases} \tag{2.118}$$

$$\boldsymbol{S}^\star = (1-D)\boldsymbol{S} \,. \tag{2.119}$$

2.8.4.3 Discretization in SPH. The model was discretized in the SPH framework by Benz and Asphaug [1994] and it is commonly used in shock-physics codes. In the discretized form, the flaws are initially distributed in the body by sequentially selecting a particle randomly and adding a flaw to it, starting with the weakest flaw and progressively assigning flaws with a higher activation threshold, until all particles contain at least one flaw. Following the Weibull distribution 2.117, activation threshold of n-th flaw assigned using the outlined method is:

$$\epsilon_{i,n} = \left(\frac{n}{kV}\right)^{\frac{1}{m}} \,, \tag{2.120}$$

where V is the total volume of the body, computed as $V = \sum_i m_i/\rho_i$.

The flaws assigned to particles need to be stored and kept in memory during the simulation in order to determine the total number of activated flaws. One solution is to explicitly store an array of flaws for each particle. The number n_{act} of activated flaws is then simply the number of flaws with activation strain lower than the current local strain ϵ. The disadvantage of such an approach is a considerable memory overhead; for N particles, this requires to store approximately $N_{\text{flaws}} = N \ln N$ flaws [Schäfer et al., 2016]. Alternatively, we can store only the

[1]For simplicity, we drop the asterisk from quantities in other equations and use the symbols P and $\boldsymbol{S}$ for the reduced pressure and deviatoric stress, respectively.

smallest activation strain $\epsilon_{\min}$, the largest activation strain $\epsilon_{\max}$ and the total number of flaws n_{flaws} assigned to each particle [as in Benz and Asphaug, 1994]. Given the current strain ϵ, the number of activated flaws can be then estimated as:

$$n_{\text{act}} = \left(\frac{\epsilon}{\epsilon_{\min}}\right)^{m_0}, \tag{2.121}$$

where $m_0 = \log(n_{\text{flaws}})/\log(\epsilon_{\max}/\epsilon_{\min})$.

The sequential filling of particle flaws is suitable for simulations with a moderate number of particles. However, we found out that for a large number of particles ($N > 10^7$), this approach becomes extremely inefficient, as each particle needs to be selected at random at least once. In such cases, we instead assign the number of flaws n_{flaws} to particles directly; as flaws are assigned to particles randomly, the number of flaws follows the Poisson statistics, we can thus get a reasonable estimate by sampling the Poisson distribution. With this approach, the computational complexity reduces to $\mathcal{O}(N)$, allowing to seed the flaws even for high-resolution simulation.

To determine the number of activated flaws, we need to find the scalar strain ϵ. Given the total stress tensor $\boldsymbol{\sigma} = -P\boldsymbol{I} + \boldsymbol{S}$, we first compute the eigendecomposition of the matrix $\boldsymbol{\sigma}$ and determine the maximum scalar stress as the largest eigenvalue $\sigma_{\max} = \max(\sigma_1, \sigma_2, \sigma_3)$. Then, the scalar strain ϵ is obtained as [Benz and Asphaug, 1994]:

$$\epsilon = \frac{\sigma_{\max}}{(1-D)E}. \tag{2.122}$$

The Young's modulus E of the material can be derived from its bulk modulus A and shear modulus μ, using formula:

$$E = \frac{9A\mu}{3A+\mu}. \tag{2.123}$$

2.8.4.4 Damage integration. Finally, the fragmentation model is integrated during the simulation together with other state quantities. The temporal evolution of damage D_i for i-th particle is given by the differential equation:

$$\frac{\mathrm{d}}{\mathrm{d}t}(D_i^{\frac{1}{3}}) = n_{\text{act}}\frac{c_{\text{g}}}{R_i}, \tag{2.124}$$

where n_{act} is the number of activated flaws, c_{g} is the speed of crack growth and R_i is the radius of the particle. The crack growth speed is calculated as:

$$c_{\text{g}} = 0.4\sqrt{\frac{A + \frac{4}{3}\mu}{\rho_0}}, \tag{2.125}$$

where A is the bulk modulus, μ is the shear modulus, ρ_0 is the initial density. Factor 0.4 comes from the observation that the speed of crack growth is a constant fraction of the longitudinal elastic wave in the material [Lawn and Wilshaw, 1975]. Particle radius R_i depends on the

selected smoothing kernel W, but it always scales linearly with the smoothing length h_i; for the standard cubic B-spline the radius is $R_i = 2h_i$.

As the Grady-Kipp model considers the scalar damage D, it is isotropic and does not take into account directionality of fractures. For this reason, some authors used a more complex damage model, which is anisotropic and treats damage as a symmetric tensor $\boldsymbol{D}$ [Lubarda and Krajcinovic, 1993; Owen, 2010].

2.9 Initial conditions

A necessary precondition for the solution of the hydrodynamic equations is the initial setup of particle positions, velocities and all state quantities. Lagrangian methods are a bit more complex in this regard compared to the grid-based methods, as there is no underlying geometrical structure that could be used to sample the computation domain. Thus, the main goal is to create a suitable spatial distribution of particles. Assigning values of quantities to each particle is then rather straightforward.

While setting initial positions of particles is somewhat arbitrary — indeed, one could run a simulation with particles generated randomly inside the domain — there are several desirable properties that all particle distributions should satisfy, because they strongly affect the accuracy, overall stability and proneness of the SPH method to numerical artifacts.

- **Low discrepancy.** A feasible method should distribute the particles evenly in space, without forming any clumps, voids or other structures. This implies the particle positions should *not* be random, as uniform random distribution forms undesirable particle groups. Formally, we say the point set should have *low discrepancy*, where the discrepancy $\mathscr{D}(P)$ of a point set $P = \{x_1, ..., x_N\}$ is defined as:

$$\mathscr{D}(P) = \sup_{B \in \mathcal{J}} \left| \frac{A(B;P)}{N} - \lambda(B) \right|, \tag{2.126}$$

  where $\lambda(B)$ is the volume of box B, $A(B;P)$ is the number of points from the set P contained in the box B and $\mathcal{J}$ is the set of boxes:

$$\mathcal{J} = \{[\boldsymbol{x}_a, \boldsymbol{x}_b) \, \forall \boldsymbol{x}_a, \boldsymbol{x}_b \; : \; x^\alpha_{\min} \leq x^\alpha_a < x^\alpha_b \leq x^\alpha_{\max}\}. \tag{2.127}$$

  Particle distributions with high discrepancy are not suitable, as the number of neighbors varies significantly and consequently the approximation of derivatives is very poor.

- **Energy minimum.** The particles should be generated using a method that avoids spurious particle motion when the simulation starts. Such a motion could trigger non-physical acoustic waves in the body and it might even lead to deformation or fragmentation. Thus, the method should place the particles to the (local) minimum of the potential energy. This condition is non-trivial even when the body has initially constant pressure, as the equation of motion (Eq. 2.44) adds numerical repulsive forces which would displace particles if they were not placed into a stable configuration. For the standard set of equations, the particle distribution with the minimum of energy is already a low-discrepancy distribution, although the opposite is not necessarily true.

- **Isotropy.** There should be no preferred directions in particle distributions. Anisotropic particle distributions, such as lattice-based ones, may lead to aliasing artifacts, clumping of particles along principal directions of the grid, etc. Although this requirement is undoubtedly desirable, it often comes at a price of worse interpolation properties and higher numerical potential energy of particles. This is not surprising, given the lattice-based distributions have optimal interpolation properties (all particles have equal number of neighbors at equal distances) and the potential energy is *globally* minimal. In fact, we can often see the particles spontaneously rearrange themselves to locally hexagonal close packing during the simulation.
- **Versatility.** Ideally, the method should be applicable to arbitrary geometries, rather than being fine-tuned for a geometry with specific symmetry. This requirement is less important for astrophysical impact simulations, as the generated bodies are often spherical. In such a case, the spherical symmetry can be utilized to generate particles on concentric shells [Raskin and Owen, 2016; Reinhardt and Stadel, 2017], satisfying the isotropy and low-discrepancy requirements.
- **Performance.** Due to the steadily increasing capabilities of computational clusters, SPH simulations with 10^8 to 10^9 particles are not uncommon [Domínguez et al., 2013; Kegerreis et al., 2019]. Therefore, the particle-generating method should be fast enough even for a large number of particles; ideally, the time needed to set up the initial conditions should be considerably lower than the actual time needed for the simulation. The method should also have low memory overhead, as the memory can become a bottleneck for billion-particle simulations.

Several methods for distributing particles inside an object are compared in Fig. 2.2. Below, we describe a few of them in more detail.

2.9.1 Lattice-based distribution

A regular lattice is a simple and commonly used method for setting up initial particle positions. The advantage is a straightforward and efficient implementation and independence on the geometry of the generated body. There is a number of possible lattice configurations which could be used for this purpose.

A cubic lattice, where the particles are separated by vectors aligned with the Cartesian axes, is not favorable, because the particle configuration is not stable. Although being in local equilibrium, particles would spontaneously rearrange to different lattice configurations upon minor displacements. Therefore, hexagonal close-packed (HCP) or face-centered cubic (FCC) lattices are used instead [Monaghan, 1992; Benz and Asphaug, 1994]. The most notable drawback of lattice distributions is their anisotropy. Since particles are aligned in the lattice, there are strongly preferred directions in the generated bodies, which might affect the speed of shock wave propagation, fragmentation patterns, etc. Such configuration is also more susceptible to tensile instability [Schäfer et al., 2016]. Layering of particles in the lattice also results in slight artificial clustering of particles when they are ejected with similar velocities.

In the case of the hexagonal close packing, the particles are generated on positions:

$$\boldsymbol{r}_{ijk} = \left[i + \frac{1}{2}(j+k) \bmod 2, \frac{\sqrt{3}}{2}\left(j + \frac{1}{3}(k \bmod 2)\right), \frac{\sqrt{6}}{3}k \right]; i,j,k \in \mathbb{N}\,. \tag{2.128}$$

The range of indices i, j, k is of course restricted by the extent of the generated body.

2.9.2 Parametrized spiraling

Raskin and Owen [2016] proposed a specific method for creating spherically symmetric bodies. Particles are generated using concentric spherical shells, resulting in a distribution that is spherically symmetric by construction. Such a method allows assigning different values of pressure, specific energy and other quantities to each spherical shell while preserving the desirable attributes such as low discrepancy and isotropy. Although the method cannot be easily generalized for non-spherical bodies, spherically symmetric initial conditions are of great importance in astrophysical applications.

Shells are created independently of each other. Particles are placed on the surface of a sphere uniformly using a method of Saff and Kuijlaars [1997]. To create a shell of N particles, we parametrize the particles using a stepping parameter $h_k = 2k/N - 1$, $1 \leq k \leq N$. The particle position in spherical coordinates is then given by:

$$\theta_k = \cos^{-1}(h_k)\,, \tag{2.129}$$

$$\phi_k = \phi_{k-1} + \frac{3.8}{\sqrt{N(1-h_k^2)}}\,. \tag{2.130}$$

As the spherical shells are equally spaced in the radial direction, the number of particles in a shell is proportional to r^2, and the number of particles in i-th shell is:

$$N_i = N_{\text{total}} \frac{r_i^2}{\sum_i r_i^2}\,, \tag{2.131}$$

where N_{total} is the total number of particles to create and r_i is the radius of the shell.

Without further modification, this method would form spirals of particles instead of an isotropic low-discrepancy distribution (hence the name of the method). To avoid this, each shell is transformed using a random rotation, i.e. we generate a random unit vector as the rotational axis and a random angle of rotation using a uniform random number generator in the interval $[0, 2\pi)$. The rotation does not affect the spherical symmetry but removes the undesired correlation between consecutive shells.

The described method is fast and easily implementable. The particles are equally spaced within each spherical shell, but the spacing of particles between consecutive shells is essentially random, thus the interpolation precision in the radial direction is generally worse compared to lattice-based distributions.

2.9.3 Blue noise sampling

Finding point sets with low discrepancy while avoiding the grid-based structure is a well-studied problem. Monte Carlo integration is a typical use case: the goal is to create a point set that uniformly covers the domain but also avoids possible aliasing artifacts. Methods solving this type of problems are usually called *blue noise sampling* [Jiang et al., 2015] in the literature and they are a good solution for initial conditions in SPH.

There are several different methods for blue noise sampling [Yan et al., 2015]. A usual approach is to initially create the particles (quasi-)randomly and then apply repulsive forces, pushing particles away from each other into a stable configuration and getting rid of all particle clusters in the process. Particles generally do not reach the equilibrium position after a single displacement, we thus repeat the step and let particles converge towards their final positions. The iterative method ends after the particle displacement in a single iteration drops under a certain threshold.

The convergence is achieved using a simple expression for particle displacements. The displacement shall depend only on the positions of particles, it shall monotonically decrease as particles recede and the direction shall be proportional to the difference vector $\boldsymbol{r}_{ij} = \boldsymbol{r}_i - \boldsymbol{r}_j$. A suitable expression is [Diehl et al., 2015]:

$$\delta \boldsymbol{r}_i = \sum_j \left(\frac{\ell}{\boldsymbol{r}_{ij}^2 / h^2 + \epsilon} - \frac{\ell}{1 + \epsilon} \right) \frac{\boldsymbol{r}_{ij}}{\|\boldsymbol{r}_{ij}\|}, \tag{2.132}$$

where ℓ is the magnitude of displacement and ϵ is a small constant to avoid numerical instabilities.

Since the particles repel each other, it is necessary to keep them inside the domain. To ensure the particles do not leave the domain, standard handling of boundary conditions in SPH can be used. The boundary of the domain is occupied by ghost particles that repel the "real" particles. This also helps to form a smooth boundary of the body, see Fig. 2.2. Importantly, simply moving the escaped particles back into the domain is not sufficient, because a dense layer of particles would be created along the boundary.

Initially, particles can be distributed randomly inside the body, although using a low-discrepancy point set, such as the Halton sequence [Halton, 1964], can considerably speed up the convergence. The method leads to isotropic, almost equally-spaced particles in a stable configuration. It is also not restricted to any particular symmetry and can be used for arbitrary shapes of the body. However, it is more difficult to implement and it also takes longer to generate the particles due to its iterative nature.

2.9.4 Obtaining equilibrium state

So far, only the particle positions have been discussed. It is however necessary to also assign values of velocities and other physical quantities to all particles. In contrast to the methods for generating particle positions, which are quite generic and problem-independent, the quantity values have to be assigned according to the problem at hand.

One case particularly important for astrophysical simulations is a self-gravitating body in hydrostatic equilibrium. We aim to set up the state quantities assigned to particles so that all temporal derivatives evaluated at the beginning of the simulation are zero.

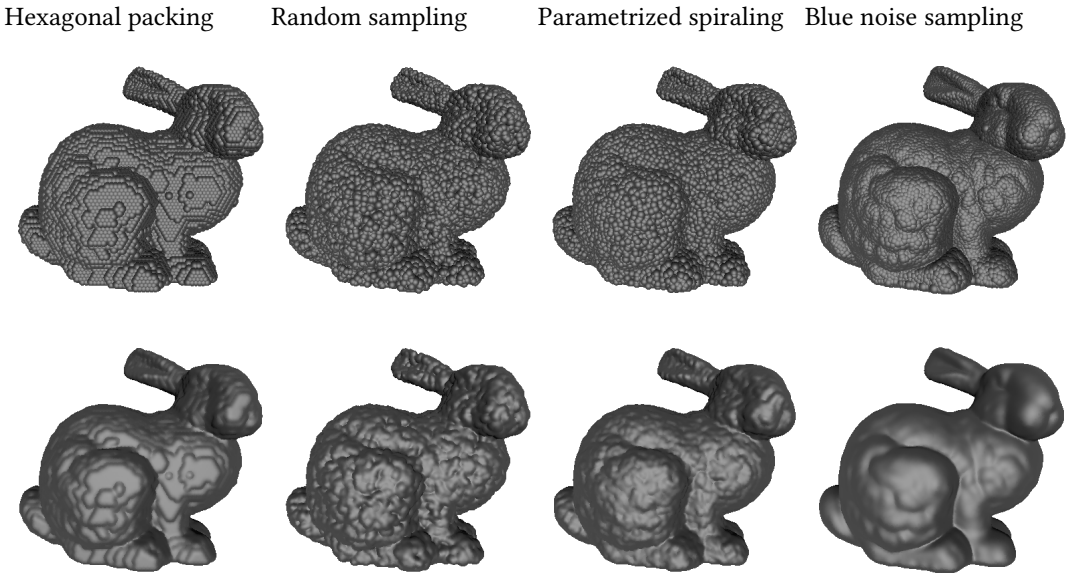

Figure 2.2: SPH particles distributed in an arbitrary domain with several particle distributions. The shape of the domain is given by the Stanford Bunny model of Turk and Levoy [1994]. The upper row shows the surface of spheres with radii $r_i = 2h_i$, while the bottom row shows an iso-surface of the color field (see Eq. 2.173).

2.9.4.1 Spherically symmetric bodies. If we assume spherical symmetry, there exists an analytic solution for such a problem. Such a solution is very useful for impacts simulations, because the spherical symmetry is expected for planets or planetesimals. Moreover, a sphere is still a reasonable default shape even for smaller objects. Hence, we search for a pressure profile $P = P(R)$ as a function of the radial coordinate R. The solution is easily found by solving an ordinary differential equation:

$$\frac{\mathrm{d}P}{\mathrm{d}R} = -\frac{GM(R)\rho}{R^2}\,, \tag{2.133}$$

where $M(R)$ is the total mass inside the sphere of radius R. In the SPH discretization, we sort the particles along the coordinate R and compute masses $M(R_i)$ by summing up the total mass of particles with $R \leq R_i$. The pressure is then computed similarly, starting from the central particle with arbitrary pressure and going outwards, setting the pressure of i-th particle to:

$$P_i = P_{i-1} - \frac{GM(R_i)\rho_i}{R_i^2}(R_i - R_{i-1})\,. \tag{2.134}$$

Finally, we subtract the pressure of the outermost particle from all particles to obtain zero pressure on the surface.

2.9.4.2 Poisson equation. Alternatively, the equilibrium pressure can be found using a more general approach, provided the equation of motion only includes the pressure gradient 2.44 and

pressure-independent conservative forces $\boldsymbol{f}_i$, such as the gravity or the centrifugal force. Then the sought pressure P is the solution to a set of equations:

$$\sum_j m_j \left(\frac{P_j}{\rho_j^2} + \frac{P_i}{\rho_i^2} \right) \nabla W_{ij} = \boldsymbol{f}_i \tag{2.135}$$

with a Dirichlet boundary condition $P_i = 0$ for surface particles. As both ∇W_{ij} and $\boldsymbol{f}_i$ are functions of particle positions only, this leads to a set of linear equations. Unfortunately, the system of equations is overdetermined, as the total number of equations is $3N$, while the number of unknowns is N. It could be still solved using a least-squares solver, however, such a solution is prone to strong noise. Instead, we solve the Poisson problem:

$$\sum_j m_j \left(\frac{P_j}{\rho_j^2} - \frac{P_i}{\rho_i^2} \right) \nabla^2 W_{ij} = \sum_j \frac{m_j}{\rho_j} (\boldsymbol{f}_j - \boldsymbol{f}_i) \nabla W_{ij} \,, \tag{2.136}$$

which represents a standard $N \times N$ sparse linear problem and its solution is generally smoother and performs better than the least-squares variant. This method is useful for simulations of rotating bodies, as it allows to compute the equilibrium states for Maclaurin spheroids or Jacobi ellipsoids, where the spherically symmetric solution would not be applicable.

2.9.4.3 Stabilization. Although the solution to Eq. 2.136 is an equilibrium pressure, the state is not necessarily stable. It is also non-trivial to generalize it for simulations with material strength or other terms. To obtain truly stable initial conditions in a generic and robust way, we choose a different approach. The idea is to set up initial conditions which are close to the stable configuration, but not necessarily equilibrium, and then follow up with a stabilization computation phase. During this phase, the solver uses the same set of equations as the actual simulation, but additionally, there is an artificial damping of particle velocities [Rosswog, 2009; Genda et al., 2012]. The damping term allows the system to settle into an equilibrium configuration. Any damping mechanism will suffice, the simplest being a reduction of the particle velocities by a damping coefficient δ every time step. However, the damping has to be done carefully if the initial velocities are not zero, for example in simulations involving bulk rotation. For setting up stable rotating bodies, we have found that the following expression works well in practice. Each timestep, we modify the particle velocities as [Ševeček et al., 2019]:

$$\boldsymbol{v}_{\mathrm{damp}} = \frac{\boldsymbol{v} - \boldsymbol{\omega} \times \boldsymbol{r}}{1 + \delta \Delta t \, (t - t_{\mathrm{stab}}) / t_{\mathrm{stab}}} + \boldsymbol{\omega} \times \boldsymbol{r} \,, \tag{2.137}$$

where $\boldsymbol{v}$ is the undamped velocity, $\boldsymbol{\omega}$ the angular frequency of the body, $\boldsymbol{r}$ the position of the particle, δ an arbitrary damping coefficient, Δt the current time step and t_{stab} the duration of the stabilization phase. We scale the damping coefficient δ by Δt to make the damping strength independent on the current time step, at least to the first order. The damping is gradually decreased and it is removed completely at the end of the phase; if one kept the damping constant during the stabilization, particles might fail to reach the equilibrium position due to over-damping and oscillate at the beginning of the simulation when the velocity damping is suddenly removed. Finally, we subtract and re-add the bulk angular frequency in Eq. 2.137, otherwise the

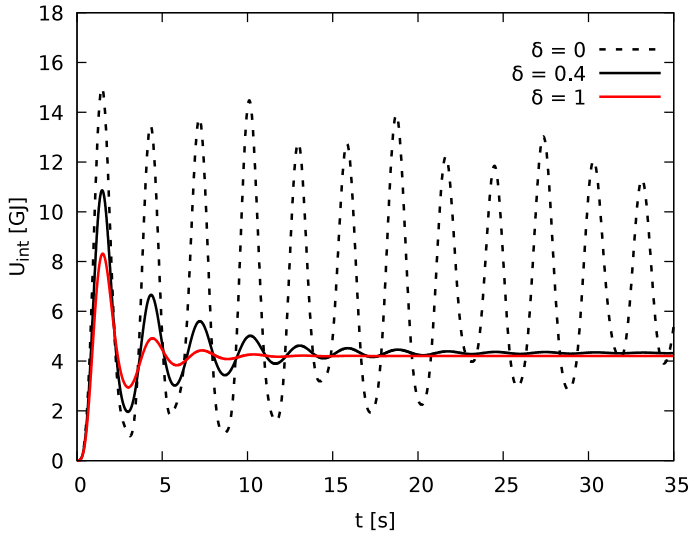

Figure 2.3: Evolution of the total internal energy U during the stabilization phase for several values of the damping parameter δ. Stronger damping leads to faster convergence to the equilibrium state.

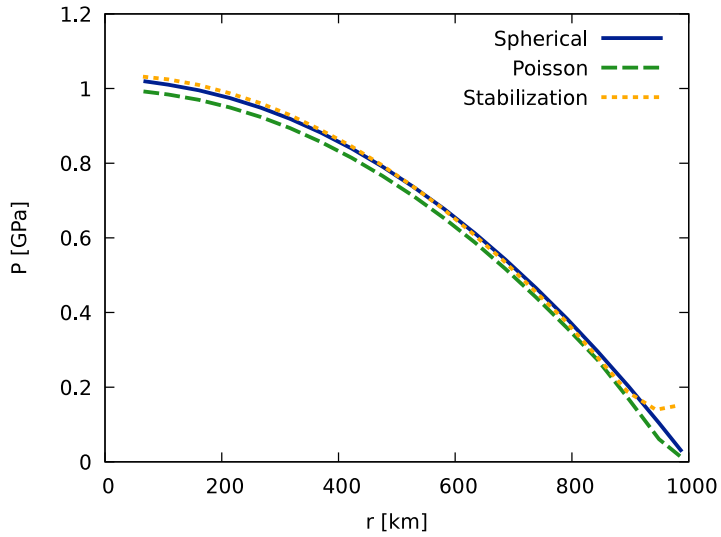

Figure 2.4: Radial pressure profile of a spherical body in hydrostatic equilibrium, obtained using various methods. The body has $N = 5000$ particles; the discretization is intentionally coarse to emphasize the differences between the methods. For large number of particles, the equilibrium profile is almost independent of the method used, as expected. The plotted profiles correspond to the radial integration using Eq. 2.134, solution of the Poisson equation Eq. 2.136 and running a stabilization simulation with velocity damping given by Eq. 2.137.

damping would cause the rotating body to slow down. A similar correction needs to be done if the body has non-zero bulk velocity. The damping of global oscillations is demonstrated on the total internal energy in Fig. 2.3.

The equilibrium solution is not unique. The accelerations are determined by the pressure (gradients ∇P) inside the body, which in turn depends on two parameters — the density and the specific internal energy — via the equation of state. Consequently, the internal energy can be computed for arbitrary density and the respective pressure with an inverted equation of state (if such an inverse exists, of course). It is important to specify a realistic density distribution in the first place, otherwise, the derived distribution of the internal energy inside the body can be unrealistic and unphysical. [2]

2.10 Boundary conditions

Setting up an exact boundary condition in the SPH framework is considerably more challenging compared to grid-based Eulerian codes. In a particle-based discretization, there is no equivalent of boundary elements. Luckily, there is no need to provide a boundary for our collisional simulations — asteroid fragments can move without spatial restrictions. SPH naturally implements the vacuum boundary condition on body surfaces, therefore all state quantities outside bodies (density, pressure, energy, etc.) are zero as expected.

2.10.1 Ghost particles

Boundary conditions are however still necessary for auxiliary tasks, such as surface cratering simulations, setting up initial conditions or numerical tests of the code. They are commonly implemented using *ghost particles* [Herant, 1994]. Ghosts are created for every particle whose distance from the boundary is less than $\eta h/2$, η being the dimensionless radius of the smoothing kernel. Given the position of the boundary particle, the ghost's position is mirrored with respect to the boundary and all state quantities are copied to the ghost. The rest of the code then treats ghosts as any other particles.

To avoid creating ghosts directly on top of the boundary particle, we set the minimal distance of ghosts to $0.1\eta h$. As the ghost positions are mirrored and the quantities are equal to their respective sources, all gradients perpendicular the to boundary are approximately zero. Hence, ghost particles effectively work as the Neumann boundary condition. There is some freedom in setting up ghosts' velocities, though.

We considered two options. The first one is to set velocities of ghosts to zero:

$$\boldsymbol{v} = \mathbf{0}\,. \tag{2.138}$$

Particles then interact with the boundary as if it was a solid, unmoving wall. In particular, there is friction between particles and the boundary. The second option is to mirror the velocities of

[2] In theory, it is possible to specify the internal energy and derive the density distribution. However, such an approach is more complex, because the density depends on the masses and positions of the particles in the neighborhood (see Eq. 2.5). Furthermore, the right-hand side of Eq. 2.135 also depends on the density via Poisson's equation. It would lead to a non-linear problem.

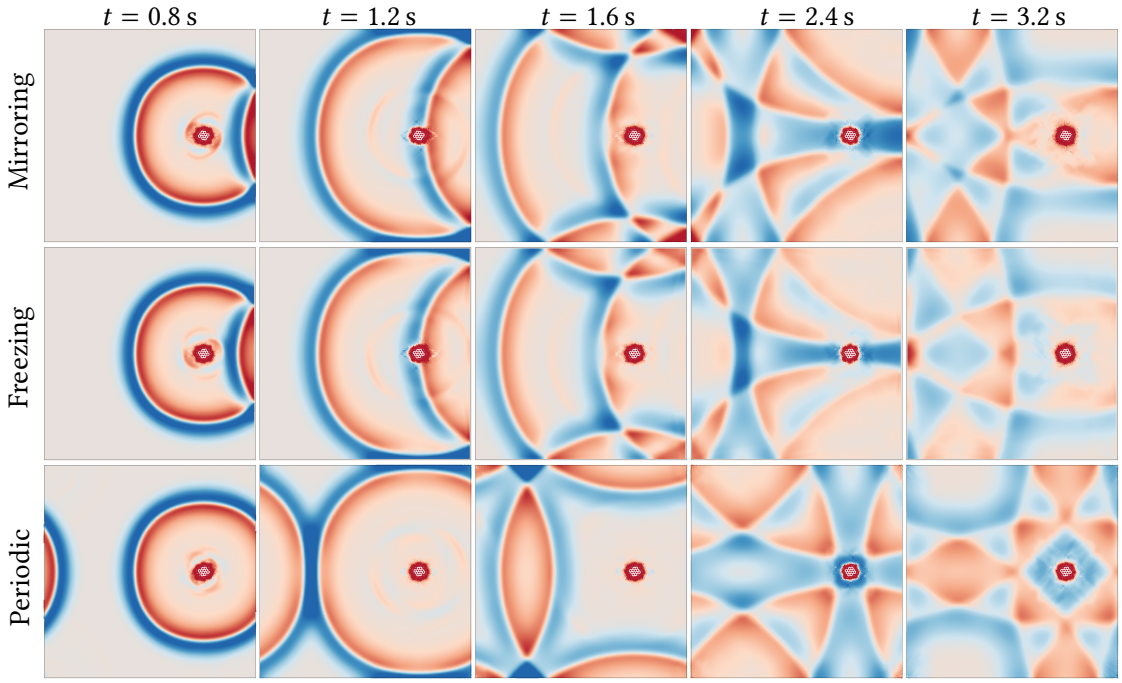

Figure 2.5: Simple two-dimensional test which demonstrates various boundary conditions. A point explosion is detonated in a homogeneous medium of $N = 40\,000$ particles made of ideal gas. The explosion creates a spherical shock wave that propagates outwards and interacts with the boundary. Top row shows the boundary condition that mirrors quantities, implemented via ghost particles. Middle row shows the freezing boundary condition, resetting derivatives of all particles near the boundary. Bottom row shows the periodic boundary condition, also implemented using ghosts. Particle color corresponds to local densities.

particles with respect to the boundary. This leads to a boundary condition [Colagrossi et al., 2009]:

$$\boldsymbol{v} \cdot \boldsymbol{n} = 0\,, \tag{2.139}$$

where $\boldsymbol{n}$ is the local normal of the boundary.

We ensure particles cannot leave the domain by moving all particles outside the domain back to the boundary. There may be multiple ghost particles created from a single real particle. This is especially noticeable in cube-shaped domains; a particle close to the corner may spawn up to three ghosts, one for each side of the cube.

Ghost particles can be also used to implement periodic boundary conditions. The implementation is rather straightforward. Instead of creating ghosts in mirror position, they are created on the opposite side of the domain. Whenever a particle leaves the domain, it exchanges its position with the ghost, moving it back to the domain on the opposite side.

2.10.2 Particle freezing

We found that boundaries supported by ghost particles sometimes have stability issues, especially near boundary corners. We thus also use another boundary condition which does not suffer

from this problem. The idea is to "freeze" particles whenever they get close to the boundary. The frozen particles are kept in place with fixed state quantities by explicitly setting all their derivatives to zero every time step. Other particles are then repelled by the frozen particles whenever they approach. Both the ghost boundary and the freezing boundary behave similarly with respect to the incoming shock wave, see Fig. 2.5, i.e. in both cases the shock wave is reflected by the boundary.

A number of other boundary conditions can be found in the literature, such as the non-reflecting boundary condition [Lastiwka et al., 2009], which ensures the shock wave is absorbed by the boundary.

2.11 Temporal discretization

In our formulation, the SPH is an explicit method; temporal derivatives of time-dependent quantities are computed using the current state at each time step. Similarly to Benz and Asphaug [1994], we use a predictor-corrector scheme for integration. It is a second-order method with only a single evaluation of derivatives per time step.

2.11.1 Time step criteria

The time step Δt in the SPH is limited by the Courant-Friedrichs-Lewy (CFL) criterion:

$$\Delta t_{\mathrm{CFL}} = C_{\mathrm{CFL}} \min_i \frac{h_i}{c_i}\,, \tag{2.140}$$

where $C_{\mathrm{CFL}} = 0.2$ is an empirical constant, h_i is the smoothing length and c_i is the local sound speed, computed using the equation of state. CFL criterion specifies the maximum allowed time step; exceeding Δt_{CFL} leads to numerical instability, which manifests as a sudden growth of energy and a spontaneous "explosion" in the simulation.

Besides the CFL criterion, our code contains other criteria to improve the precision of integration. Namely, we limit the time step using derivatives of time-dependent quantities, such as the specific internal energy u, in order to constrain the relative change of the quantity in a single time step. Such a criterion implies time step:

$$\Delta t_u = C_u \min_i \frac{|u_i| + u_0}{|\frac{\mathrm{d}u_i}{\mathrm{d}t}|}\,, \tag{2.141}$$

where $C_u = 0.2$ and u_0 is a small value with the same dimensions as u, which needs to be chosen according to typical values of u in the simulation. Adding u_0 to the numerator is necessary, as the time step would otherwise drop to zero when $u = 0$. Such a correction means the time step is determined by the *absolute* change of u instead of relative change whenever u is close to the zero. In our simulations, the specific energy u is often a limiting quantity that controls the time step, however, a similar criterion is added (automatically) for *all* time dependent quantities in the simulation, such as the density ρ, the damage D, the deviatoric stress components $S^{\alpha\beta}$, etc. These criteria control the discretization error of respective quantities and also prevent

overshooting in case of rapid changes of quantity values. The final step is then given by the minimum of all time step criteria:

$$\Delta t = \min(\Delta t_{\mathrm{CFL}}, \Delta t_u, \Delta t_\rho, \Delta t_{\boldsymbol{S}}, \ldots)\,. \tag{2.142}$$

Following Goswami and Pajarola [2011], we further restrict the time step by the velocity divergence $\nabla \cdot \boldsymbol{v}$ as:

$$\Delta t_{\nabla\cdot\boldsymbol{v}} = \frac{C_{\nabla\cdot\boldsymbol{v}}}{|\nabla \cdot \boldsymbol{v}|}\,, \tag{2.143}$$

where $C_{\nabla\cdot\boldsymbol{v}} = 0.005$. The divergence criterion helps to constrain the time step in supersonic flows, where the CFL criterion, given by the sound speed, is generally not sufficient to guarantee numerical stability. In collision simulations, the limiting time step criterion typically changes in the course of time. The initial impact and fragment ejection is often constrained by the derivative of specific energy or stress tensor, while the reaccumulation phase is integrated with the divergence or CFL time step.

2.11.2 Gravitational time step

At each time step, the code computes the derivatives, i.e. the right-hand sides of the SPH equations, and the self-gravitational interaction of particles. Both of these tasks take comparable amount of time to compute; usually, the calculation of self-gravity is about 50% slower than hydrodynamics in our code. However, they act on significantly different time scales. We demonstrate the difference on a typical setup of our simulations: let us assume a body of radius $R = 50\,\mathrm{km}$, made of $N = 10^5$ particles and the density $\rho = 2700\,\mathrm{kg/m^3}$. A characteristic time scale of hydrodynamics can be inferred from the crossing time of sound wave across a single particle:

$$t_{\mathrm{hydro}} \simeq \frac{h}{c} \simeq 0.1\,\mathrm{s}\,. \tag{2.144}$$

As for the self-gravitation, the time scale can be estimated from the gravitational acceleration $\boldsymbol{a}_g$. Given a single particle close to the surface of the body, the time scale is:

$$t_{\mathrm{gravity}} \simeq \sqrt{\frac{h}{\|\boldsymbol{a}_g\|}} \simeq 10\,\mathrm{s}\,. \tag{2.145}$$

We see that the gravity time scale is larger than the hydrodynamics time scale by two orders of magnitude. The changes of the gravitational potential are much slower compared to changes of state quantities like pressure or specific energy. Recalculating the gravity on every time step is unnecessary and quite inefficient. We thus significantly optimize the simulation by integrating the hydrodynamics and self-gravity with different time steps.

The disparity between hydrodynamical and gravitational time steps further increases in simulations with larger particle counts N or simulations with smaller targets, as $t_{\mathrm{CFL}} \propto h$ while $t_{\mathrm{gravity}} \propto \sqrt{h}$. Moreover, t_{CFL} represents the *maximum* allowed time step for hydrodynamics, but the actual time step is determined by Eq. 2.142 and it is often much smaller. Naturally, recomputing the gravity is pointless if the particles barely move during one hydrodynamical time step.

```
// Compute gravitational accelerations
a_gravity = computeBarnesHut( r + 1/2 v Δt_gravity ) ;
while t < t_0 + Δt_gravity do
    // Make predictions
    r = r + v Δt_SPH + 1/2 a Δt_SPH^2 ;
    v = v + a Δt_SPH ;
    // Compute hydrodynamical accelerations
    a_SPH = computeSPH(r, v) ;
    a_corr = a_SPH + a_gravity ;
    // Make corrections
    r = r + 1/3 (a_corr − a) Δt_SPH^2 ;
    v = v + 1/2 (a_corr − a) Δt_SPH ;
    a = a_corr ;
    // Advance time
    Δt_SPH = min(Δt_CFL, Δt_a, Δt_u, ...);
    t = t + Δt_SPH ;
end
```

Algorithm 1: Description of a single gravitational time step in our `OpenSPH` code. The equations are integrated using a predictor-corrector scheme.

Our approach is summarized in Algorithm 1. The gravitation is recomputed with the period $\Delta t_{\text{gravity}}$, using predicted particle positions in the middle of the time step:

$$\boldsymbol{r}_{\text{est}} = \boldsymbol{r} + \frac{1}{2}\boldsymbol{v}\Delta t_{\text{gravity}}\,. \tag{2.146}$$

The computed gravitational accelerations are cached and used to integrate particle velocities every time step until the next recomputation. Motivated by Eq. 2.145, the gravitational time step is computed as:

$$\Delta t_{\text{gravity}} = C_{\text{gravity}} \min_i \sqrt{\frac{h_i}{\|\boldsymbol{a}_i\|}}\,, \tag{2.147}$$

where $C_{\text{gravity}} = 0.2$ and $\boldsymbol{a}_i$ is the current acceleration of i-th particle. We further set a maximal allowed value of the step, which is usually $\Delta t_{\text{gravity}} = 5\,\text{s}$.

2.12 Self-gravitation

Gravity is a fundamental force of astrophysics. It is dominant on large scales and it is absolutely necessary to include gravity in the physical model of collisional simulation of large asteroids.

In the scaling law, the transition between the strength regime and the gravitation regime occurs at $D \simeq 100\,\text{m}$ [Benz and Asphaug, 1999], even small $D \simeq 10\,\text{km}$ bodies are thus significantly affected by gravity, especially if one carries out the simulation for long-enough time,

beyond the initial shock wave passage and fragmentation of the target. It mainly comes into play during the reaccumulation of fragments ejected during the impact and formation of the asteroidal family. Nevertheless, gravity should be already included prior to the initial impact to set up a hydrostatic equilibrium in the target.

In this section, we describe how self-gravitation is integrated into our model in the SPH discretization. Although the computation of gravity is quite similar to N-body approach, SPH particles are not point masses, they rather have a density profile described by the smoothing kernel W. Hence, the gravitational potential of particles needs to be softened as well, consistently with the smoothing used in hydrodynamics. Furthermore, the inclusion of gravity should not break any of the important properties of SPH, mainly the Galilean invariance and the conservation of integrals of motion.

2.12.1 Gravity in SPH discretization

For a set of N point-mass particles, the acceleration of the i-th particle due to gravity is simply:

$$\frac{\mathrm{d}\boldsymbol{v}_i}{\mathrm{d}t} = G \sum_{i \neq j} \frac{m_j(\boldsymbol{r}_j - \boldsymbol{r}_i)}{\|\boldsymbol{r}_j - \boldsymbol{r}_i\|^3} \,. \tag{2.148}$$

This equation still holds for smoothed particles when the smoothing kernel W is isotropic, provided they do not intersect each other (i.e. the corresponding kernel value W_{ij} is zero). However, it is necessary to account for softening of the gravitational potential for neighboring particles. The more two smoothed particles overlap, the smaller their gravitational attraction is compared to point masses. We follow Cossins [2010] by introducing a gravitational softening kernel ψ associated with the SPH smoothing kernel W as:

$$\phi(\boldsymbol{r}) = G \sum_j m_j \psi(\boldsymbol{r} - \boldsymbol{r}_j) \,, \tag{2.149}$$

where ϕ is the gravitational potential. The relationship between the gravitational softening kernel ψ and the smoothing kernel W can be derived from the Poisson equation:

$$\nabla^2 \phi(\boldsymbol{r}) = 4\pi G \rho(\boldsymbol{r}) = 4\pi G \sum_j m_j W(\boldsymbol{r} - \boldsymbol{r}_j) \,. \tag{2.150}$$

The left-hand side depends on the gravitational kernel ψ, while the right-hand side depends on the smoothing kernel W. Considering Eq. 2.150 has to hold for *any* particle distribution, we can relate the gravity kernel ψ and the smoothing kernel W directly. If we further consider that kernel $W(\boldsymbol{r})$ is a spherically symmetric function, the gravity kernel ψ can be found by solving the following ordinary differential equation:

$$\frac{1}{r^2} \frac{\mathrm{d}}{\mathrm{d}r} \left(r^2 \frac{\mathrm{d}\psi}{\mathrm{d}r} \right) = 4\pi W(r) \,. \tag{2.151}$$

This equation can be directly integrated to obtain the gradient of the gravity kernel ψ:

$$\frac{\mathrm{d}\psi}{\mathrm{d}r} = \frac{4\pi}{r^2} \int_0^r r'^2 W(r') \,\mathrm{d}r' + \frac{C}{r^2} \,. \tag{2.152}$$

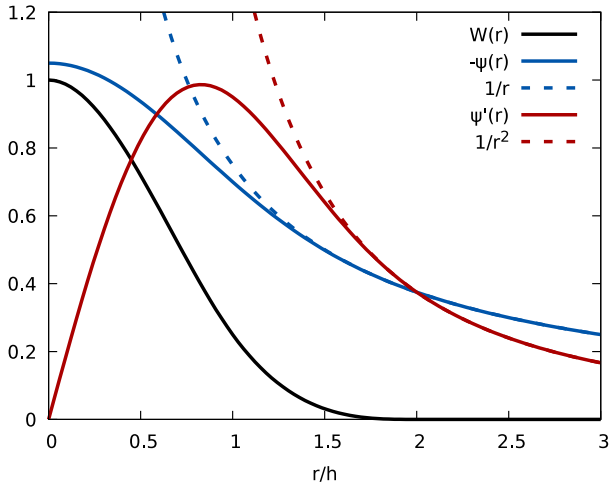

Figure 2.6: Cubic-spline kernel W, associated gravitational softening kernel ψ (with a negative sign) and its gradient ψ'. Dashed lines correspond to the gravitational kernel of a point mass with no softening.

Moreover, the kernel ψ has to fall back to the Newtonian potential of a point mass if the particles are sufficiently distant from each other. The constant C is thus determined from the boundary condition:

$$\frac{\mathrm{d}\psi}{\mathrm{d}r} \to \frac{1}{r^2}, \quad r \to \infty\,. \tag{2.153}$$

To obtain the final expression for the kernel gradient $\mathrm{d}\psi/\mathrm{d}r$, we have to specify the smoothing kernel W. For the cubic B-spline M_4 (Eq. 2.33), the gravity softening kernel gradient is:

$$\frac{\mathrm{d}\psi}{\mathrm{d}r} = \begin{cases} \frac{1}{h^2}\left(\frac{4}{3}q - \frac{6}{5}q^3 + \frac{1}{2}q^4\right), & 0 \le q < 1\,, \\ \frac{1}{h^2}\left(\frac{8}{3}q - 3q^2 + \frac{6}{5}q^3 - \frac{1}{2}q^5 - \frac{1}{15q^2}\right), & 1 \le q < 2\,, \\ \frac{1}{r^2}\,, & q \ge 2\,, \end{cases} \tag{2.154}$$

where $q = r/h$. Actually, we do not need to know the kernel ψ, because the gravitational acceleration depends only on kernel gradient. However, having the formula for kernel ψ is still useful, e.g. for evaluation of the total energy in the simulation. For the M_4 kernel, the associated kernel ψ is:

$$\psi = \begin{cases} \frac{1}{h}\left(\frac{2}{3}q^2 - \frac{3}{10}q^4 + \frac{1}{10}q^5 - \frac{7}{5}\right), & 0 \le q < 1\,, \\ \frac{1}{h}\left(\frac{4}{3}q^2 - q^3 + \frac{3}{10}q^4 - \frac{1}{30}q^5 - \frac{8}{5} + \frac{1}{15q}\right), & 1 \le q < 2\,, \\ -\frac{1}{r}\,, & q \ge 2\,. \end{cases} \tag{2.155}$$

Unlike the SPH smoothing kernel W, this kernel does not have a compact support. An example of the softening kernel is plotted on Fig. 2.6

2.12.2 Multipole approximation

Gravity is a long-distance force and therefore its effects cannot be restricted to neighboring particles like for the hydrodynamic forces. The right-hand side of Eq. 2.148 needs to be computed for every particle. This leads to computational complexity $\mathcal{O}(N^2)$, which is prohibitively time-consuming for any simulation with $N \gtrsim 10^4$ particles.

2.12.2.1 Barnes-Hut algorithm. To compute gravitational accelerations in simulations with a large number of particles, we have to employ a faster, albeit approximative method — the Barnes-Hut algorithm. It was first introduced by Barnes and Hut [1986] and since then it has been used commonly in N-body as well as hydrodynamic simulations. The key idea is to replace a group of particles, located far away from the given point, with a single particle, located at the center of mass with a mass equal to the sum of masses of all particles in the group. This allows us to significantly reduce the number of evaluated gravitational interactions with little loss of accuracy. Furthermore, the error introduced by the Barnes-Hut approximation can be constrained by grouping together more or fewer particles, depending on the size of the group and the distance from the point where the acceleration is evaluated.

The accuracy of the method can be further improved by calculating higher gravitational moments for grouped particles. The computed accelerations then depend on the mass distribution within the group, rather than just the total mass. While the multipole expansion is usually performed in spherical coordinates using spherical harmonics as the basis functions, we follow Stadel [2001] and perform the expansion in Cartesian coordinates. The n-th moment is then simply:

$$M^{\underline{n}} = \sum_i m_i x_i^{\underline{n}}, \tag{2.156}$$

where the underscored $\underline{n}$ represents n indices, i.e. the dipole moment is $M^\alpha = \sum_i m_i x_i^\alpha$, the quadrupole moment $M^{\alpha\beta} = \sum_i m_i x_i^{\alpha\beta} = \sum_i m_i x_i^\alpha x_i^\beta$ and the octupole moment $M^{\alpha\beta\gamma} = \sum_i m_i x_i^{\alpha\beta\gamma} = \sum_i m_i x_i^\alpha x_i^\beta x_i^\gamma$. The number of tensor components and the complexity of the resulting expressions grows significantly and it quickly becomes impractical, which is why the spherical harmonics approach is generally preferred. However, we truncate the multipole expansion at the octupole order, providing a viable trade-off between precision and complexity, and unlike the spherical harmonics, we avoid costly computations of trigonometric functions when calculating the moments in Cartesian coordinates.

2.12.2.2 Traceless multipoles. When the moments are computed, not all components of moment tensors need to be stored in memory. In fact, we can significantly reduce the number of stored values by using the reduced multipole moment [Stadel, 2001]:

$$Q^{\underline{n}} = \sum_{j=0}^{\lfloor \frac{n}{2} \rfloor} (-1)^j \frac{(2n-2j-1)!!}{j!(2n-1)!!} \delta^{(\underline{2j}} T_j^{\underline{n-2j)}}(M^{\underline{n}}) \tag{2.157}$$

where $T^{\underline{n}}_{\underline{n-2j}}$ is defined as:

$$T_j^{\underline{n-2j}}(M^{\underline{n}}) = \delta_{\underline{2j}} M^{\underline{2j}\,\underline{n-2j}}. \tag{2.158}$$

The brackets grouping superscripts of different quantities indicate a sum over all *unique permutations* of indices. This expression also uses the Einstein convention, summing over common indices. The reduced multipole $Q^{\underline{n}}$ is traceless and it only has $2n + 1$ independent components.

To compute the moments, we first have to define the groups of particles. In the Barnes-Hut method, a hierarchical spatial structure is constructed over the particles in the simulation. `OpenSPH` implements the K-d tree, a generalization of the binary tree in multiple dimensions. The gravitational accelerations are computed in two steps. First, the tree is traversed starting from leaf nodes going to the root node (bottom-up traversal) and the gravitational moments are computed for each node. Second, the tree is traversed from the root node going downwards (top-down traversal) and the gravitational accelerations are computed for all individual particles, using the precomputed moments. The bottom-up and the top-down traversal are described in Algorithm 2 and Algorithm 3, respectively.

2.12.2.3 Bottom-up traversal. The bottom-up traversal starts by computing moments in leaf nodes of the K-d tree. In our code, the maximal number of particles in a leaf node is set to 20. All moments are evaluated at the center of mass of the node, the dipole moment is thus always zero. Moving to the parent nodes, the multipole moments are computed by summing up the moments in the child nodes. However, the summed moments have to be first moved to the center of mass of the parent node, as only moments defined with respect to the same point can be summed. A moment translated by an arbitrary vector $\boldsymbol{d}$ can be computed using the parallel axis theorem [Stadel, 2001]:

$$M^{\underline{n}}_{\boldsymbol{d}} = \sum_j M^{(\underline{n-j}} d^{\underline{j})} \,. \tag{2.159}$$

The nodes are processed recursively until the root node of the tree is reached.

2.12.2.4 Top-down traversal. The top-down traversal uses the gravitational moments to compute the accelerations. Rather than traversing the tree for each particle, we traverse the tree only once and accumulate the accelerations for all particles at the same time, which greatly improves code performance. Starting from the root node of the tree, the algorithm recursively descends to child nodes. During the traversal, each node obtains three lists from its parent. *Node list* contains nodes for which the gravitational interaction can be approximated using the multipole moments. *Particle list* contains particles whose gravity cannot be approximated and it has to be computed by pair-wise interactions, using Eq. 2.148. Finally, *check list* contains the nodes that are yet to be decided; they might be added to the node list, they might be "opened" and the stored particles added to the particle list, or they can be left in the check list, deferring this decision to the child nodes.

2.12.2.5 Opening angle. The opening of nodes during traversal is linked to the error introduced by the multipole approximation. It is controlled by the code parameter named the opening angle θ_{open}. Larger values of θ_{open} imply fewer nodes are opened, hence the code performance improves at the cost of accuracy. In the extreme case of $\theta_{\text{open}} = 0$, all the nodes are opened and

Input : Particle positions and masses
Output : Multipole moments for each node Q[node]

Function `buildNode(node)`
  if `isLeaf(node)` **then**
    r_{com} = `centerOfMass(node)`;
    Q[node] = `computeMultipole(node,` r_{com}`)`;
  else
    `buildNode(node→left)`;
    `buildNode(node→right)`;
    r_{com} = `centerOfMass(node→left, node→right)`;
    Q_{left} = `parallelAxisTheorem(node→left,` r_{com}`)`;
    Q_{right} = `parallelAxisTheorem(node→right,` r_{com}`)`;
    Q[node] = $Q_{\text{left}} + Q_{\text{right}}$;
  end
end
`buildNode(rootnode)`

Algorithm 2: Bottom-up traversal of the K-d tree, computing multipole moments for each tree node.

the algorithm falls back to the brute-force $\mathcal{O}(N^2)$ gravity computation. Using the opening angle, we compute the opening radius r_{open} for each node as:

$$r_{\text{open}} = \frac{2}{\sqrt{3}\theta_{\text{open}}} r_{\text{max}} , \tag{2.160}$$

where r_{max} is the maximal distance of a particle from the center of mass of the node. The opening radius defines a sphere, centered at the center of mass of the node.

For each evaluated node, we go through the nodes in the check list. We compute the bounding box of particles in the evaluated node and the opening sphere of the checked node. There are three possible configurations of a box and a sphere. Either the box is fully contained within the sphere, the box is intersected by the sphere, or the box lies outside the sphere. In the first case, we know that the evaluated note and *all* of its child nodes lie inside the opening sphere, and thus the checked node cannot be approximated by multipole expansion. Therefore, if the checked node is a leaf node, all of its particles are added into the particle list of the evaluated node, otherwise the check list is extended by child nodes of the checked node and the checked node itself is removed from the check list. In case the sphere intersects the box, it is possible some of the child nodes still lie outside the opening sphere. The checked node is thus kept in the check list, the same decision process is then performed by the child nodes. Finally, if there is no intersection of the bounding box and the opening sphere, the checked node can be approximated using multipoles. It is thus added into the node list and removed from the check list.

2.12.2.6 Evaluation of acceleration. Once the traversal descents into a leaf node, the gravitational accelerations are computed for all particles contained in the node, using the particle

Input : Multipole moments Q for each tree node
Output : Gravitational accelerations of all particles

```
Function evalNode(node, checklist, particlelist, nodelist)
    box = getBoundingBox(node);
    for checknode in checklist do
        sphere = getOpeningSphere(checknode);
        if sphereContainsBox(sphere, box) then
            // Do exact gravity evaluation for all particles
            if isLeaf(checknode) then
                particlelist = particlelist ∪ checknode;
            else
                checklist = checklist ∪ (checknode → left);
                checklist = checklist ∪ (checknode → right);
            end
            checklist = checklist \ checknode;
        else if not intersects(sphere, box) then
            // We can approximate the node by multipole expansion
            nodelist = nodelist ∪ checknode;
            checklist = checklist \ checknode;
        else
            // Keep in the checklist, will be decided by children
        end
    end
    if isLeaf(node) then
        evalParticleList(node, particlelist);
        evalNodeList(node, nodelist);
    else
        evalNode(node → left, checklist ∪ (node → right), particlelist, nodelist);
        evalNode(node → right, checklist ∪ (node → left), particlelist, nodelist);
    end
end

evalNode(rootnode, ∅, ∅, ∅);
```

Algorithm 3: Top-down traversal of the K-d tree for the evaluation of acceleration, using precomputed multipoles stored in each node of the tree.

list and the node list aggregated during the descend. The exact acceleration is computed for all pairs of particles from the leaf node and the particle list, using Eq. 2.148. The approximate accelerations are computed by evaluating the gradient of the potential, given by the multipole expansion up to octupole order:

$$a^{\underline{1}} = \sum_n \left(\gamma_{n+1} x^{\underline{1}} Q_n^{\underline{0}} + \gamma_n Q_n^{\underline{1}} \right) , \tag{2.161}$$

where the values γ_n are defined recursively as:

$$\gamma_0 = -\frac{1}{r}\,, \tag{2.162}$$

$$\gamma_{n+1} = -\frac{2n+1}{r^2}\gamma_m\,, \tag{2.163}$$

and the tensors $Q_n^{\underline{m}}$ relate to the traceless tensors $Q^{\underline{n}}$ as:

$$Q_n^{\underline{m}} = \frac{1}{(n-m)!}x_{\underline{n-m}}Q^{\underline{m}\,\underline{n-m}}\,. \tag{2.164}$$

2.13 Implementation notes

Since practical aspects of an SPH solver implementation are rarely mentioned in scientific papers, I believe it is worthwhile to briefly describe our solvers used in `OpenSPH`, including implementation details.

2.13.1 SPH solvers

We implemented two different solvers, code-named *symmetric* and *asymmetric* solver. Both solvers have their advantages (and disadvantages). Which solver is better depends on the machine running the simulation and on the problem to be solved. Of course, both solvers produce the same output (give or take minor round-off errors), they only differ in the way SPH derivatives are evaluated.

The symmetric and asymmetric solvers are summarized in Algorithms 4 and 5, respectively. Their main differences are outlined in Table 2.1.

2.13.1.1 Evaluation of derivatives. The main difference between the two solvers is in the accumulation of derivatives for each particle. Asymmetric solver evaluates each particle independently; for i-th particle, it finds all of its neighbors and sums the derivatives calculated for each particle pair i and j, the result of which is then assigned to the i-th particle.

On the other hand, symmetric solver utilizes the fact that all terms in SPH equations (forces, velocity derivatives, energy sources, etc.) are either symmetric or antisymmetric with a respect to particles i and j. It is thus superfluous to evaluate the interaction of particles i and j twice; the contribution of the j-th particle to the derivative of the i-th particle is equal to (possibly with a negative sign) the contribution of the i-th particle to the derivative of the j-th particle. For this reason, the symmetric solver iterates over each particle pair only once, it computes the summands and adds the result to the derivatives of both particles i and j. The symmetric solver thus does considerably fewer computations compared to the asymmetric one.

2.13.1.2 Search radius. There is another advantage of the symmetric solver. To explain it, let us first discuss the required search radius R_i of i-th particle. Since the smoothing kernel W has compact support, the radius required to find all neighbors of the i-th particle is proportional to the smoothing length h. However, the smoothing lengths used to evaluate the kernel are

Input : Particle positions $\boldsymbol{r}_i$ and smoothing lengths h_i
Output: Derivatives of time-dependent quantities

```
rankH = findRankH(h);
parallelFor i = 1 to N do
    neighs = findNeighbors(r_i, η h_i);
    for j in neighs do
        if rankH_j > rankH_i then
            continue;
        end
        h_bar = 1/2 (h_i + h_j);
        grad = ∇W(r_i − r_j, h_bar);
        // Accumulate the derivatives to a thread-local storages
        derivsTL = derivs[threadId()];
        evalParticlePair(derivsTL, i, j, grad);
        evalParticlePair(derivsTL, j, i, grad);
    end
end
// Sum up the thread-local results
derivs = reduce(derivsTL);
```

Algorithm 4: Description of the symmetric solver used in `OpenSPH`.

symmetrized using Eq. 2.26 in order to conserve the total momentum. Assuming the support radius of the smoothing kernel $W(\boldsymbol{r}, h)$ is ηh ($\eta = 2$ for the cubic spline kernel), the required search radius for the i-th particle is:

$$R_i = \eta \max_j \left(\frac{h_i + h_j}{2} \right), \tag{2.165}$$

where the sum iterates over all interacting particles. This leads to an egg-or-chicken problem; to determine the search radius of the particle i, we first need to find the most extended particle j that interacts with the particle i, for which we need to know the search radius R_i.

The symmetric solver provides an elegant solution to the search radius problem. As each particle pair is evaluated only once, we can sort the particles by their smoothing lengths to find their *ranks*, i.e. unique indices, in the sorted sequence. The smoothing length h_j of the particle with a lower rank than particle i is then always smaller than or equal to the smoothing length h_i. Therefore, we can simply set the search radius of each particle to:

$$R_i = \eta h_i \tag{2.166}$$

and restrict the neighbor search only to particles with a lower rank. This trick ensures that we correctly find all interacting particles and also that all particle pairs are evaluated only once.

To our knowledge, there is no straightforward way to compute the optimal search radius for the asymmetric solver in constant time. If the smoothing lengths are equal or similar for

all particles, we can simply find the maximal smoothing length $h_{\max} = \max_i h_i$ and define the search radius as:

$$R_i = \eta \frac{h_i + h_{\max}}{2} . \tag{2.167}$$

Unfortunately, this method becomes extremely inefficient when smoothing lengths are adaptively adjusted during the simulation using Eq.2.25. The largest particle can easily exceed other particles by an order of magnitude and the computed search radius R_i is significantly larger than the optimal value.

To improve the code performance in such cases, we use a two-phase approach. First, we create a spatial hash grid, using spatial coordinates of particles as a key. The cell size of the hash grid is set to $\eta h_{\max}$. In each time step, the particles are assigned to the cells based on their current positions. Given a cell at grid coordinates x, y, z, we then find the maximal smoothing length $h_{x,y,z}$ of all particles assigned to this cell. To make sure we do not skip any potentially interacting particles from neighboring cells, we increase the value of each cell to the maximum of the cell and all its neighbor cells. We finally compute the search radius R_i for each particle using the smoothing length $h_{x,y,z}$ of the cell containing the i-th particle as:

$$R_i = \eta \frac{h_i + h_{x,y,z}}{2} . \tag{2.168}$$

Since the size of the cell is equal to the maximal kernel radius in the simulation, we can guarantee no neighbors are missing. Although both the construction of the hash grid and the evaluation of the required search radius for each particle add additional computational overhead, it greatly improves the code performance whenever the smoothing lengths vary significantly. In case the smoothing lengths are constant during the simulation and all the particles have either equal or similar smoothing lengths, we can skip constructing the hash grid and simply use the maximal smoothing length instead, thus avoiding the extra complexity and performance overhead.

2.13.1.3 Correction tensor computation. When the symmetric solver is used, each particle finds only half (on average) of its neighbors. In fact, the sum over neighbors of any given particle is completed only after *all* the particles are evaluated. This poses a problem when the correction tensor C_i, defined by Eq.2.58, is used in the simulation. The correction tensor requires to first compute a complete sum over particle neighbors, invert the resulting matrix and then use the matrix inverse when evaluating the velocity gradient for each particle. However, since the sum is completed only after iterating over all particles, this requires doing *two* loops over all particle pairs — the first one to compute the correction tensors C_i for all particles and the second one to finally compute the corrected gradients. This is a significant performance penalty of the solver. Asymmetric solver has no such issue. It requires only to iterate over the list of neighbors twice, and since the neighbors are likely to be stored in the CPU cache, the performance penalty is minimal.

2.13.1.4 Parallelization. Both solvers differ significantly in parallelization. In `OpenSPH`, the work is split among available threads using a task-based scheduler. Particles are split into chunks

Input : Particle positions $\boldsymbol{r}$ and smoothing lengths h
Output: Derivatives of time-dependent quantities

$R_{\max} = \eta \max(h_1, ..., h_N)$;
`// Compute a hash grad storing maximal radius in each cell`
hashgrid = $\emptyset$;
for $i = 1$ **to** N **do**
    $\boldsymbol{c} = \lfloor \boldsymbol{r}_i / R_{\max} \rfloor$;
    hashgrid[$\boldsymbol{c}$] = max(hashgrid[$\boldsymbol{c}$], ηh_i);
end
`// Propagate maximum values to neighboring cells`
`dilate(hashgrid);`
parallelFor $i = 1$ **to** N **do**
    $\boldsymbol{c} = \lfloor \boldsymbol{r}_i / R_{\max} \rfloor$;
    `// Determine search radius using the hash grid`
    R = hashgrid[$\boldsymbol{c}$];
    neighs = `findNeighbors(`$\boldsymbol{r}_i$, $\frac{1}{2}(h_i + R)$`);`
    for j **in** neighs **do**
        $h_{\text{bar}} = \frac{1}{2}(h_i + h_j)$;
        if $\|\boldsymbol{r}_i - \boldsymbol{r}_j\| > h_{\text{bar}} R_W$ **then**
            continue;
        end
        grad = $\nabla \mathrm{W}\left(\boldsymbol{r}_{\mathrm{i}} - \boldsymbol{r}_{\mathrm{j}}, \mathrm{h}_{\mathrm{bar}}\right)$;
        `evalParticlePair(`derivs, i, j, grad`);`
    end
end

Algorithm 5: Description of the asymmetric solver used in `OpenSPH`.

and assigned to worker threads, which then compute the derivatives for the assigned particles. As performance is an important aspect of the code, it is essential to utilize all available CPU cores optimally. This shows the strength of the asymmetric solver. Particles only accumulate their own derivatives, the interacting particles are never modified. Therefore, each thread can simply work independently without the need for synchronization.

However, the same is not true for the symmetric solver, because each particle i accumulates to both the derivatives of the particle i and the interacting particle j, which may be assigned to a different thread. Accumulating from multiple threads without synchronization would then result in a race condition and potentially an incorrect result. We decided to store the accumulated derivatives in temporary thread-local storage. Each thread thus computes a fraction of the result and the thread-local sums are then reduced to get the final results. This inevitably increases the memory overhead. A standard double-precision simulation requires storing 192 bytes per particle per thread. For 1 000 000 particles and 32 threads, about 6 GB of additional memory needs to be accumulated and reduced every time step.

Asymmetric solver	Symmetric solver
N evaluations per time step	$N/2$ evaluations per time step
Performs best for equal-sized particles	Same number of interactions regardless of h
Material-independent	Performance penalty for solid materials
Embarrassingly parallel	Requires thread-local derivatives
Suitable for highly-parallel computation	Suitable for single-threaded computation

Table 2.1: Bullet points outlining the main differences between the asymmetric and symmetric solver implemented in `OpenSPH`.

Unfortunately, even the asymmetric solver does not guarantee perfectly linear scaling with the number of threads, as there is other work to be done outside the main loop evaluating derivatives, mainly building the K-d tree, computing the time step and also self-gravitational accelerations.

We used Intel Threading Building Blocks [Pheatt, 2008] for parallelization. The code further uses intrinsic instructions for vectorization which optimize the vector and tensor algebra, the performance is thus significantly improved compared to the code `SPH5` [Benz and Asphaug, 1994] we used previously.

2.13.2 Neighbor queries

An efficient algorithm for finding particles within a certain radius is a fundamental part of the code. Apart from the evaluation of gravity, a search for neighbors is generally the computational bottleneck of simulations. It is thus necessary to ensure the search for neighbors is fast and that the performance does not deteriorate during the simulation as particles recede from each other.

An exhaustive search of neighbors, although useful for tests and verification of other algorithms, is not viable due to its $\mathcal{O}(N^2)$ complexity. In `OpenSPH`, we thus use a K-d tree or alternatively a spatial hash grid for neighbor queries. Both approaches belong to a set of classical algorithms of computer science [Bentley, 1975; Samet, 1990; Teschner et al., 2003; Kipfer and Westermann, 2006; Onderik and Ďurikovič, 2008; Lefebvre and Hoppe, 2006]. The K-d tree is the default, since it is robust and works well for any particle distribution, although the hash grid can be faster in some situations.

2.13.2.1 K-d tree. The K-d tree is a generalization of the binary tree to multiple dimensions. It is constructed by recursively subdividing the particles into groups along the dimension of the largest extent. The subdivision ends when the number of particles in the node is below a certain threshold; this is a parameter of the code; the default value $n_{\text{leaf}} = 20$ seems to be the optimal value in most situations. Neighbors of a given particle are then found by tree traversal, descending into nodes that are closer than the query radius. The computational complexity for a single particle is only $\mathcal{O}(\log N)$, assuming a balanced tree.

There are two main advantages of K-d tree. First, it works remarkably well even for extremely uneven distributions of particles in space, which is often the case for impact simulations. During

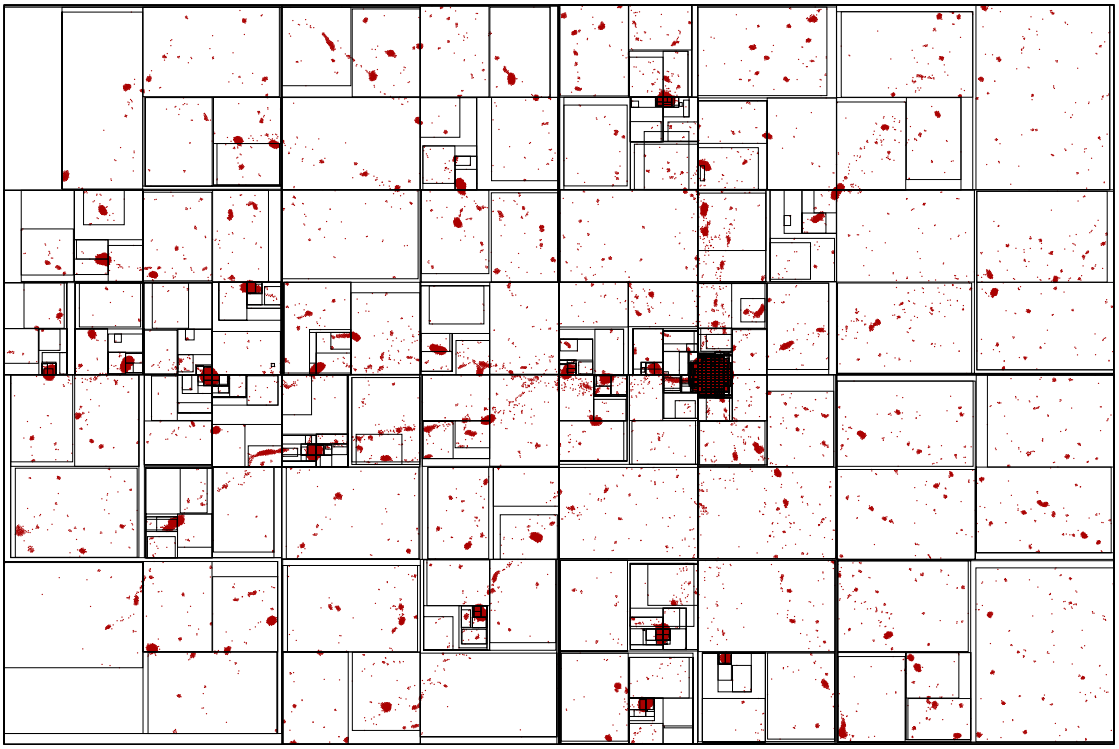

Figure 2.7: Snapshot of a simulation, showing the K-d tree clustering of particles. Individual particles are drawn red, black boxes show the bounding boxes of particles in tree nodes. Each leaf node holds $n_{\text{leaf}} = 400$ particles.

the late stages of reaccumulation, the fragments are separated by distances that are larger by several orders of magnitude compared to the sizes of fragments. Second, tree nodes can also store multipole moments which are used for the evaluation of self-gravity (see Sec. 2.12.2). Hence, there is no need to build another structure to compute gravity, which would require computational and memory overhead.

2.13.2.2 Spatial hash grid. Alternatively, the particles are partitioned to a three-dimensional grid with a fixed cell size, i.e. a particle with coordinates x, y, z is assigned to a grid cell with integer indices:

$$i = \left\lfloor \frac{x}{h_{\text{cell}}} \right\rfloor, \; j = \left\lfloor \frac{y}{h_{\text{cell}}} \right\rfloor, \; k = \left\lfloor \frac{z}{h_{\text{cell}}} \right\rfloor, \tag{2.169}$$

where h_{cell} denotes the cell size. We set the cell size to:

$$h_{\text{cell}} = \eta \max_i h_i \,, \tag{2.170}$$

where η is the support radius of the kernel ($\eta = 2$ for the standard cubic kernel) and h_i is the smoothing length of the i-th particle. Rather than allocating the entire grid in memory, we store all cells in a hash map. The hash for three-dimensional cell index i,j,k is computed as:

$$H(i, j, k) = (73856093i) \oplus (19349663j) \oplus (83492791k) \,, \tag{2.171}$$

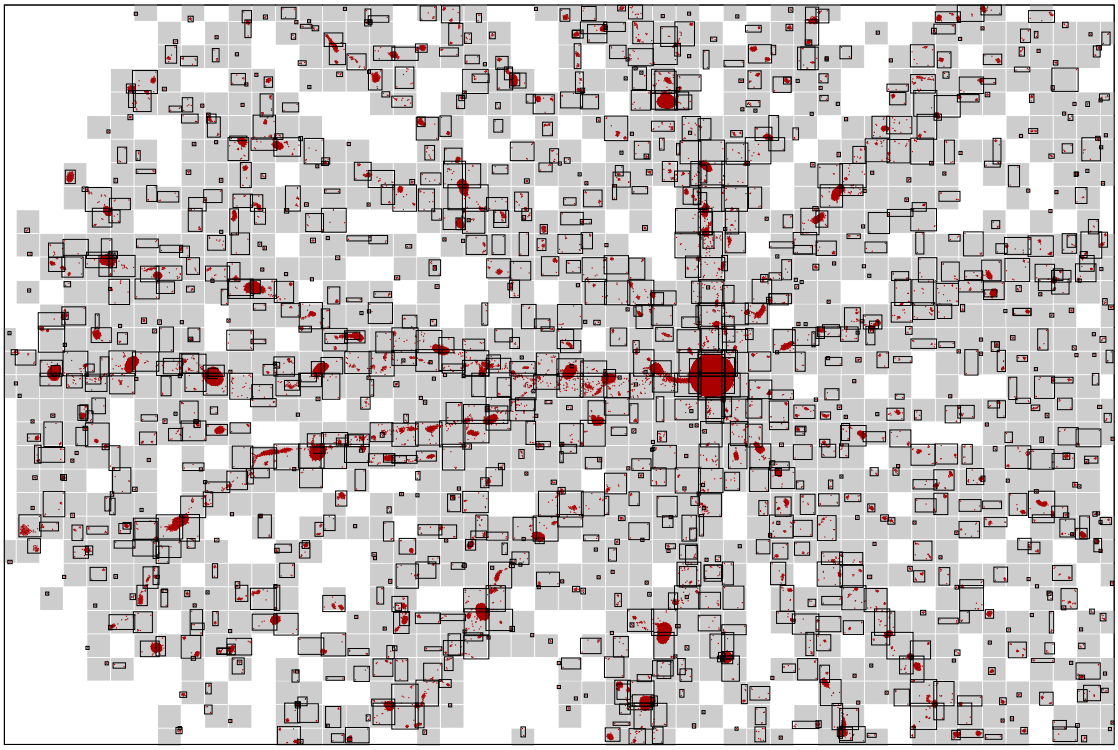

Figure 2.8: Snapshot of a simulation, showing cells of a spatial hash grid. The particle configuration is the same as in Fig. 2.7. Gray squares show the allocated cells, black boxes represent the bounding boxes of particles stored in the cells. The cell size is set to $30h$.

where the symbol $\oplus$ denotes binary XOR operation. Using the hash map, only cells occupied by particles need to be allocated, hence the required memory does not increase as the particles move away from each other. When looking for neighbors of a given particle, only particles in the corresponding cell and possibly the neighboring cells need to be checked.

The advantage of the hash grid over the K-d tree is a generally faster look-up of particles in cells. Compared to $\mathcal{O}(\log N)$ of the K-d tree, the hash grid allows to search neighbors in $\mathcal{O}(1)$, provided hash collisions can be neglected. The implementation is also considerably simpler, as we make use of `std::unordered_map` from the C++ standard library. Unfortunately, it is not suitable for simulations involving gravity, as a K-d tree (or possibly other hierarchical structure) needs to be built anyway to evaluate gravitational interactions.

2.14 Surface reconstruction

Collisional simulations usually do not require extracting a surface within a continuum, because all forces and other terms in the equations are volumetric. While surface terms can be used in some SPH simulations, e.g. to add a surface tension or radiative cooling into the physical model, no such terms are present in our problem formulation. Nevertheless, surface extraction is a part of `OpenSPH` code, as it can be utilized to determine shapes of fragments. The surface is also

convenient for visualization purposes, because it allows to render a fragment as a continuous volume rather than a group of discrete spherical particles.

Surface reconstruction from particles is a well-known problem in computer graphics [Blinn, 1982; Müller et al., 2003; Ihmsen et al., 2014]. We follow the approach of Yu and Turk [2013] and define a *color field* function C as:

$$C(\boldsymbol{r}) = \sum_i \frac{m_i}{\rho_i} \frac{1}{h_i^3} w\left(\frac{\|\boldsymbol{r} - \boldsymbol{r}_i\|}{h_i}\right), \tag{2.172}$$

where $w(\|\boldsymbol{r}\|/h)/h^3 = W(\boldsymbol{r}, h)$ is a dimensionless form of the smoothing kernel. This definition is similar to the SPH density (Eq. 2.5), except the summand is divided by the particle density ρ_i. The color field C is thus a dimensionless quantity, which serves as an indicator function of the volume. Given a point $\boldsymbol{r}$ inside the body, $C(\boldsymbol{r})$ is close to 1; deviations from value 1 are only caused by particle disorder and local density gradient. If $\boldsymbol{r}$ is outside the body with no particles in the vicinity, the sum is empty and $C(\boldsymbol{r})$ is thus trivially zero. Due to particle smoothing, the function $C(\boldsymbol{r})$ is not discontinuous but falls from $C \simeq 1$ to $C = 0$ gradually. The surface of the SPH continuum can be then defined implicitly as the *isosurface* $C(\boldsymbol{r}) = c_0$, where c_0 is a suitable constant. Increasing c_0 makes the surface more smooth and less sensitive to noise in particle distributions, but it may also remove surface details or small asteroid fragments. We empirically determined that $c_0 = 0.13$ is usually the best choice.

The surface quality can be further improved by using an anisotropic smoothing kernel. The color field is then redefined as:

$$C(\boldsymbol{r}) = \sum_i \frac{m_i}{\rho_i} |\det \boldsymbol{G}_i| w\left(\|\boldsymbol{G}_i \cdot (\boldsymbol{r} - \boldsymbol{r}_i)\|\right), \tag{2.173}$$

where $\boldsymbol{G}_i$ is the anisotropy tensor. Tensor $\boldsymbol{G}_i$ represents the particle distribution in the neighborhood of $\boldsymbol{r}_i$. To find $\boldsymbol{G}_i$, we first need to construct the covariance matrix:

$$\boldsymbol{K}_i = \sum_j (\boldsymbol{r}_j - \boldsymbol{r}_i) \otimes (\boldsymbol{r}_j - \boldsymbol{r}_i), \tag{2.174}$$

where the sum goes over neighboring particles. Matrix $\boldsymbol{G}_i$ is then essentially an inverse of matrix $\boldsymbol{K}_i$, however, care must be taken to avoid inverting singular matrices. To make it robust, we compute the singular value decomposition of $\boldsymbol{K}_i$:

$$\boldsymbol{K}_i = \boldsymbol{U}\boldsymbol{\Sigma}\boldsymbol{V}^{\mathrm{T}}. \tag{2.175}$$

Here, $\boldsymbol{\Sigma}$ is a diagonal matrix with elements $\boldsymbol{\Sigma} = \mathrm{diag}(\Sigma_1, \Sigma_2, \Sigma_3)$, where $\Sigma_1 \geq \Sigma_2 \geq \Sigma_3$ is assumed. To avoid small singular values, which could cause numerical instabilities, and also to limit the anisotropy of the kernel, the diagonal elements are thresholded using:

$$\tilde{\Sigma}_{2,3} = \max(\Sigma_{2,3}, k\Sigma_1), \tag{2.176}$$

where $k = 0.25$ is a user-defined constant. Finally, the anisotropy tensor $\boldsymbol{G}_i$ is defined as:

$$\boldsymbol{G}_i = \boldsymbol{V}\tilde{\boldsymbol{\Sigma}}^{-1}\boldsymbol{U}^{\mathrm{T}}. \tag{2.177}$$

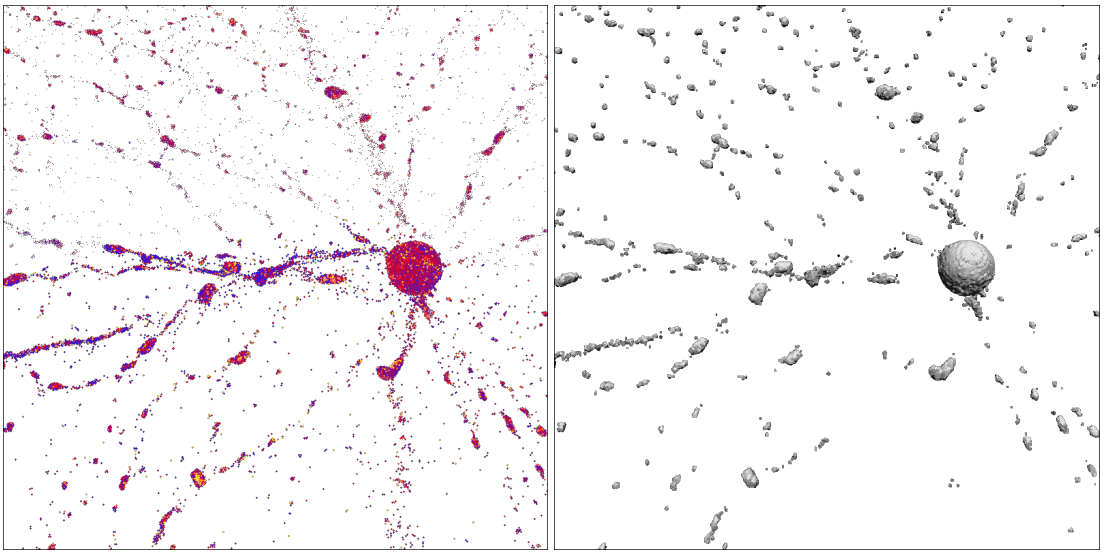

Figure 2.9: Snapshot of a reaccumulation phase during impact simulation. The image on the left shows individual particles, encoding particle speed as color. Particles are used to compute the color field 2.173, from which a triangle mesh is extracted using marching cubes. The resulting mesh is rendered with flat shading in the right image.

Once the color function $C(\boldsymbol{r})$ is known, the surface mesh can be extracted using an off-the-shelf algorithm, such as the marching cubes [Lorensen and Cline, 1987]. If there is no need for triangle mesh, the implicit surface can also be rendered directly using raymarching. In that case, the color field C can be also used to compute the surface normal, which is necessary for surface shading. The (unnormalized) normal vector $\boldsymbol{n}$ is given by the color field gradient:

$$\boldsymbol{n} = \nabla C = \sum_i \frac{m_i}{\rho_i} \nabla W(\boldsymbol{r} - \boldsymbol{r}_i, h_i)\,. \tag{2.178}$$

— Chapter iii —

NUMERICAL AND LABORATORY EXPERIMENTS

Validation is a crucial part of a development of any numerical code. In this chapter, we review tests of the `OpenSPH` code we developed, comparing a numerical solution with an analytical one if such a solution exists, checking the integrals of motion, and discussing results of selected laboratory experiments. All plots and visuals were obtained using our code.

3.1 Sod shock tube test

One simple test that hydrocodes have to "pass" is a numerical solution of a one-dimensional Riemann problem. While the test is quite rudimentary, it can reliably reveal gross (but sometimes indiscernible) errors in equations, such as an incorrect sign. Still, it shows the basic properties of fluid dynamics, such as sound waves, shock waves, rarefaction waves, etc. As for the SPH discretization, the shock tube test mainly demonstrates the importance of the artificial viscosity.

The test calculates the temporal evolution of a gas tube by solving the Euler equations in one dimension:

$$\frac{\partial \rho}{\partial t} + \frac{\partial}{\partial x}(\rho v) = 0\,, \tag{3.1}$$

$$\frac{\partial v}{\partial t} + v\frac{\partial v}{\partial x} + \frac{1}{\rho}\frac{\partial P}{\partial x} = 0\,, \tag{3.2}$$

$$\frac{\partial u}{\partial t} + v\frac{\partial u}{\partial x} + \frac{P}{\rho}\frac{\partial v}{\partial x} = 0\,, \tag{3.3}$$

together with the ideal gas equation of state:

$$P = (\gamma - 1)\rho u\,. \tag{3.4}$$

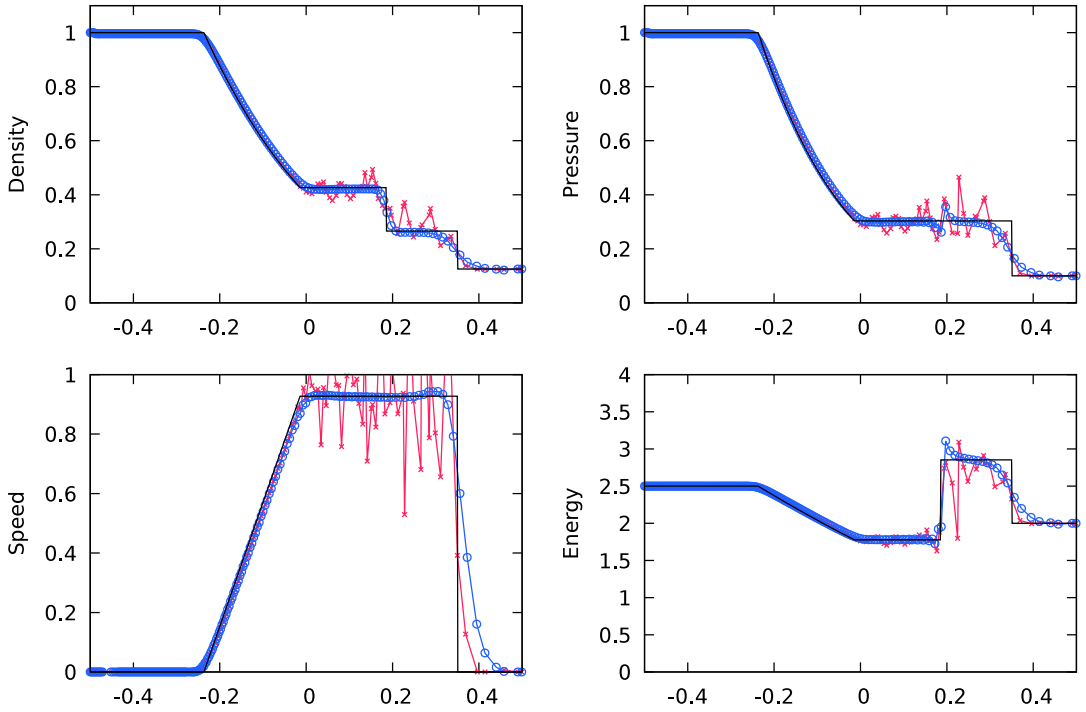

Figure 3.1: Numerical solution of the one-dimensional Sod shock tube problem (blue circles) compared to the analytical solution (black solid line) and unphysical numerical solution computed without the artificial viscosity (red crosses) at time $t = 0.2$. The simulations contains $N = 400$ particles.

Initially, the gas is divided into two regions along $x = 0$, denoted L and R. Following Sod [1978], we set up the initial conditions as follows:

$$\begin{aligned} \rho_L &= 1\,, & P_L &= 1\,, & v_L &= 0\,, \\ \rho_R &= 0.125\,, & P_R &= 0.1\,, & v_R &= 0\,. \end{aligned} \tag{3.5}$$

Despite the relatively simple setup, the solution is surprisingly complex. The computational domain is split into five regions, with the boundaries moving at different speeds. Although the solution is trivial in some parts, one part of the domain has no closed-form solution; the analytical solution can only be computed using an iterative procedure.

The analytical solution can be found in Toro [2009]. We plot the numerical result computed by the SPH as well as the expected result in Fig. 3.1. The plots show that the SPH solution follows the analytical solution well, except for the characteristic "blip" visible in the pressure distribution (and consequently also in the energy distribution). This is a known deficiency of the standard SPH discretization, caused by fact that volume elements only take into account the particle mass and local density[1]. Besides the blip, the computed solution diverts from the

[1]The issue could be mitigated by using the density-independent SPH discretization instead, see Saitoh and Makino [2013].

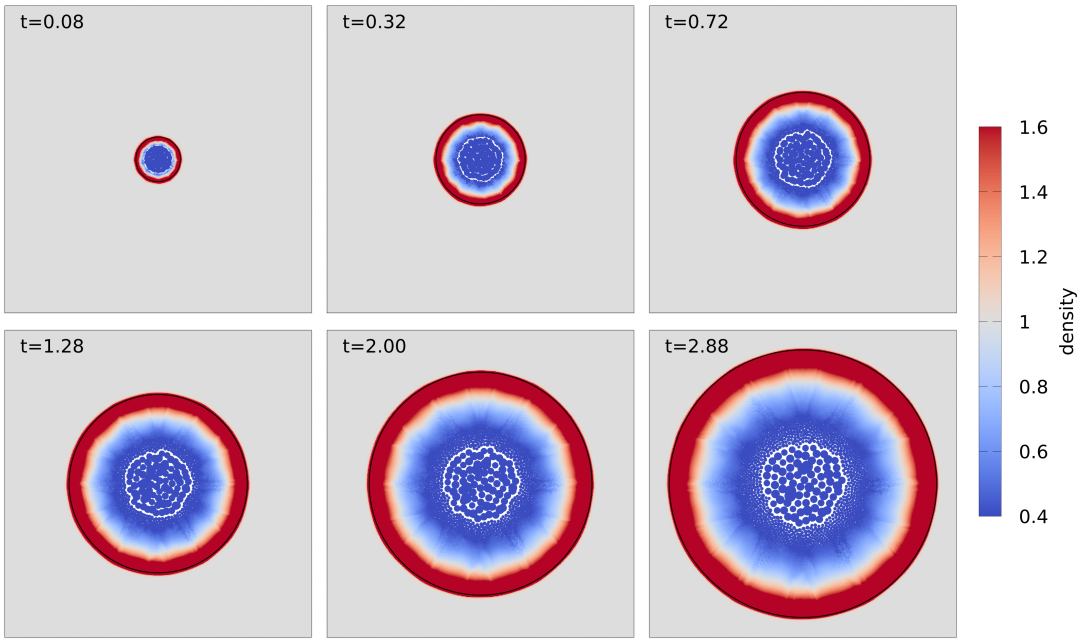

Figure 3.2: Snapshots of a two-dimensional Sedov-Taylor blast. The color palette shows the density ρ; the initial background density was set to $\rho = 1$ (gray), compressed and expanded gas is marked red and blue, respectively. Black outline represents the expected shock front radius according to Eq. 3.6.

analytical solution only at discontinuities, which is to be expected due to smoothing, caused by artificial viscosity. If no artificial viscosity is used, the solution contains strong oscillations near discontinuities (see the red curve in Fig. 3.1).

3.2 Sedov-Taylor blast wave test

Another classical test is known as the Sedov-Taylor blast wave. It is often used to test the propagation of a spherical wave through a discretized medium; specifically, it can be used to check for artifacts arising from grid-based structures of voxels or particles [Tasker et al., 2008].

A two-dimensional computational domain is initially filled with a homogeneous ideal gas with a density of $\rho = 1$. A strong detonation is placed at the center of the domain. The central detonation point thus contains a large internal energy E_0, which creates a spherical shock wave propagating outwards, centered at the point of detonation.

The analytical solution of the explosion can be found in Sedov [1959]. The complete solution is rather complex, however the radius of the shock front can be readily computed. At time t, the radius is:

$$R(t) = \left(\frac{E_0 t^2}{\alpha \rho_0} \right)^{\frac{1}{2+\nu}}, \tag{3.6}$$

where $\nu = 2$ is the number of spatial dimensions of the simulation and α is a dimensionless constant of order unity. The constant α depends on the adiabatic index γ of the gas; for $\gamma = 5/3$, it is approximately $\alpha \approx 0.64$ [Frontiere et al., 2017].

Our simulation contains $N = 100\,000$ particles. The initial detonation energy is set to $E_0 = 2.76 \times 10^{-3}$. Particles are initially placed on a hexagonal grid, mainly to test whether such an anisotropic configuration creates noticeable artifacts. Simulation snapshots can be seen in Fig. 3.2. The radius of the shock front, given by Eq. 3.6, matches the SPH simulation well. We can also see that the shock wave is indeed spherical, despite the hexagonal layout of particles; however some anisotropy in the computed density distribution is still noticeable. It could be improved by using an anisotropic particle distribution instead (see Sec. 2.9.3). We can further see that the densities between the pre-shock and post-shock regions differ significantly. The simulation demonstrates the importance of an adaptive spatial resolution; keeping the smoothing lengths of particles constant would lead to separation of particles in the center of the explosion and generally incorrect results.

3.3 Kelvin-Helmholtz instability test

The importance of artificial thermal conductivity can be seen in simulations that involve a mixing of two different fluids. Such a situation appears when two fluids move along an interface in a shearing motion. Any initial perturbation of the boundary triggers the Kelvin-Helmholtz instability, mixing the fluids and creating vortices that grow over time.

In our example, we set up a square two-dimensional computational domain:

$$\Omega = \{-0.5 \leq x \leq 0.5, -0.5 \leq y \leq 0.5\}, \tag{3.7}$$

split vertically into two regions. Both regions contain ideal gas with an adiabatic index $\gamma = 1.4$, but they differ in initial densities and they move in opposite directions with equal speeds. We set up the initial conditions as:

$$\begin{aligned} |y| < 0.25 \ : \quad & \rho = 2, v_x = 0.5\,, \\ \text{otherwise} \ : \quad & \rho = 1, v_x = -0.5\,. \end{aligned} \tag{3.8}$$

Fluid regions are in pressure equilibrium with $P = 2.5$. The boundaries of the domain are connected using periodic boundary conditions (see Sec. 2.10).

To create a seed for the instability, a small sinusoidal perturbation is added to the vertical component of the velocity. Following Read et al. [2010], we set:

$$v_y = \begin{cases} A \sin(-2\pi x/\lambda) & |y - 0.25| < 0.025\,, \\ A \sin(2\pi x/\lambda) & |y + 0.25| < 0.025\,, \\ 0 & \text{elsewhere}\,. \end{cases} \tag{3.9}$$

In this test, we consider $A = 0.025$ and $\lambda = 1/6$.

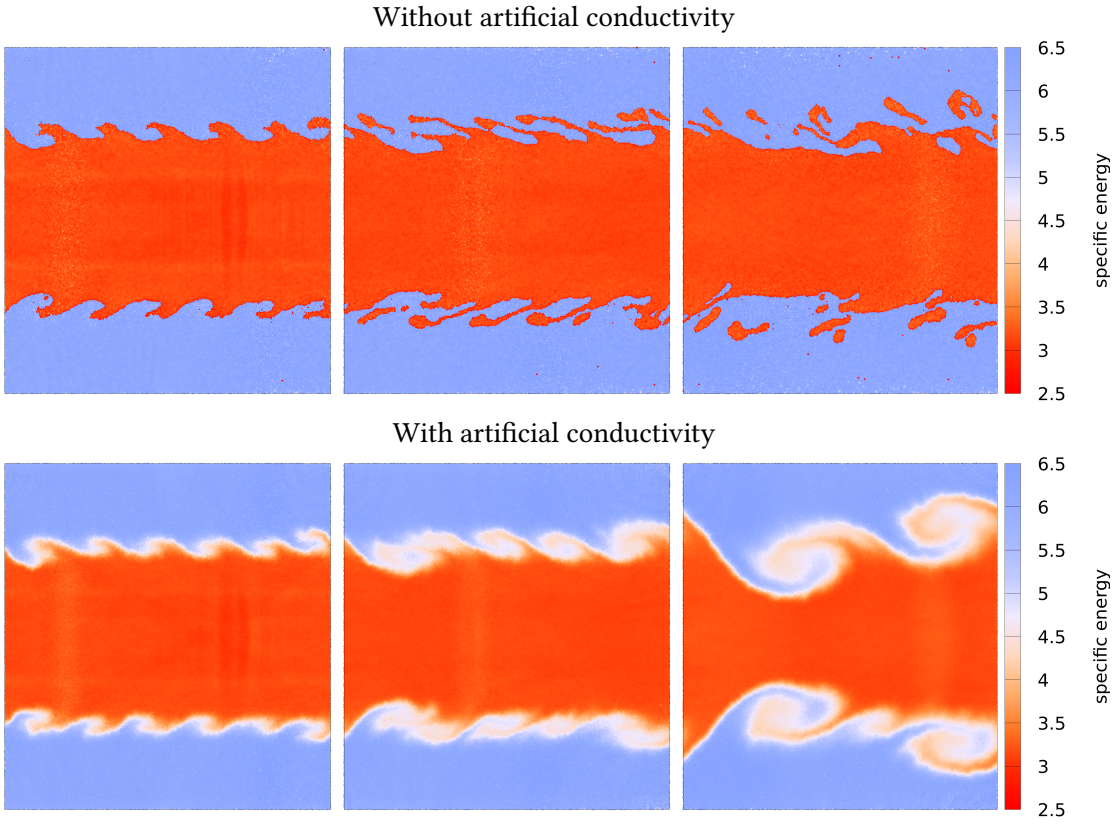

Figure 3.3: Simulations of the Kelvin-Helmholtz instability. The panels show the instability at times $t = 0.4$ s (left), 0.8 s (center) and 1.6 s (right). The top row corresponds to the simulation without the artificial conductivity, while the artificial conductivity is enabled in the bottom row, using $\alpha_u = 1.5$. The color palette shows the specific internal energy. "Vanilla" SPH creates an unphysical surface tension on the interface of interacting fluids, which leads to a deformation of the interface and a separation of bubbles. The artificial conductivity allows the different fluids to mix and the instability can properly develop.

We solve the problem using a symmetric SPH solver. Both regions are initially filled with equal-mass particles in a hexagonal closely packed configuration. The regions differ in particle spacing to obtain the required densities. The total number of particles is approximately $N = 175\,000$. The periodic boundary condition is implemented using ghost particles.

We run two simulations, one with no treatment of the discontinuity and one with an artificial thermal conductivity, using $\alpha_u = 1.5$. Results of these simulations can be seen in Fig. 3.3. In case the conductivity is missing, the instability fails to develop and the fluids remain separated, forming bubbles of constant density. As explained by Read et al. [2010], the standard SPH formulation ignores the extra terms related to the discontinuity of the specific energy. These terms (or lack thereof) cause a numerical surface tension at the interface of two fluids, which effectively prevents their mixing. The artificial thermal conductivity helps to smooth the energy field, reducing the surface tension and allowing the fluids to mix.

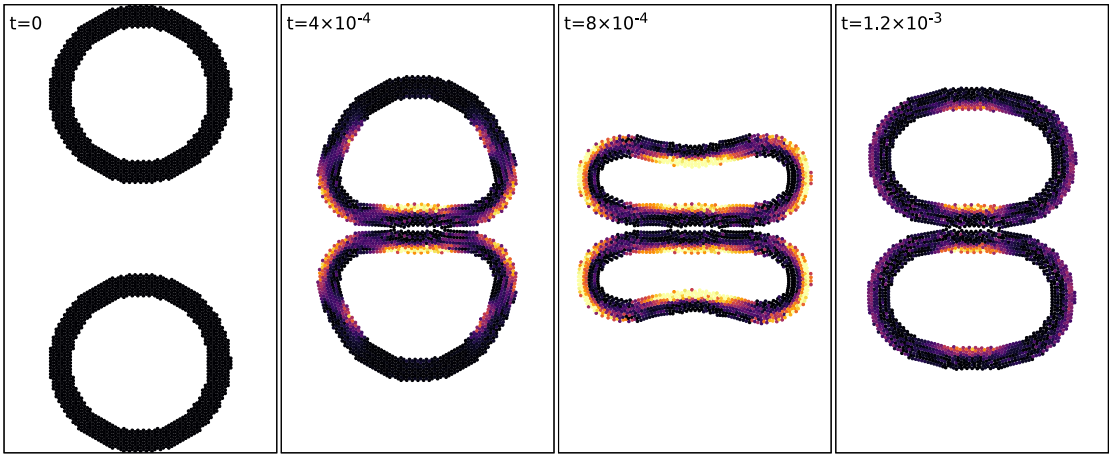

Figure 3.4: Four snapshots of elastic bands, showing an impact, deformation and a subsequent rebound. The color palette represents a measure of the artificial stress $\boldsymbol{R}_i$. As expected, the artificial stress appears only in tension, while it remains zero in compression.

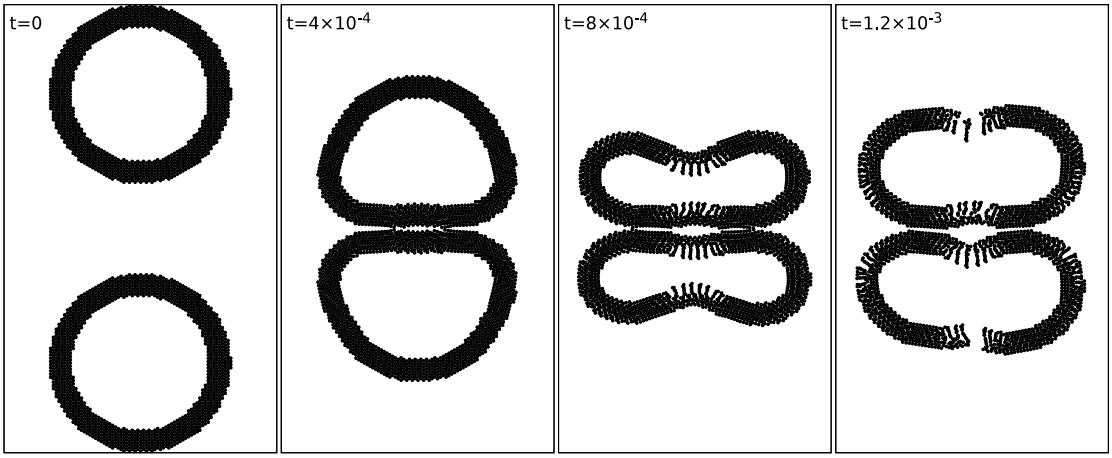

Figure 3.5: Snapshots of elastic bands without the artificial stress, corresponding to snapshots in Fig. 3.4. Due to untreated tensile instability, unphysical fractures appear under tension, eventually leading to a fragmentation of both bands.

3.4 Colliding elastic bands test

To demonstrate the effect of artificial stress, we perform a simple numerical experiment. Following Monaghan [2000], we create two equal cylindrical bands and run a collision simulation. The bands are made of an ideal elastic material, the strain-stress relation thus follows Hooke's law for all plausible values of the strain and stress in the material.

The height of the bands is set to $h = 1\,\mathrm{cm}$, the inner and the outer radius is $r_1 = 3\,\mathrm{cm}$ and $r_2 = 4\,\mathrm{cm}$, respectively. The relative impact speed of bands is $v = 160\,\mathrm{m/s}$. As for the material, we assume the density $\rho = 2700\,\mathrm{kg/m^3}$, shear modulus $\mu = 10^9\,\mathrm{Pa}$ and Tillotson's equation of

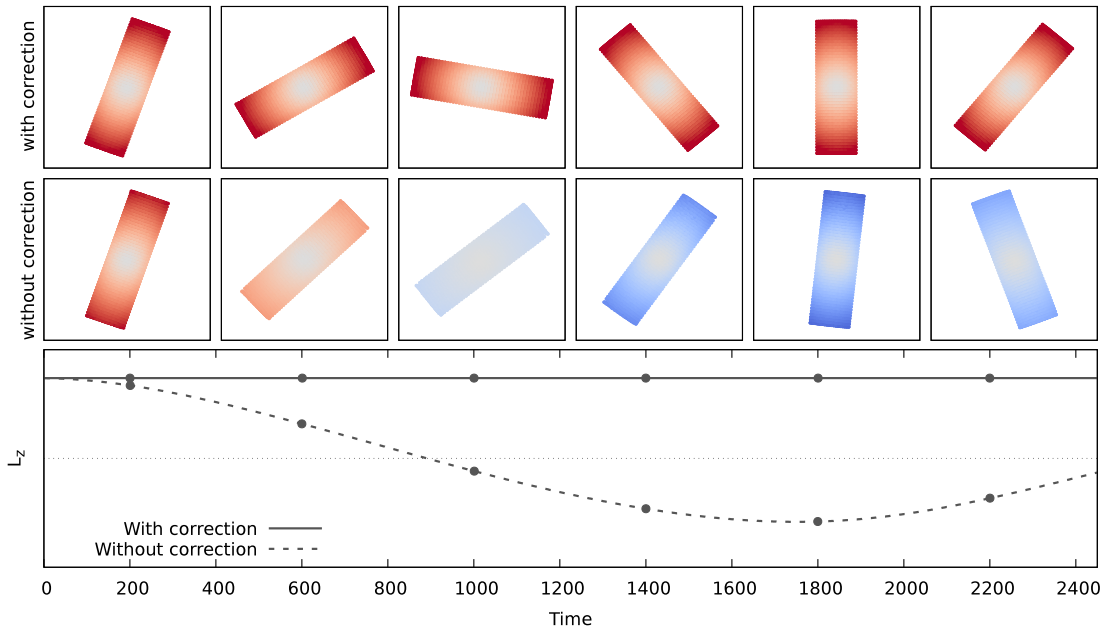

Figure 3.6: Results of the rotating rod test. The upper panel shows the rod at several phases during the simulation. Color represents the particle velocities, red for rotation in the clockwise direction, blue for counter-clockwise direction. The lower panel shows the z-component of angular momentum. Points correspond to times for which the rod is rendered. The correction tensor 2.58 is clearly essential in simulations involving rotating elastic bodies.

state. Each ring consists of approximately $N = 10\,000$ particles, the SPH solver uses standard artificial viscosity (2.86) with $\alpha = 1.5$ and $\beta = 3$. We run two simulations, one that includes the artificial stress with $\zeta = 0.04$ and one with no artificial stress.

Although no analytical solution to the described problem exists, a qualitative result is adequate for this test. We are only interested in whether the topology of the bands remains unchanged upon the collision. Despite a considerable deformation, the material is perfectly elastic and any fragmentation occurring in the simulation is therefore necessarily unphysical. The results are shown in the Figs. 3.4 and 3.5.

If no artificial stress is used, the particles form clumps in regions where the bands are stretched, which causes the particles to lose the connection to their neighbors, ultimately breaking the bands apart. Adding the artificial stress ensures the particles remain connected. The improvement and successful mitigation of the tensile instability can be seen clearly.

3.5 Rotating rod test

We perform a simple test to demonstrate how the correction tensor changes the simulation of solid bodies. The simulation consists of a single cylindrical rod with a height $h = 10\,\mathrm{m}$ and radius $r = 1.5\,\mathrm{m}$, which is initially spun up with a spin rate $\omega = 20\,\mathrm{s}^{-1}$. It is made of perfectly elastic material (i.e. no plasticity nor fragmentation) with the shear modulus $\mu = 2.27 \times 10^{10}\,\mathrm{Pa}$.

The simulation is run with $N = 5000$ particles. We measure the total angular momentum during the simulation and plot it as a function of time, see Fig. 3.6. The test demonstrates that the correction tensor is necessary to conserve angular momentum and maintain the initial spin rate of the rod. If no correction tensor is used, the rod gradually decelerates, until it stops entirely and starts rotating in the opposite direction. In such a case, rotation behaves like deformation, inducing stresses in the rod that act in the opposite direction of the rotation, which is of course unphysical.

The described issue is caused by discretization errors, hence it is mitigated by increasing the spatial resolution; here we intentionally chose a coarse discretization to make the issue pronounced. In actual impact simulations, where the resolution is larger by two or three orders of magnitude, the problem is much less severe. However, it still alters the rotation of small fragments and it can even affect larger bodies in the simulation if the integration time is sufficiently long.

3.6 Cliff collapse test

The rheological model can be tested against empirical data. We create a rectangular column made from granular material and restrict its movement into a single direction with boundary conditions. The column has a width $w = 1\,\mathrm{km}$ and height $h = 3.2\,\mathrm{km}$. This configuration is highly unstable and since we assume zero cohesion of the material, it will spontaneously collapse and create a cliff.

We compare the slope of the collapsed cliff and also overall shape of the column during the collapse with empirical data of Lajeunesse et al. [2005]. They tested several initial setups of the columns, one of which matches our setup described above; only the scale of the column is (obviously) smaller. However, the problem is scale-invariant and we can still compare our results by adjusting the time scale accordingly.

The column in these experiments was made of glass beads with density $\rho = 2500\,\mathrm{kg/m^3}$ and measured angle of repose $\theta = 22 \pm 0.5^\circ$. To match the conditions in the numerical code, the column is made of fully damaged ($D = 1$) material. Boundary conditions are implemented using ghost particles, which mirror the physical quantities of real particles. However, the velocity of ghosts created on the ground ($y \simeq 0$) needs to be set to zero to produce friction between the source particle and its ghost, otherwise, the material would slide on the ground and no cliff would be formed.

Particles are placed into a gravitational field with acceleration $\boldsymbol{g} = (0, -9.81, 0)\,\mathrm{ms^{-2}}$. The simulation runs until all particles come to rest. Our numerical result is compared with experimental data of Lajeunesse et al. [2005] in Fig. 3.7. We see that the rheological model in our code behaves physically, both the motion of the cliff and the final slope approximately match experimental data.

3.7 Fragmentation validation test

The strength model is arguably the most complex part of the code. Naturally, no analytical solution for fragmentation exists, nevertheless, we can make use of laboratory impact experiments.

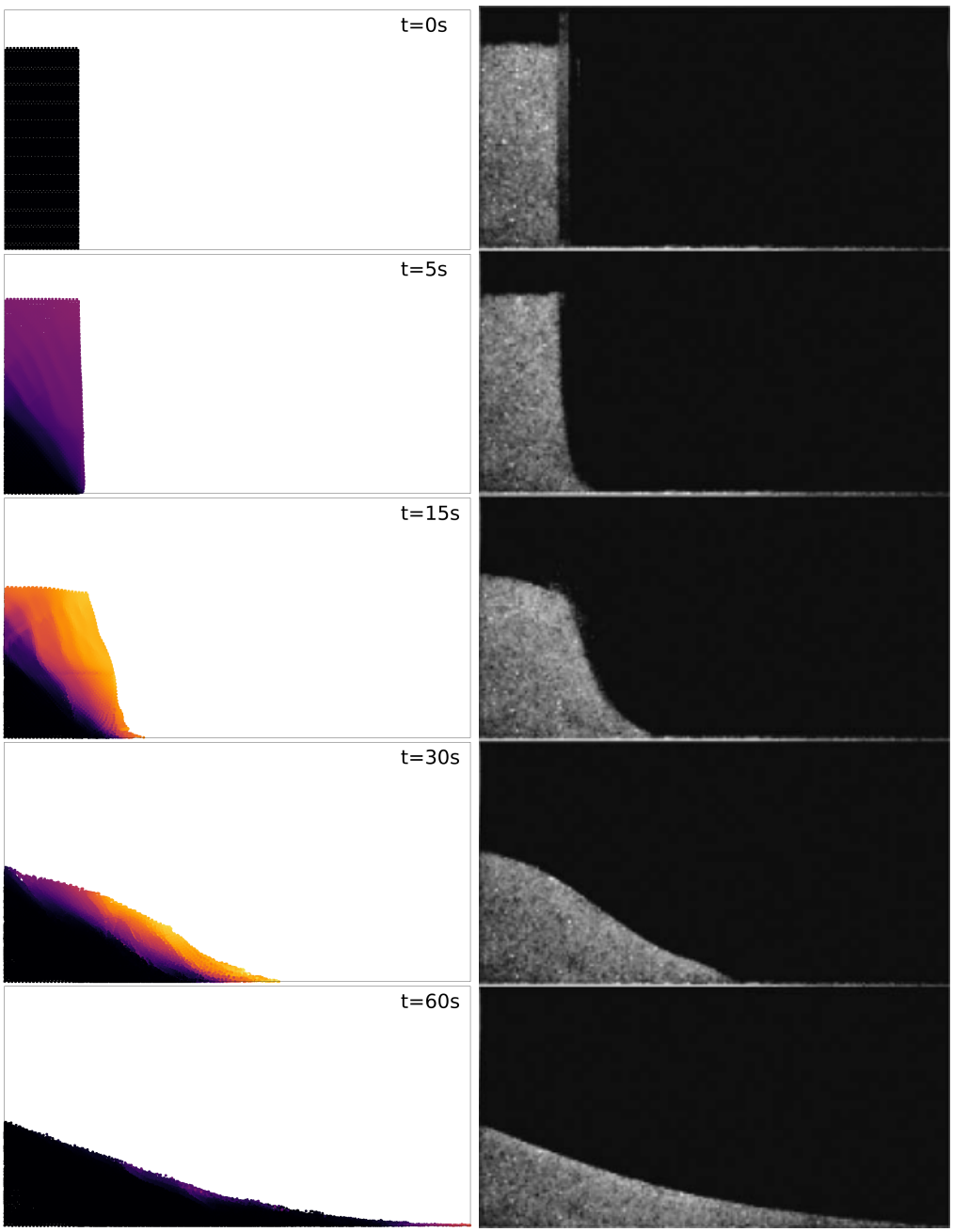

Figure 3.7: Cliff collapse experiment used to test the rheological model in `OpenSPH`. Left images are the simulation results, showing a section through the cliff at several times. Color coding corresponds to the local speed of the material. Right panels are photos of the experiment at matching time points [Lajeunesse et al., 2005].

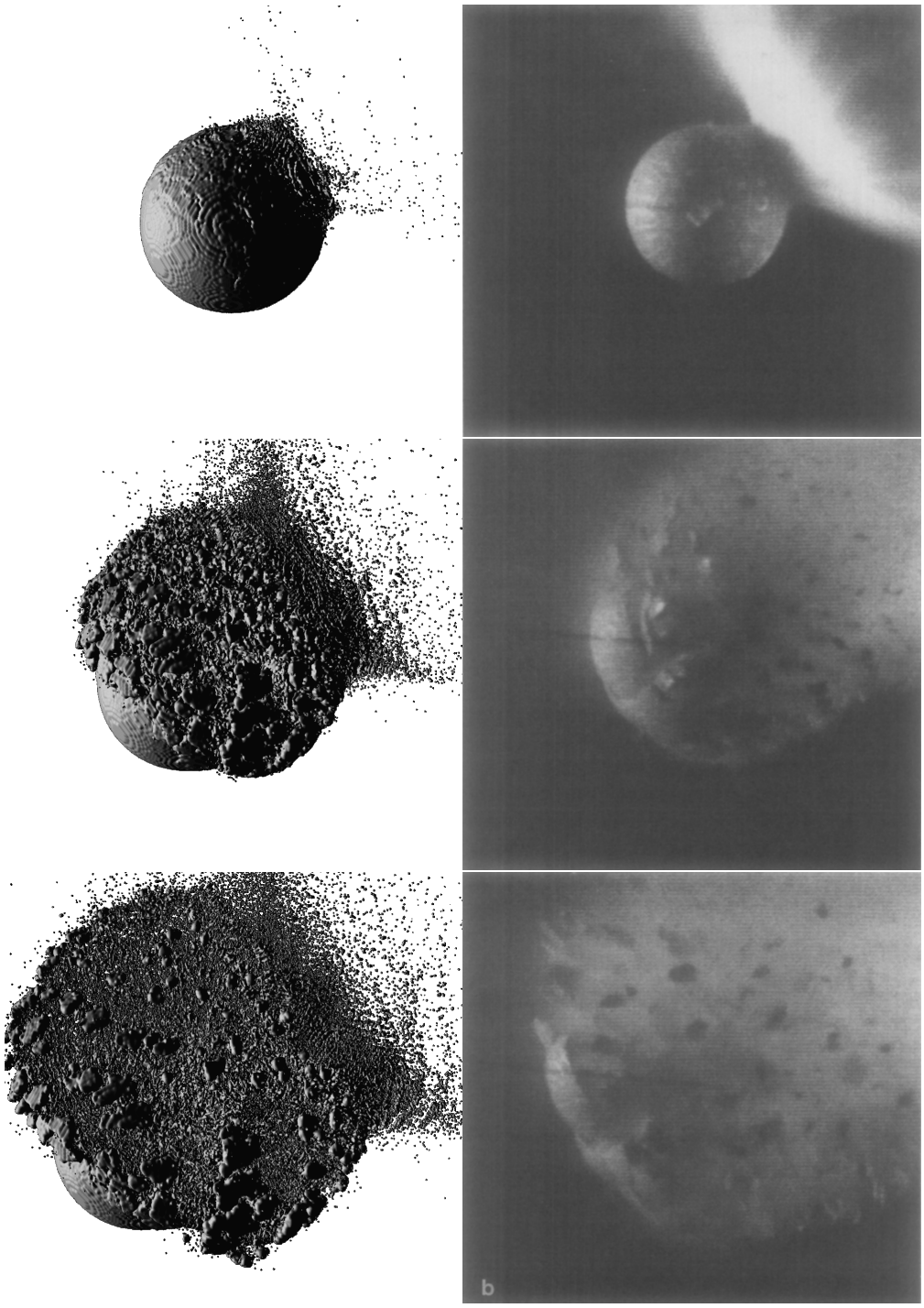

Figure 3.8: Snapshots of the impact simulation and corresponding images from the experiment of Nakamura and Fujiwara [1991] at times $t = 0.1$ ms, 1.4 ms and 2.7 ms. The simulation snapshots were rendered using the ray marching algorithm.

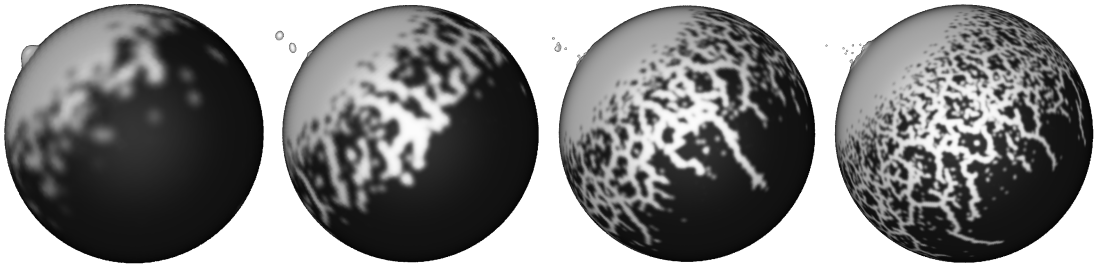

Figure 3.9: Fragmentation pattern on the surface of the target for several different resolutions. The numbers of particles is (left to right) $N = 2 \times 10^4, 10^5, 4 \times 10^5$ and 10^6.

We decided to use a classical work of Nakamura and Fujiwara [1991]. Their experiment consisted of shooting a high-speed projectile into an anchored spherical target and capturing the impact using a high-speed camera. To compare how our numerical model matches these experimental data, we ran a corresponding simulation with a basalt target and a nylon projectile. The diameter of the target was $D = 6\,\mathrm{cm}$, the projectile diameter $d = 7\,\mathrm{mm}$, the impact angle $\phi_{\mathrm{imp}} = 30^\circ$ and the impact speed $v_{\mathrm{imp}} = 3.2\,\mathrm{km/s}$. Both the target and the impactor used a Tillotson material; the density of the target was $\rho = 2700\,\mathrm{km/m^3}$, while the impactor density was $\rho = 1150\,\mathrm{km/m^3}$ in order to match the projectile mass. We assumed the Weibull parameters $k = 4 \times 10^{35}\,\mathrm{m^{-3}}$ and $m = 9$. The target contained approximately $N \simeq 500\,000$ particles.

One of our simulations is compared with images of Nakamura's experiment in Fig. 3.8. We see that the simulation is qualitatively very similar to the experiment. The collision "strips" the surface layer while keeping the core of the target undamaged. Ejected fragments have various sizes, from large pieces originating from the antipode to tiny dust particles. Although the ejecta curtain of high-speed fragments originating from the impact point seems to be almost missing in our simulations, this is certainly only due to the limited resolution.

For a quantitative comparison, we measured the mass of the intact core using the friends-of-friends algorithm. Depending on the exact relation for determining neighbors (limit distance, including/excluding fully damaged particles), we obtain values between 25 % and 35 % of the total mass, which is consistent with the empirical value of 31 %. The velocity field of multiple-particle fragments is also matched, according to the sequence of images. The typical ejection velocity in this small-scale experiment is $v_{\mathrm{ej}} \simeq 10\,\mathrm{m/s}$; in large-scale collisions, it is often comparable to the escape velocity from the parent body.

3.8 Convergence tests

We also ran several tests to ensure our results are not strongly dependent on the spatial resolution. It can be tested by running the same simulation several times with increasing number of particles; however, these simulations will necessarily differ, as our problem is stochastic in its nature and slightly different initial conditions (even if not related to the number of particles) can cause noticeable differences. The stochasticity is introduced by the distribution of Weibull flaws in the target and also by gravitational reaccumulation, which is a chaotic N-body problem (especially when N eventually becomes low, corresponding to a few sizeable individual fragments).

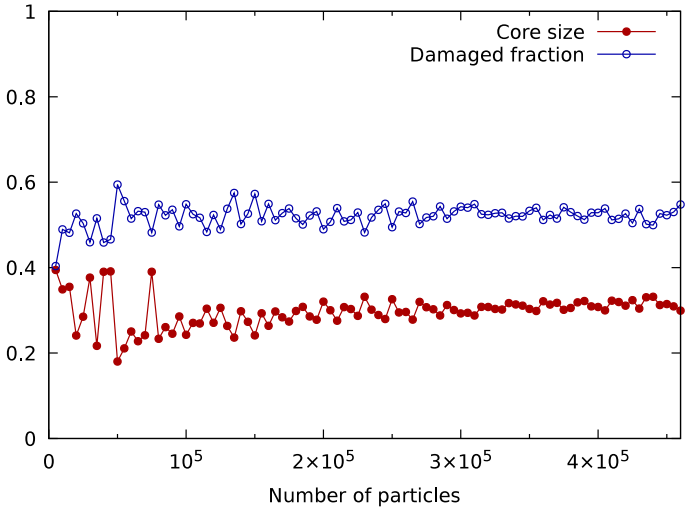

Figure 3.10: Convergence test of simulations with increasing numbers of particles. The plots show quantities computed from the end state of each simulation. *Core size* is the relative mass of the undamaged core of the target, and *damaged fraction* is the fraction of fully damaged particles.

To avoid issues related to self-gravitation, we first separately test the fragmentation model. For this purpose, we set up a simple cratering simulation with $D_{\mathrm{pb}} = 10\,\mathrm{km}$ target, $d_{\mathrm{imp}} = 100\,\mathrm{m}$ impactor, the impact speed $v_{\mathrm{imp}} = 4\,\mathrm{km/s}$ and the impact angle $\phi_{\mathrm{imp}} = 40^{\circ}$. Particles are generated using the parametrized spiraling approach (see Sec. 2.9.2). There is no self-gravity and the target is initially in a zero-pressure state. The simulations run for $t = 10\,\mathrm{s}$, which is enough time for the fragmentation pattern to fully develop.

Of course, the exact fragmentation pattern will be different in each simulation, because the flaw distribution is randomized (see Fig. 3.9). Nevertheless, we compute some integral quantities related to the fragmentation, which should ideally be resolution-independent, namely the size of the largest fragment and the fraction of fully damaged particles. The largest fragment, corresponding to the undamaged core of the target, was identified by first removing the damaged particles and then using the friends-of-friends algorithm. In some cases, the fragment would remain connected to the undamaged shell of particles located at the antipode, in which case we further split them using a graph partitioner. These quantities are plotted as functions of the number N of particles in Fig. 3.10.

For low particle counts, the quantities differ significantly from the high-resolution results and oscillate between consecutive simulations, which is to be expected given the fragmentation pattern is strongly underresolved. With increasing resolution, the differences between subsequent simulations further decrease, although the quantities are still not exactly constant and a slight dependence on the resolution is observed.

These conclusions apply to this specific simulation, which is a weak cratering event ($Q/Q^{\star}_{\mathrm{D}} \simeq 10^{-3}$). For mid-energy or catastrophic impacts, the fragmentation is less important since the target is fully damaged anyway. On the other hand, simulations of even weaker impacts require

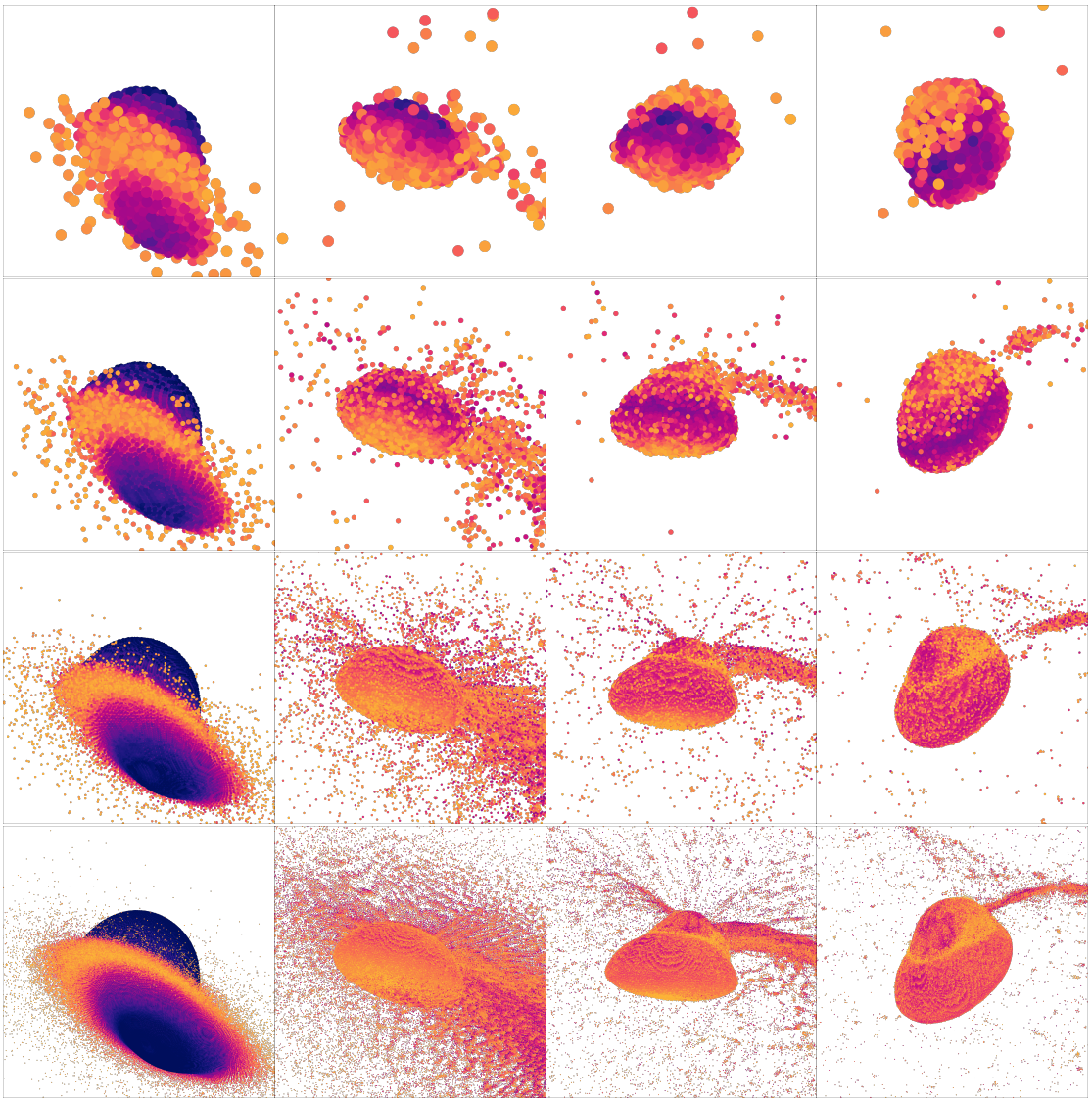

Figure 3.11: Simulation with the same geometric parameters and increasing resolution ($N = 10^3, 10^4, 10^5, 10^6$ particles). Columns correspond to times $t = 1600, 4800, 9600, 14400$ seconds. The sizes of the target and the impactor were $D_{\mathrm{pb}} = 2000\,\mathrm{km}$ and $d_{\mathrm{imp}} = 1500\,\mathrm{km}$, respectively. Color coding shows the specific energy.

much higher resolution to resolve the area around the impact point in great detail. For such simulations, it is more suitable to consider only a small block of the target around the impact point instead of the whole body and set up appropriate boundary conditions.

We finally test the convergence of longer simulations that include reaccumulation. Therefore, we run a similar set of simulations with self-gravitation. For simplicity, we assume a simple fluid-like rheology with no fragmentation nor plasticity. The target size is set to $D_{\mathrm{pb}} = 2000\,\mathrm{km}$ and the projectile size $d_{\mathrm{imp}} = 1500\,\mathrm{km}$, which allows for much larger time steps. The simulations run for $t = 7\,\mathrm{hours}$.

Individual snapshots can be compared in Fig. 3.11. We see that simulations match each other qualitatively well, even for very coarse resolutions. Low-resolution simulations still capture the large-scale features of reaccumulation (e.g. the formation of the largest remnant, its overall shape, the size of the largest fragment), higher resolutions then add fine details, such as the stream of matter incident to the largest remnant, reaccumulation of individual fragments, etc.

— Chapter iv —

IMPACTS INTO SMALL TARGETS

Asteroid collisions played a major role in the formation of the Main Belt. Past collisions are preserved in the structure of the Main Belt as asteroid families, groups of asteroids with similar trajectories and taxonomic types [Hirayama, 1918]. To date, over 100 distinct families have been identified [Nesvorný et al., 2005; Brož et al., 2013; Nesvorný et al., 2015; Vinogradova, 2015] using the hierarchical clustering method [Zappalà et al., 1995], each containing from less than ten to several thousand members. Although the collisional origin of families has been widely accepted, explaining and interpreting size-frequency distributions of families remained an unsolved problem until hydrodynamical and N-body codes were used to simulate impact events.

4.1 Hybrid model for family-forming events

Impacts are commonly studied using numerical methods [Michel et al., 2015]. Although some constraints on the size-frequency distribution (SFD) can be obtained using purely geometric arguments [Tanga et al., 1999; Bagatin et al., 2001], the standard method of choice is a hybrid SPH/N-body approach [Michel et al., 2001, 2002, 2003, 2004; Durda et al., 2007; Benavidez et al., 2012, 2018]. Computation is split to two phases — fragmentation and reaccumulation. During the fragmentation phase, an SPH code is used to solve the set of hydrodynamical equations. It consists of the initial impact, projectile deformation, propagation of the shock wave, target breakup and ejection of fragments. Once the fragmentation phase ends, smoothed particles are converted to hard spheres in a procedure called *hand-off*. The spheres are then used as initial conditions for an N-body integrator that computes mutual gravitational interactions and collisions of fragments until reaccumulated fragments are sufficiently distant from each other that any remaining collisions will not have a significant influence to the resulting synthetic family.

The split of the simulation to phases is possible due to substantially different characteristic time scales associated with the shock wave and the self-gravitation. The time scale of fragmen-

tation is given by the crossing time of the shock wave. Using $D_{\mathrm{pb}} = 10\,\mathrm{km}$ and $v_{\mathrm{imp}} = 5\,\mathrm{km/s}$, we get an order-of-magnitude estimate:

$$t_{\mathrm{frag}} = \frac{D_{\mathrm{pb}}}{v_{\mathrm{imp}}} \simeq 10^{0}\,\mathrm{s}\,. \tag{4.1}$$

For reaccumulation, the time scale is mainly determined by the largest remnant, as the gravitational acceleration is maximal at its surface. Approximating the density of the largest remnant by the initial density ρ, the time scale can be estimated from the free-fall time:

$$t_{\mathrm{ff}} \simeq \frac{1}{G\rho} \simeq 10^{3}\,\mathrm{s}\,. \tag{4.2}$$

Clearly, the time scale associated with self-gravity is much larger than the shock wave time scale. For this reason, gravitational acceleration is often neglected during the fragmentation phase; instead, the target is created with an overburden stress to account for gravitation compression [Benz and Asphaug, 1999; Durda et al., 2007].

The resulting size-frequency distribution (SFD) can be directly compared with young families in the Main Belt. Such data is used to constrain the size of the parent body or the geometrical parameters of the impact that formed the family or even detect probable interlopers. Karin family is a good example as it was formed only $(5.8 \pm 0.2)\,\mathrm{Myr}$ ago; Nesvorný et al. [2006] analyzed it in detail using SPH/N-body simulations and they were able to find an excellent match between the synthetic and observed SFDs.

The same analysis is more difficult for older families, because they underwent considerable evolution due to the Yarkovsky effect, planetary perturbations, including mean-motion and secular resonances, and secondary collisions. Care must be taken when interpreting SFDs of such families; either limit the analysis to the largest family members which are less affected by the evolution, or follow up the impact simulation with a numerical integration of orbital and collisional evolution, as in Brož and Morbidelli [2019] or Marsset et al. [2020].

4.1.1 Related work

Benz and Asphaug [1999] pioneered the hydrodynamical simulations of asteroid collisions. Their code was the first to properly discretize the Grady-Kipp model of fragmentation in SPH. The hydrocode was coupled with an algorithm for fragment search in order to identify the largest remnant of the impact. They computed 480 runs for targets with a diameter from $D_{\mathrm{pb}} \simeq 10^{-2}$ to $10^{5}\,\mathrm{m}$ at different impact speeds and derived scaling laws of ice and basalt.

The developed code was used for studies of individual asteroid families, such as Eunomia, Koronis [Michel et al., 2001, 2004] or Karin [Nesvorný et al., 2006]. These families are of the S taxonomic type, likely made of ordinary chondrite material, hence the targets in the simulations were monolithic spheres made of basalt, which is a viable terrestrial analog [Michel et al., 2015]. The SPH simulations were followed by N-body simulations of the reaccumulation phase to obtain the size-frequency distribution of the synthetic family.

A large suite of SPH/N-body simulations for $D_{\mathrm{pb}} = 100\,\mathrm{km}$ monolithic targets was later performed by Durda et al. [2007]. They studied how the size-frequency distribution depends

on various impact parameters, mainly on the impact speed v_{imp}, the impactor diameter d_{imp} and the impact angle ϕ_{imp}. This set of SFDs was used to estimate the sizes of parent bodies of observed families, assuming the SFD scales linearly with the size of the target, i.e. shifts left or right on the log-log plot of the SFD.

A similar set of simulations was carried out by Benavidez et al. [2012], using $D_{\mathrm{pb}} = 100\,\mathrm{km}$ targets with macroscopic voids to model rubble-pile bodies (i.e. macroscopic porosity). They compared the SFDs of rubble-pile and monolithic targets and discussed where the fit to the observed SFDs can be improved by using the rubble-piles. This work was followed up with simulations of $D_{\mathrm{pb}} = 400\,\mathrm{km}$ targets, using both monolithic and rubble-pile bodies [Benavidez et al., 2018].

The rheological model was also extended to simulate *micro*-porous bodies. Unlike the macro-porous targets, the model assumes sub-resolution porosity using a P-alpha model rather than macroscopic voids in the distribution of particles [Jutzi et al., 2008]. Considering most asteroids in the range $D = 10$ to 100 km are expected to be rubble piles [Bagatin and Petit, 2001], integrating such rheology to an SPH code is valuable, as it makes it possible to find accurate parametric relations of collisions which can then be used in collisional models of Main Belt evolution [Morbidelli et al., 2009; Cibulková et al., 2014]. SPH simulations with microporosity were used in a number of works. For example, Jutzi and Benz [2017] performed sub-catastrophic collision simulations to explain the bi-lobed shape of comet 67P/Churyumov-Gerasimenko, similar simulations were also used to study shapes of collisional remnants of small $D_{\mathrm{pb}} \sim 1\,\mathrm{km}$ [Jutzi et al., 2019] and large $D_{\mathrm{pb}} \sim 100\,\mathrm{km}$ targets [Sugiura et al., 2018].

4.2 Methods and aims

Our work is mostly a follow-up of simulations done by Durda et al. [2007]. We kept the same rheological model, i.e. monolithic non-porous basalt bodies, but we assumed smaller $D_{\mathrm{pb}} = 10\,\mathrm{km}$ targets. Although observed families likely originated from larger parent bodies, small families with the size of the parent body closer to 10 km have already been found, such as the Iannini family [Nesvorný et al., 2003] or the Datura family [Vokrouhlický et al., 2009]. Since the strength of $D_{\mathrm{pb}} = 10\,\mathrm{km}$ bodies is substantially smaller compared to the 100 km ones due to the decreasing role of self-gravity, the asteroid impact occurs under different conditions, potentially with a very different outcome. We thus ran a set of simulations to understand these breakups and discussed differences between our simulations and $D_{\mathrm{pb}} = 100\,\mathrm{km}$ simulations from the dataset of Durda et al. [2007].

Another goal of our work was to quantitatively analyze the error introduced by linear scaling of SFDs which is being used to estimate the sizes of the parent bodies of observed families. It is widely accepted that such scaling is useful for obtaining a first-order estimate; to get an accurate result, one should run a dedicated set of simulations instead with a specific size of the parent body. We studied how the SFDs differ when they are scaled by an order of magnitude, from $D_{\mathrm{pb}} = 100\,\mathrm{km}$ down to 10 km, and how this difference depends on impact parameters.

We further analyzed velocity fields of fragments. Namely, we constructed speed histograms relative to the largest remnant and discussed their relation to the escape velocity v_{esc} of the

parent body. Similarly, we computed angular histograms of velocity directions in the x-y plane (i.e. the plane of symmetry of the impact). Considering simplified collisional models often assume the velocity field is isotropic, we investigated whether this assumption was justified.

To compare two simulations with different targets, we quantify the impact using a dimensionless value $Q/Q^\star_\mathrm{D}$, where Q is the specific kinetic energy of the impactor and $Q^\star_\mathrm{D}$ is the threshold energy needed to eject 50% of the target's mass, as given by the scaling law of Benz and Asphaug [1999]. Hence, the impactors in our simulations are systematically smaller relative to the target size than in the corresponding simulations of Durda et al. [2007].

4.2.1 Model used for simulations

To avoid any systematic bias in our results, we tried to match the setup of Durda et al. [2007] as closely as possible. We assumed monolithic basalt material and used Tillotson's equation of state and von Mises rheology (see Sec. 2.8.1). Although such a model is more suitable for simulation of metallic materials and the results may differ significantly if the Drucker-Prager model is used instead [Jutzi et al., 2015], we use it intentionally to separate the effect of target size. Nevertheless, the material model is still viable for simulations of catastrophic impacts, as the material strength is less important in these cases.

Our simulations contain about $N \simeq 1.4 \times 10^5$ particles. This is relatively coarse resolution (these days, many works use $N \gtrsim 10^6$ particles), we want to avoid possible systematic errors introduced by increased resolution. For 10 km targets, this implies a resolution limit of about $h \simeq 200$ m.

We performed two-phase simulations for each set of impact parameters ϕ_imp, v_imp and d_imp. The fragmentation phase was computed with `SPH5` code [Benz and Asphaug, 1994], modified for double-precision computations. During this phase, we solved the following set of SPH equations:

$$\frac{\mathrm{d}\rho_i}{\mathrm{d}t} = -\rho_i \sum_j \frac{m_j}{\rho_j}(\boldsymbol{v}_j - \boldsymbol{v}_i)\cdot\nabla W_{ij}\,, \tag{4.3}$$

$$\frac{\mathrm{d}\boldsymbol{v}_i}{\mathrm{d}t} = \sum_j m_j \left(\frac{\boldsymbol{\sigma}_i + \boldsymbol{\sigma}_j}{\rho_i\rho_j} + \Pi_{ij}\mathbf{1}\right)\cdot\nabla W_{ij}\,, \tag{4.4}$$

$$\frac{\mathrm{d}u_i}{\mathrm{d}t} = -\frac{P_i}{\rho_i}\mathrm{Tr}\,\dot{\boldsymbol{\epsilon}}_i + \frac{1}{\rho_i}\boldsymbol{S}_i \,:\, \dot{\boldsymbol{\epsilon}}_i + \sum_j \frac{1}{2} m_j \Pi_{ij}(\boldsymbol{v}_i - \boldsymbol{v}_j)\cdot\nabla W_{ij}\,, \tag{4.5}$$

$$\frac{\mathrm{d}\boldsymbol{S}_i}{\mathrm{d}t} = 2\mu\left(\dot{\boldsymbol{\epsilon}}_i - \frac{1}{3}\mathbf{1}\mathrm{Tr}\,\dot{\boldsymbol{\epsilon}}_i\right)\,, \tag{4.6}$$

$$\frac{\mathrm{d}h_i}{\mathrm{d}t} = -\frac{h_i}{3}\frac{\mathrm{d}\rho_i}{\mathrm{d}t}\,, \tag{4.7}$$

$$\dot{\boldsymbol{\epsilon}}_i = \frac{1}{2\rho_i}\sum_j m_j\left[(\boldsymbol{v}_j - \boldsymbol{v}_i)\otimes\nabla W_{ij} + (\boldsymbol{v}_j - \boldsymbol{v}_i)\otimes\nabla W_{ij}{}^\top\right]\,, \tag{4.8}$$

and Π_{ij} is the artificial velocity term, defined by Eq.2.86. Material parameters are summarized in Table 1 of the reprint below. The code `SPH5` uses slightly different discretization of the equation motion and velocity divergence than we derived in Sec. 2.2. Although these equations are also

conservative due to symmetries in the stress $\boldsymbol{\sigma}_i$ and velocity $\boldsymbol{v}_i$, the results might be slightly different, especially in simulations with a small number of particles.

The reaccumulation phase was computed using `pkdgrav` code [Richardson et al., 2000]. We assumed perfect merging of collided particles, regardless of their relative velocity. Similarly, any overlapping particles were merged to larger spheres. The hand-off was performed by converting each SPH particle to a hard sphere with the same volume, skipping all particles in expanded phase (i.e. most impactor particles).

4.2.2 Numerical issues

The analysis of our simulations with small parent bodies showed some numerical problems that were not present in simulations with $D_{\mathrm{pb}} = 100\,\mathrm{km}$ bodies, or at least not to the same extent. There were strong high-frequency oscillations in the target after the shock wave passed, which induced further growth of fractures until eventually the whole target has been disintegrated.

Issues mainly appeared on the smallest targets, for $D_{\mathrm{pb}} = 1\,\mathrm{km}$ bodies which we studied originally. Compared to $D_{\mathrm{pb}} \simeq 100\,\mathrm{km}$ targets, these bodies have much smaller strength, because this size range still lies in the gravity regime of the scaling law [Benz and Asphaug, 1999]. Hence, for small targets, an impact with the given $Q/Q^{\star}_{\mathrm{D}}$ requires a much smaller impactor. Consequently, impact leaves an undamaged core of the target where the pressure may oscillate; larger $D_{\mathrm{pb}} \simeq 100\,\mathrm{km}$ bodies are fully damaged by the impact, the pressure inside the remnant is thus always positive. Furthermore, the ejection speeds are generally lower for small bodies, meaning the integration time has to be longer (relative to the size of the target).

The pressure oscillations are necessarily numerical artifacts, given their wavelength exactly corresponds to the spatial resolution. They appear due to the evolution of density using the continuity equation 2.45. The density of every particle is evolved independently, based only on the local velocity divergence, hence there is no spatial continuity of density enforced, similarly how the continuity of the velocity field is not enforced without the artificial conductivity. No such oscillations are present if the density is computed by the direct summation 2.5, however, this approach has its own drawbacks, as discussed in Sec. 2.4.

Instead, `OpenSPH` adds a numerical term to the continuity equation which works as diffusion in presence of high-frequency oscillations. Such a term is analogous to the artificial viscosity in the equation of motion or the artificial conductivity in the energy equation. Following Marrone et al. [2011], we add the so-called δ-SPH term:

$$\left(\frac{\mathrm{d}\rho_i}{\mathrm{d}t}\right)_{\delta} = \delta h c \sum_j \frac{m_j}{\rho_j} \boldsymbol{\psi}_{ij} \cdot \nabla W_{ij}\,, \tag{4.9}$$

where $\delta \simeq 0.01$ is a small constant controlling the magnitude of diffusion, c is the sound speed and:

$$\boldsymbol{\psi}_{ij} = (\rho_j - \rho_i)\frac{\boldsymbol{r}_j - \boldsymbol{r}_i}{\|\boldsymbol{r}_j - \boldsymbol{r}_i\|^2} - \frac{1}{2}\left(\nabla\rho_i + \nabla\rho_j\right)\,. \tag{4.10}$$

The sum in Eq. 4.9 and also in the computation of $\nabla\rho_i$ enumerates neighbors of the i-th particle, but it skips fully damaged ($D = 1$) particles. Such an approach is necessary to prevent the δ-SPH term from further damaging particles with fully damaged neighbors. Additionally, the gradient $\nabla\rho_i$ is corrected using the correction tensor 2.58.

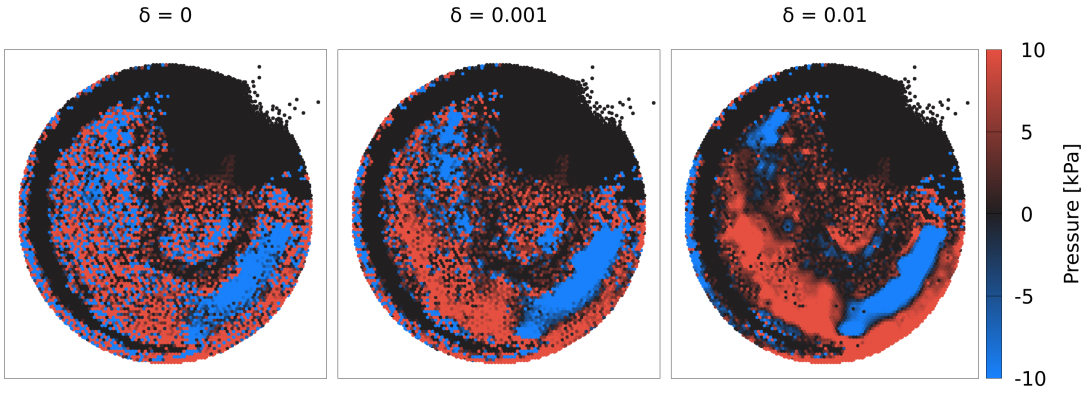

Figure 4.1: Pressure distribution inside a damaged $D_{\mathrm{pb}} = 1$ km target at time $t = 10$ s for several values of parameter δ of the δ-SPH modification. Strong high-frequency oscillations can be efficiently attenuated with even a small value of δ, while the large-scale pressure distribution and the fracture pattern remains unchanged.

Vector $\boldsymbol{\psi}_{ij}$ is defined as a difference of two discretizations of the density gradient. If the density field is smooth, both gradients give a similar result and the term is efficiently zero, however, if the densities of neighboring particles differ significantly, the term acts as a smoothing operator. We have found that even small values of δ can efficiently diminish the high-frequency oscillations in the pressure field, see results in Fig. 4.1. This modification was not included in the original code SPH5, though.

4.3 Major results

We performed 125 SPH/N-body runs, i.e. a matrix with five different values of the impact angle ϕ_{imp}, the impact speed v_{imp} and the impactor diameter d_{imp}. The five different impactor diameters correspond to mass ratii $\log_{10}(m_{\mathrm{imp}}/M_{\mathrm{pb}}) = 3.0, 2.6, 2.2, 1.8$ and 1.0. Henceforth, the impact angle ϕ_{imp} is defined as the angle between the impact velocity vector and the *inward* normal at the impact point[1], i.e. a head-on impact corresponds to $\phi_{\mathrm{imp}} \simeq 0^{\circ}$, while a grazing (hit-and-run) impact corresponds to $\phi_{\mathrm{imp}} \simeq 90^{\circ}$.

We observed major differences in the compared SFDs. The deviations of the scaled-down $D_{\mathrm{pb}} = 100$ km SFDs are most pronounced for weak craterings ($Q/Q^{\star}_{\mathrm{D}} \ll 1$) and also for super-catastrophic ($Q/Q^{\star}_{\mathrm{D}} \gg 1$) impacts. Cratering events generally produce shallower distribution, the power-law slope is considerably smaller than in the corresponding 100 km simulations. Our 10 km simulations appear to be weaker in this regime, despite having the same $Q/Q^{\star}_{\mathrm{D}}$. Catastrophic events also appear to be shallower and produce more larger fragments. The SFDs contain a characteristic "knee" that is not present in the 100 km runs. This makes it difficult to find a linear fit of some SFDs, hence we instead used a two-slope function for fitting.

On the other hand, the SFDs of mid-energy impacts with $Q/Q^{\star}_{\mathrm{D}} \sim 1$ generally match quite well. This is partly due to the application of the scaling law to quantify the impact energy; since

[1]Some authors use a different convention for the impact angle. For example, Nakamura and Fujiwara [1991] used an angle between the velocity vector and tangential plane at the impact point.

the mid-energy impacts were used to derive the scaling law in the first place, the total mass of fragments is approximately 50 % of the mass of the parent body in both cases, so it is not surprising that the SFDs are similar. Nevertheless, our results show certain universality of SFDs. Both the 10 km and 100 km impacts produce SFDs with the same morphology in the mid-energy regime. This "canonical SFD" always contains a separated largest remnant (LR) and a much smaller largest fragment (LF), followed by a power-law of remaining fragments. The slope of this power-law is comparable as well, suggesting that impacts generally produce very similar SFDs even if the target is scaled by an order of magnitude.

There are noticeable differences at oblique impact angles, especially for impacts with $\phi_{\text{imp}} = 75^\circ$. However, this angle-dependence is a purely geometric effect, as previously recognized by Leinhardt and Stewart [2012]. During these oblique impacts, a large part of the impactor misses the target, the kinetic energy actually delivered to the target is thus significantly smaller than the total kinetic energy of the impactor. To correct for this effect and make the results less sensitive to the impact angle, we defined the effective specific energy of the impact:

$$Q_{\text{eff}} = Q \frac{A}{\pi r_{\text{imp}}^2}, \tag{4.11}$$

where A is the cross-sectional area of the impact. We used this quantity instead of the energy Q when deriving the parametric relations for the masses M_{lr} of the largest remnants in order to avoid outliers in fitted data.

Although there seem to be significant differences between some of the compared SFDs, that alone does not mean the $D_{\text{pb}} = 100$ km simulations cannot be used to estimate the size of the parent body in $D \sim 10$ km size range. To determine the systematic errors the scaling introduces, we tried to find the best matching SFD from the dataset of Durda et al. [2007] for several of our synthetic data with $D_{\text{pb}} = 10$ km. The factor required to scale down the SFDs is then used to compute the size of the parent body, which — unlike for the observed families — we can compare with the ground truth.

Our SFDs with three best fits from 100 km runs are shown in Fig. 4.2. The scaling is precise within 10 % for cratering impacts. This is of course not surprising, given the size of the largest remnant is close to the size of the parent body. Nevertheless, the scaling works reasonably well even for more energetic impacts. The discrepancy is largest for super-catastrophic events with $\phi_{\text{imp}} = 15^\circ$, the parent body is predicted to be larger by up to ~50 %. On average, however, the error seems to be about ~20 %, which indicates the method is surprisingly accurate, considering the SFDs were scaled down by an order of magnitude.

Another finding is that the method systematically overestimates the true size; only one of the fits predicted size smaller than 10 km. As the scaling law is a monotonically increasing function in this regime, the method is likely to behave similarly if used for $D_{\text{pb}} \gg 100$ km bodies, we thus expect that the fit will underestimate the real size of the parent body. Therefore, the method can be used to find an upper limit of D_{pb} when scaling down and a lower limit when scaling up.

In the paper, we further compared estimates of the size of the parent body on the example of the Karin family. As our upscaled 10 km simulations predicted $D_{\text{pb}} \simeq 25$ km and the downscaled 100 km simulations predicted $D_{\text{pb}} \simeq 63$ km, this led us to a rather pessimistic conclusion that the

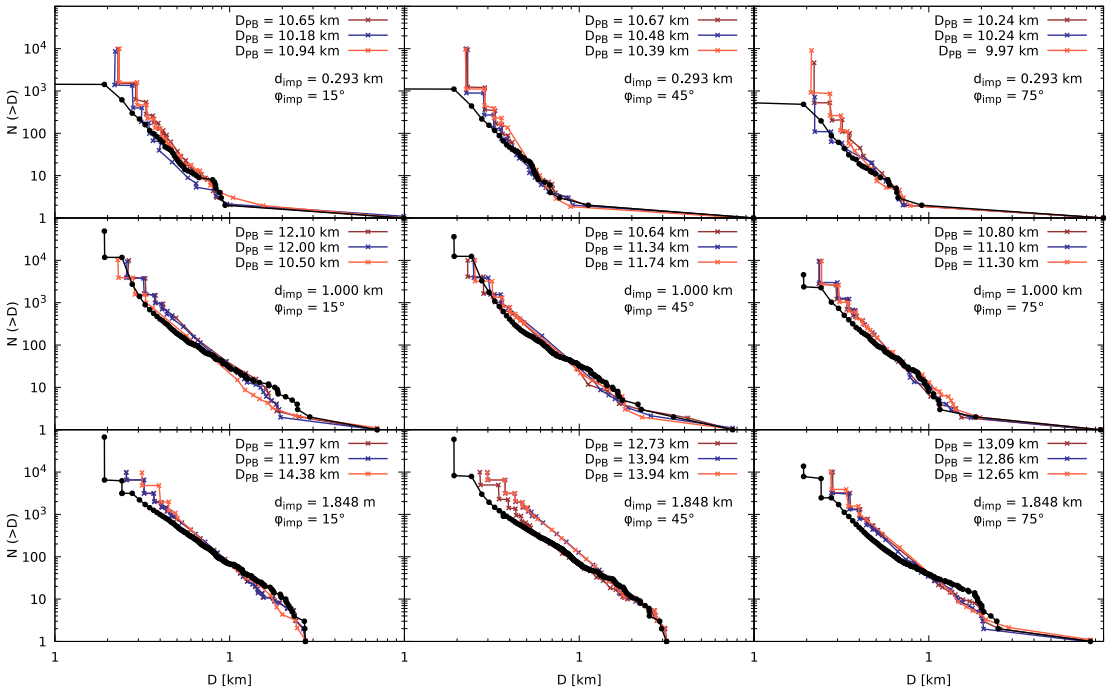

Figure 4.2: Scaling of $D_{\mathrm{pb}} = 100\,\mathrm{km}$ SFDs applied to our synthetic $D_{\mathrm{pb}} = 10\,\mathrm{km}$ data. Each plot shows three best fits from the dataset of Durda et al. [2007] along with the estimated diamater of the parent body. Our SFDs (black) are computed from $v_{\mathrm{imp}} = 5\,\mathrm{km/s}$ runs.

error of the scaling method can be as large as 100 %. However, this was based on an erroneous result of Durda et al. [2007]. After re-examining a fit of $D_{\mathrm{pb}} = 100\,\mathrm{km}$ SFDs to the observed SFD of the Karin family, we obtained an estimate of $D_{\mathrm{pb}} = (33 \pm 3)\,\mathrm{km}$, remarkably similar to the value $D_{\mathrm{pb}} = 33\,\mathrm{km}$ obtained by Nesvorný et al. [2006]. Consequently, we now believe the scaling method is actually much more precise than previously stated.

We also analyzed the velocity distributions of fragments. For cratering events, we found that the mode of the speed histogram is located near the escape speed v_{esc}. With increasing energy, however, this peak of the histogram moves towards higher values and the tail of the histogram grows as more high-speed fragments are being ejected; for super-catastrophic events, the histogram becomes almost flat for a wide range of speeds. As for the angular distribution, we noticed impacts can be assigned to three categories that are sorted by the impact energy. The weakest impacts only cause minor cratering, the velocity distribution of fragments is thus clustered around the point of the impact. When the energy exceeds a certain threshold, the impact causes fragment ejection from the antipode of the target, we can thus see two distinct groups of fragments in the angular histogram. Finally, for high-energy impacts, the whole target is disintegrated and the velocity field is essentially isotropic.

4.4 Reprint

See pages 96 to 113.

Icarus 296 (2017) 239–256

Contents lists available at ScienceDirect

Icarus

journal homepage: www.elsevier.com/locate/icarus

SPH/*N*-Body simulations of small ($D = 10$ km) asteroidal breakups and improved parametric relations for Monte–Carlo collisional models

P. Ševeček[a,*], M. Brož[a], D. Nesvorný[b], B. Enke[b], D. Durda[b], K. Walsh[b], D.C. Richardson[c]

[a] Institute of Astronomy, Charles University, Prague, V Holešovičkách 2, 18000 Prague 8, Czech Republic
[b] Southwest Research Institute, 1050 Walnut Street, Suite 400, Boulder, CO 80302, USA
[c] Department of Astronomy, University of Maryland, College Park, MD 20742, USA

ARTICLE INFO

Article history:
Received 4 January 2017
Revised 15 May 2017
Accepted 14 June 2017
Available online 17 June 2017

Keywords:
Asteroids
Dynamics
Collisional physics
Impact processes

ABSTRACT

We report on our study of asteroidal breakups, i.e. fragmentations of targets, subsequent gravitational reaccumulation and formation of small asteroid families. We focused on parent bodies with diameters $D_{pb} = 10$ km. Simulations were performed with a smoothed-particle hydrodynamics (SPH) code combined with an efficient *N*-body integrator. We assumed various projectile sizes, impact velocities and impact angles (125 runs in total). Resulting size-frequency distributions are significantly different from scaled-down simulations with $D_{pb} = 100$ km targets (Durda et al., 2007). We derive new parametric relations describing fragment distributions, suitable for Monte-Carlo collisional models. We also characterize velocity fields and angular distributions of fragments, which can be used as initial conditions for *N*-body simulations of small asteroid families. Finally, we discuss a number of uncertainties related to SPH simulations.

© 2017 Elsevier Inc. All rights reserved.

1. Introduction and motivation

Collisions between asteroids play an important role in the evolution of the main belt. Understanding the fragmentation process and subsequent reaccumulation of fragments is crucial for studies of the formation of the solar system or the internal structure of the asteroids. Remnants of past break-ups are preserved to a certain extent in the form of asteroid families – groups of asteroids located close to each other in the space of proper elements a_p, e_p, I_p (Hirayama, 1918; Nesvorný et al., 2015).

The observed size-frequency distribution (SFD) of the family members contains a lot of information and can aid us to determine the mass M_{pb} of the parent body. However, it cannot be determined by merely summing up the observed family members, as a large portion of the total mass is presumably 'hidden' in fragments well under observational completeness. The SFD is also modified over time, due to ongoing secondary collisional evolution and dynamical removal by the Yarkovsky drift and various gravitational resonances, etc. This makes the procedure a bit difficult for ancient asteroid families and relatively simple for very young (< 10 Myr) clusters, such as Karin or Veritas (Nesvorný et al., 2006; Michel et al., 2011).

Disruptive and cratering impacts have been studied experimentally, using impacts into cement mortar targets (e.g. Davis and Ryan, 1990; Nakamura and Fujiwara, 1991). However, in order to compare those results to impacts of asteroids we need to scale the results up in terms of the mass of the target and kinetic energy of the projectile by several orders of magnitude. The scaled impact experiments can still have significantly different outcomes, compared to the asteroid collisions, due to the increasing role of gravitational compression, different fragmentation mechanisms etc. Experiments yield valuable information about properties of materials, but they are not sufficient to unambiguously determine results of asteroid collisions.

Numerical simulations are thus used to solve a standard set of hydrodynamic equations; however, the physics of fragmentation is much more complex than that. Especially for low-energy cratering impacts, it is necessary to simulate an explicit propagation of cracks in the target. There is no *ab initio* theory of fragmentation, but phenomenological theories has been developed to describe the fragmentation process, such as the Grady–Kipp model of fragmentation (Grady and Kipp, 1980), used in this paper, or more complex models including porosity based on the P-α model (Herrmann, 1969).

Common methods of choice for studying impacts are shock-physics codes and particle codes (Jutzi et al., 2015). The most important outputs of simulations are masses M_{lr} and M_{lf} of the largest remnant and largest fragment, respectively, and the exponent q of the power-law approximation to the cumulative

* Corresponding author.
E-mail address: sevecek@sirrah.troja.mff.cuni.cz (P. Ševeček).

http://dx.doi.org/10.1016/j.icarus.2017.06.021
0019-1035/© 2017 Elsevier Inc. All rights reserved.

size-frequency distribution $N(>D)$, i. e. the number N of family members with diameter larger than given D. Parametric relations, describing the dependence of M_{lr} and q on input parameters, can be then applied on collisional models of the main asteroid belt, such as those presented in Morbidelli et al. (2009) or Cibulková et al. (2014); however, if we aim to determine the size of the parent body, we need to solve an *inverse* problem.

A single simulation gives us the SFD for a given size of the parent body and several parameters of the impactor. However, if one wishes to derive the size of the parent body and impactor parameters from the observed SFD, it is necessary to conduct a large set of simulations with different parameters and then find the SFD that resembles the observed one as accurately as possible. This makes the problem difficult as the parameter space is quite extensive. For one run, we usually have to specify the parent body size D_{pb}, the projectile size d_{project}, the impact speed v_{imp}, and the impact angle ϕ_{imp} (i.e. the angle between the velocity vector of the impactor and the inward normal of the target at the point of collision). Other parameters of the problem are the material properties of considered asteroids, such as bulk density, shear modulus, porosity etc.

Due to the extent of the parameter space, a thorough study would be highly demanding on computational resources. It is therefore reasonable to fix the size of the parent body and study breakups with various parameters of the impactor.

A large set of simulations was published by Durda et al. (2007), who studied disruptions of 100 km monolithic targets. Similarly, Benavidez et al. (2012) performed an analogous set of simulations with rubble-pile targets. They also used the resulting SFDs to estimate the size of the parent body for a number of asteroid families. As the diameter of the parent body is never exactly 100 km, the computed SFDs have to be multiplied by a suitable scaling factor f_{scale} to match the observed one. However, small families have been already discovered (e.g. Datura, Nesvorný et al. (2015)) and their parent-body size is likely $D_{\mathrm{pb}} = 10\,\mathrm{km}$, i.e. an order-of-magnitude smaller. The linearity of the scaling is a crucial assumption and we will assess the plausibility of this assumption in this paper.

To fill up a gap in the parameter space, we proceed with small targets. We carried out a set of simulations with $D_{\mathrm{pb}} = 10\,\mathrm{km}$ parent bodies and carefully compared them with the simulations of Durda et al. (2007).

The paper is organised as follows. In Section 2, we briefly describe our numerical methods. The results of simulations are presented in Section 3. Using the computed SFDs we derive parametric relations for the slope q and the masses M_{lr} and M_{lf} of the largest remnant and the largest fragment, respectively, in Section 4. Finally, we summarize our work in Section 5.

2. Numerical methods

We follow a hybrid approach of Michel et al. (2001, 2002, 2003, 2004), employing an SPH discretization for the simulation of fragmentation and an N-body integrator for subsequent gravitational reaccumulation. Each simulation can be thus divided into three phases: i) a fragmentation, ii) a hand-off, and iii) a reaccumulation. We shall describe them sequentially in the following subsections.

2.1. Fragmentation phase

The first phase of the collision is described by hydrodynamical equations in a lagrangian frame. They properly account for supersonic shock wave propagation and fragmentation of the material. We use the SPH5 code by Benz and Asphaug (1994) for their numerical solution. In the following, we present only a brief description of equations used in our simulations and we refer readers to extensive reviews of the method (Rosswog, 2009; Cossins, 2010; Price, 2008, 2012) for a more detailed description.

Our problem is specified by four basic equations, namely the equation of continuity, equation of motion, energy equation and Hooke's law:

$$\frac{\mathrm{d}\rho}{\mathrm{d}t} = -\rho\nabla\cdot\vec{v}\,, \tag{1}$$

$$\frac{\mathrm{d}\vec{v}}{\mathrm{d}t} = \frac{1}{\rho}\nabla\cdot\boldsymbol{\sigma}\,, \tag{2}$$

$$\frac{\mathrm{d}U}{\mathrm{d}t} = -\frac{P}{\rho}\mathrm{Tr}\,\dot{\boldsymbol{\epsilon}} + \frac{1}{\rho}\boldsymbol{S}:\dot{\boldsymbol{\epsilon}}\,, \tag{3}$$

$$\frac{\mathrm{d}\boldsymbol{S}}{\mathrm{d}t} = 2\mu\left(\dot{\boldsymbol{\epsilon}} - \tfrac{1}{3}\mathbf{1}\,\mathrm{Tr}\,\dot{\boldsymbol{\epsilon}}\right), \tag{4}$$

supplemented by the Tillotson equation of state (Tillotson, 1962). The notation is as follows: ρ is the density, $\vec{v}$ the speed, $\boldsymbol{\sigma}$ the stress tensor (total), where $\boldsymbol{\sigma} \equiv -P\mathbf{1} + \boldsymbol{S}$, P the pressure, $\mathbf{1}$ the unit tensor, $\boldsymbol{S}$ the deviatoric stress tensor, U the specific internal energy, $\dot{\boldsymbol{\epsilon}}$ the strain rate tensor, where $\dot{\boldsymbol{\epsilon}} \equiv \frac{1}{2}\left[\nabla\vec{v} + (\nabla\vec{v})^{\mathrm{T}}\right]$, with its trace $\mathrm{Tr}\,\dot{\boldsymbol{\epsilon}} = \nabla\cdot\vec{v}$, μ the shear modulus.

The model includes both elastic and plastic deformation, namely the yielding criterion of von Mises (1913) — given by the factor $f \equiv \min[Y_0^2/(\frac{3}{2}\boldsymbol{S}:\boldsymbol{S}), 1]$, where Y_0 is the (material-dependent) yield stress — and also failure of the material. The initial distribution of cracks and their growth to fractures is described by models of Weibull (1939) and Grady and Kipp (1980), which use a scalar parameter $\mathcal{D} \in \langle 0, 1\rangle$ called damage, as explained in Benz and Asphaug (1994). The stress tensor of damaged material is then modified as $\boldsymbol{\sigma} = -(1 - \mathcal{D}H(-P))P\mathbf{1} + (1-\mathcal{D})f\boldsymbol{S}$, where $H(x)$ denotes the Heaviside step function. In this phase, we neglect the influence of gravity, which is a major simplification of the problem.

In a smoothed-particle hydrodynamic (SPH) formalism, Eqs. (1) to (4) are rewritten so as to describe an evolution of individual SPH particles (denoted by the index $i = 1..N$):

$$\frac{\mathrm{d}\rho_i}{\mathrm{d}t} = -\rho_i\sum_j \frac{m_j}{\rho_j}(\vec{v}_j - \vec{v}_i)\cdot\nabla W_{ij}\,, \tag{5}$$

$$\frac{\mathrm{d}\vec{v}_i}{\mathrm{d}t} = \sum_j m_j\left(\frac{\boldsymbol{\sigma}_i + \boldsymbol{\sigma}_j}{\rho_i\rho_j} + \Pi_{ij}\mathbf{1}\right)\cdot\nabla W_{ij}\,, \tag{6}$$

$$\frac{\mathrm{d}U_i}{\mathrm{d}t} = -\frac{P_i}{\rho_i}\sum_\gamma \dot{\epsilon}_i^{\gamma\gamma} + \frac{1}{\rho_i}\sum_\alpha\sum_\beta S_i^{\alpha\beta}\dot{\epsilon}_i^{\alpha\beta} + \left(\frac{\mathrm{d}U_i}{\mathrm{d}t}\right)_\Pi, \tag{7}$$

$$\frac{\mathrm{d}\boldsymbol{S}_i}{\mathrm{d}t} = 2\mu\left(\dot{\boldsymbol{\epsilon}}_i - \tfrac{1}{3}\mathbf{1}\sum_\gamma \dot{\epsilon}_i^{\gamma\gamma}\right), \tag{8}$$

with:

$$\dot{\epsilon}_i^{\alpha\beta} = \frac{1}{2\rho_i}\sum_j m_j\left[(v_j^\alpha - v_i^\alpha)\frac{\partial W_{ij}}{\partial x^\beta} + (v_j^\beta - v_i^\beta)\frac{\partial W_{ij}}{\partial x^\alpha}\right], \tag{9}$$

where m_j denote the masses of the individual SPH particles, $W_{ij} \equiv W(|\vec{r}_i - \vec{r}_j|, h)$ the kernel function, h the symmetrized smoothing length, $h = \frac{1}{2}(h_i + h_j)$. Both the equation of motion and the energy equation were also supplied with the standard artificial viscosity term Π_{ij} (Monaghan and Gingold, 1983):

$$\Pi_{ij} = \begin{cases} \frac{1}{\rho}\left(-\alpha_{\mathrm{AV}}c_{\mathrm{s}}\mu_{ij} + \beta_{\mathrm{AV}}\mu_{ij}^2\right) & (\vec{v}_i - \vec{v}_j)\cdot(\vec{r}_i - \vec{r}_j) \le 0\,, \\ 0 & \text{otherwise}\,, \end{cases} \tag{10}$$

where:

$$\mu_{ij} = \frac{h(\vec{v}_i - \vec{v}_j)\cdot(\vec{r}_i - \vec{r}_j)}{\|\vec{r}_i - \vec{r}_j\|^2 + \epsilon h^2}\,, \tag{11}$$

c_s is the sound speed and α_{AV}, β_{AV} are free parameters of the viscosity model, values of which were $\alpha_{AV} = 1.5$ and $\beta_{AV} = 3$, as in Benz and Asphaug (1994). The corresponding term in the energy equation is then $(\mathrm{d}U_i/\mathrm{d}t)_\Pi = \sum_j \frac{1}{2} m_j \Pi_{ij}(\vec{v}_i - \vec{v}_j)\cdot\nabla W_{ij}$. We sum over all particles, but since the kernel has a compact support, the algorithm has an asymptotic complexity $\mathcal{O}(NN_{\mathrm{neighbours}})$. The actual number of SPH particles we used (including both the particles of the target and the impactor) is $N \doteq 1.4 \times 10^5$, and the number of neighbours is usually $N_{\mathrm{neighbours}} \simeq 50$. There is also an evolution equation for the smoothing length h_i in order to adapt to varying distances between SPH particles.

2.2. Hand-off procedure

Although SPH is a versatile method suitable for simulating both the fragmentation and the gravitational reaccumulation, the time step of the method is bounded by the Courant criterion and the required number of time steps for complete reaccumulation is prohibitive. In order to proceed with inevitably simplified but efficient computations, we have to convert SPH particles to solid spheres, a procedure called hand-off. In this paper, we compute the corresponding radius R_i as:

$$R_i = \left(\frac{3m_i}{4\pi\rho_i}\right)^{\frac{1}{3}}. \tag{12}$$

The time t_{handoff} at which the hand-off takes place is determined by three conditions:

1. It has to be at least $2D_{\mathrm{pb}}/c_s \simeq 1\,\mathrm{s}$ (c_s being the sound speed), i.e. until the shock wave and rarefaction wave propagate across the target;
2. Fractures (damage) in the target should not propagate anymore, even though in catastrophic disruptions the shock wave usually damages the whole target and material is then practically strengthless;
3. The pressure in the fragmented parent body should be zero so that the corresponding acceleration $-\frac{1}{\rho}\nabla P$ is zero, or at least negligible. According to our tests for $D_{\mathrm{pb}} = 10\,\mathrm{km}$ targets, such relaxation takes up to 10 s.

On the other hand, there is an upper limit for t_{handoff} given by the gravitational acceleration of the target, $g = GM_{\mathrm{pb}}/R_{\mathrm{pb}}^2$, where $G = 6.67408 \times 10^{-11}\,\mathrm{m^3\,kg^{-1}\,s^{-2}}$ is the gravitational constant. This acceleration has to be small compared to the escape speed $v_{\mathrm{esc}} = \sqrt{2GM_{\mathrm{pb}}/R_{\mathrm{pb}}}$, i.e. a typical ejection speed v_{ej} of fragments. The corresponding time span should thus be definitely shorter than $v_{\mathrm{esc}}/g \simeq 10^3$ s.

2.3. Reaccumulation phase

Finally, gravitational reaccumulation of now spherical fragments is computed with an N-body approach. We use the `pkdgrav` code as modified by Richardson et al. (2000) for this purpose. It accounts for mutual gravitational interactions between fragments:

$$\ddot{\vec{r}}_i = -\sum_{j\neq i} \frac{Gm_j}{r_{ij}^3}\vec{r}_{ij}\,, \tag{13}$$

An $\mathcal{O}(N^2)$ problem is simplified significantly using a tree code algorithm, i.e. by clustering fragments to cells and evaluating gravitational moments up to hexadecapole order, provided they fit within the opening angle $\mathrm{d}\theta = 0.5\,\mathrm{rad}$. The time step was $\Delta t = 10^{-6}$ (in $G = 1$ units, or about 5 s in SI), and the time span 50, 000 Δt, long enough that the reaccumulation is over, or negligible.

Regarding mutual collisions, we assumed perfect sticking only, meaning no bouncing or friction. Consequently, we have no information about resulting shapes of fragments, we rather focus on their sizes, velocities and corresponding statistics.

Table 1
Constant parameters used in our SPH simulations. We assumed the same material parameters as Durda et al. (2007), which allows for a direct comparison of results..

Material parameters	
density at zero pressure	$\rho = 2700\,\mathrm{kg/m^3}$
bulk modulus	$A = 2.67 \times 10^{10}$ Pa
non-linear Tillotson term	$B = 2.67 \times 10^{10}$ Pa
sublimation energy	$u_0 = 4.87 \times 10^8$ J/kg
energy of incipient vaporization	$u_{\mathrm{iv}} = 4.72 \times 10^6$ J/kg
energy of complete vaporization	$u_{\mathrm{cv}} = 1.82 \times 10^7$ J/kg
shear modulus	$\mu = 2.27 \times 10^{10}$ Pa
von Mises elasticity limit	$Y_0 = 3.50 \times 10^9$ Pa
Weibull coefficient	$k = 4.00 \times 10^{29}$
Weibull exponent	$m = 9$
SPH parameters	
number of particles in target	$N_{\mathrm{pb}} \simeq 1.4 \times 10^5$
number of particles in projectile	$N_{\mathrm{pb}} = 100$ to 630
Courant number	$C = 1$
linear term of artificial viscosity	$\alpha_{\mathrm{AV}} = 1.5$
quadratic term of artificial viscosity	$\beta_{\mathrm{AV}} = 3.0$
duration of fragmentation phase	$t_{\mathrm{handoff}} = 10\,\mathrm{s}$

3. A grid of simulations for $D_{\mathrm{pb}} = 10\,\mathrm{km}$ targets

We performed a number of simulations with $D_{\mathrm{pb}} = 10\,\mathrm{km}$ parent bodies, impact speed v_{imp} varying from 3 to 7 km/s, diameter d_{project} of the impactor from 0.293 km to 1.848 km (with a logarithmic stepping) and the impact angle ϕ_{imp} from 15° to 75°. The kinetic energy of the impact:

$$Q = \frac{\frac{1}{2}m_{\mathrm{project}}v_{\mathrm{imp}}^2}{M_{\mathrm{pb}}} \tag{14}$$

therefore varies from $\sim 10^{-2}Q_{\mathrm{D}}^\star$ to $\sim 20Q_{\mathrm{D}}^\star$, where $Q_{\mathrm{D}}^\star$ is the critical energy for shattering and dispersing 50% of the parent body. The critical energy $Q_{\mathrm{D}}^\star$ is also used to compare runs with a different size of the parent body (see Section 3.4). We adopted the $Q_{\mathrm{D}}^\star(D)$ value from the scaling law of the basaltic material and impact speed $v_{\mathrm{imp}} = 5\,\mathrm{km}$, as given by Benz and Asphaug (1999). We use the same value of $Q_{\mathrm{D}}^\star$ for all impact velocities and angles, for simplicity. Using this law, the critical energy for $D_{\mathrm{pb}} = 10\,\mathrm{km}$ is $Q_{\mathrm{D}}^\star \simeq 7.68 \times 10^7\,\mathrm{erg/g}$. For comparison, the critical energy for $D_{\mathrm{pb}} = 100\,\mathrm{km}$ is $Q_{\mathrm{D}}^\star(100\,\mathrm{km}) = 1.74 \times 10^9\,\mathrm{erg/g}$. Note that the selected values of $Q_{\mathrm{D}}^\star$ do not influence the simulations at all; we use them only as a unit to get a convenient, dimensionless measures of impact energies.

The total number of performed runs is 125. We assume a monolithic structure of both the target and the impactor, and the material properties were selected those of basalt (summarized in Table 1).

3.1. Size-frequency distributions

For each run we constructed a cumulative size-frequency distributions $N(>D)$ of fragments and we plotted them in Fig. 1.

At first sight, the SFDs are well-behaved. Both cratering and catastrophic events produce mostly power-law-like distributions. Some distributions, mainly those around $Q/Q_{\mathrm{D}}^\star \sim 1$, have an increasing slope at small sizes (at around $D \sim 0.3\,\mathrm{km}$), but since this is close to the resolution limit, it is possibly a numerical artifact.

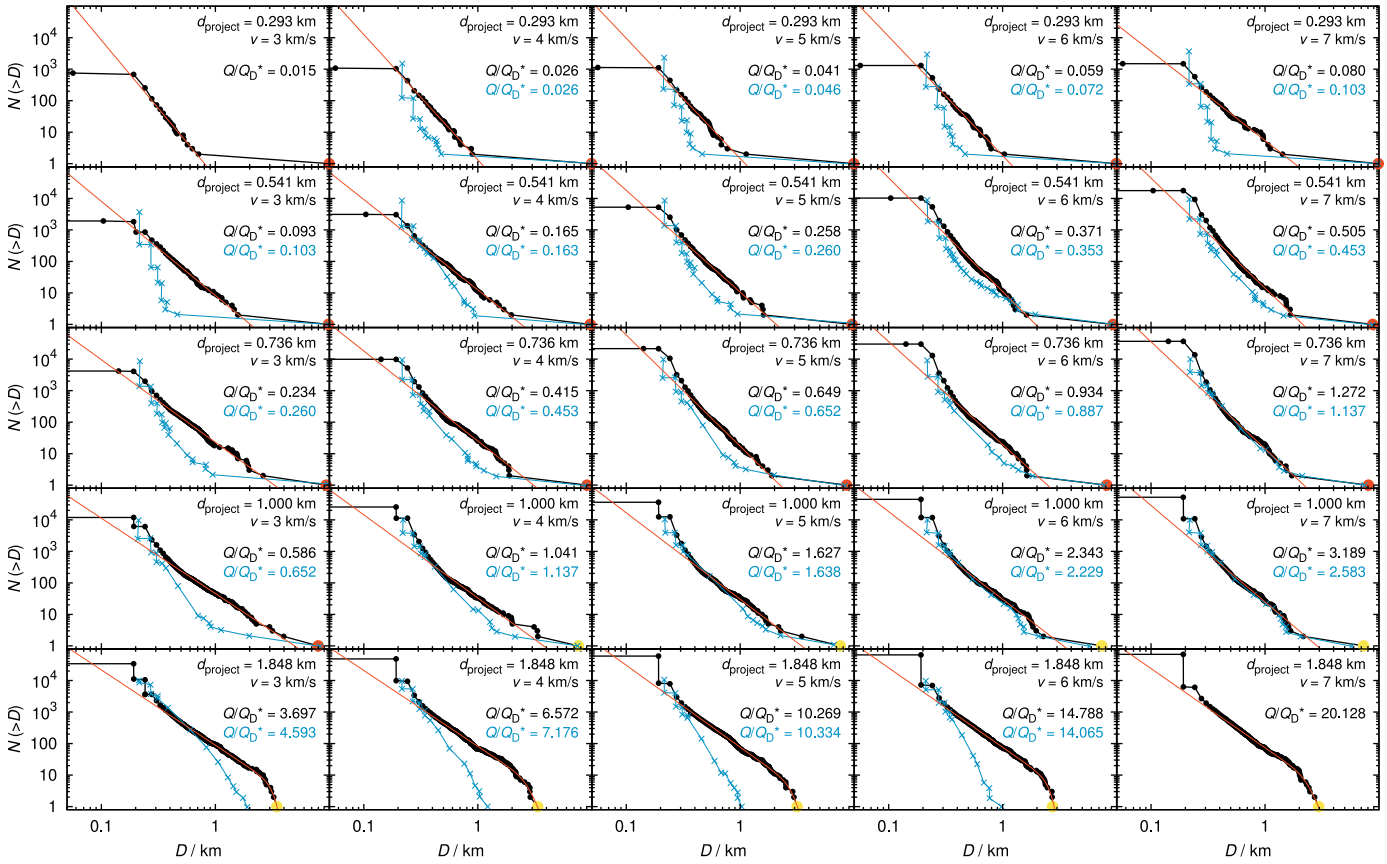

Fig. 1. Cumulative size-frequency distributions $N(>D)$ of fragments ejected during disruptions of parent bodies with sizes $D_{pb} = 10$ km. The impact angle was $\phi_{imp} = 45°$; results for different impact angles are shown in Appendix D. The projectile size is increasing downwards, from $d_{project} = 0.293$ km to 1.848 km, so that the logarithm of the mass ratio $\log_{10}(m_{project}/M_{pb}) = 3.0, 2.6, 2.2, 1.8$ and 1.0. The impact speed is increasing to the right, from $v_{imp} = 3$ to 7 km s^{-1}. Both of the quantities are also indicated in individual panels, together with the ratio $Q/Q^{\star}_{D}$ of the specific energy Q and strength $Q^{\star}_{D}$ inferred from the scaling law of Benz and Asphaug (1999). Largest remnant size D_{LR} is coloured red or yellow for cratering or catastrophic events, respectively. For a discussion of scaling we overplot simulated SFD's from Durda et al. (2007) computed for disruptions of $D_{pb} = 100$ km targets and scaled down by dividing sizes by a factor of 10 (blue lines and labels). To compare 'apples with apples', we compare runs with (approximately) the same $Q/Q^{\star}_{D}$ ratios and the same impact angle, see Section 3.4. For some impact parameters, the scaled SFD is missing as there is no run in the dataset of Durda et al. (2007) with comparable $Q/Q^{\star}_{D}$. Finally, the red curves are fits of a suitable function, used to derive parametric relations (see Section 4). (For interpretation of the references to colour in this figure legend, the reader is referred to the web version of this article.)

For supercatastrophic impacts with $d_{project} = 1.848$ km, the distributions differ from power laws substantially; the slope becomes much steeper at large sizes of fragments. These are the cases where the gap between the largest remnant and the largest fragment disappears (we therefore say the largest remnant does not exist).

The situation is quite different for impacts with an oblique impact angle, mainly for $\phi_{imp} = 75°$. We notice that these impacts appear much less energetic compared to other impact angles, even though the ratio $Q/Q^{\star}_{D}$ is the same. The cause of this apparent discrepancy is simply the geometry of the impact. At high impact angles , the impactor does not hit the target with all its cross-section and a part of it misses the target entirely (grazing impacts, see Leinhardt and Stewart, 2012). Therefore, a part of the kinetic energy is not deposited into the target and the impact appears less energetic, compared to head-on impacts.

3.2. Speed histograms

Similarly to the size-frequency distributions, we computed speed distributions of fragments. The results are shown in Fig. 2. As we are computing an absolute value of the velocity, the resulting histogram depends on a selected reference frame. We chose a barycentric system for all simulations; however, we excluded high-speed remainders of the projectile with velocities $v_{ej} > v_{cut} \equiv 1$ km/s. These outliers naturally appear mainly for oblique impact angles. Because of very large ejection velocities, such fragments cannot belong to observed families and if we had included them in the constructed velocity field of the synthetic family, it would artificially shift velocities of fragments to higher values.

The main feature of cratering events is the peak around the escape velocity v_{esc}. This peak is created by fragments ejected at the point of impact. With an increasing impact energy, the tail of the histogram extends as the fragments are ejected at higher velocities.

Interestingly, there is a second peak at around $Q/Q^{\star}_{D} \sim 0.3$. This is because of ejection of fragments from the antipode of the target. If the shockwave is energetic enough, it causes an ejection of many fragments. The second peak is barely visible at oblique impact angles.

One should be especially careful when interpreting the speed histograms of cratering events. The ejected fragments are often poorly resolved as they are mergers of only a few SPH particles. When we drop the smallest fragments from the distribution, the overall velocities are slightly lower, but this is an expected outcome, as the small fragments usually have high velocities. For mid-energy and catastrophic events, the fragments close to the resolutions limit fit mainly in the tail of the histogram and are of lesser importance to the result.

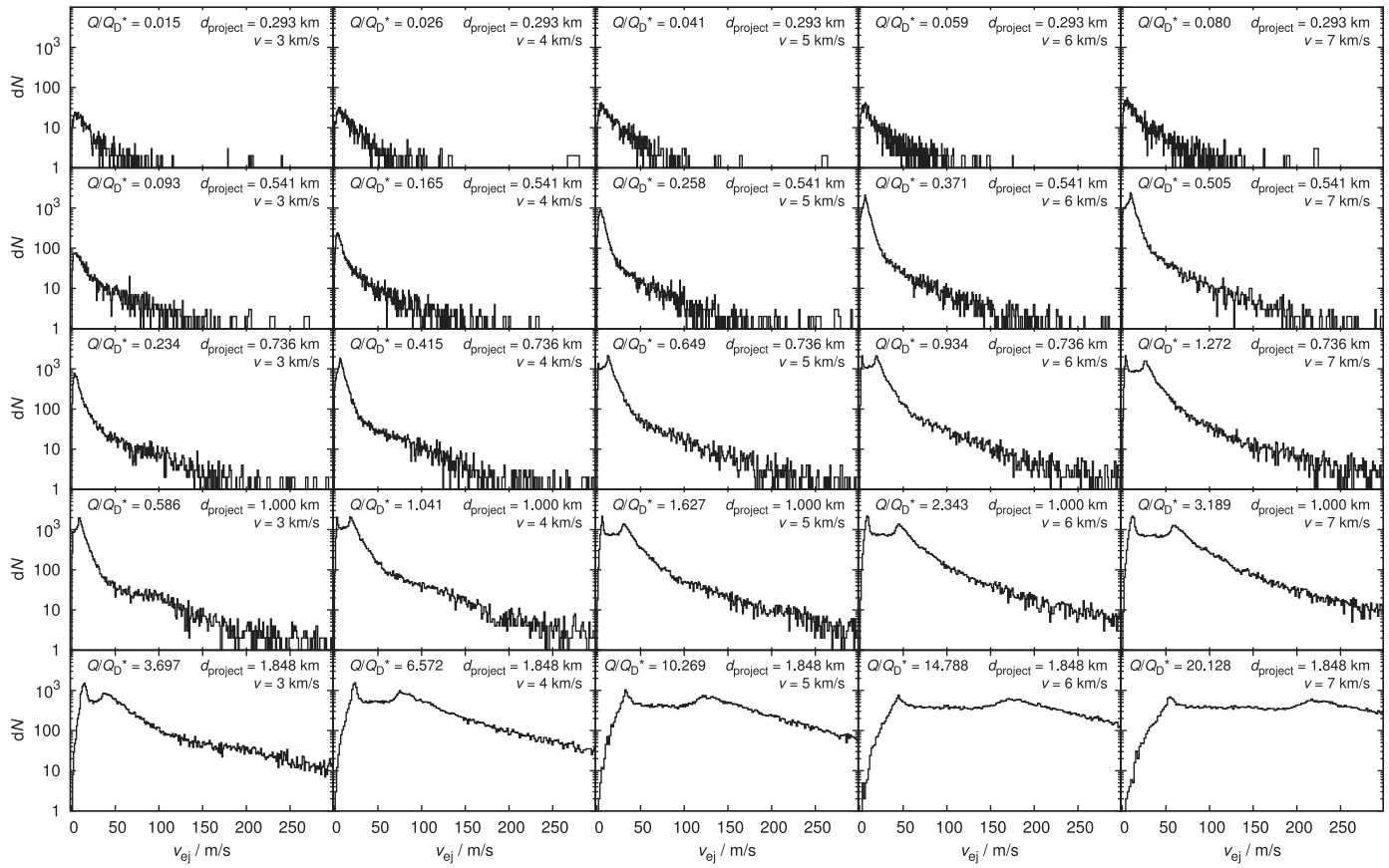

Fig. 2. Differential histograms dN of ejection velocities $v_{\rm ej}$ of fragments for the same set of simulations as in Fig. E.11. The speed is computed in a barycentric reference frame with outliers ($v_{\rm imp} > 1$ km/s) are removed as they are mostly remnants of the projectile. The escape velocity from the target $D_{\rm pb} = 10$ km in size is $v_{\rm esc} = 6.1\,{\rm m\,s^{-1}}$, histogram peaks are thus of order $v_{\rm esc}$, at least for the majority of simulations. However, there is also a significant second peak visible. It is close to the first peak for cratering to mid-energy impacts and extends to velocities $v_{\rm ej} > 100$ m/s for supercatastrophic breakups with $Q/Q^\star_{\rm D} \gtrsim 10$. The impact angle $\phi_{\rm imp} = 45^\circ$ in this case.

3.3. Isotropy vs anisotropy of the velocity field

Fig. 3 shows angular distributions of the velocity fields in the plane of the impact. The histograms are drawn as polar plots with a 5° binning. The angles on plots correspond to the points of impact for given impact angle $\phi_{\rm imp}$; for cratering events, all the ejecta are produced at the point of impact and the distribution of fragments is therefore nicely clustered around $\phi_{\rm imp}$.

Cratering impacts tend to produce velocity fields mainly in the direction of the impact angle. Catastrophic impacts, on the other hand, generally produce much more isotropic velocity fields. However, the isotropy is not perfect, even though we removed outliers as above. Even for the supercatastrophic impacts, the number of fragments in different directions can vary by a factor of 5. Further changes of the reference frame may improve the isotropy. Note that for observed families, it is also not clear where is the reference points, as the identification of family members (and interlopers) is ambiguous.

3.4. A comparison with scaled-down $D_{\rm pb} = 100$ km simulations

To compare $D_{\rm pb} = 10$ km runs with $D_{\rm pb} = 100$ km runs, we need to choose collisions in approximately the same regimes (compare cratering events with cratering events, etc.). The regime can be determined using the scaling law, or more specifically using the ratio $Q/Q^\star_{\rm D}$. We thus compare the runs with approximately the same ratio $Q/Q^\star_{\rm D}$ and the same impact angle $\phi_{\rm imp}$. This means impactors for 10 km runs are (even relatively) much smaller than the ones for 100 km runs. As we require the same $Q/Q^\star_{\rm D}$ ratio for the two simulations, in some cases it was necessary to select a slightly different impact velocity, as all 100 km runs with the same velocity have significantly different ratios $Q/Q^\star_{\rm D}$; for example the $D_{\rm pb} = 10$ km simulation with $d_{\rm project} = 0.736$ km and $v_{\rm imp} = 5$ km/s is being compared to the $D_{\rm pb} = 100$ km simulation with $d_{\rm project} = 18$ km and $v_{\rm imp} = 6$ km/s.

Looking at Fig. 1, we can see that the mid-energy events with $Q/Q^\star_{\rm D} \sim 1$ have SFDs comparable to scaled 100 km ones. In this regime, down-scaling of the distribution for $D_{\rm pb} = 100$ km targets seems to be a justifiable way to approximate SFDs for targets of smaller sizes. There is also a noticeable dependence on the impact angle, due to different sizes of impactors in corresponding simulations. Comparing the SFDs for each impact angle, we can see that for $\phi_{\rm imp} = 15^\circ$ the best match of SFDs is achieved in the interval of $Q/Q^\star_{\rm D} = 0.4$ to 0.9; for $\phi_{\rm imp} = 30^\circ$ this interval is shifted to $Q/Q^\star_{\rm D} = 0.5$ to 1.0, and for $\phi_{\rm imp} = 45^\circ$, it is moved further to $Q/Q^\star_{\rm D} = 1.0$ to 3.0. The match between SFDs is generally worse for $\phi_{\rm imp} = 60^\circ$ and 75° due to the geometric effect mentioned in Section 3.1.

In case of cratering events, our simulations differ significantly from scaled ones. Impacts into 10 km targets produce a much shallower fragment distribution compared to 100 km impacts; see impacts with $d_{\rm project} = 0.293$ km. We also note that supercatastrophic runs have different outcomes than the 100 km ones; our distributions are much shallower and have a much larger largest

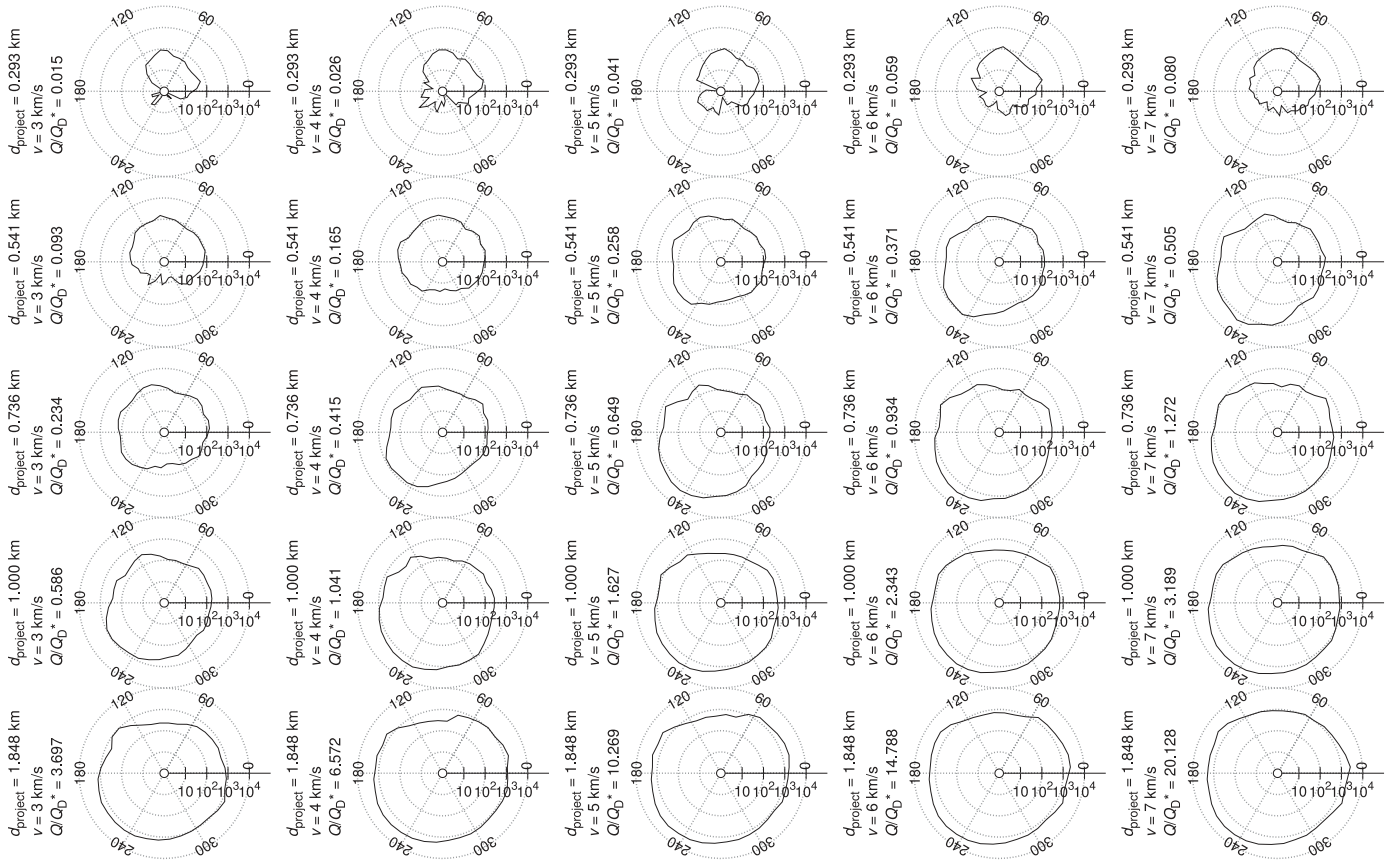

Fig. 3. Histograms of velocity angular distribution (in the plane of the collision) of fragments. The velocities are evaluated in the barycentric coordinate system with outliers removed. The angle 180° corresponds to the velocity direction of the projectile. The impact angle $\phi_{\mathrm{imp}} = 45°$.

fragment.[1] The $D_{\mathrm{pb}} = 10\,\mathrm{km}$ supercatastrophic impacts also also produce a steeper part of the SFD at larger diameters, which is *not* visible for 100 km simulations, at least not to the same extent.

4. Parametric relations for Monte–Carlo collisional models

Size-frequency distributions constructed from our simulations consist mostly of three parts: the largest remnant separated from all the fragments, the middle part of the SFD with a power-law shape (i.e. a straight line in a log-log plot) and a "staircase" of small fragments, marking the resolution limit of our simulations. Ignoring the staircase, the slope of the middle part between $D =$ 0.3 and 2 km can be fitted with a linear function:

$$\log N(>D) = q \log[D]_{\mathrm{km}} + c\,. \tag{15}$$

Supercatastrophic events behave differently though, and their SFDs can be well fitted with a two-slope function:

$$\log N(>D) = K(\log[D]_{\mathrm{km}} - \log[D_0]_{\mathrm{km}}) + c\,, \tag{16}$$

where:

$$K(x) = \frac{1}{2}(q_1 + q_2)x + \frac{1}{2}\frac{q_1 - q_2}{k}\log(2\cosh kx)\,. \tag{17}$$

In this approximation of the SFD, q_1 and q_2 are the limit slopes for $D \to \infty$ and $D \to 0$, respectively, and k characterizes the "bend-off" of the function. As the fitting function is highly non-linear and the dependence on k is very weak (given rather sparse input data), the fit doesn't generally converge, we thus fix $k = 10$ and perform the fit using only four parameters: q_1, q_2, D_0 and c.

Because impacts at high angles appear weaker due the geometry (see Section 3.1), we have to account for the actual kinetic energy delivered into the target. We chose a slightly different approach than Leinhardt and Stewart (2012) and modified the specific impact energy Q by a ratio of the cross-sectional area of the impact and the total area of the impactor. Using a formula for circle-circle intersection: let R be the radius of the target, r the radius of the projectile and d a projected distance between their centers. The area of impact is then given by:

$$A = r^2\cos^{-1}\left(\frac{d^2 + r^2 - R^2}{2dr}\right) + R^2\cos^{-1}\left(\frac{d^2 + R^2 - r^2}{2dR}\right) - \\ - \frac{1}{2}\sqrt{(R + r - d)(d + r - R)(d - r + R)(d + r + R)}\,. \tag{18}$$

As both spheres touch at the point of the impact, we have:

$$d = (r + R)\sin\phi_{\mathrm{imp}}\,. \tag{19}$$

Using these auxiliary quantities, we define the *effective* specific impact energy:

$$Q_{\mathrm{eff}} = Q\frac{A}{\pi r^2}\,. \tag{20}$$

In Fig. 4, we separately plot slopes q, constants c of the linear fits of the SFDs, and the masses of the largest remnants M_{lr} and largest fragment M_{lf}. Each of these quantities shows a distinct dependence on the impact speed v_{imp}, suggesting parametric relations cannot be well described by a single parameter $Q_{\mathrm{eff}}/Q_{\mathrm{D}}$. We

[1] Even though the 100 km bodies have higher self-gravity and a bigger largest fragment might be expected, the higher self-gravity is already accounted for in the critical energy Q^*_{D}.

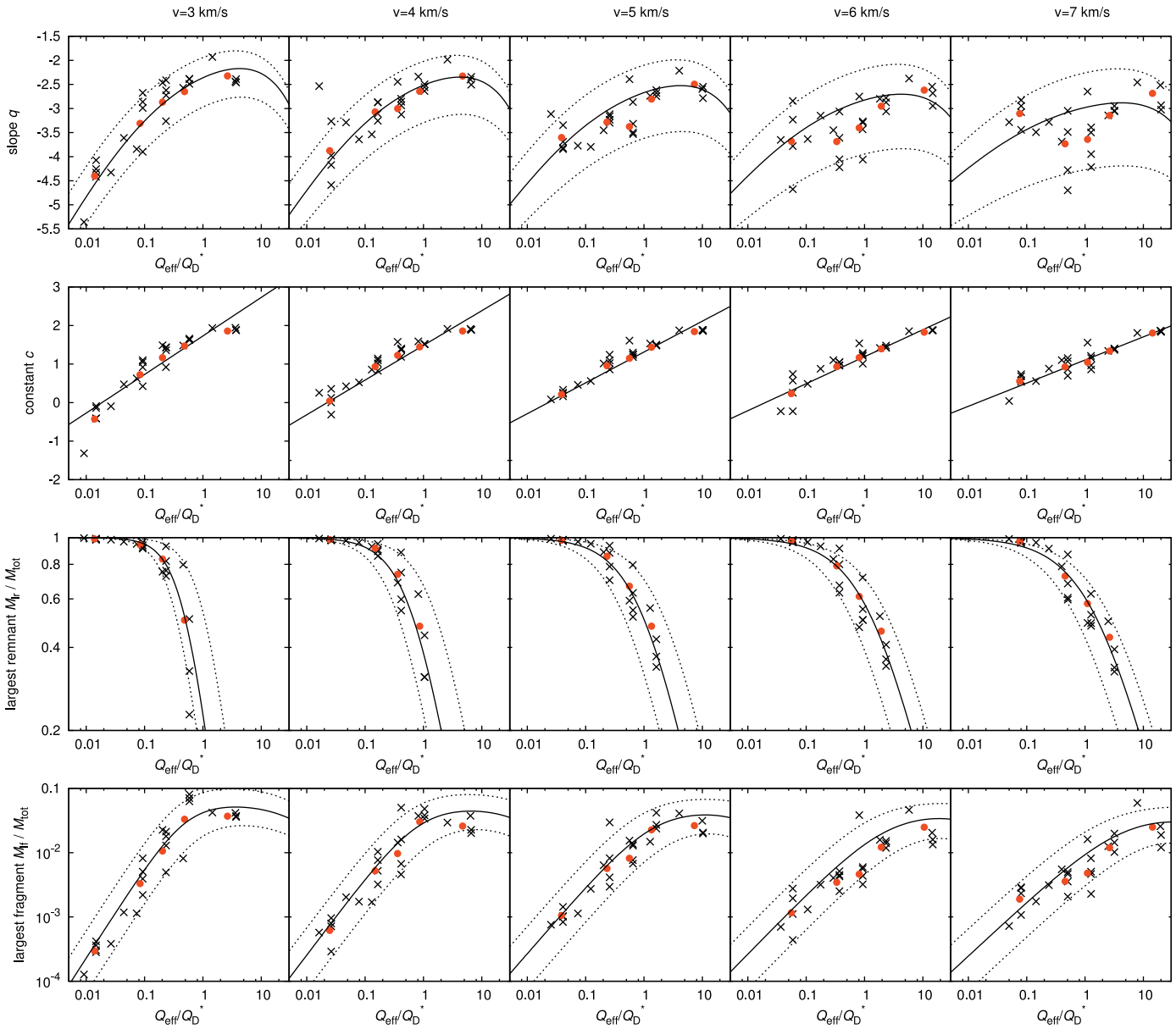

Fig. 4. Parameters of the power-law fits of size-frequency distributions (first and second row) and masses of the largest remnant M_{lr} and the largest fragment M_{lf} (third and fourth row) as functions of the effective impact energy $Q_{\mathrm{eff}}/Q_{\mathrm{D}}^{\star}$, defined by Eq. (20). We plotted these quantities for each value of impact speed separately as considering $Q_{\mathrm{eff}}/Q_{\mathrm{D}}^{\star}$ as a single parameter would imply a large variance of data and therefore a large uncertainty of parametric relations. Each black cross represents one SPH/*N*-body simulation, and the red circles are given by averaging over impact angles ϕ_{imp}. The data are fitted with suitable functions and the scatter of values propagates to the parametric relations as uncertainties, (see Section 4). (For interpretation of the references to colour in this figure legend, the reader is referred to the web version of this article.)

therefore plot each dependence separately for different v_{imp} and we explicitly express the dependence on v_{imp} in parametric relations.

For low speeds, slopes q can be reasonably fitted with a function:

$$q = -12.3 + 0.75 v_{\mathrm{imp}} + \frac{(11.5 - 1^{+0.2}_{-0.1} v_{\mathrm{imp}}) \exp\left(-5 \cdot 10^{-3} \dfrac{Q_{\mathrm{eff}}}{Q_{\mathrm{D}}^{\star}}\right)}{1 + 0.1^{+0.01}_{-0.02} \left(\dfrac{Q_{\mathrm{eff}}}{Q_{\mathrm{D}}^{\star}}\right)^{-0.4}}, \tag{21}$$

where v_{imp} is expressed in km/s. However, for high speeds (especially for $v = 7$ km/s), the individual values of q for different impact angles differ significantly and thus the fit has a very high uncertainty. We account for this behaviour in Eq. (21), where the uncertainty increases with an increasing speed.

The constant c can be well fitted by linear function:

$$c = 0.9 + 2.3 \exp(-0.35 v_{\mathrm{imp}}) + \left(1.3 - 0.1 v_{\mathrm{imp}}\right) \left(\frac{Q_{\mathrm{eff}}}{Q_{\mathrm{D}}^{\star}}\right). \tag{22}$$

The high scatter noted in the parametric relation for the slope q is not present here. This parameter is of lesser importance for Monte-Carlo models though, as the distribution must be normalized anyway to conserve the total mass.

Largest remnants are also plotted in Fig. 4. Notice that some points are missing here as the largest remnant does not exist for supercatastrophic impacts. As we are using the effective impact en-

ergy Q_{eff} as an independent variable, the runs with impact angle $\phi = 75^\circ$ produce largest remnants of sizes comparable to other impact angles. This helps to decrease the scatter of points and make the derived parametric relation more accurate. We selected a fitting function:

$$M_{\mathrm{lr}} = \frac{M_{\mathrm{tot}}}{1 + \left[0.6^{+0.5}_{-0.2} + 56\exp(-1.0^{+0.6}_{-0.2}v_{\mathrm{imp}})\right]\left(\frac{Q_{\mathrm{eff}}}{Q^\star_{\mathrm{D}}}\right)^{0.8+8\exp(-0.7v_{\mathrm{imp}})}}. \tag{23}$$

Largest fragments (fourth row) exhibit a larger scatter, similarly as the slopes q. The masses of the largest fragment can differ by an order of magnitude for different impact angles (notice the logarithmic scale on the y-axis). Nevertheless, the values averaged over impact angles (red circles) lie close the fit in most cases. The fitting function for the largest remnant is:

$$M_{\mathrm{lf}} = \frac{M_{\mathrm{tot}}}{0.24^{+0.60}_{-0.15}v^3_{\mathrm{imp}}\left(\frac{Q_{\mathrm{eff}}}{Q^\star_{\mathrm{D}}}\right)^{-0.6-2\exp(-0.3v_{\mathrm{imp}})} + \exp\left(-0.3^{+0.2}_{-0.2}v_{\mathrm{imp}}\right)\frac{Q_{\mathrm{eff}}}{Q^\star_{\mathrm{D}}} + 11^{+15}_{-8} + 2v_{\mathrm{imp}}}. \tag{24}$$

This function bends and starts to decrease for $Q_{\mathrm{eff}}/Q^\star_{\mathrm{D}} \gg 1$. Even though this behaviour is not immediately evident from the plotted points, the largest fragment *must* become a decreasing function of impact energy in the supercatastrophic regime.

The relations derived above could be compared with relations for $D_{\mathrm{pb}} = 100\,\mathrm{km}$ bodies, published in Cibulková et al. (2014) . The comparison is not straightforward, though, as we chose different fitting functions and also different variables to parametrize the relations. Nevertheless, the parametric relations only approximate SFDs, whilst the differences between SFDs of $D_{\mathrm{pb}} = 10\,\mathrm{km}$ and 100 km bodies have already been discussed in Section 3.4.

5. Conclusions and future work

In this paper, we studied disruptions and subsequent gravitational reaccumulation of asteroids with diameter $D_{\mathrm{pb}} = 10\,\mathrm{km}$. Using an SPH code and an efficient N-body integrator, we performed impact simulations for various projectile sizes d_{project}, impact speeds v_{imp} and angles ϕ_{imp}. The size-frequency distributions, constructed from the results of our simulations, appear similar to the scaled-down simulations of Durda et al. (2007) only in the transition regime between cratering and catastrophic events ($Q/Q^\star_{\mathrm{D}} \simeq 1$); however, they differ significantly for both the weak cratering impacts and for supercatastrophic impacts.

The resulting size-frequency distributions can be used to estimate the size of the parent body, especially for small families. As an example, we used our set of simulations to determine D_{pb} of the Karin family. This cluster was studied in detail by Nesvorný et al. (2006) and we thus do not intend to increase the accuracy of their result, but rather to assess the uncertainty of linear SFD scaling. The closest fit to the observed SFD of the Karin cluster yields a parent body with $D_{\mathrm{pb}} = 25\,\mathrm{km}$ — a smaller, but comparable value to $D_{\mathrm{pb}} = 33\,\mathrm{km}$, obtained by Nesvorný et al. (2006). Using the set of $D_{\mathrm{pb}} = 100\,\mathrm{km}$ simulations, Durda et al. (2007) obtained an estimate $D_{\mathrm{pb}} \simeq 60\,\mathrm{km}$. It is therefore reasonable that the best estimate is intermediate between the result from upscaled 10 km runs and downscaled 100 km runs. We do not consider our result based on "generic" simulations more accurate than the result of Nesvorný et al. (2006); however, the difference between the results can be seen as an estimate of uncertainty one can expect when scaling the SFDs by a factor of 3.

We derived new parametric relations, describing the masses M_{lr} and M_{lf} of the largest remnant and the largest fragment, respectively, and the slope q of the size-frequency distribution as functions of the impact parameters. These parametric relations can be used straightforwardly to improve the accuracy of collisional models, as the fragments created by a disruption of small bodies were previously estimated as scaled-down disruptions of $D_{\mathrm{pb}} = 100\,\mathrm{km}$ bodies.

In our simulations, we always assumed monolithic targets. The results can be substantially different for porous bodies, though, as the internal friction has a significant influence on the fragmentation (Jutzi et al., 2015; Asphaug et al., 2015). This requires using a different yielding model, such as Drucker–Prager criterion. We postpone a detailed comparison between monolithic and porous bodies for future work.

Acknowledgements

The work of MB and PŠ was supported by the Grant Agency of the Czech Republic (grant no. P209/15/04816S).

Appendix A. Initial distribution of SPH particles

For a unique solution of evolutionary differential equations, initial conditions have to be specified. In our case, this means setting the initial positions and velocities of SPH particles. We assume non-rotating bodies, all particles of the target are therefore at rest and all particles of the impactor move with the speed of the impactor.

Optimal initial positions of SPH particles have to meet several criteria. First of all, the particles have to be distributed evenly in space. This requirement eliminates a random distribution as a suitable method, for using such a distribution would necessarily lead to clusters of particles in some parts of space and a lack of particles in other parts.

We therefore use a hexagonal-close-packing lattice in the simulations. They are easily set up and have an optimal interpolation accuracy. However, no lattice is *isotropic*, so there are always preferred directions in the distribution of SPH particles. This could potentially lead to numerical artifacts, such as pairing instability (Herant, 1994). Also, since the particle concentration is uniform, the impact is therefore resolved by only a few SPH particles for small impactors. We can increase accuracy of cratering impacts by distributing SPH particles nonuniformly, putting more particles at the point of impact and fewer in more distant places.

Here we assess the uncertainty introduced by using different initial conditions of SPH particles. A suitable method for generating a nonuniform isotropic distribution has been described by Diehl et al. (2012) and Rosswog (2015). Using initial conditions generated by this method, we ran several SPH/N-body simulations, and we compared the results to the simulations with lattice initial conditions.

The comparison is in Fig. A.5. Generally, the target shatters more for the nonuniform distribution. The largest remnant is smaller; the difference is up to 10% for the performed simulations. There are also more fragments at larger diameters, compared to the lattice distribution. This is probably due to slightly worse interpolation properties of the nonuniform distribution. A test run for a *random* distribution of particles led to a complete disintegration of the target and a largest remnant smaller by an order of magnitude, suggesting the smaller largest remnant is a numerical artifact of the method. On the other hand, the SFD is comparable at smaller diameters. This leads to more bent, less power-law-like SFDs for nonuniform runs.

The differences between both particle distributions are the largest for cratering impacts with a very small impactor. The

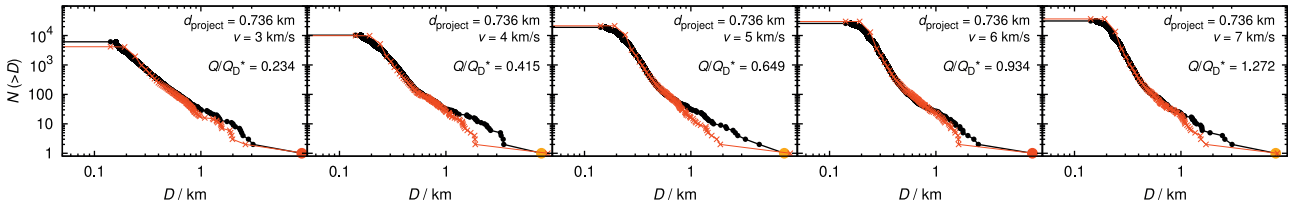

Fig. A.5. SFDs constructed from five different simulations with $D_{pb} = 10$ km, $d_{project} = 0.736$ km and impact angle $\phi_{imp} = 45°$. Black histogram shows the runs with the nonuniform distribution generated by the method of Diehl et al. (2012), while red are the previous (lattice) results shown in Fig. E.11. (For interpretation of the references to colour in this figure legend, the reader is referred to the web version of this article.)

bigger the impactor, the more similar the SFD is to the SFD of the "standard" particle grid.

Appendix B. Sensitivity to Weibull parameters

In the computed grid of simulations, we kept all the material parameters fixed to the nominal values listed in Table 1. We did not study the dependence of the resulting distributions $N(>D)$ and $\mathrm{d}N(v)/\mathrm{d}v$ on these parameters, as the size of the parameter space would be exceedingly large, and also to make the comparison with the 100 km runs of Durda et al. (2007) easier; both sets of simulations used the same material parameters.

However, the fragmentation process is mainly determined by the flaw distribution in the selected material, approximated by the Weibull power-law (Weibull, 1939):

$$n(\epsilon) = k\epsilon^m, \tag{B.1}$$

where m is the Weibull exponent and k is the normalization coefficient. For a basaltic material, the Weibull exponent can range from $m = 6$ to 12 (Jaeger et al., 2007) and the coefficient k can possibly vary by an order of magnitude, making them the most uncertain material parameters.

To assess the uncertainty that propagates to the resulting SFDs, we ran a few simulations with $d_{project} = 0.736$ km, $v_{imp} = 5$ km and $\phi_{imp} = 45°$, varying the Weibull parameters. Two simulations have a different value of the exponent, $m = 6$ and $m = 12$, and two simulations differ in the coefficient k by a factor of 2. The produced SFDs can be seen in Fig. B.6. As expected, the differences between individual runs are noticeable, however, they do not change the overall characteristics of the SFD. The slope of the SFD between $D = 0.3$ and 1 km is approximately the same in all runs, while the sizes of the largest remnant differ in a predictable way: more flaws with higher activation strains means higher fragmentation and subsequently a smaller largest remnant. We can conclude that the Weibull parameters may introduce a (systematic) uncertainty, but there are also other model parameters, for example the initial distribution of SPH particles, that may result in a bias of similar order.

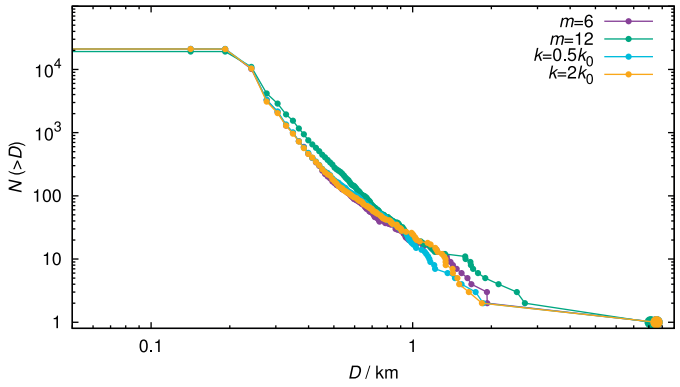

Fig. B.6. Size-frequency distributions for various Weibull parameters k and m. Here $k_0 = 4.0 \times 10^{29}$ is the nominal value used in main text, see Table 1.

Appendix C. Energy conservation vs. timestepping

Modelling of smaller breakups seems more difficult. Apart from poor resolution of the impactor, if one uses the same (optimum) SPH particle mass as in the target, and a relatively low number of ejected fragments, weak impacts may also exhibit problems with energy conservation (see Fig. C.7). This is even more pronounced in the case of low-speed collisions, e.g. of $D = 1$ km target, $d = 22$ m projectile, at $v_{imp} = 3$ km/s and $\phi_{imp} = 45°$.

At first, we thought that small oscillations of density — with relative changes $\Delta\rho/\rho$ smaller than the numerical precision — are poorly resolved, and subsequently cause the total energy to increase. But when we performed the same simulation in quadruple precision (with approximately 32 valid digits) we realised there is essentially no improvement (see Fig. C.8), so this cannot be the true reason.

Instead, we changed the timestepping scheme and superseded the default predictor/corrector with the Bulirsch–Stoer integrator (Press et al., 1992), which performs a series of trial steps with Δt divided by factors $2, 4, 6, \ldots$, and checks if the relative difference between successive divisions is less than small dimensionless factor ϵ_{BS} and then extrapolates to $\Delta t \to 0$. In our case, a scaling of quantities is crucial. In principle, we have three options: (i) scaling by expected maximum values, which results in a constant absolute error; (ii) current values, or constant relative error; (iii) derivatives times time step, a.k.a. constant cumulative error. The option (i) seems the only viable one, otherwise the integrator is exceedingly slow during the initial pressure build-up. According to Fig. C.9, we have managed to somewhat improve the energy conservation this way, but more work is needed to resolve this issue.

Appendix D. Energy conservation vs. sub-resolution acoustic waves

Even though we always start with intact monolithic targets, we realized that prolonged computations of the fragmentation phase require a more careful treatment of undamaged/damaged boundaries. The reason is the following rather complicated mechanism: (i) The shock wave, followed by a decompression wave, *partially* destroys the target. After the reflection from the free surface, the rarefaction (or sound) wave propagates back to the target. (ii) However, neither wave can propagate into already damaged parts, so there is only an undamaged cavity. (iii) This cavity has an *irregular* boundary, so that reflections from it create a lot of small waves, interfering with each other. (iv) As a result of this interference, there is a lot of particles that have either high positive or high negative pressure, so that the pressure gradient — computed

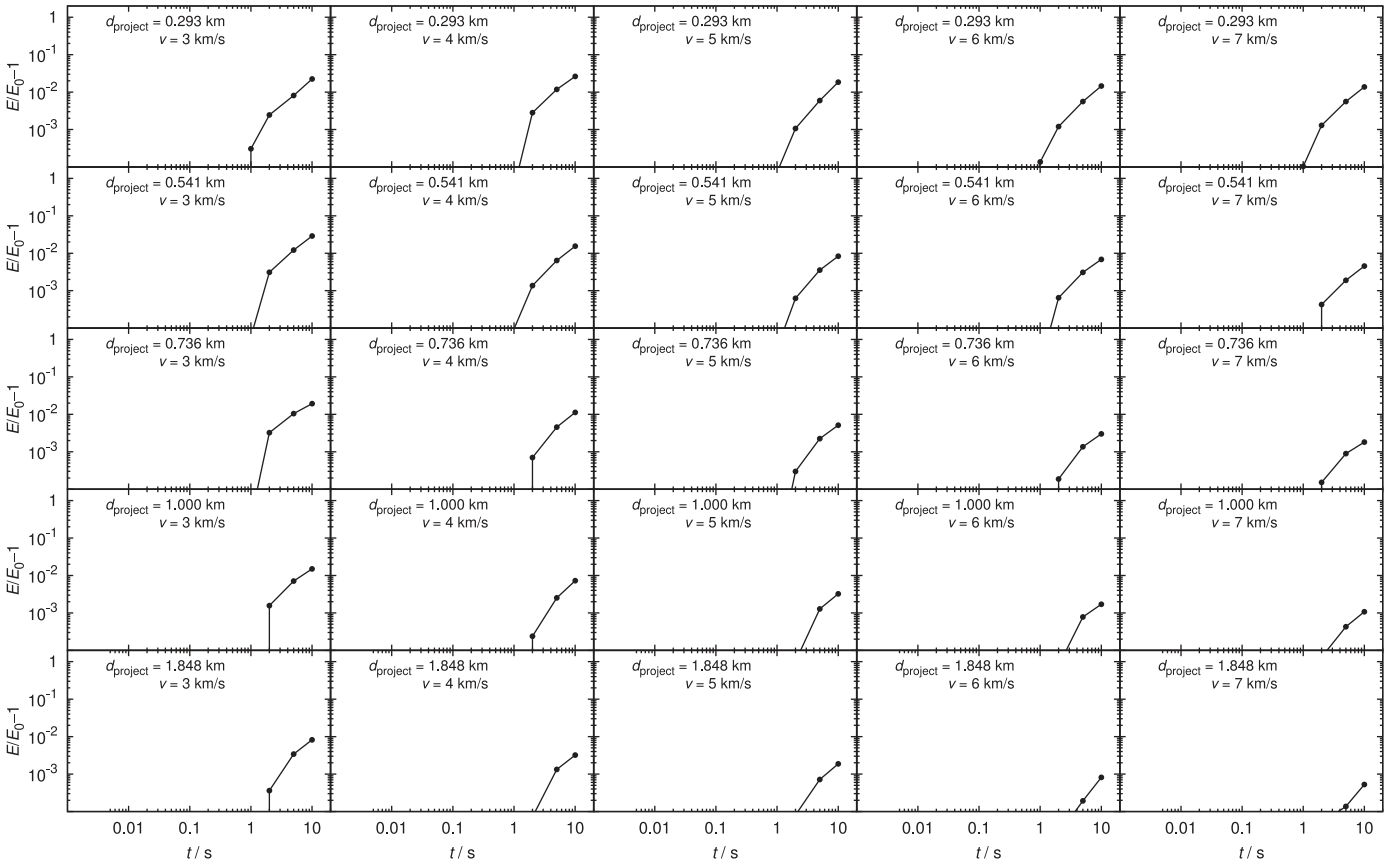

Fig. C.7. Relative total energy E vs time t for the same grid of simulations as presented in Section 3. The diameter of the target was always $D = 10$ km and the impact angle $\phi_{imp} = 45^\circ$. The maximum relative energy error is of the order of 10^{-2} at the final time $t = 10$ s.

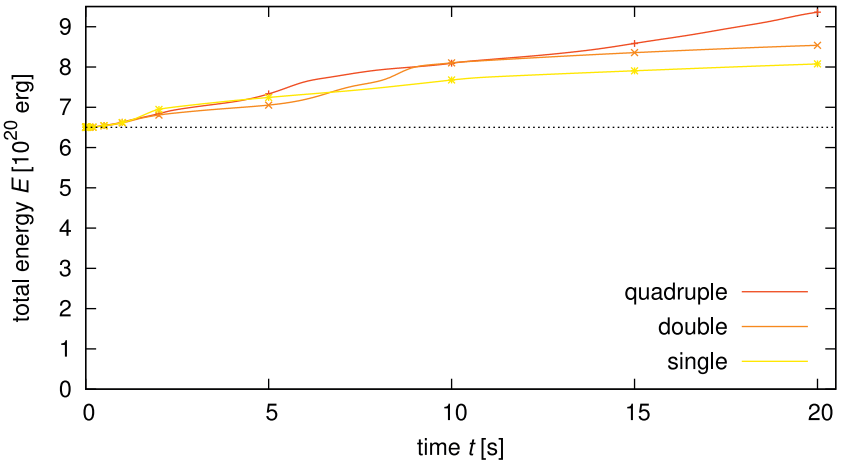

Fig. C.8. Total energy E vs time t for a small cratering impact, with a $D = 1$ km target and $d = 22$ m projectile, and several compiled numerical precisions of the SPH5 code: quadruple (128-bit), double (64-bit) and single (32-bit). Because the computation in quadruple precision is very slow, we use $N \doteq 1.4 \times 10^4$ particles only in this test. Other parameters were set up similarly as in other simulations presented in Section 3. Neither version conserves the energy sufficiently, which is an indication that round-off errors are *not* the dominant cause of the energy increase.

as a sum over neighbours – is *zero*! (v) $\nabla P = 0$ means no motion, and consequently no pressure release is possible. (vi) However, at the *boundary* between undamaged/damaged material, there are some particles with $P > 0$, next to the damaged ones with $P = 0$, which slowly push away the undamaged particles in the surroundings. (vii) Because the pressure is still not released, the steady pushing eventually destroys the whole target (see Fig. D.10).

In reality, this does not happen, because the waves can indeed become very small and dissipate. In SPH, the dissipation of waves at the resolution limit is impossible. Increasing resolution does not help at all – the boundary is even more irregular and the sound waves will anyway become as small as the resolution.

As a solution, we can use an upper limit for damage, very close to 1, but not equal to 1, e.g. $(1 - \mathcal{D}) = 10^{-12}$. Then the acoustic

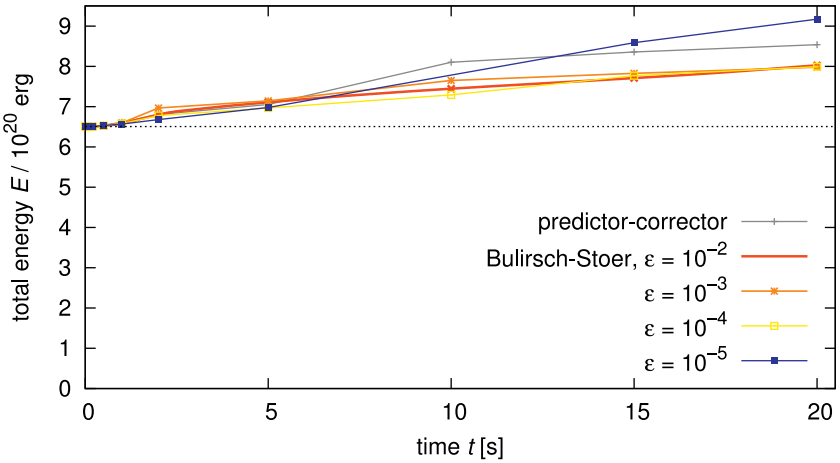

Fig. C.9. Total energy E vs time t for the same impact as in Fig. C.8, but with different timestepping schemes, namely the default predictor–corrector (controlled by the Courant number $C = 1.0$ and other time step restrictions) and the Bulirch–Stoer with the unitless parameter $\epsilon_{BS} = 10^{-2}$ to 10^{-5}. The scaling by maximum values of variables was used, which corresponds to constant absolute errors. The energy conservation was somewhat improved this way, with the exception of the lowest ϵ_{BS} at late times.

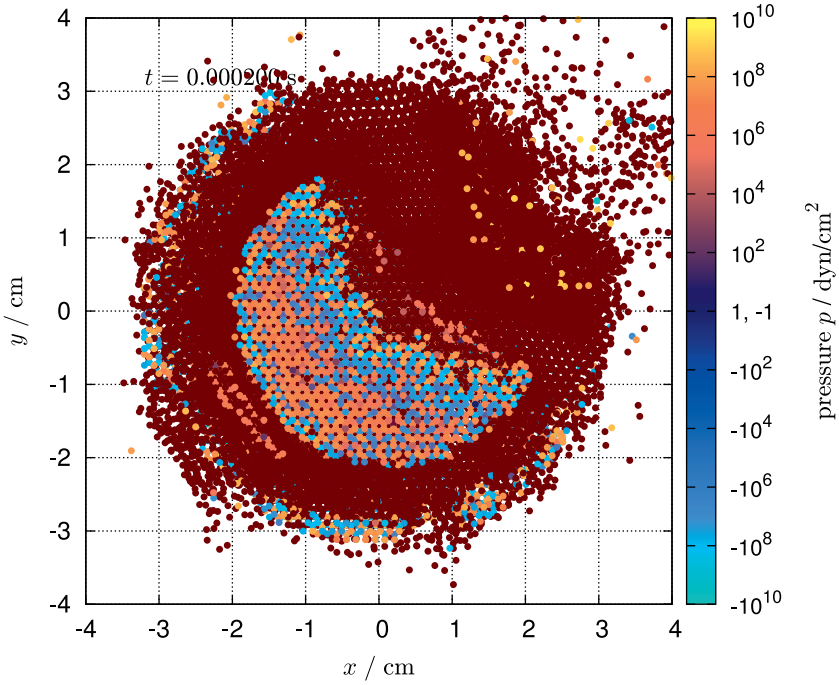

Fig. D.10. A simulation of the classical Nakamura (1993) experiment, but prolonged up to 200 μs, which exhibits problems with energy conservation, as explained in the main text. We show a cross section in the (x, y) plane and pressure P in colour logarithmic scale. There are acoustic waves with wavelengths close to the resolution limit in the inner monolithic cavity, surrounded by fully damaged material (with $\mathcal{D} = 1$). In our setup, $D_{target} = 6$ cm, $d_{project} = 0.7$ cm, $\rho = 2.7$, or 1.15 g cm^{-3} respectively, $v_{imp} = 3.2$ km s^{-1}, $\phi_{imp} = 30°$, $N_{part} \doteq 7 \cdot 10^5$.

waves are damped (in a few seconds for $D = 1$ km targets) and the energy is conserved perfectly. Another option would be to use a more detailed rheology of the material, namely the internal friction and Drucker–Prager yield criterion (as in Jutzi et al., 2015).

Appendix E. Additional figures

Figs. E.11, E.12, E.13, E.14, E.15, E.16, E.17, E.18, E.19, E.20, E.21, E.22 show the situation for non-standard impact angles.

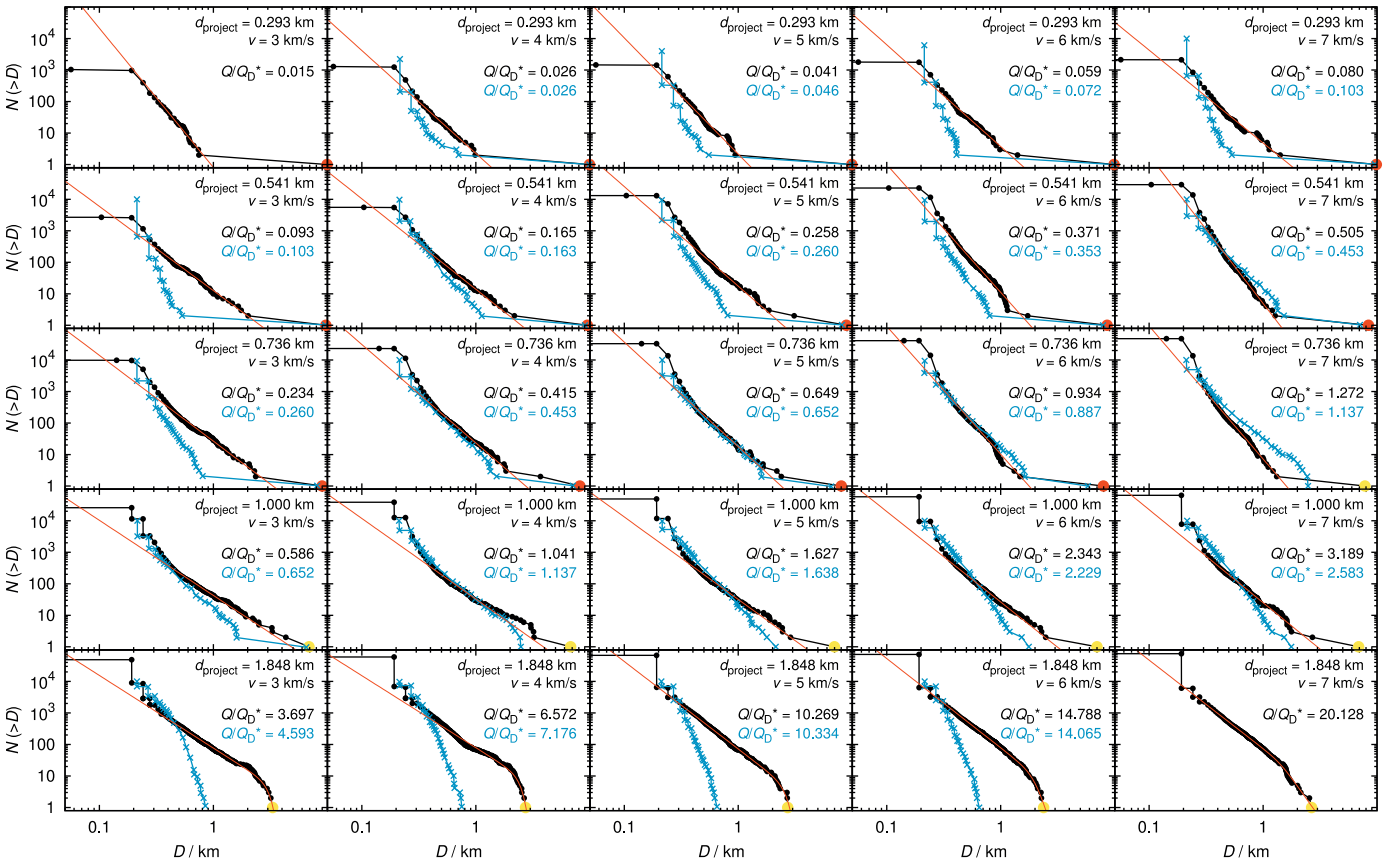

Fig. E.11. Impact angle 15°.

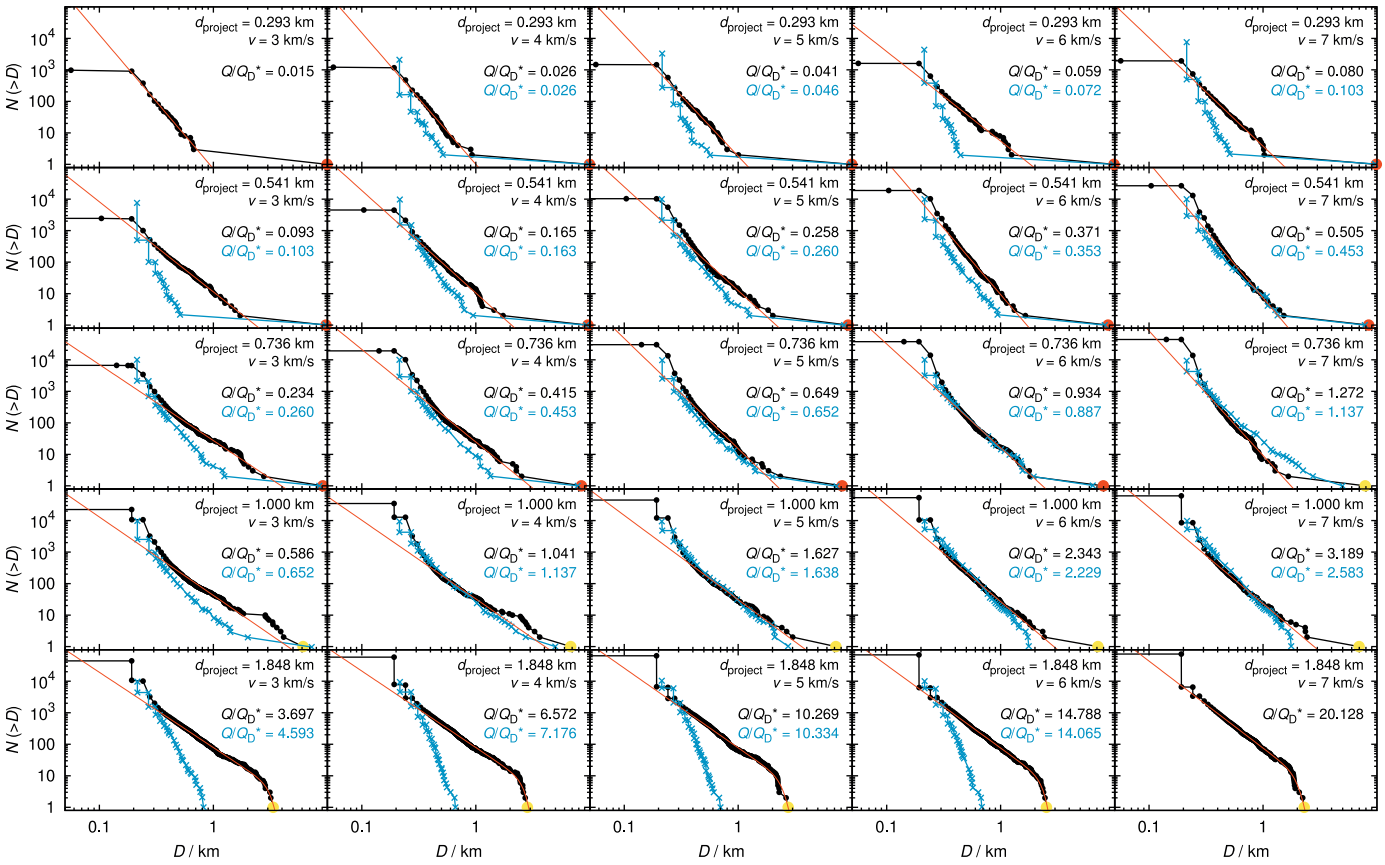

Fig. E.12. Impact angle 30°.

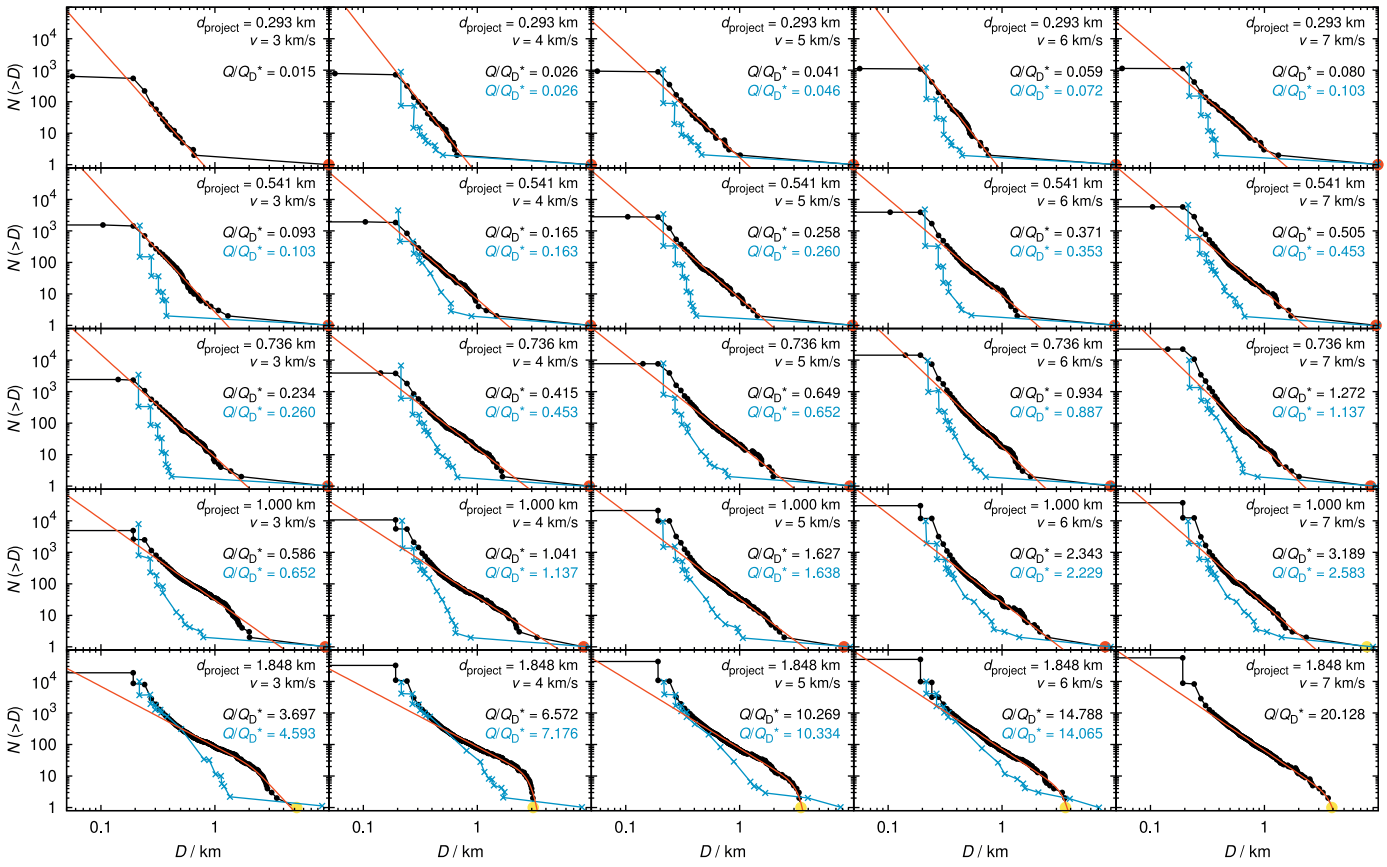

Fig. E.13. Impact angle 60°.

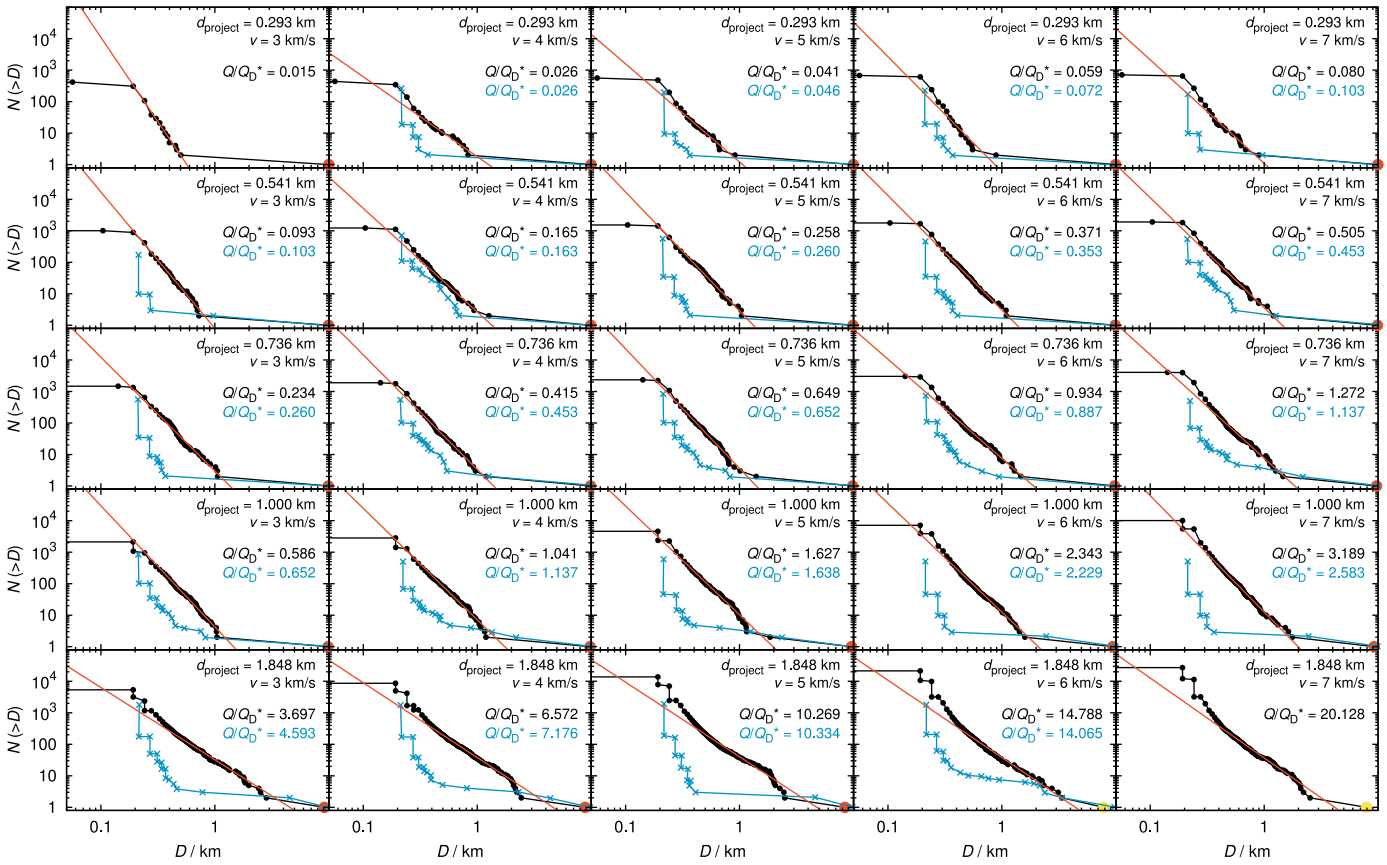

Fig. E.14. Impact angle 75°.

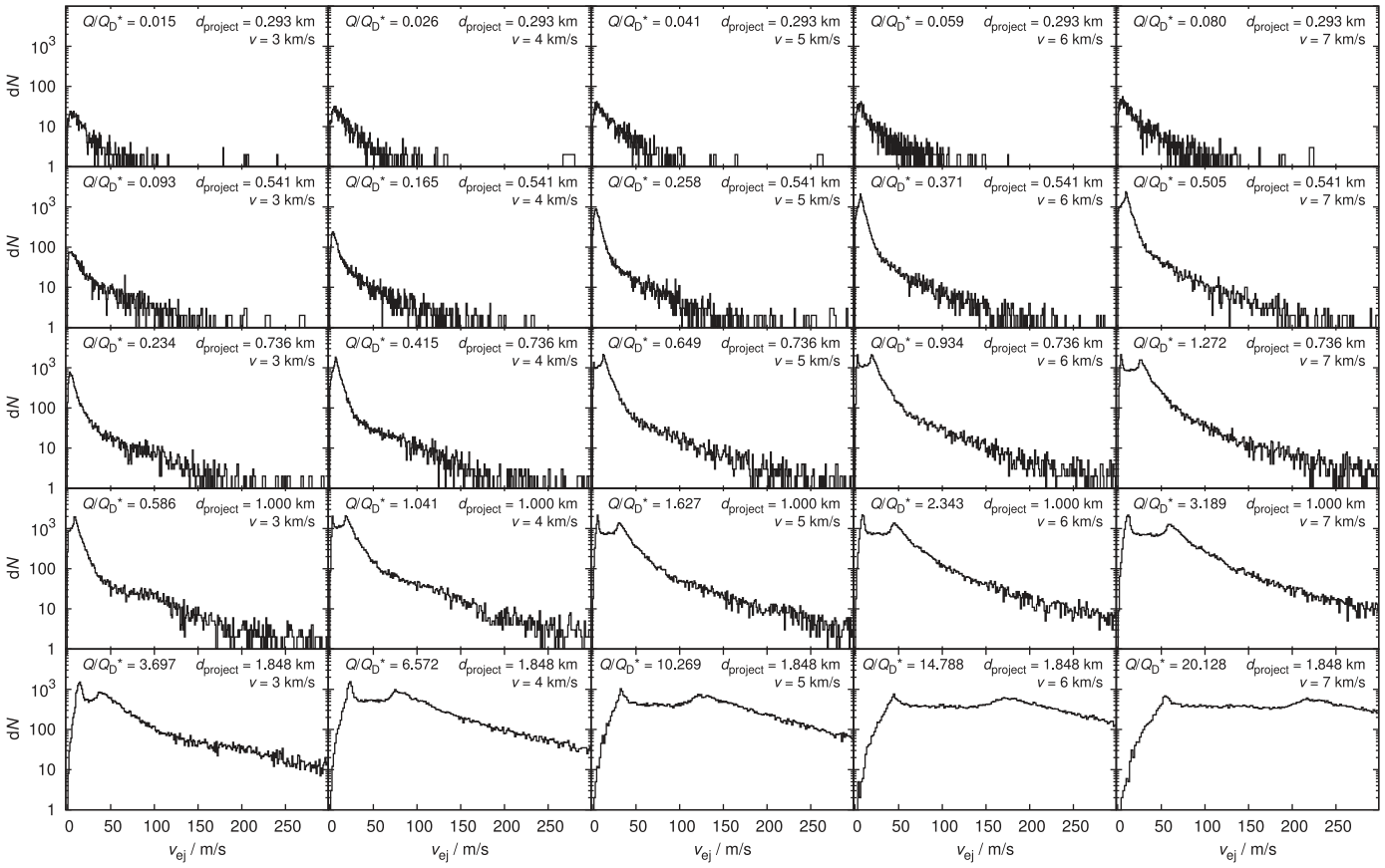

Fig. E.15. Impact angle 15°.

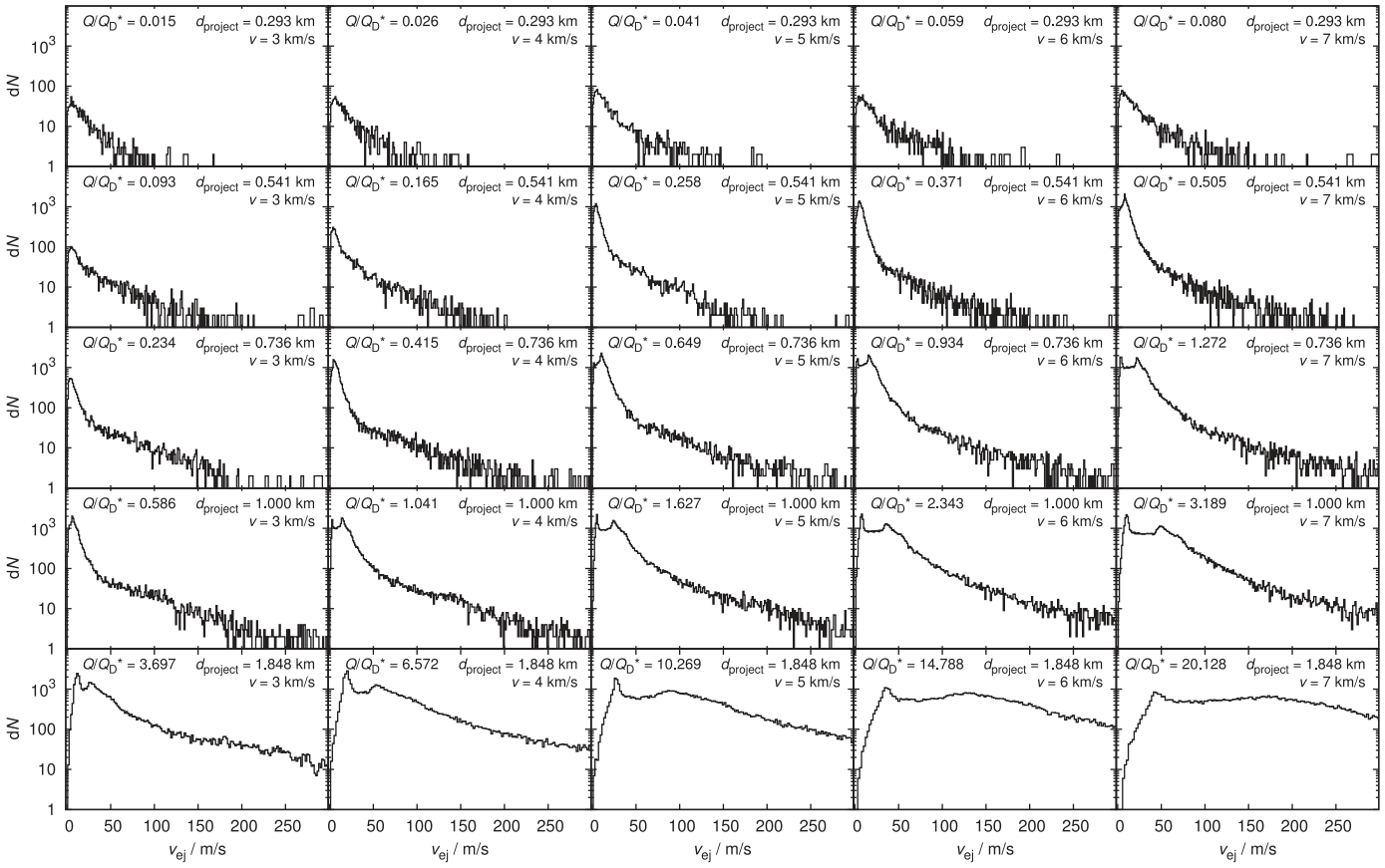

Fig. E.16. Impact angle 30°.

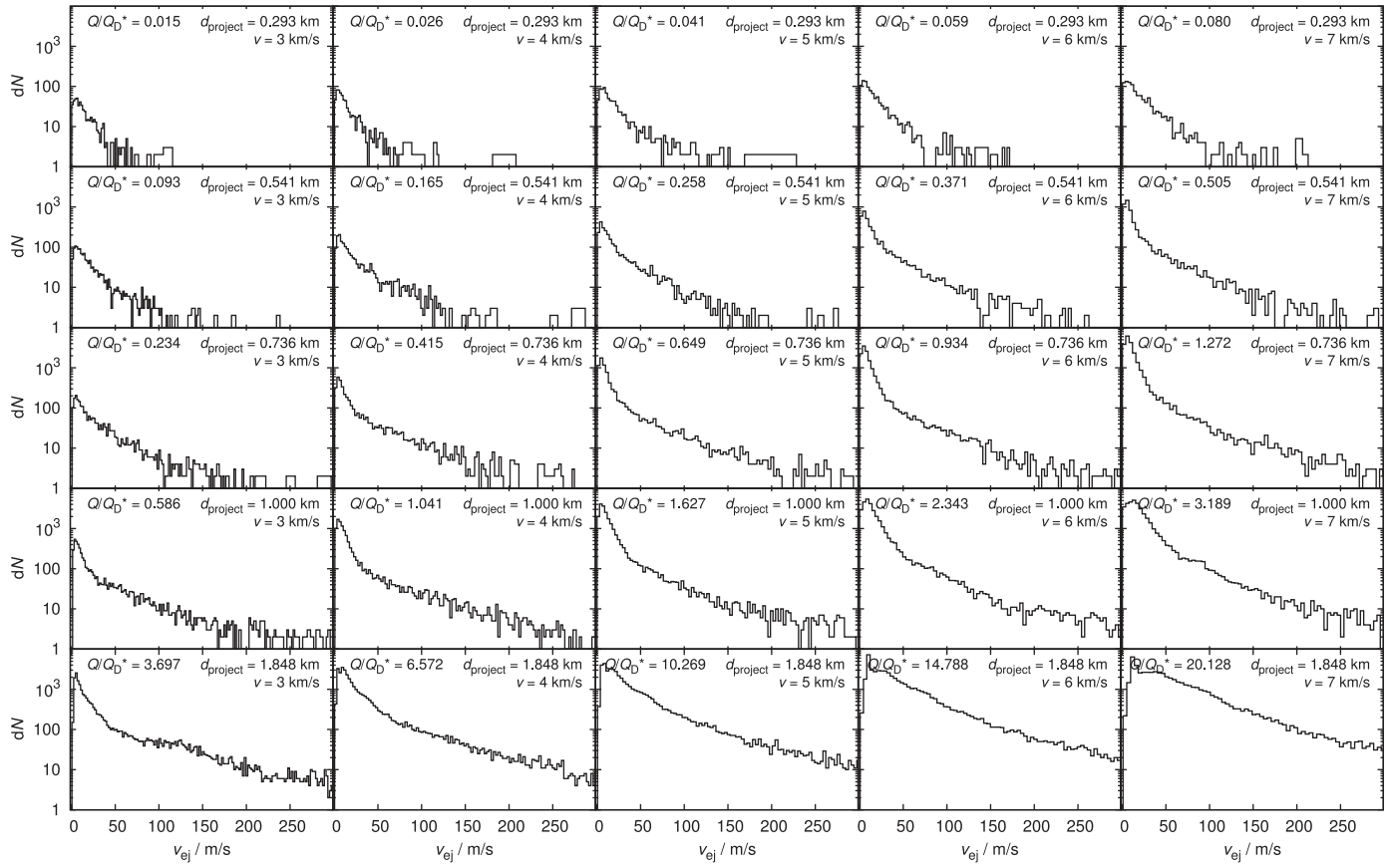

Fig. E.17. Impact angle 60°.

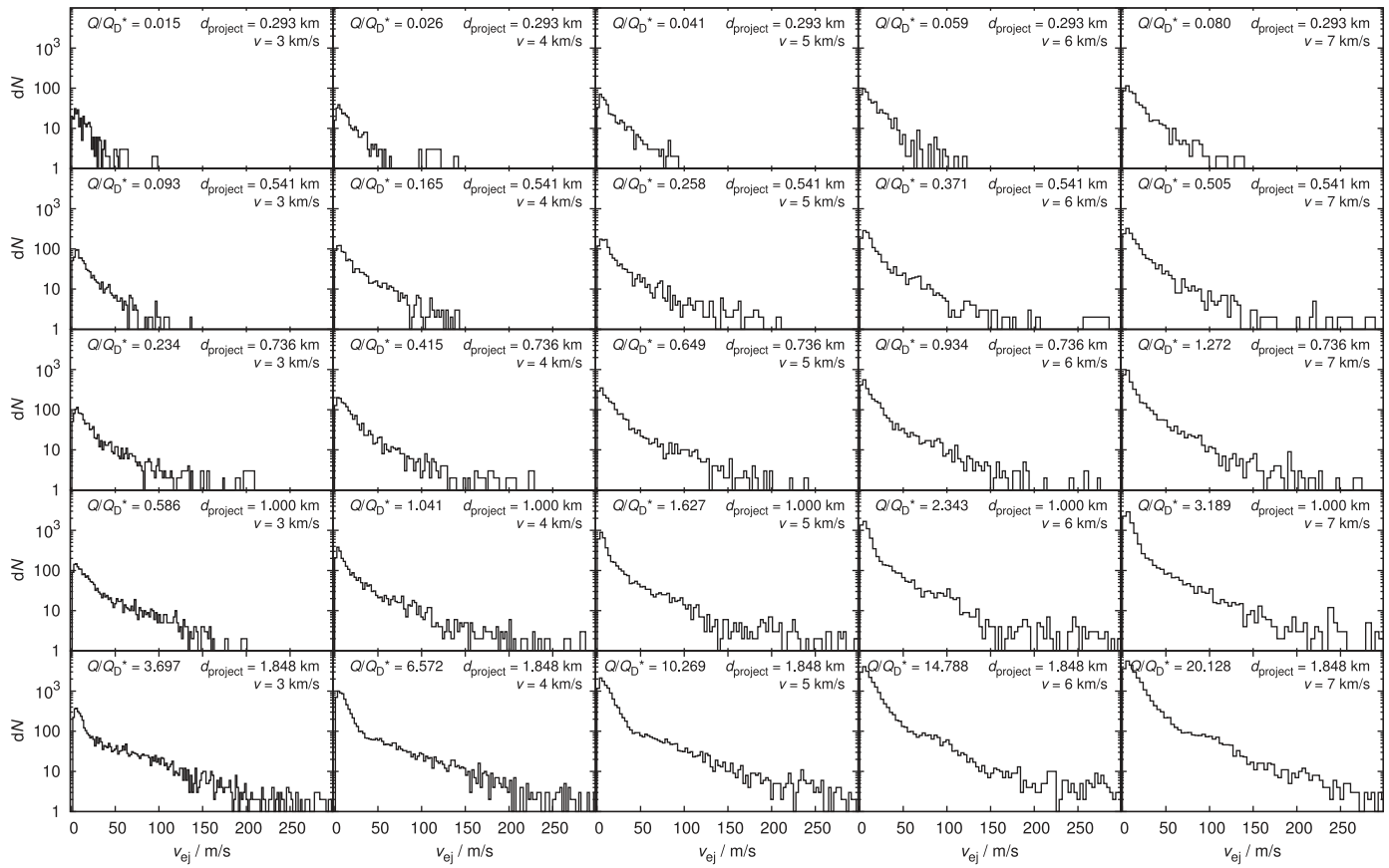

Fig. E.18. Impact angle 75°.

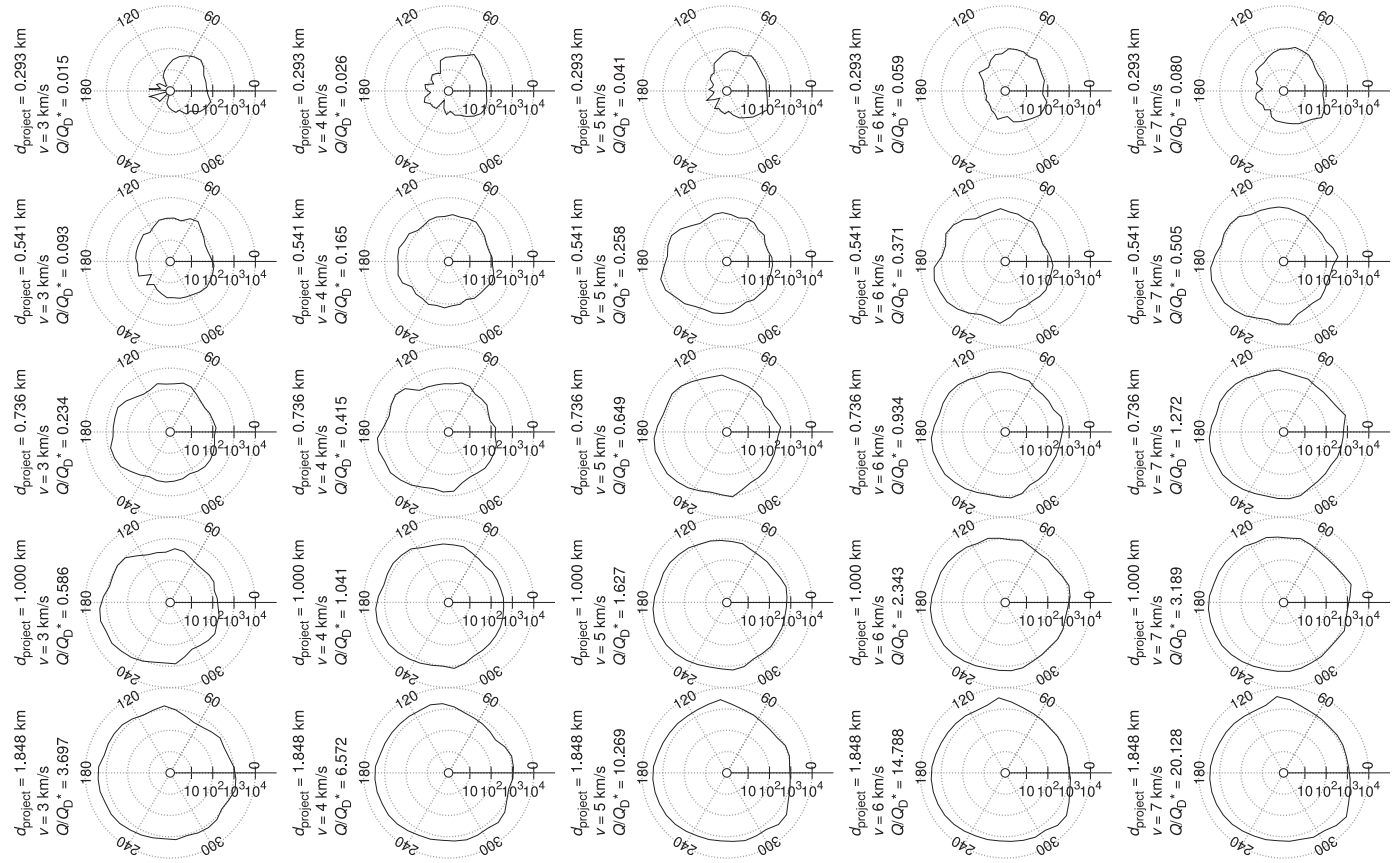

Fig. E.19. Impact angle 15°.

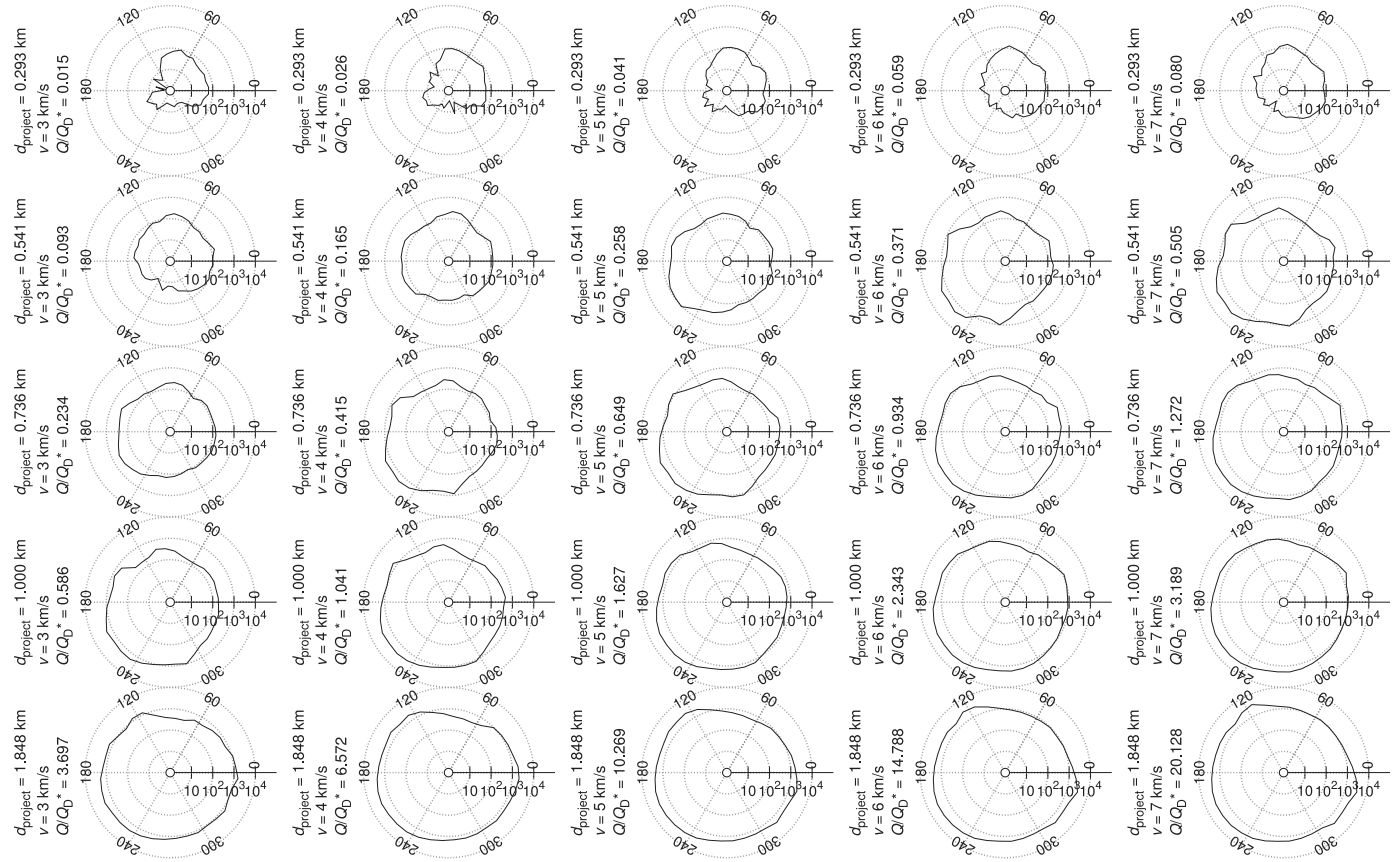

Fig. E.20. Impact angle 30°.

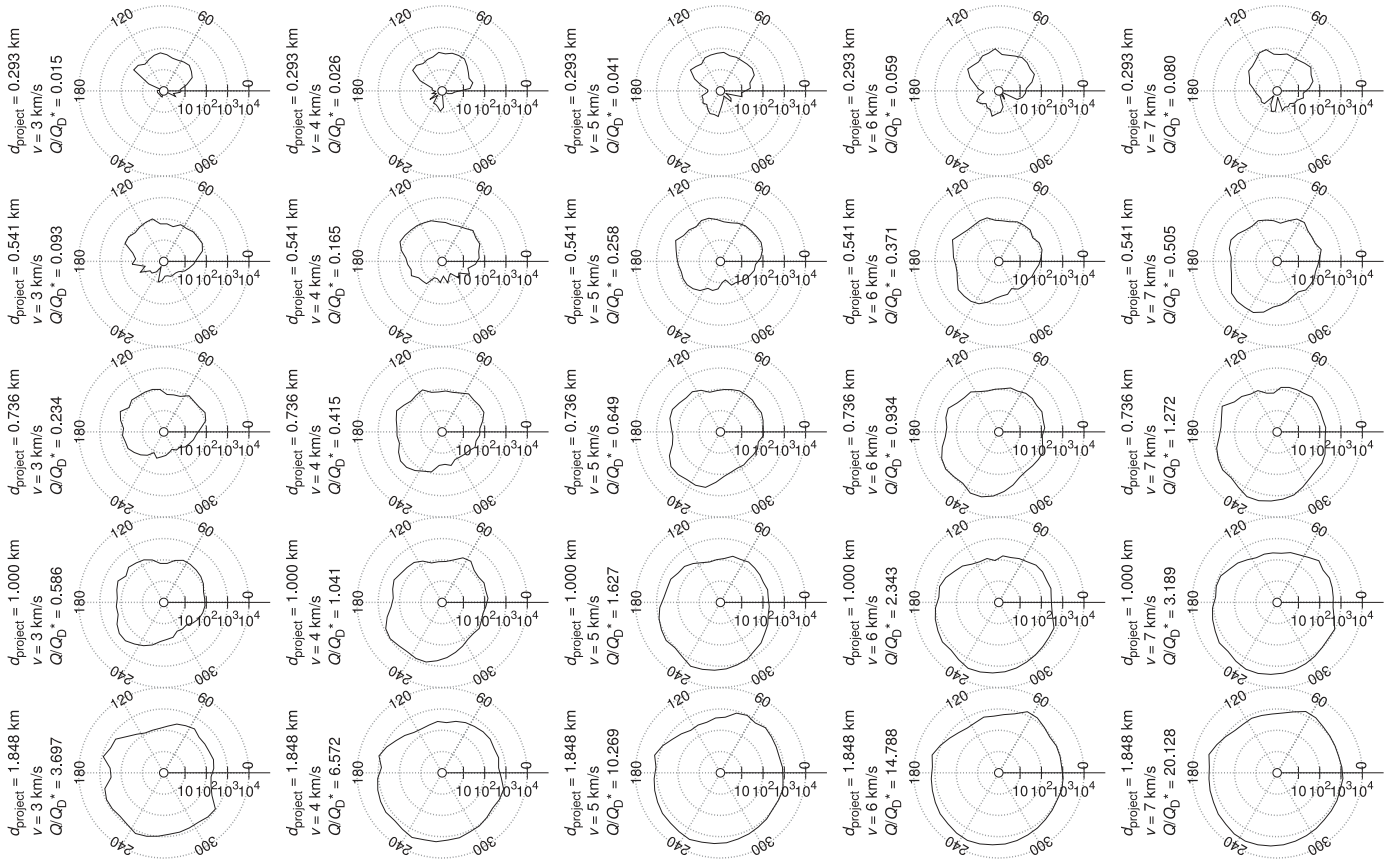

Fig. E.21. Impact angle 60°.

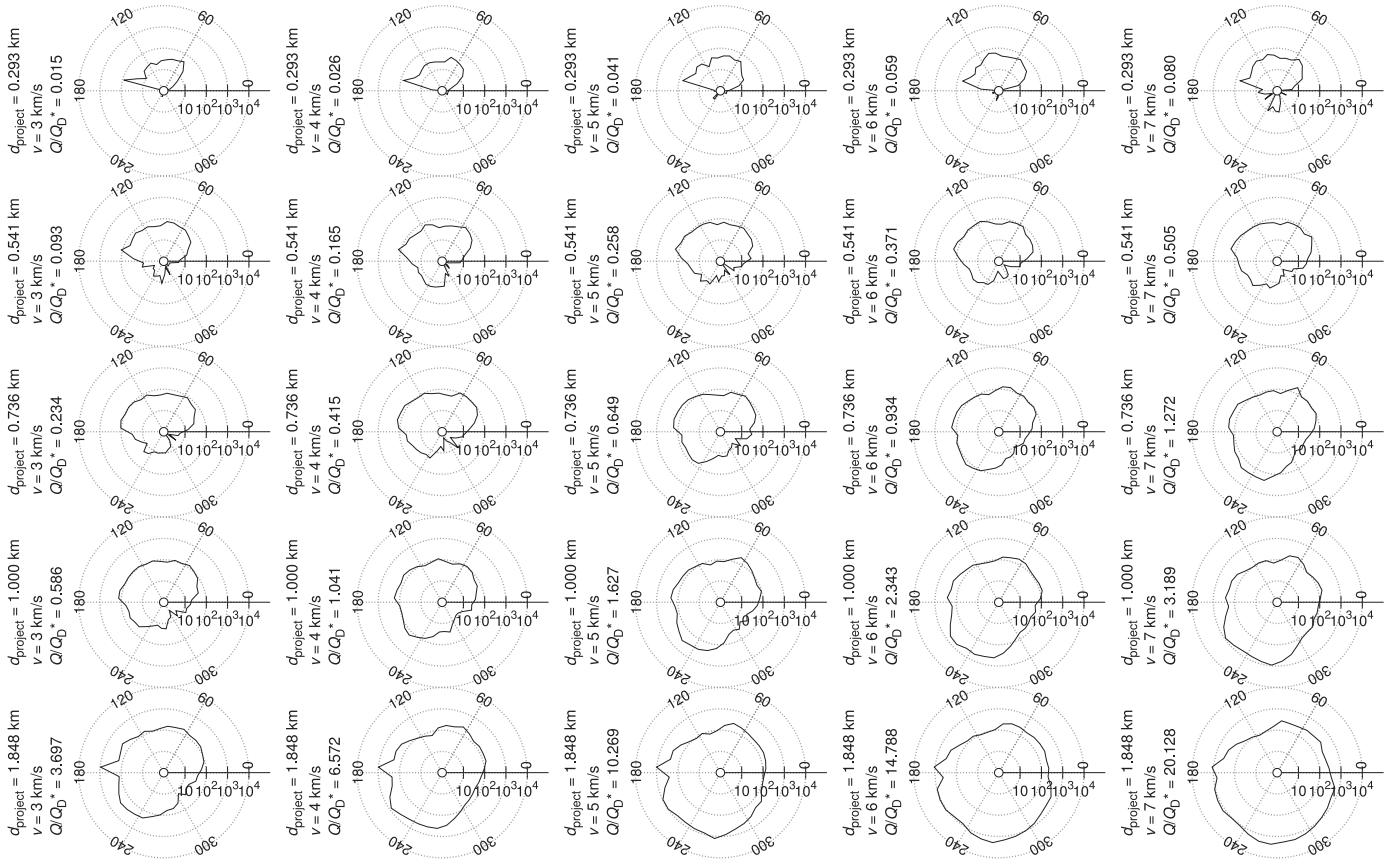

Fig. E.22. Impact angle 75°.

References

Asphaug, E., Collins, G., Jutzi, M., 2015. Global scale impacts. Asteroids IV 661–677. doi:10.2458/azu_uapress_9780816530595-ch034.

Benavidez, P.G., Durda, D.D., Enke, B.L., Bottke, W.F., Nesvorný, D., Richardson, D.C., Asphaug, E., Merline, W.J., 2012. A comparison between rubble-pile and monolithic targets in impact simulations: application to asteroid satellites and family size distributions. Icarus 219, 57–76. doi:10.1016/j.icarus.2012.01.015.

Benz, W., Asphaug, E., 1994. Impact simulations with fracture. I - Method and tests. Icarus 107, 98. doi:10.1006/icar.1994.1009.

Benz, W., Asphaug, E., 1999. Catastrophic disruptions revisited. Icarus 142, 5–20. doi:10.1006/icar.1999.6204.

Cibulková, H., Brož, M., Benavidez, P.G., 2014. A six-part collisional model of the main asteroid belt. Icarus 241, 358–372. doi:10.1016/j.icarus.2014.07.016.

Cossins, P.J., 2010. The Gravitational Instability and its Role in the Evolution of Protostellar and Protoplanetary Discs. University of Leicester Ph.D. thesis.

Davis, D.R., Ryan, E.V., 1990. On collisional disruption: experimental results and scaling laws. Icarus 83 (1), 156–182. doi:10.1016/0019-1035(90)90012-X.

Diehl, S., Rockefeller, G., Fryer, C.L., Riethmiller, D., Statler, T.S., 2012. Generating optimal initial conditions for smooth particle hydrodynamics simulations. ArXiv e-prints.

Durda, D.D., Bottke, W.F., Nesvorný, D., Enke, B.L., Merline, W.J., Asphaug, E., Richardson, D.C., 2007. Size-frequency distributions of fragments from SPH/N-body simulations of asteroid impacts: comparison with observed asteroid families. Icarus 186, 498–516. doi:10.1016/j.icarus.2006.09.013.

Grady, D., Kipp, M., 1980. Continuum modelling of explosive fracture in oil shale. Int. J. Rock Mech. Min. Sci. Geomech. Abstr. 17 (3), 147–157. doi:10.1016/0148-9062(80)91361-3.

Herant, M., 1994. Memorie della Società Astronomia Italiana 65, 1013.

Herrmann, W., 1969. Constitutive equation for the dynamic compaction of ductile porous materials. J. Appl. Phys. 40 (6), 2490–2499. doi:10.1063/1.1658021.

Hirayama, K., 1918. Groups of asteroids probably of common origin. AJ 31, 185–188. doi:10.1086/104299.

Jaeger, J., Cook, N., Zimmerman, R., 2007. Fundamentals of Rock Mechanics. Wiley.

Jutzi, M., Holsapple, K., Wünneman, K., Michel, P., 2015. Modeling asteroid collisions and impact processes. Asteroids IV.

Leinhardt, Z.M., Stewart, S.T., 2012. Collisions between gravity-dominated bodies. I. outcome regimes and scaling laws. Astrophys. J. 745, 79. doi:10.1088/0004-637X/745/1/79.

Michel, P., Benz, W., Paolo, T., Richardson, D.C., 2001. Collisions and gravitational reaccumulation: forming asteroid families and satellites. Science 294 (5547), 1696–1700. doi:10.1126/science.1065189. http://www.sciencemag.org/content/294/5547/1696.full.pdf

Michel, P., Benz, W., Richardson, D.C., 2003. Disruption of fragmented parent bodies as the origin of asteroid families. Nature 421, 608–611.

Michel, P., Benz, W., Richardson, D.C., 2004. Catastrophic disruption of pre-shattered parent bodies. Icarus 168, 420–432. doi:10.1016/j.icarus.2003.12.011.

Michel, P., Jutzi, M., Richardson, D.C., Benz, W., 2011. The asteroid veritas: an intruder in a family named after it? Icarus 211, 535–545. doi:10.1016/j.icarus.2010.10.012.

Michel, P., Tanga, P., Benz, W., Richardson, D.C., 2002. Formation of asteroid families by catastrophic disruption: simulations with fragmentation and gravitational reaccumulation. Icarus 160 (1), 10–23. doi:10.1006/icar.2002.6948.

von Mises, R., 1913. Mechanik der festen krper im plastisch- deformablen zustand. Nachrichten von der Gesellschaft der Wissenschaften zu Gttingen, Mathematisch-Physikalische Klasse 1913, 582–592.

Monaghan, J., Gingold, R., 1983. Shock simulation by the particle method SPH. J. Comput. Phys. 52 (2), 374–389. doi:10.1016/0021-9991(83)90036-0.

Morbidelli, A., Bottke, W.F., Nesvorný, D., Levison, H.F., 2009. Asteroids were born big. Icarus 204, 558–573. doi:10.1016/j.icarus.2009.07.011.

Nakamura, A., Fujiwara, A., 1991. Velocity distribution of fragments formed in a simulated collisional disruption. Icarus 92, 132–146. doi:10.1016/0019-1035(91)90040-Z.

Nesvorný, D., Brož, M., Carruba, V., 2015. Identification and dynamical properties of asteroid families. Asteroids IV.

Nesvorný, D., Enke, B.L., Bottke, W.F., Durda, D.D., Asphaug, E., Richardson, D.C., 2006. Karin cluster formation by asteroid impact. Icarus 183, 296–311. doi:10.1016/j.icarus.2006.03.008.

Press, W.H., Teukolsky, S.A., Vetterling, W.T., Flannery, B.P., 1992. Numerical recipes in FORTRAN. the art of scientific computing.

Price, D.J., 2008. Modelling discontinuities and Kelvin Helmholtz instabilities in SPH. J. Comput. Phys. 227, 10040–10057. doi:10.1016/j.jcp.2008.08.011.

Price, D.J., 2012. Smoothed particle hydrodynamics and magnetohydrodynamics. J. Comput. Phys. 231, 759–794. doi:10.1016/j.jcp.2010.12.011.

Richardson, D.C., Quinn, T., Stadel, J., Lake, G., 2000. Direct large-Scale N-Body simulations of planetesimal dynamics. Icarus 143, 45–59. doi:10.1006/icar.1999.6243.

Rosswog, S., 2009. Astrophysical smooth particle hydrodynamics. New A Rev. 53, 78–104. doi:10.1016/j.newar.2009.08.007.

Rosswog, S., 2015. Boosting the accuracy of SPH techniques: Newtonian and special-relativistic tests. Mon. Not. R. Astron. Soc. 448, 3628–3664. doi:10.1093/mnras/stv225.

Tillotson, J.H., 1962. Metallic equations of state for hypervelocity impact. Gen. Atomic Rep. GA-3216.

Weibull, W., 1939. A statistical theory of the strength of materials. Generalstabens litografiska anstalts förlag.

— Chapter v —

ROTATING TARGETS AND ANGULAR MOMENTUM TRANSFER

All asteroids have a non-zero spin rate. The rotation state is modified over time by sub-catastrophic impacts, radiation forces [Rubincam, 2000; Ćuk and Burns, 2005], or tidal interactions. However, there is no mechanism to efficiently dissipate the angular momentum, hence we currently observe only about ∼800 asteroids with a rotation period above $P = 10$ days, such as (253) Mathilde with $P \simeq 17$ days [Mottola et al., 1995]. Our previous work, as well as most of the other impact studies, did not consider pre-impact rotation of the target body, though. A static target greatly simplifies the numerical model and reduces the number of free parameters, which is why non-rotating bodies are generally preferred. However, the mean rotational period of $D = 10\,\mathrm{km}$ asteroids is about $P \simeq 6\,\mathrm{h}$ [Pravec and Harris, 2000]. One can presume that rotation does not play a major role, given the speed of revolution is much lower than the speed of impact or ejection, however, this assumption has not been thoroughly scrutinized before. We analyze the effect of rotation in this chapter.

5.1 Collisions of rotating bodies

The rotation certainly affects asteroids rotating close to the spin barrier. For an asteroid with bulk density $\rho = 2700\,\mathrm{kg/m^3}$, the barrier lies at about $P \simeq 2\,\mathrm{h}$, independently of the asteroid size. Fast rotators may undergo rotational fission and split to binary asteroids [Pravec et al., 2010], even if no collision triggers mass ejection. It is clear that for fast rotators, we can expect major differences in outcomes of collisions.

About 10 % of the observed asteroids are fast rotators with a rotational period below $P = 3\,\mathrm{h}$. Few asteroids even rotate super-critically, e.g. asteroid 2001 UC_5 has a rotational period of only $P \simeq 104$ seconds [Hergenrother and Whiteley, 2011]. Such fast rotation is only possible due to the cohesive strength of the body, meaning the asteroid cannot be a rubble pile (provided the derived spin rate is correct, of course). Although the rotation strongly affects critically rotating

asteroids, it is not *a priori* clear how it affects bodies with an average rotational period which is longer by a factor of 3.

Impacts also change the rotational state of the target. Subsequent cratering impacts may gradually reduce the spin rate of asteroids, as statistically more fragments are ejected in the direction of rotation, thus the fragments carry away the angular momentum of the target. This process is known as the angular momentum draining [Dobrovolskis and Burns, 1984] and it is one possible explanation of the excess of slow rotators in the Main Belt.

Rotation introduces additional parameters of the model. For simplicity, we only study impacts along the equatorial plane of the target. We distinguish *prograde* impacts in which the projectile velocity is aligned with the rotational velocity of the target, and *retrograde* impacts in which the velocity has the opposite orientation. Henceforth, we denote the prograde events with a positive value of the impact angle ϕ_{imp}, while retrograde events have negative ϕ_{imp}.

5.1.1 Numerical issues

There are major numerical issues related to SPH simulations of rotating bodies with material strength. The "vanilla" SPH code conserves the total angular momentum only for isotropic forces; once the stress tensor is introduced to the model, the angular momentum usually decreases over time, especially in simulations with coarse spatial resolution.

Johnson and Beissel [1996] identified the root of the problem. It is caused by the linear inconsistency of the smoothing kernel. They suggested scaling the kernel by per-particle factors to reduce the error. The precise correction of the smoothing kernel that allows to reconstruct linear functions without numerical errors was derived by Krongauz and Belytschko [1997] and with slight modifications also by Libersky et al. [1997] and Bonet and Lok [1999]. The kernel gradient needs to be corrected using a tensor defined in Eq. 2.58. This modification allows to properly simulate rotating bodies and it is thus commonly included in SPH codes [Schäfer et al., 2007; Lastiwka et al., 2009; Peer et al., 2017; Koschier et al., 2019].

To simulate rotating targets, it was also necessary to include self-gravity in the fragmentation phase. There are two reasons. First, the rotation of the target complicates the set-up of initial conditions. We need to ensure the constructed body is stable and does not spontaneously fracture before the impact. We discussed the initial conditions of rotating bodies in Sec. 2.9. To create robust and stable targets in hydrostatic equilibrium, self-gravity needs to be taken into account. Second, we found that the simulation of fragmentation needs to be prolonged in order to reveal rotational effects. The difference between a rotating and a static target is often quite small and an early hand-off would then convert fragments to the largest remnant regardless of their ejection speeds. To run the simulations over long time intervals, gravity can no longer be neglected.

5.1.2 Related work

Small rotating targets did not get much attention in impact studies. Most works that explored the parametric space of impact simulations simply assumed that the targets are static [Durda et al., 2007; Benavidez et al., 2012; Jutzi et al., 2019]. Collisional spin-up of targets, albeit initially non-rotating, was analyzed by Love and Ahrens [1997]. They performed SPH simulations to

test a range of target sizes, from $D_{\mathrm{km}} = 10\,\mathrm{km}$ to 1000 km, although they assumed strengthless bodies, thus avoiding the numerical issues linked with the material strength of rotating bodies.

The rotation has been already accounted for in large-scale impact simulations. Canup [2005] used an SPH code to study the origin of Pluto and Charon. She ran simulations for both non-rotating targets and targets with initial rotation. Canup [2008] then used similar methods to simulate the Moon-forming impact, studying the effect of the initial spin rate of the proto-Earth. Target rotation has also been into account by Jutzi et al. [2013] for simulations of asteroid (4) Vesta in order to explain the origin of the Rheasilvia impact basin. They have shown that the topographical patterns observed in the crater can be attributed to the Coriolis force acting on ejected fragments.

Furthermore, the effect of rotation has been examined using N-body methods. Takeda and Ohtsuki [2007] used an N-body code to model rubble-pile bodies and simulate the transfer of angular momentum from the impactor to the target. The simulations were later generalized for targets with initial rotation [Takeda and Ohtsuki, 2009]. Similarly, Ballouz et al. [2014] utilized the code `pkdgrav` to study the influence of pre-impact rotation on the strength of gravitational aggregates. Ballouz et al. [2015] then extended these studies by varying the material properties of the target.

5.2 Methods and aims

Our work mainly focused on the formation of synthetic families from impacts to rotating targets. Similarly to our previous simulations, we studied $D_{\mathrm{pb}} = 10\,\mathrm{km}$ monolithic bodies made of basalt, but we extended the parameter space and also simulated larger $D_{\mathrm{pb}} = 100\,\mathrm{km}$ bodies to determine how the influence of rotation scales with target size. Our goal was to compare the size-frequency distributions of synthetic families created by an impact to rotating targets for several initial rotational periods. As we expected that the rotation mostly affects critically rotating bodies, the initial period of targets was selected close to the spin barrier. Given a spherical body with the bulk density $\rho_0 = 2700\,\mathrm{kg/m^3}$, the critical period can be computed as [Pravec and Harris, 2000]:

$$P_{\mathrm{crit}} = \sqrt{\frac{3\pi}{G\rho_0}} \simeq 2.009\,\mathrm{h}\,. \tag{5.1}$$

We compared SFDs for three rotational states of the target: critically rotating target with $P = P_{\mathrm{crit}}$, target with the spin rate lower by one third, hence $P = 1.5P_{\mathrm{crit}}$, and a static target with $P = \infty$ for reference.

We further examined the change of the rotational state of the target. It is expected that a single sub-catastrophic impact can both increase and decrease the angular momentum of the target. However, if the target encounters a larger number of consecutive impacts at random impact angles, it is not clear what the net effect on its rotational state is. As suggested by Dobrovolskis and Burns [1984], we expected to observe a deceleration of the target, thus our goal was to quantify the amount of angular momentum draining and its dependence on impact parameters and initial spin rate of the target.

As in our previous work, we used a hybrid SPH/N-body method. However, we had to extend the code to include the stabilization phase, necessary to obtain stable initial conditions. The entire process thus has several steps:

1. generate target particles,
2. run stabilization SPH phase with the damping term given by Eq. 2.137,
3. generate impactor particles at the position given by the impact angle ϕ_{imp},
4. run the fragmentation phase using an SPH solver,
5. convert all smoothed particles to hard spheres,
6. run the reaccumulation phase using an N-body solver.

This motivated us to write a new SPH code from scratch, named `OpenSPH`. The code is open-sourced[1], hoping it will make it easier to compare and validate results with other researchers.

5.2.1 Extensions of the numerical model

The SPH method with the changes necessary to simulate rotating bodies as well as the implementation in our code has already been described in Chapter 2. Here, we summarize the main differences between `OpenSPH` and `SPH5` code, used in the previous work. Although our code contains a number of modifications and add-ons, the following changes were the most relevant for this work:

- **Lagrangian-based SPH discretization**. The set of equations solved in the code has been derived from the Lagrangian, making it more consistent and reliable compared to an *ad hoc* discretization. Although various SPH discretizations can be found in the literature, ours is the most common and thus likely to yield results comparable with other works.
- **Self-gravitation** using the Barnes-Hut algorithm. This is by far the biggest change in the code. The self-gravity allows us to set up hydrostatic equilibrium in the target and it also removes the upper limit of the integration time in the SPH phase, making it only restricted by the available computational resources.
- **Consistent bulk rotation** of bodies with material strength. The strain rate had to be computed using the correction tensor 2.58 in order to conserve the total angular momentum.
- **Artificial stress** to mitigate the tensile instability. The untreated SPH method is unstable in tension, resulting in a numerical fracture that unfortunately looks similar to the physical fracture due to crack growth.

[1]The code can be found at `https://gitlab.com/sevecekp/sph`, together with a graphical interface and documentation (as of August 2021).

- Set-up of **stable initial conditions**. We had to ensure the target body will not break up immediately after the start of the simulation, even if there was no impact.
- **Inertial forces** to confirm a self-consistency of the model. The target rotation can be easily emulated by running the simulation in a co-rotating reference frame. This way, the issues related to the conservation of the total angular momentum are avoided. Comparing simulations ran in the inertial and non-inertial frames is useful for testing that rotating bodies behave correctly in the SPH discretization.
- **N-body solver**, allowing us to run the full simulations with a single code. As the self-gravitation was already included in the code, it was relatively easy to implement an N-body solver as well. It replaces the evaluation of SPH derivatives with collision detection and a simplified "billiard ball" physics. Furthermore, by using the same algorithm for gravity computation in the fragmentation and the reaccumulation phase, we avoid potential systematic errors caused by different settings.
- **Parallelization**. The code can utilize all available CPU cores. As the present-day CPUs often have tens of cores, parallelization is essential for optimal performance of the code. It also allowed us to compute simulations in a higher resolution compared to our previous work, which was computed using a single-threaded code.

As explained above, we start each simulation with a stabilization phase to prevent undesirable oscillations of the target. During this phase, the fragmentation model is not integrated to avoid growing cracks, otherwise, the solver is the same as in the fragmentation phase. We found that the total internal energy is a good measure for determining when to end the stabilization. It oscillates as the energy is converted from internal to kinetic form and vice versa; once the oscillations are attenuated, we start the impact simulation.

For these simulations, the run time of the fragmentation phase was prolonged up to $t_{\text{handoff}} = 30\,\text{min}$ to make sure the fragments are sufficiently separated in space. While this is a considerably longer time than in our previous work, it does not imply the computation time is proportionally longer, considering the initial impact and fragmentation are the most computationally demanding parts of the run. Once the body is fragmented and the fragments start to recede, the time step is mostly limited by the CFL criterion 2.140 and the simulation progresses at a much higher pace.

Taking advantage of the improved performance of our code, we used higher resolution in our simulations and constructed targets with $N = 500\,000$ particles[2]. In this work, we do not directly compare our results to the previous work, thus we preferred a more precise solution instead of consistency.

We found that the resulting differences between the rotating and static targets are quite sensitive to the hand-off time and the parameters of the N-body solver used for the reaccumulation phase, specifically the collision and overlap handling. When two spheres collide, they are either merged to a larger sphere or undergo an inelastic bounce, losing part of their kinetic energy.

[2]Unfortunately, it is difficult to significantly increase the spatial resolution. As we perform three-dimensional simulations and the time step is further limited by CFL criterion, the computation time scales roughly as $\mathcal{O}(h^4)$; increasing the linear resolution by a factor of 2 thus implies about *sixteen* times longer computation time.

Following Michel et al. [2002], the normal and the tangential coefficient of restitution were set to $\eta_\mathrm{n} = 0.5$ and $\eta_\mathrm{t} = 1$, respectively. If merging occurs, the resulting merger is constructed so that the momentum, angular momentum, mass and volume of the collided spheres are conserved.

5.2.2 Merging parameters

Perfect merging of spheres significantly improves the performance of the code, especially in the case of cratering events, however, it is clearly a rough approximation. We avoided perfect merging used previously in the `pkdgrav` code as it substantially exaggerates the degree of reaccumulation and also creates unphysical super-critically rotating particles. In our code, two colliders are only merged if their relative velocity is lower than a certain fraction of the escape velocity:

$$v_\mathrm{rel} < \alpha_v \sqrt{\frac{2G(m_i + m_j)}{r_i + r_j}}\,, \tag{5.2}$$

where m_i, m_j are the masses, r_i, r_j are the radii and α_v is a free parameter, used to fine-tune the reaccumulation process; perfect merging corresponds to $\alpha = \infty$.

Similarly, the merging is also conditioned by a spin-rate criterion; particles can only merge if the spin rate of the merger is lower than a fraction of the breakup spin rate ω_crit:

$$\omega_\mathrm{merger} < \alpha_\omega \sqrt{\frac{G(m_i + m_j)}{r_\mathrm{merger}^3}}\,, \tag{5.3}$$

where α_ω is a free parameter, set to $\alpha = \alpha_v = \alpha_\omega$ for simplicity.

We tried to constrain the α parameter by comparing an N-body reaccumulation with the same simulation computed by the SPH solver. To do this, a catastrophic head-on impact to $D_\mathrm{pb} = 200\,\mathrm{km}$ target was first computed with the SPH solver. The intermediate state of the simulation at $t = 10\,\mathrm{min}$ was then handed over to the N-body solver and computed for various values of α. The results are shown in Fig. 5.1. To get similar patterns in the fragment cloud as in our reference SPH simulation, α has to be sufficiently low, we estimated optimal $\alpha = 0.2$ for our simulations. Occasionally, the simulation ends with fast-spinning overlapping fragments that cannot be merged due to criterion 5.3. Therefore, we always merge all overlapping particles before the construction of SFDs to avoid artifacts.

5.2.3 Code validation

We carefully checked that `OpenSPH` code calculates correct results for a number of test cases, documented in Chapter 2. As for self-gravitation, the Barnes-Hut approximation was validated using the brute-force algorithm. We also confirmed the code works as expected using well-studied N-body simulations, such as the M31–Milky Way collision [Schiavi et al., 2020].

Furthermore, we made sure that our code yields identical results as the code `SPH5` when it is configured identically, i.e. equal number of particles, same discretization of equations, no self-gravitation, same time step criteria, etc. Although there are some inherent differences between the codes (C++ vs. Fortran 77, object-oriented vs. procedural programming), we managed

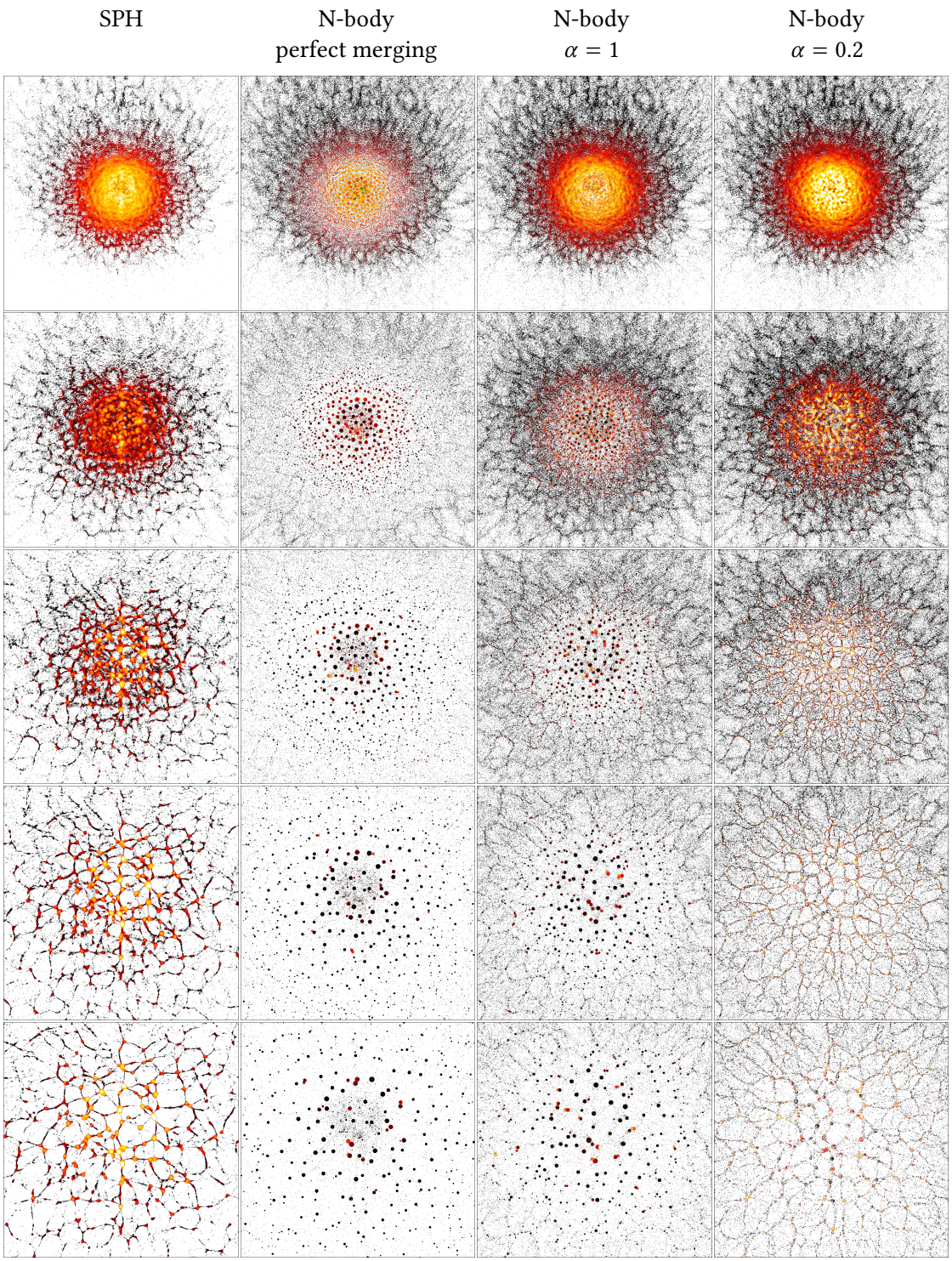

Figure 5.1: Snapshots of a reaccumulative event, comparing an SPH simulation with N-body runs for several values of the α parameter (see Eq. 5.2). The images were rendered at times $t = 50, 100, 150, 200$ and 250 min after the impact. The particle colors correspond to the local gravitational acceleration. To avoid excessive reaccumulation, α has to be as low as 0.2.

to get *almost* the same result, meaning the relative difference between the quantities of the corresponding particles was $\sim 10^{-6}$. We attribute this difference to compiler optimizations, nevertheless, this validation is certainly sufficient.

5.3 Major results

5.3.1 SFDs of static and rotating targets

We ran a matrix of simulations for all combinations of relevant parameters: the target diameters $D_{\mathrm{pb}} = 10\,\mathrm{km}$ and 100 km, the initial rotational periods of the target $P = 2\,\mathrm{h}$, 3 h and ∞, the impact energies $Q/Q^{\star}_{\mathrm{D}} = 0.1, 0.3, 1, 3$ and the impact angles $\phi_{\mathrm{imp}} = 75^{\circ}, 45^{\circ}, 15^{\circ}, -45^{\circ}, -75^{\circ}$ (from oblique prograde to oblique retrograde impacts). The impact speed was set to $v_{\mathrm{imp}} = 5\,\mathrm{km/s}$, i.e. the mean velocity for Main-belt collisions [Dahlgren, 1998], in all simulations to reduce already large parameter space.

For simulations with $D_{\mathrm{pb}} = 10\,\mathrm{km}$, we observed significant differences for targets rotating at $P = 2\,\mathrm{h}$, however, the slower $P = 3\,\mathrm{h}$ target is already similar to the static target in most runs. Rotation is the most pronounced for less energetic impacts — either impacts with a small impactor or oblique impact angles. On the other hand, the catastrophic head-on impacts produce SFDs almost independent of the initial rotational state of the target, because the energy is already sufficient to disperse >50 % of the target mass.

Our results are also predictable considering the rotation effectively decreases the strength of the target. Given that the material strength is generally less important for catastrophic impacts, it makes sense that the differences appear mostly in the cratering regime.

We can estimate the importance of the initial rotation of the target by relating the rotation angular momentum of the target and the angular momentum of the impactor with respect to the center of mass of the target. The former can be computed as the angular momentum of a homogeneous sphere:

$$L_{\mathrm{target}} = \frac{8}{15}\pi\rho R^{5}_{\mathrm{target}}\omega_{\mathrm{target}}\,. \tag{5.4}$$

The latter follows from the impact parameters:

$$L_{\mathrm{imp}} = \frac{4}{3}\pi\rho r^{3}_{\mathrm{imp}}(R_{\mathrm{target}} + r_{\mathrm{imp}})v_{\mathrm{imp}}\sin\phi_{\mathrm{imp}}\,. \tag{5.5}$$

Using $P = 3\,\mathrm{h}$, $v_{\mathrm{imp}} = 5\,\mathrm{km}$ and $\phi_{\mathrm{imp}} = 45^{\circ}$ as an example, we get $L_{\mathrm{target}}/L_{\mathrm{imp}} \simeq 0.16$ for $d_{\mathrm{imp}} = 1226\,\mathrm{m}$ and $L_{\mathrm{target}}/L_{\mathrm{imp}} \simeq 5.18$ for $d_{\mathrm{imp}} = 394\,\mathrm{m}$. This back-of-the-envelope calculation also suggests that head-on impacts are affected by rotation more than the oblique impacts, which seems to contradict our results; however, the impactor angular momentum L_{imp} should be further multiplied by an (unknown) efficiency of the angular momentum transfer, which can be positive or negative.

On the other hand, simulations with $D_{\mathrm{pb}} = 100\,\mathrm{km}$ show substantial differences between the static and rotating targets. It is consistent with the reasoning above; L_{target} is much larger than L_{imp} due to the fifth power of R_{target}. A target of such size rotating close to the spin barrier can thus completely change the impact regime from cratering to catastrophic. Nevertheless, we

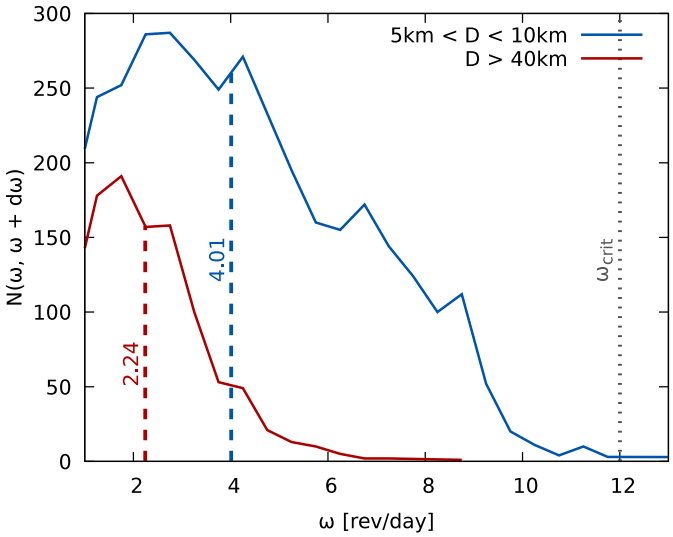

Figure 5.2: Differential histograms of asteroid spin rates in two size ranges, representing the $D = 10$ km and 100 km bodies we studied. The bin size is $\mathrm{d}\omega = 0.5$ rev/day. Vertical dashed lines show the average value for each histogram, the dotted line is an approximate position of the critical spin rate at $P = 2$ h. Data from Warner et al. [2009].

again observe a significant drop of ejected mass between the $P = 2$ and 3 h run, suggesting that targets with a spin rate well below the critical value are not overly affected by the rotation.

The rotation seems to be more relevant for collisions of larger bodies; however, the 100 km bodies in the Main Belt also have statistically lower spin rates compared to the 10 km bodies, as shown in Fig. 5.2. Although asteroids rotating close to the spin barrier exist in this size range, such as (216) Kleopatra [Ostro et al., 2000; Hirabayashi and Scheeres, 2014; Shepard et al., 2018; Brož et al., 2021], larger bodies are on average slower and thus more distant from the barrier. It is however possible that there were more fast rotators in the past, but the rotation made them more fragile and less impact resistant, which is why they are no longer observed.

5.3.2 Angular momentum transfer and mass loss

It is quite difficult to read the total mass of fragments from the SFDs. To better understand how the ejected mass depends on the initial rotation of the target, we ran a large set of simulations with $D_{\mathrm{pb}} = 10$ km that densely covered the parameter space, from fast-spinning targets with $P = P_{\mathrm{crit}}$ up to almost static targets with $P = 50P_{\mathrm{crit}}$. In total, we computed over 400 simulations. To be able to run all simulations with available computing power, we chose a lower resolution of $N = 100\,000$ particles. Here, we only focused on the largest remnant of the impact, hence the family does not have to be resolved in great detail and the coarse resolution is acceptable.

As in the previous section, we were mostly interested in the relative difference between rotating and static targets rather than absolute values. We thus quantified the simulations with the quantity μ_{ej}, defined as the ratio of the total mass of fragments in the given simulation and the total mass of fragments in the reference simulation with a static target. Using the computed

simulations, we evaluated the quantity μ_{ej} as a function of the period P, the impact angle ϕ_{imp} and the impact energy $Q/Q^{\star}_{\mathrm{D}}$.

The results confirmed our previous findings, but they also gave us concrete numbers. We found that the rotation may amplify the mass ejection by up to five times. This happens in extreme cases, namely, we observe significant mass loss amplification for oblique prograde cratering impacts to critically rotating targets. The rotation is less important for catastrophic impacts at head-on or retrograde impact angles; in such cases, $\mu_{\mathrm{ej}} \lesssim 2$.

We further averaged μ_{ej} over impact angles, taking into account the probability of impacts at a given angle. This averaged $\overline{\mu}_{\mathrm{ej}}$ can be interpreted as an average mass ejection increase for asteroids of given sizes and rotation periods, or a time-averaged effect on a single asteroid caused by a number of subsequent cratering events. This angle-averaged value shows that rotation amplifies the mass loss by up to 100 %.

Using our simulation matrix, we further computed the change of the spin rate due to impact, i.e. the difference between the spin rate of the target ω_{pb} and the largest remnant ω_{lr}. We used the spin rates ω instead of periods P to avoid the undefined period of static targets. To measure the fraction of angular momentum embedded to the target, we defined the dimensionless effectivity γ of the angular momentum transfer as:

$$\gamma = \mathrm{sgn}(\phi_{\mathrm{imp}}) \frac{L_{\mathrm{lr}} - L_{\mathrm{pb}}}{L_{\mathrm{imp}}} \,. \tag{5.6}$$

The value γ is not determined by the state just after the impact but after the very end of reaccumulation. Only the difference between the initial and the final state is relevant, thus it can be lower than 0 if the target is slowed down by a prograde impactor, and similarly, it can exceed 1 if the target loses more angular momentum than a retrograde impactor delivered.

The cratering events exhibit the expected behavior — the prograde impacts cause spin-up while the retrograde impacts cause spin-down. The only exception appears for critically rotating targets that can no longer be accelerated and therefore the impacts always slow the target down, regardless of the impact angle.

However, we saw that the outcome starts to change with increasing impact energy. For $Q/Q^{\star}_{\mathrm{D}} = 1$, the behavior appears to be reversed; prograde impacts cause strong deceleration, while the retrograde impacts tend to speed up the target's rotation. This could be due to change of the spin direction, as we only computed the absolute value of the spin rate.

The angular momentum transfer effectivity γ is generally higher for cratering impacts; it appears to be the highest for retrograde impacts to critically rotating targets, however, these targets lose the angular momentum mostly due to mass ejection and the impact regime is not very relevant. On average, the effectivity is around $\gamma \sim 0.5$. For catastrophic impacts, the effectivity is significantly lower, because the targets again lose their angular momentum by ejecting fragments.

Finally, we evaluated an angle-averaged change of the spin rate, analogously to the average mass loss. This quantity showed that an average impact to rotating targets indeed causes a deceleration. Of course, static targets cannot be decelerated anymore, hence we also observed an acceleration of slowly rotating targets. The transition between these regimes occurs around $P \sim 10 P_{\mathrm{crit}}$.

5.4 Reprint

See pages 126 to 137.

A&A 629, A122 (2019)
https://doi.org/10.1051/0004-6361/201935690
© ESO 2019

Astronomy & Astrophysics

Impacts into rotating targets: angular momentum draining and efficient formation of synthetic families

P. Ševeček[1], M. Brož[1], and M. Jutzi[2]

[1] Institute of Astronomy, Charles University, Prague, V Holešovičkách 2, 18000 Prague 8, Czech Republic
e-mail: sevecek@sirrah.troja.mff.cuni.cz
[2] Physics Institute, University of Bern, NCCR PlanetS, Sidlerstrasse 5, 3012 Bern, Switzerland

Received 13 April 2019 / Accepted 7 August 2019

ABSTRACT

About 10% of the observed asteroids have rotational periods lower than $P = 3$ h and seem to be relatively close to the spin barrier. Yet, the rotation has often been neglected in simulations of asteroid collisions. To determine the effect of rotation, we performed a large number of impact simulations with rotating targets. We developed a new unified smoothed particle hydrodynamics and N-body code with self-gravity, suitable for simulations of both fragmentation phase and gravitational reaccumulation. The code has been verified against previous ones, but we also tested new features, such as rotational stability, tensile stability, etc. Using the new code, we ran simulations with $D_{\rm pb} = 10$ and 100 km monolithic targets and compared synthetic asteroid families created by these impacts with families corresponding to non-rotating targets. The rotation affects mostly cratering events at oblique impact angles. The total mass ejected by these collisions can be up to five times larger for rotating targets. We further computed the transfer of the angular momentum and determined conditions under which impacts accelerate or decelerate the target. While individual cratering collisions can cause both acceleration and deceleration, the deceleration prevails on average. Collisions thus cause a systematic spin-down of the asteroid population.

Key words. minor planets, asteroids: general – methods: numerical

1. Asteroid collisions in the main belt

The main belt of asteroids is a collisional system. The breakups of asteroids have been recorded in the form of asteroid families (Nesvorný et al. 2015; Vinogradova 2019). We can also see impact features, such as craters or boulders, on surfaces of asteroids. These features can be observed directly during a satellite flyby or even with ground-based instruments (Vernazza et al. 2018; Fétick et al. 2019).

Physical processes during asteroid collisions are rather complicated for purely analytical estimates to yield precise quantitative results, as it is necessary to model a propagation of shock wave in the target, crack growth and consequent fragmentation, gravitational reaccumulation of ejected fragments, etc. Fragmentation of targets due to hyper-velocity impacts has been studied using laboratory experiments (Nakamura & Fujiwara 1991; Morris & Burchell 2017; Wickham-Eade et al. 2018). While the experiments can produce valuable constraints, the results cannot be directly compared with the breakups of asteroids, as the sizes of targets and kinetic energies of the impact would have to be extrapolated over several orders of magnitude. Experiments also do not take into account a gravitational reaccumulation. The collisions of asteroids are therefore commonly studied using numerical methods; the experiments then provide the calibration for the respective numerical codes.

Common methods for studying the collisions can be divided into particle-based (for example the N-body code `pkdgrav`, see Richardson et al. 2000) and shock-physics ones, such as mesh-based methods (used by code `iSALE`, see Suetsugu et al. 2018), or the smoothed particle hydrodynamics (Jutzi et al. 2015), used in this work. This is a Lagrangian, gridless method, which makes it suitable for impact simulations, as the computational domain is not a priori known. Especially in a hit-and-run impact, fragments of the projectile can travel to considerable distances from the target. In the smoothed particle hydrodynamics (SPH), the distant fragments do not require any special handling (they only might affect the performance of the code). SPH is also versatile, allowing the relatively easy implementation of new physics. The model of fragmentation can be straightforwardly incorporated into SPH, but it would be a difficult task for grid-based methods.

An outcome of a collision depends on a number of parameters, namely the diameter $D_{\rm pb}$ of the target, the diameter $d_{\rm imp}$ of the projectile, the specific impact energy Q, the impact angle $\phi_{\rm imp}$, but also the rotational periods of the colliding bodies, their shapes, material properties, etc. For completeness, we should also include parameters introduced by the numerical scheme, such as the spatial resolution, the time step, the artificial viscosity $\Pi_{\rm AV}$, etc. The extent of this parameter space prohibits a thorough analysis of every collision as a function of all the mentioned parameters, we thus have to restrict ourselves to a particular set of simulations, varying some parameters and keeping the others constant.

Asteroidal targets have been considered non-rotating in most previous studies of asteroid families (Durda et al. 2007; Benavidez et al. 2012; Ševeček et al. 2017; Benavidez et al. 2018; Jutzi et al. 2019). Jutzi et al. (2013) considered a rotating Vesta, though rotating bodies have also been studied by Jutzi & Benz (2017). Ćuk & Stewart (2012) and Canup (2008) take the rotation into account for simulations of the Moon-forming impact and Canup (2005) for the impact event forming Pluto and Charon.

Ballouz et al. (2015) used an N-body code to simulate collisions of rotating rubble-pile asteroids, while Takeda & Ohtsuki (2007, 2009) studied the angular momentum transfer for both stationary and rotating rubble-piles. In this work, we study formation of asteroid families from monolithic targets, extending the parameters of the simulation by the initial rotational period $P_{\rm pb}$ of the target, including cases close to the spin barrier.

The paper is organized as follows. In Sect. 2, we describe our numerical model. Section 3 analyzes differences between synthetic families created from parent bodies with various rotational periods. Section 4 is focused on largest remnants, specifically on their accelerations or decelerations and the angular momentum transfer. Finally, we summarize our results in Sect. 5.

2. Numerical model

We developed a new SPH and N-body code. The code is publicly available, see Appendix C. In this section, we do not attempt to present a thorough review of the SPH method (as e.g., Cossins 2010), but instead we summarize the exact equations used in the code, emphasizing the modifications introduced in order to properly deal with rotating bodies.

2.1. Equations

The set of hydrodynamical equations is solved with a smoothed particle hydrodynamics (Monaghan 1985). The continuum is discretized into particles comoving with the continuum, with the density profile of the particles given by a kernel W, which is a cubic spline in our case:

$$W(r,h) = \frac{\sigma}{h^3}\begin{cases} \frac{1}{4}(2-q)^3 - (1-q)^3, & 0 \le q < 1, \\ \frac{1}{4}(2-q)^3, & 1 \le q < 2, \\ 0 & q \ge 2, \end{cases} \tag{1}$$

where $q \equiv r/h$.

Below, we denote indices of particles with Latin subscripts (usually i, j, ...), the components of vector and tensor quantities with Greek superscripts (usually α, β, ...). We also use Einstein notation to sum over components (but not for particles).

The equation of motion for ith particle reads:

$$\frac{\mathrm{d}v_i^\alpha}{\mathrm{d}t} = \sum_j m_j \left(\frac{\sigma_i^{\alpha\beta}}{\rho_i^2} + \frac{\sigma_j^{\alpha\beta}}{\rho_j^2} + \Pi_{ij}\delta^{\alpha\beta} + \zeta_{ij}^{\alpha\beta} f^n \right) \frac{\partial W_{ij}}{\partial x^\beta} + \nabla\Phi - [\boldsymbol{\omega} \times (\boldsymbol{\omega} \times \boldsymbol{r}_i)]^\alpha - [2\boldsymbol{\omega} \times \boldsymbol{v}_i]^\alpha , \tag{2}$$

where $\sigma^{\alpha\beta} = -P\delta^{\alpha\beta} + S^{\alpha\beta}$ is the total stress tensor, Π is the artificial viscosity (Monaghan & Gingold 1983), $\zeta^{\alpha\beta} f^n$ is the artificial stress (Monaghan 2000), Φ is the gravitational potential (including both external fields and self-gravity of particles), and $\boldsymbol{\omega}$ is the angular velocity of the reference frame.

The respective terms in the Eq. (2) correspond to the stress divergence, gravitational acceleration, centrifugal force, and Coriolis force. Inertial forces are only applied if the simulation is carried out in a non-inertial reference frame, corotating with the target asteroid (see Appendix B).

We used the standard artificial viscosity with linear and quadratic velocity divergence terms and coefficients $\alpha_{\rm AV}$ and $\beta_{\rm AV}$, respectively. This term is essential for a proper shock propagation and thus was always enabled in our simulations. Optionally, the code allows enabling the Balsara switch (Balsara 1995), which reduces the artificial viscosity in shear motions in order to reduce an unphysical angular momentum transfer. Additionally, the code includes the artificial stress term $\zeta^{\alpha\beta} f^n$, which reduces the tensile instability, meaning an unphysical clustering of particles due to negative pressure. We tested the effects of this term using the "colliding rubber cylinders" test (cf. Schäfer et al. 2016).

We used a different discretization of the equation than in Ševeček et al. (2017), as we found the above equation to be more robust, avoiding a high-frequency oscillation in the pressure field. This is a recurring problem in high-velocity impact simulations and while it can be suppressed by a larger kernel support, additional modifications of the method have been suggested to address the issue, for example the δ-SPH modification (Marrone et al. 2011). The density is evolved using the continuity equation:

$$\frac{\mathrm{d}\rho_i}{\mathrm{d}t} = \sum_j m_j \frac{\partial v_i^\alpha}{\partial x^\alpha} . \tag{3}$$

We solved the evolution equation instead of direct summation of particle masses to avoid the artificial low-density layer at the surface of the asteroid (Reinhardt & Stadel 2017). The velocity gradient at the right-hand side of Eq. (3) is computed as:

$$\rho_i \frac{\partial v_i^\alpha}{\partial x^\beta} = \sum_j m_j (v_j^\alpha - v_i^\alpha)\, C_i^{\beta\gamma} \frac{\partial W_{ij}}{\partial x^\gamma}, \tag{4}$$

where the correction tensor $C^{\alpha\beta}$ is defined as (Schäfer et al. 2016):

$$C_i^{\alpha\beta} \equiv \left[\sum_j \frac{m_j}{\rho_j} (r_j^\alpha - r_i^\alpha) \frac{\partial W_{ij}}{\partial x^\beta} \right]^{-1} . \tag{5}$$

In the case the bracketed matrix was not invertible, we used the Moore–Penrose pseudo-inverse instead. The correction tensor is further set to 1 for fully damaged material.

The correction tensor has been introduced to tackle the linear inconsistency of the standard SPH formulation. It is a fundamental term in the velocity gradient that allows for a stable bulk rotation of the simulated body and significantly improves the conservation of the total angular momentum. We evolved the internal energy u using the energy equation:

$$\frac{\mathrm{d}u_i}{\mathrm{d}t} = -\frac{\sigma^{\alpha\beta}}{\rho_i} \frac{\partial v_i^\alpha}{\partial x^\beta} + \sum_j \frac{1}{2} m_j \Pi_{ij} \left(v_i^\alpha - v_j^\alpha \right) \frac{\partial W_{ij}}{\partial x^\alpha} + \sum_j \frac{1}{2} m_j \zeta_{ij}^{\alpha\beta} f^n \left(v_i^\beta - v_j^\beta \right) \frac{\partial W_{ij}}{\partial x^\alpha} . \tag{6}$$

In this equation the velocity gradient is also corrected by the tensor $C^{\alpha\beta}$. While this is required for a consistent handling of rotation, the inequality of kernel gradients used in the energy equation (Eq. (6)) and in the equation of motion (Eq. (2)) implies the total energy is generally not conserved in the simulations. This is usually not an issue, as the total energy does not increase by more than 5%.

However, in some cases (e.g., weak cratering impacts or exceedingly long integration time), the energy growth can be prohibitive. For such cases, the code also offers an alternative way to evolve the internal energy, using a compatibly-differenced scheme (Owen 2014). Instead of computing the energy derivative, the energy change is computed directly from particle pairwise accelerations a_{ij}^α and half-step velocities $w_i^\alpha = v_i^\alpha + \frac{1}{2} a_i^\alpha \Delta t$, using the equation:

$$\Delta u_i = \sum_j f_{ij} \left(w_j^\alpha - w_j^\beta \right) a_{ij}^\alpha \Delta t, \tag{7}$$

where the energy partitioning factors f_{ij} can be chosen arbitrarily, provided they fulfill constraint $f_{ij} + f_{ji} = 1$. With this form of SPH, the total energy can be conserved to machine precision, at a cost of performance overhead. However, this does not solve the inconsistency mentioned above.

The listed set of equations is supplemented by the Tillotson equation of state (Tillotson 1962). To close the set of equations, we have to specify the constitutive equation. We used the Hooke's law, evolving the deviatoric stress tensor in time using:

$$\frac{\mathrm{d}S_i^{\alpha\beta}}{\mathrm{d}t} = 2\mu\left(\frac{\partial v_i^\alpha}{\partial x^\beta} - \frac{1}{3}\delta^{\alpha\beta}\frac{\partial v_i^\gamma}{\partial x^\gamma}\right), \tag{8}$$

where μ denotes the shear modulus. To account for plasticity of the material, we further used the von Mises criterion, which reduces the deviatoric stress tensor by the factor:

$$f = \min\left[\frac{Y_0^2(1-u/u_{\mathrm{melt}})^2}{\frac{3}{2}S^{\alpha\beta}S^{\alpha\beta}}, 1\right], \tag{9}$$

where Y_0 is the yield stress and u_{melt} is the specific melting energy. While more complex, pressure-dependent rheology models exist (Jutzi et al. 2015), von Mises rheology is reasonable for monolithic asteroids and still consistent with laboratory experiments (Remington et al. 2018). The effects of friction have been studied by Jutzi et al. (2015) or Kurosawa & Genda (2018) so we do not discuss such effect in this work.

Additionally, we integrated the fragmentation model to model an activation of flaws and a propagation of fractures in the material. Following Benz & Asphaug (1994), we define a scalar quantity damage D, modifying the total stress tensor as

$$\sigma_D^{\alpha\beta} = -(1 - DH(-P))\,P\delta^{\alpha\beta} + (1-D)S^{\alpha\beta}, \tag{10}$$

where $H(x)$ is the Heaviside step function. A fully damaged material ($D = 1$) has no shear nor tensile strength, it only resists compressions.

Smoothing lengths of particles are evolved to balance the changes of particle concentration. We thus derived the equation directly from the continuity equation:

$$\frac{\mathrm{d}h_i}{\mathrm{d}t} = \frac{h_i}{3}\frac{\partial v_i^\alpha}{\partial x^\alpha}. \tag{11}$$

Since it is also an evolution equation, we need to specify the initial conditions for smoothing lengths:

$$h = \eta\left(\frac{V}{N}\right)^{\frac{1}{3}}, \tag{12}$$

where V is the volume of the body, N is the number of particles in the body and η is a free non-dimensional parameter, which we set to $\eta = 1.3$. This corresponds to an average number of neighboring particles $N_{\mathrm{neigh}} \simeq 65$.

2.2. Gravity

Beyond hydrodynamics, the code also computes accelerations of SPH particles due to self-gravity. To compute it efficiently (albeit approximately), we employed the Barnes-Hut algorithm (Barnes & Hut 1986). Instead of computing pair-wise interactions of particles, we first clustered the particles hierarchically and evaluated gravitational moments of particles in each node of the constructed tree. The accelerations were then computed by a tree-walk; if the evaluated node was distant enough, the acceleration could be approximated by evaluating the multipole moments up to the octupole order, otherwise we descended into child nodes. The precision of the method is controlled by an opening radius r_{open}. For an extensive description of the method, see Stadel (2001).

As our SPH particles are spherically symmetric, they can be replaced by point masses, provided they do not intersect each other (the corresponding kernel W_{ij} is zero). However, it is absolutely necessary to account for softening of the gravitational potential for neighboring particles. We follow Cossins (2010) by introducing a gravitational softening kernel ϕ (associated with the SPH smoothing kernel W) using the equation:

$$\frac{\partial\phi}{\partial r} = \frac{4\pi}{r}\int_0^r r'^2 W(r')\,\mathrm{d}r' + \frac{h}{r^2}. \tag{13}$$

The gravitational kernel ϕ corresponding to our M4 spline kernel W is then:

$$\phi(r,h) = \begin{cases} \frac{2}{3}q^2 - \frac{3}{10}q^4 + \frac{1}{10}q^5 - \frac{7}{5}, & 0 \le q < 1, \\ \frac{4}{3}q^2 - q^3 + \frac{3}{10}q^4 - \frac{1}{10}q^5 & \\ \qquad -\frac{8}{5} + \frac{1}{15q}, & 1 \le q < 2, \\ -\frac{1}{q}, & q \ge 2, \end{cases} \tag{14}$$

where $q \equiv r/h$. However, this kernel does not have compact support.

2.3. Temporal discretization

Using derivatives computed at each time step, the equations were integrated using explicit timestepping. The scheme used in this work is the predictor-corrector, however other schemes are implemented in the code, such as the leapfrog, fourth order Runge–Kutta, or Bulirsch–Stoer.

The value of the time step is determined by the Courant–Friedrichs–Lewy (CFL) criterion:

$$\Delta t \le C_{\mathrm{CFL}} \min_i \frac{h_i}{c_{\mathrm{s}}}, \tag{15}$$

where h_i is the smoothing length of ith particle, c_{s} the local sound speed, and C_{CFL} is the Courant number. In our simulations, we usually used $C_{\mathrm{CFL}} = 0.25$, as higher values can lead to instabilities in some cases. Moreover, we restricted the time step by the value-to-derivative ratio of all time-dependent quantities in the simulation to control the discretization errors. The upper limit of the time step is therefore:

$$\Delta t \le C_{\mathrm{d}}\frac{|x| + s_x}{|\dot{x}|}, \tag{16}$$

where s_x is a parameter with the same dimensions as x, assigned to each quantity in order to avoid zero time step if the quantity x is zero. Constant C_{d} is 0.2 for all quantities.

2.4. Equilibrium initial conditions

Setting up the initial conditions for the impact simulation is not a trivial task. It is necessary to assign a particular value to the density ρ, internal energy u, and deviatoric stress tensor S to each particle, so that the configuration is stable when the impact simulation starts and the particles do not oscillate.

This problem is not restricted to simulations with rotating targets. A proper handling of initial conditions is essential in simulations of the Moon formation, collisions of planetary embryos,

etc. If neglected, the initial gravitational compression would introduce macroscopic radial oscillations in the target.

For small and stationary asteroids with $D \simeq 10$ km, the self-gravity is much less important, in fact it was often completely neglected during the fragmentation phase (as in Ševeček et al. 2017). These asteroids are assumed to be undifferentiated, hence it was reasonable to set up a homogeneous bulk density of $\rho_0 =$ const. For these stationary targets, the stress tensor of particles is zero in equilibrium.

For rotating targets, however, such initial conditions are unstable due to the emerged centrifugal force (in the corotating frame). To prevent any unphysical fractures in the target, the configuration of particles has to be set up carefully, especially for asteroids rotating close to the critical spin rate. For this reason, we run a stabilization phase before the actual impact simulation, with an artificial damping of particle velocities:

$$\boldsymbol{v}_{\mathrm{damp}} = \frac{\boldsymbol{v} - \boldsymbol{\omega} \times \boldsymbol{r}}{1 + \delta \Delta t} + \boldsymbol{\omega} \times \boldsymbol{r}, \tag{17}$$

where $\boldsymbol{v}$ is the undamped velocity, $\boldsymbol{\omega}$ the angular frequency of the target, $\boldsymbol{r}$ the position vector of the particle, δ an arbitrary damping coefficient (gradually being decreased during the stabilization phase), and Δt the actual time step. In this equation, we need to subtract and re-add the bulk rotation velocity, otherwise the damping would cause the target to slow down. We also did not integrate the fragmentation model during this phase, as the oscillations of the particles might damage the target prematurely.

While more general approaches for setting up the initial conditions exist (Reinhardt & Stadel 2017), the presented method is simple, robust, and sufficient for our purposes. A disadvantage of our method is a significant computational overhead, as for some simulations the time needed to converge into a stable solution is comparable to the duration of the actual impact simulation. However, here we performed many simulations with fixed target diameter D_{pb} and period P, so we had to precompute the initial conditions only once and then used the cached particle configuration for other runs.

2.5. Reaccumulation phase

As our numerical model contains both the hydrodynamics and the gravitational interactions, it could be used for the entire simulation – from the stabilization, pre-impact flight, fragmentation phase until the gravitational reaccumulation of all fragments. However, the time step is often severely limited by the CFL criterion (Eq. (15)).

We can increase the time step by several orders of magnitude and hence speed up the simulation considerably by changing the numerical scheme from SPH to N-body integration. This is a common approach in studies of asteroid families (Durda et al. 2007; Michel et al. 2015; Ševeček et al. 2017; Jutzi et al. 2019). Once the target is fully fractured and the fragments start to recede, we converted all SPH particles into hard spheres and replaced the complexity of hydrodynamic equations with a simple collision detection. This allows us to overcome the time step limitation.

We further optimized the simulation by merging the collided particles into larger spheres. By doing so, we lost information about the shape of the fragments; to preserve the shapes, it is necessary to either form rigid aggregates of particles instead of mergers (Michel & Richardson 2013), or simulate the entire reaccumulation using the SPH (as in Sugiura et al. 2018). Here, as we are mainly interested in distribution of sizes and rotational periods, merging the particles is thus a viable option.

Merging not only affects the shape, but also the dynamics of fragments. As it modifies the moment of inertia, the merger has a generally different rotational period than a real non-spherical fragment would have. Merging also removes higher gravitational moments, thus altering motion of near fragments. This is a slight limitation of the presented model.

Hard spheres are created directly from SPH particles. Their mass is unchanged, and the radius of the formed spheres is computed as:

$$r_i = \sqrt[3]{\frac{3m_i}{4\pi\rho_i}}, \tag{18}$$

so that the volume of spheres is equal to the volume of SPH particles. As the total volume is conserved, created spheres inevitably overlap. Appendix A describes how the code handles such overlaps.

When two spheres collide, they are merged only if their relative speed is lower than the mutual escape speed

$$v < v_{\mathrm{esc}} \equiv \sqrt{\frac{2G(m_i + m_j)}{r_i + r_j}} \tag{19}$$

and if the rotational angular frequency of the merger does not exceed the critical frequency

$$\omega < \omega_{\mathrm{crit}} \equiv \sqrt{\frac{G(m_i + m_j)}{r_{\mathrm{merger}}^3}}\,. \tag{20}$$

In this way we prevent formation of unphysically fast rotators. If any of these conditions is not fulfilled, particles undergo an inelastic bounce. The damping of velocities is determined by the normal η_{n} and tangential η_{t} coefficient of restitution, which we set to 0.5 and 1, respectively.

When merging the particles, we determined the mass, radius, velocity, and angular frequency of the merger, so that the total mass, volume, momentum, and angular momentum are conserved. As the tangential components of velocities are not damped by a bounce, merging is the only way to spin up fragments in our simulations.

3. Synthetic families created from rotating targets

To better understand how the rotation influences impact events, we decided to compute a matrix of simulations for various impact parameters. We ran simulations for two different target sizes, $D_{\mathrm{pb}} = 10$ km and $D_{\mathrm{pb}} = 100$ km, in order to ascertain the scaling of the rotational effect. We tested head-on impacts, having the impact angle $\phi_{\mathrm{imp}} = 15°$, the intermediate cases with $\phi_{\mathrm{imp}} = 45°$, and oblique impacts with $\phi_{\mathrm{imp}} = 75°$. We have to further distinguish prograde events, meaning impacts where the orbital velocity has the same direction as the impact velocity, and retrograde events, where the orbital velocity has the opposite direction. In the following, the prograde impacts have positive values of impact angles, while the retrograde impacts have negative values.

In all of our simulations, we set the impact velocity to $v_{\mathrm{imp}} = 5\,\mathrm{km\,s^{-1}}$, which is close to the mean velocity for Main-belt collisions (Dahlgren 1998). The simulation matrix covers both the cratering and the catastrophic events. We ran simulations with relative impact energies $Q/Q_{\mathrm{D}}^{\star} = 0.1, 0.3, 1$, and 3, where the critical energy $Q_{\mathrm{D}}^{\star}$ is given by the scaling law of Benz & Asphaug (1999). As $Q_{\mathrm{D}}^{\star}$ is defined as the specific impact energy (relative

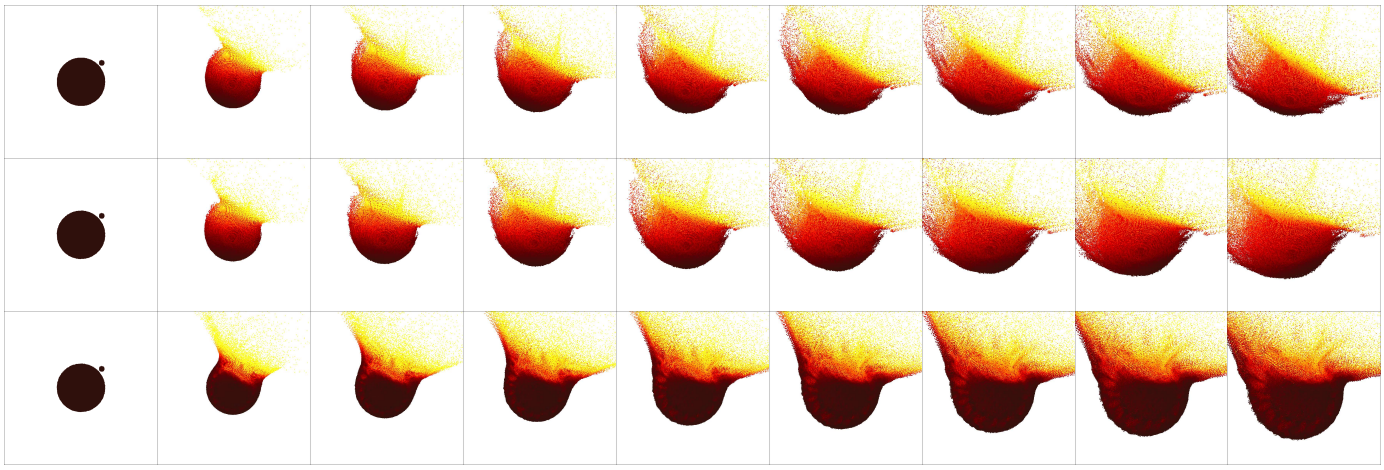

Fig. 1. Impacts into $D_{\rm pb} = 100$ km targets without rotation (*first row*), rotational period $P_{\rm pb} = 3$ h (*second row*), and $P_{\rm pb} = 2$ h (*third row*). The period of two hours is approximately the critical period of the target. The color brightness corresponds to specific internal energy of the particles.

Table 1. Material parameters used in simulations.

Density at zero pressure	$\rho = 2700\,\mathrm{kg\,m^{-3}}$
Bulk modulus	$A = 2.67 \times 10^{10}$ Pa
Non-linear Tillotson term	$B = 2.67 \times 10^{10}$ Pa
Sublimation energy	$u_0 = 4.87 \times 10^8\,\mathrm{J\,kg^{-1}}$
Energy of incipient vaporization	$u_{\rm iv} = 4.72 \times 10^6\,\mathrm{J\,kg^{-1}}$
Energy of complete vaporization	$u_{\rm cv} = 1.82 \times 10^7\,\mathrm{J\,kg^{-1}}$
Shear modulus	$\mu = 2.27 \times 10^{10}$ Pa
Von Mises elasticity limit	$Y_0 = 3.50 \times 10^9$ Pa
Melting energy	$u_{\rm melt} = 3.4 \times 10^6\,\mathrm{J\,kg^{-1}}$
Weibull coefficient	$k = 4.00 \times 10^{29}$
Weibull exponent	$m = 9$

to mass of the target) required to eject 50% of the target's mass as fragments, it necessarily depends on the rotational period of the target. However, we consider $Q^\star_{\rm D}$ to be independent of rotation and used the same value for all performed simulations, as it provides a convenient dimensionless measure of the impact energy.

We assume that both the target and the impactor are monolithic bodies, the material parameters are summarized in Table 1. The spatial resolution of the target was approximately $N = 500\,000$ SPH particles and the number of projectile particles was selected to match the particle density of the target. Three simulations with different periods $P_{\rm pb}$ are shown in Fig. 1.

3.1. Coordinate system

Due to the rotation, the impact geometry is more complex compared to the stationary case, where it was determined by a single parameter – the impact angle $\phi_{\rm imp}$ between the normal at the impact point and the velocity vector of the impactor. To describe the impact into a rotating target, we first defined a coordinate system of the simulations. We placed the target at origin with zero velocity. The impactor has velocity $[-v_{\rm imp}; 0; 0]$ and its position in x-y plane is given by $\phi_{\rm imp}$, specifically:

$$\boldsymbol{r}_0 = \begin{bmatrix} x_0 + 0.5(D_{\rm pb} + d_{\rm imp})\cos\phi_{\rm imp}, \\ 0.5(D_{\rm pb} + d_{\rm imp})\sin\phi_{\rm imp}, \\ 0 \end{bmatrix},$$

where x_0 is the distance of the impactor from the impact point. These initial conditions have a mirror symmetry in z.

The rotation vector $\boldsymbol{\omega}_{\rm pb}$ of the target adds an additional three free parameters into the simulation setup. Generally, the vector does not have to be aligned with any coordinate axis. We reduced the number of free parameters and thus simplified the analysis by aligning the vector with z-axis, meaning we only consider impacts in the equatorial plane of the target. We expect these impacts will be affected by the rotation the most, as the centrifugal force is the largest on the equator. Furthermore, the angular momentum of the target is aligned with the angular momentum of the impactor. We can thus expect the largest changes in the angular momentum. These expectations have been confirmed for rubble-pile bodies by N-body simulations of Takeda & Ohtsuki (2009).

3.2. Size-frequency distributions for $D_{pb} = 10$ km targets

The first set of simulations was carried out with the target size $D_{\rm pb} = 10$ km. The diameters of impactors were $d_{\rm imp} = 394, 570, 850$, and 1226 m, respectively. We ran a number of simulations for different $P_{\rm pb}$, $d_{\rm imp}$, and $\phi_{\rm imp}$ and compared the size-frequency distribution (SFD) of a family created by an impact into a rotating target with corresponding impact into a stationary target. The resulting distributions are plotted in Fig. 2.

At first glance, the differences between the targets rotating with a period of $P_{\rm pb} = 3$ h and the non-rotating targets are relatively small. The slope of the SFD is almost unchanged in most simulations, it is only shifted as more mass is ejected from the rotating target. In several simulations, like for $\phi_{\rm imp} = -45°$ and $d_{\rm imp} = 0.85$ km, we can see a larger number of fragments in the middle part of the SFD for rotating targets; fragments that would reaccumulate to the largest remnant in the stationary case now escape due to the extra speed from rotation and contribute to the family.

Much larger differences in SFDs can be seen for the target with period $P_{\rm pb} = 2$ h, which is rather expected; for $\rho_0 = 2700\,\mathrm{kg\,m^{-3}}$ the critical period is $P_{\rm crit} \simeq 2.009$ h, so a $P_{\rm pb} = 2$ h target actually rotates very slightly supercritically, although it is held stable by the material strength. The difference is the most prominent for oblique $\phi_{\rm imp} = \pm 75°$ impacts. In several cases, the rotation seems to make the SFD less steep, although this

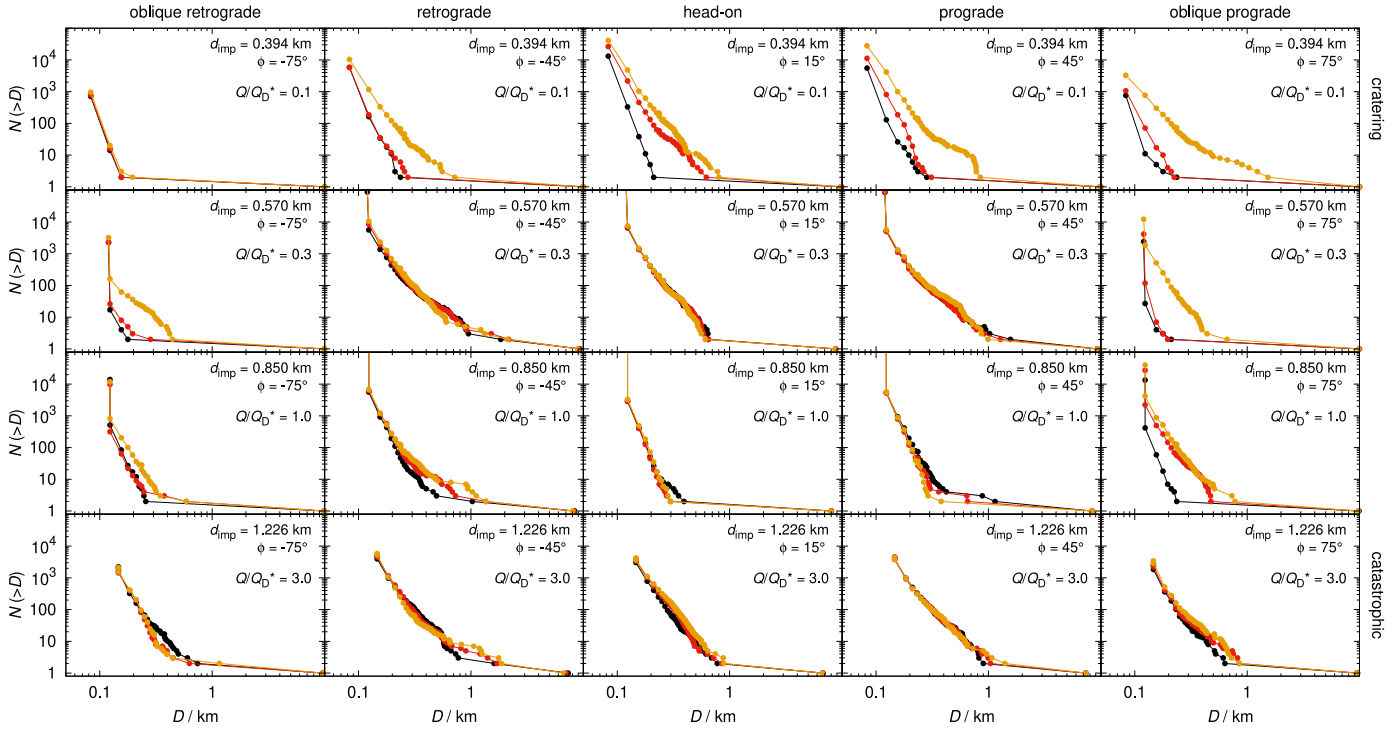

Fig. 2. Cumulative size-frequency distributions $N(>D)$ of synthetic families for $D_{\rm pb} = 10$ km targets. Stationary targets are plotted in black; red and yellow plots correspond to targets with rotational period $P = 3$ h and $P = 2$ h, respectively. Columns 3–5 of the plot show prograde impacts (i.e., positive impact angles); Cols. 1 and 2 are retrograde impacts (i.e., negative impact angles).

might be partially attributed to a numerical artifact, as the synthetic families of non-rotating targets are already very close to the resolution limit.

On the other hand, energetic impacts produce practically the same SFDs regardless of $P_{\rm pb}$. In this regime, angular momentum of projectiles is larger than the rotational angular momentum of the target; for $Q/Q^{\star}_{\rm D} = 3$ and $P_{\rm pb} = 2$ h, the angular momentum of a projectile is five times larger. Ejection velocities are also considerably larger than orbital velocities, hence it is not surprising that the rotation does not make a substantial difference.

It is not probable that these differences come from different fragmentation patterns, as targets are fully damaged by the impact. In our model, such damaged material is strengthless and it essentially behaves like a fluid. Since there is no internal friction nor a mechanism to regain the material strength, this model is insufficient to determine shapes of the fragments; however, here we are only interested in size distributions and using a simplified model is therefore justified.

3.3. Size-frequency distributions for $D_{pb} = 100$ km targets

It is a priori not clear how rotation affects targets of different sizes. To preliminarily estimate the importance of initial rotation, we computed the ratio of the angular frequency $\omega_{\rm pb}$ of the target and $\omega_{\rm imp}$ of the impactor with respect to the target:

$$\frac{\omega_{\rm pb}}{\omega_{\rm imp}} \sim \frac{D_{\rm pb}}{v_{\rm imp} P_{\rm pb} \sin\phi_{\rm imp}} . \tag{21}$$

Because the ratio scales linearly with the target size $D_{\rm pb}$, we expect that the rotation will play a bigger role for impacts into larger targets; however, this back-of-the-envelope computation is by no means definite proof and it needs to be tested.

To this point, we ran a set of simulations with target size $D_{\rm pb} = 100$ km. The set is analogous to the one in Sect. 3.2: we used the same impact angles and rotational periods, the impactor diameters were $d_{\rm imp} = 11.170, 16.110, 24.064,$ and 34.706 km in order to obtain the required relative energies $Q/Q^{\star}_{\rm D}$. The size-frequency distributions of the synthetic families are plotted in Fig. 3.

As expected, the differences between rotating and non-rotating targets are indeed substantially larger than for $D_{\rm pb} = 10$ km. The rotation can completely change the impact regime from cratering to catastrophic; see for example the impact with $\phi_{\rm imp} = 15°$ and $d_{\rm imp} = 16.110$ km, where a cratering gradually changes to a catastrophic disruption as we decrease $P_{\rm pb}$. Focusing on $P_{\rm pb} = 3$ h targets, they produce very shallow SFD in case of oblique prograde impacts. For $\phi_{\rm imp} = \pm 45°$ cratering impacts, we see numerous intermediate-sized fragments (somewhat separated in the SFD) if the target is non-rotating, but the SFD becomes continuous when rotation is introduced.

The effects are even stronger for critically rotating bodies with $P_{\rm pb} = 2$ h, of course. Generally, SFDs of formally cratering events are more similar to catastrophic ones. It also seems that oblique retrograde craterings produce more fragments than prograde ones. For the impact $\phi_{\rm imp} = 15°$ and $d_{\rm imp} = 24.064$ km, the SFD is well below the non-rotating case and most of the mass is contained in the smallest fragments.

Although large ($D \gg 10$ km) asteroids typically rotate much slower than smaller bodies, there are a few that rotate close to the critical spin rate for elongated bodies, such as (216) Kleopatra (Hirabayashi & Scheeres 2014). Rotation in collisional simulations of such bodies should therefore not be neglected.

3.4. Total ejected mass

While Figs. 2 and 3 clearly show the differences between the SFDs, it is quite difficult to read the total mass ejected from the target during the impact. Even when the SFDs of a rotating

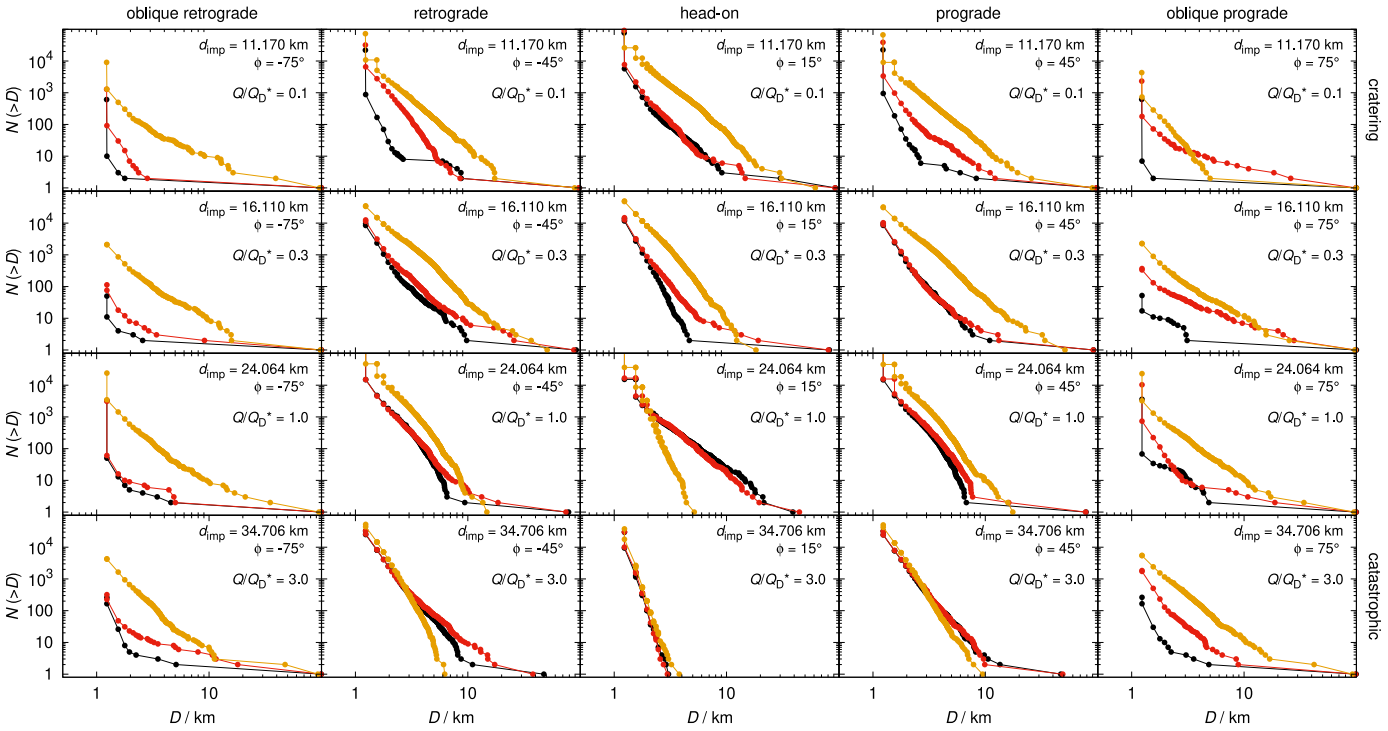

Fig. 3. Cumulative size-frequency distribution for $D_{\mathrm{pb}} = 100\,\mathrm{km}$ targets. The notation is the same as in Fig. 2.

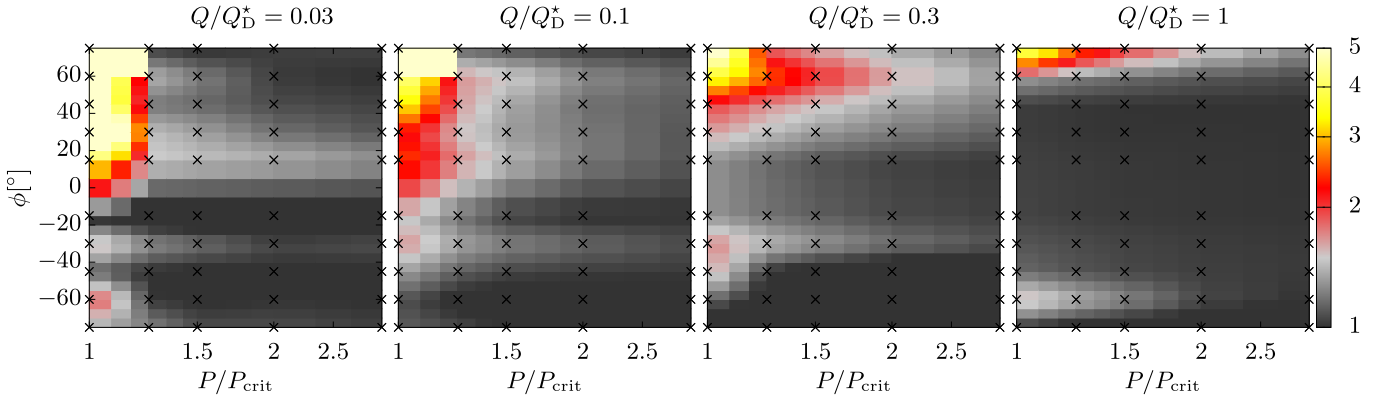

Fig. 4. Total mass of fragments $M_{\mathrm{ej}}(P)/M_{\mathrm{ej}}(\infty)$ ejected by collisions, normalized by mass of fragments from corresponding collision into stationary target. The four figures correspond to different relative impact energies, from cratering (*left*) to mid-energy (*right*) events. The ejected mass is plotted as a function of the impact angle ϕ_{imp} and initial period P_{pb} of the target.

and a stationary target seem to differ only negligibly, the total integrated mass of fragments may be significantly different.

To show the effect of the initial rotation on the ejected mass clearly, we performed over 400 simulations with the target size $D_{\mathrm{pb}} = 10\,\mathrm{km}$, various impact angles ϕ_{imp}, projectile diameters d_{imp}, and initial periods P_{pb} of the target. These simulations have a lower spatial resolution compared to the simulations of family formation in previous sections, as here we do not need to resolve individual fragments in detail. The target is resolved by approximately $N = 100\,000$ particles.

We ran simulations for ϕ_{imp} ranging from 15°–75° (both prograde and retrograde). To capture the dependence on P_{pb}, we selected nine different values from $P_{\mathrm{pb}} = P_{\mathrm{crit}}$ to $50\,P_{\mathrm{crit}}$. The impact energies of the simulations were $Q/Q_{\mathrm{D}}^{\star} = 0.03, 0.1, 0.3$, and 1, meaning the simulations range from cratering events to mid-energy events.

Our goal is to compute the total mass of the fragments as a function of the impact angle ϕ_{imp}, the initial rotational period P_{pb} and the diameter d_{imp}. We are actually not interested in the absolute value of the ejected mass, but rather in the ejected mass relative to the mass that would be ejected if the targets were stationary. Therefore, we computed the ratio:

$$\mu_{\mathrm{ej}} = \frac{M_{\mathrm{ej}}(\phi_{\mathrm{imp}}, d_{\mathrm{imp}}, P_{\mathrm{pb}})}{M_{\mathrm{ej}}(\phi_{\mathrm{imp}}, d_{\mathrm{imp}}, \infty)} \tag{22}$$

and plot the result in Fig. 4. Values $\mu_{\mathrm{ej}} < 1$ would mean that the impact into the rotating target ejected fewer fragments, compared to the stationary target; no such result was found in the performed simulations.

Generally, the rotation amplifies the ejection by several tens of percent. However, the increase is significantly higher if the following conditions are satisfied:

– Target rotates near the critical period. As expected, the effect of rotation decreases rapidly with the increasing period of the target.

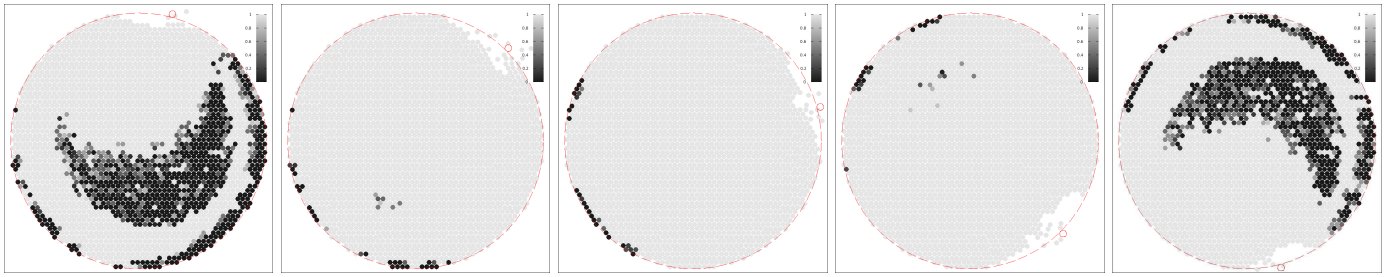

Fig. 5. Damage D of the target at time $t = 10$ s after impact for various impact angles, *from left to right*, $\phi_{\rm imp} = 75°, 45°, 15°, -45°, -75°$. Simulations were carried out with the impactor of size $d_{\rm imp} = 314$ m and speed $v_{\rm imp} = 5\,{\rm km\,s^{-1}}$; target was not rotating. The red outline shows the original position of the target and the impactor. There is an undamaged cavity only for oblique impacts, otherwise the target is fully damaged by the impact.

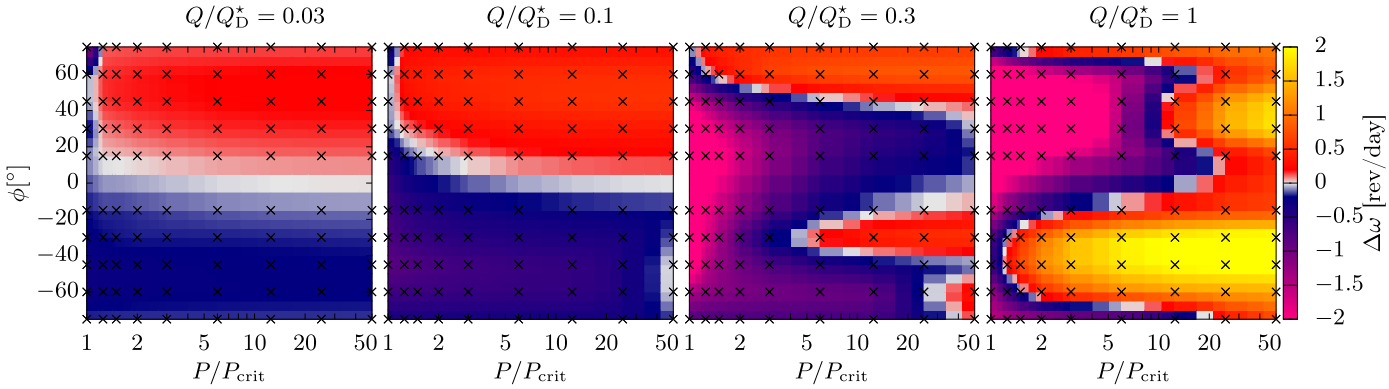

Fig. 6. Change of spin rate $\Delta\omega$ of target (or largest remnant in case $Q/Q^\star_{\rm D} \simeq 1$) as function of initial period $P_{\rm pb}$ of target (here in units of critical period $P_{\rm crit}$) and impact angle $\phi_{\rm imp}$. The four images correspond to different sizes of the impactor. The energy of the impact is *from left to right* $Q/Q^\star_{\rm D} = 0.03, 0.1, 0.3$ and 1. The impact velocity was $v_{\rm imp} = 5\,{\rm km\,s^{-1}}$ in all cases.

– The impact results in a cratering rather than a catastrophic event. While high-energy impacts eject more fragments in an absolute measure, the initial rotation does not affect the value notably in this regime.
– The impact is oblique and has a prograde direction. Head-on impacts and the impacts in retrograde directions are not affected by the rotation to the same degree.

In extreme cases, the rotation can amplify the ejected mass by a factor of five. On the other hand, the ejection ratio $\mu_{\rm ej}$ does not exceed 1.6 for rotational periods $P_{\rm pb} > 2P_{\rm crit}$ in any of the performed simulations.

Although it is a different rheology, rubble-pile bodies also exhibit a minor effect of rotation (on $Q^\star_{\rm D}$ as well as $\mu_{\rm ej}$) in this range of $P_{\rm pb}$ (Takeda & Ohtsuki 2009, see Fig. 2 therein). However, their strength is an order of magnitude lower than for monoliths of Benz & Asphaug (1999), so the comparison is not straightforward.

4. Embedding and draining the angular momentum

Impact into a rotating target can cause either an acceleration or a deceleration of the target's rotation. This can be immediately seen from two limit cases: a stationary target is always spun by the impact, on the other hand a target rotating at the breakup limit cannot be accelerated any further and the collision thus always causes a deceleration.

It has been proposed that rotating asteroids are decelerated over time by numerous subsequent cratering collisions, as a fraction of the angular momentum is carried away by fragments. Coined the angular momentum drain (Dobrovolskis & Burns 1984), this effect could explain the excess of slow rotators in the main belt. In this section, we examine whether this effect emerges in our simulations and we determine the functional dependence of the deceleration on the impact parameters.

We analyze the angular momentum transfer as a function of impact parameters, using the set of simulations described in Sect. 3.4. The impacts range from cratering ($Q/Q^\star_{\rm D} \sim 0.03$) to mid-energy ($Q/Q^\star_{\rm D} \sim 1$) events. For $Q/Q^\star_{\rm D} \sim 1$, the whole target asteroid is disintegrated by the collision and fragments with mass of about $0.5\,M_{\rm pb}$ are reaccumulated later, forming the largest remnant. This can no longer be viewed as a cratering event that merely modifies the rotational state of the target, nevertheless we can still formally compute the relation between the period of the target and the largest remnant.

In a majority of performed simulations, the target is completely damaged by the impact. There remained an undamaged cavity only for the weakest oblique impacts with $Q/Q^\star_{\rm D} = 0.03$, as shown in Fig. 5. Otherwise all particles of the target have damage $D = 1$ after the fragmentation phase.

The change of spin rate $\Delta\omega$ of the target is plotted in Fig. 6. We plot the change of frequency rather than period, as the period is formally infinite for a non-rotating body; a change of period is thus not a meaningful quantity.

For cratering events, the prograde events (denoted with positive $\phi_{\rm imp}$) mostly accelerate the target, while retrograde events cause deceleration. The two exceptions from this rule are:

1. a prograde impact into a critically rotating body, in which case it cannot be accelerated any more and some deceleration is expected; and
2. a retrograde impact to an almost stationary body.

Impacts with higher energies show a different pattern. It seems that the two regions described above expand. Prograde impacts

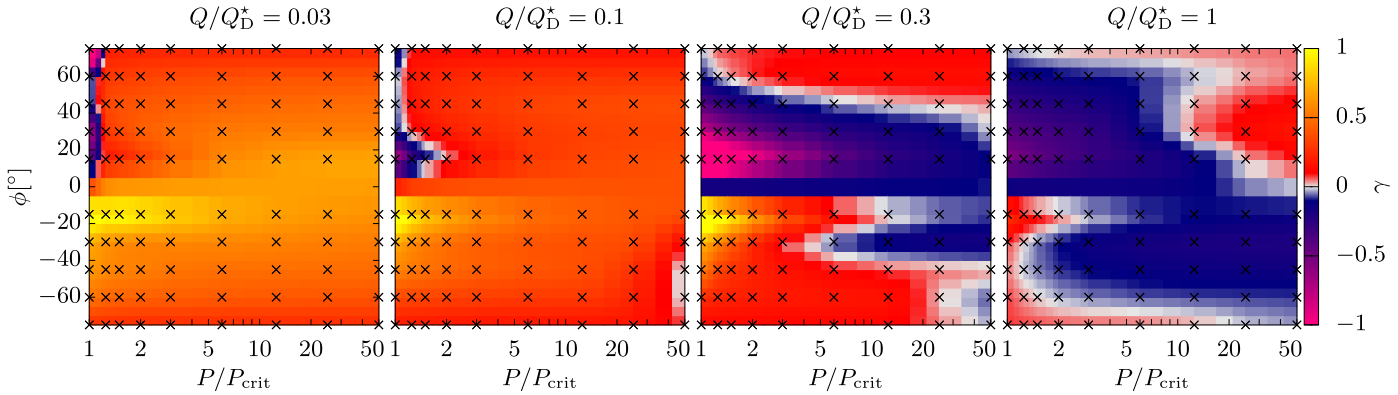

Fig. 7. Dimensionless effectivity γ of angular momentum transfer. The other quantities are the same as in Fig. 6.

into fast rotators actually decelerate the target, while retrograde impacts start to accelerate it. For the most energetic event we studied, $Q/Q^\star_\mathrm{D} \simeq 1$, it seems that the two regions completely swapped: most prograde impacts cause a deceleration while retrograde impacts cause an acceleration.

The despinning (or angular momentum draining) on rubble-piles in catastrophic disruptions was confirmed by Takeda & Ohtsuki (2009). In our simulations, the pattern is more complex, likely because the parameter space ($Q/Q^\star_\mathrm{D}$, P_pb) is significantly more extended; additionally rubble-piles cannot initially rotate critically.

4.1. Effectivity of the angular momentum transfer

Let us define the effectivity γ of the angular momentum transfer as:

$$\gamma \equiv \frac{L_\mathrm{lr} - L_\mathrm{pb}}{L_\mathrm{imp}}, \tag{23}$$

where L_pb is the rotational angular momentum of the target before the impact, L_pb is the rotational angular momentum of the largest remnant, and L_imp is the angular momentum of the impactor with respect to the target. As these values are scalars, we assign a negative sign to the value L_imp for retrograde impacts.

We emphasize that the effectivity γ is not necessarily in the unit interval $\langle 0; 1\rangle$. Specifically, it may be significantly larger than one for head-on impacts, as the delivered angular momentum is very low; in fact, L_imp approaches zero for $\phi_\mathrm{imp} = 0$. The effectivity can also be a negative number for impacts to critically rotating targets, as in these cases, the target cannot accelerate over the breakup limit, so a zero or even negative values of γ are expected.

The effectivity γ as a function of the initial period P_pb, the impact angle ϕ_imp, and the impactor diameter d_imp is plotted in Fig. 7. We can see that cratering impacts have generally higher effectivity than high-energy impacts. This result might have been expected, as the cratering impacts eject less mass and thus transfer less angular momentum to fragments, compared to the catastrophic impacts. A less expected outcome is the negative effectivity for the high-energy impacts. We predicted the negative values only for prograde impacts into critically rotating targets, but for $d_\mathrm{imp} = 850$ m the effectivity is negative for the majority of performed simulations.

Finally, the highest effectivity is achieved for retrograde impacts into critically rotating targets. However, this results is slightly false, because in this regime the target is always decelerated; γ can therefore exceed one as the angular momentum lost in the collision is higher than L_imp (in absolute value). Impacts into slower rotators have values of γ around 0.5.

4.2. Angle-averaged ejection and momentum transfer

To express an overall effect of collisions on a rotational state of a target, it is useful to consider a large number of collisions at random impact angles and compute the average change of spin rate:

$$\overline{\Delta\omega} \equiv \int_0^{\pi/2} \Delta\omega \sin 2\phi \,\mathrm{d}\phi \approx \frac{\sum_i \Delta\omega_i \sin 2\phi_i}{\sum_i \sin 2\phi_i}, \tag{24}$$

where $\sin 2\phi$ is the probability of the impact with the impact angle ϕ. The averaged change $\overline{\Delta\omega}$ is plotted in Fig. 8, together with a plot of the relative mass ejection $\overline{\mu}_\mathrm{ej}$, defined in Sect. 3.4.

The figures show that targets are on average decelerated for both low-energy and mid-energy impacts. A target is only accelerated if it was originally a very slow rotator, since it cannot be decelerated any more. The transition between these two regimes (plotted in white) is where the target does not change its angular frequency upon the impact. It seems to depend on the energy of the impact; for $Q/Q^\star_\mathrm{D} \sim 0.1$, the transition occurs at around $P \sim 20 P_\mathrm{crit}$, while for $Q/Q^\star_\mathrm{D} \sim 1$, it is shifted to around $P \sim 6 P_\mathrm{crit}$.

5. Conclusions and future work

In this paper, we showed that a fast initial rotation of targets may significantly affect resulting synthetic families. The effect is more prominent for larger target bodies and for oblique impact angles. Generally, more fragments are ejected from prograde ($\phi_\mathrm{imp} > 0$) compared to the retrograde ($\phi_\mathrm{imp} < 0$) targets.

In extreme cases, the mass ejection can be amplified by a factor five. Neglecting the rotation would therefore introduce a considerable bias. Other parameters of the simulation do introduce similar (or sometimes larger) uncertainties, for example the Weibull parameters of the fragmentation model (Ševeček et al. 2017), the rheological model of the target, etc. As shown in Jutzi & Benz (2017), the initial shape can also have a significant effect.

Throughout this paper, we assumed that both the targets and impactors are monolithic bodies. It is a priori not clear whether the rotation would be more important for rubble-pile bodies

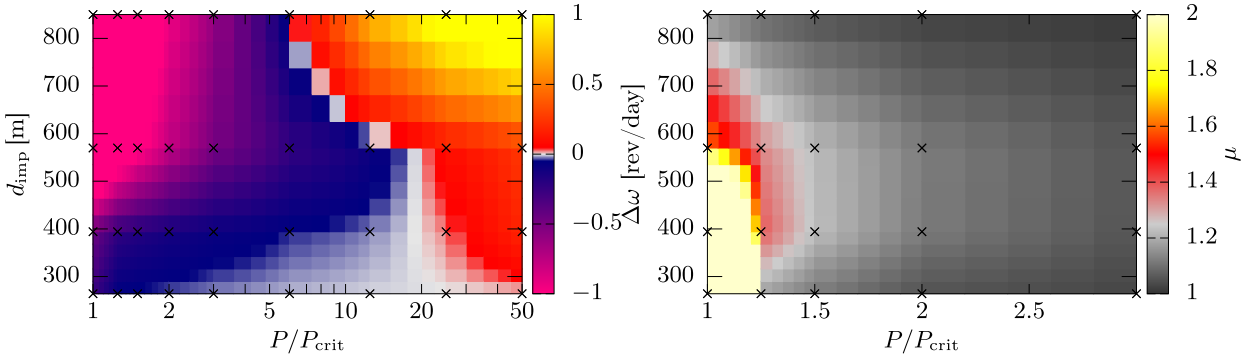

Fig. 8. Quantities averaged over impact angles using Eq. (24) as function of period $P_{\rm pb}$ of target and impactor diameter $d_{\rm imp}$. *The left figure* shows the change of spin rate $\Delta\omega$, *the right one* the total mass of fragments, normalized by the mass of fragments from corresponding collision into a stationary target.

(with macro-porosity), or when a rheological model with crushing (microporosity) is used in the simulations (Jutzi et al. 2019). It should also be explored how initial shapes relate to spin rates of fragments. We postpone such studies to future works.

In the future, we also plan to determine the scaling law as a function of both $D_{\rm pb}$ and $P_{\rm pb}$. It is clear that the critical energy $Q^\star_{\rm D}$ is a steep function of $P_{\rm pb}$ close to the critical spin rate. Finding a functional dependence $Q^\star_{\rm D} = Q^\star_{\rm D}(P_{\rm pb})$ might be a valuable result for studies of main belt evolution, as it could be used to construct a combined model that includes both collisions and rotations.

Acknowledgements. The work of P.Š. and M.B. has been supported by the Czech Science Foundation (GACR 18-04514J) and Charles University (GAUK 1584517). M.J. acknowledges support from the Swiss National Centre of Competence in Research PlanetS.

References

Ballouz, R.-L., Richardson, D. C., Michel, P., Schwartz, S. R., & Yu, Y. 2015, Planet. Space Sci., 107, 29
Ballouz, R.-L., Walsh, K. J., Richardson, D. C., & Michel, P. 2018, Lunar Planet. Sci. Conf., 49, 2816
Balsara, D. S. 1995, J. Comput. Phys., 121, 357
Barnes, J., & Hut, P. 1986, Nature, 324, 446
Benavidez, P. G., Durda, D. D., Enke, B. L., et al. 2012, Icarus, 219, 57
Benavidez, P. G., Durda, D. D., Enke, B., et al. 2018, Icarus, 304, 143
Benz, W., & Asphaug, E. 1994, Icarus, 107, 98
Benz, W., & Asphaug, E. 1999, Icarus, 142, 5
Canup, R. M. 2005, Science, 307, 546
Canup, R. M. 2008, Icarus, 196, 518
Cossins, P. J. 2010, PhD Thesis, University of Leicester, UK
Ćuk, M., & Stewart, S. T. 2012, Science, 338, 1047
Dahlgren, M. 1998, A&A, 336, 1056
Dobrovolskis, A. R., & Burns, J. A. 1984, Icarus, 57, 464
Durda, D. D., Bottke, W. F., Nesvorný, D., et al. 2007, Icarus, 186, 498
Fétick, R. J., Jorda, L., Vernazza, P., et al. 2019, A&A, 623, A6
Hirabayashi, M., & Scheeres, D. J. 2014, ApJ, 780, 160
Jutzi, M., & Benz, W. 2017, A&A, 597, A62
Jutzi, M., Asphaug, E., Gillet, P., Barrat, J.-A., & Benz, W. 2013, Nature, 494, 207
Jutzi, M., Holsapple, K., Wünneman, K., & Michel, P. 2015, in Asteroids IV, eds. P. Michel, F. E. DeMeo, & W. F. Bottke (Tucson: University of Arizona Press), 679
Jutzi, M., Michel, P., & Richardson, D. C. 2019, Icarus, 317, 215
Kurosawa, K., & Genda, H. 2018, Geophys. Res. Lett., 45, 620
Marrone, S., Antuono, M., Colagrossi, A., et al. 2011, Comput. Methods Appl. Mech. Eng., 200, 1526
Michel, P., & Richardson, D. C. 2013, A&A, 554, L1
Michel, P., Richardson, D. C., Durda, D. D., Jutzi, M., & Asphaug, E. 2015, in Asteroids IV, eds. P. Michel, F. E. DeMeo, & W. F. Bottke (Tucson: University of Arizona Press), 341
Monaghan, J. J. 1985, Comput. Phys. Rep., 3, 71
Monaghan, J. J. 2000, J. Comput. Phys., 159, 290
Monaghan, J., & Gingold, R. 1983, J. Comput. Phys., 52, 374
Morris, A. J. W., & Burchell, M. J. 2017, Icarus, 296, 91
Nakamura, A., & Fujiwara, A. 1991, Icarus, 92, 132
Nesvorný, D., Brož, M., & Carruba, V. 2015, in Asteroids IV, eds. P. Michel, F. E. DeMeo, & W. F. Bottke (Tucson: University of Arizona Press), 297
Owen, J. M. 2014, Int. J. Numer. Methods Fluids, 75, 749
Reinhardt, C., & Stadel, J. 2017, MNRAS, 467, 4252
Remington, T., Owen, J. M., Nakamura, A., Miller, P. L., & Bruck Syal, M. 2018, in AAS/Division for Planetary Sciences Meeting Abstracts #50, 312.02
Richardson, D. C., Quinn, T., Stadel, J., & Lake, G. 2000, Icarus, 143, 45
Schäfer, C., Riecker, S., Maindl, T. I., et al. 2016, A&A, 590, A19
Ševeček, P., Brož, M., Nesvorný, D., et al. 2017, Icarus, 296, 239
Stadel, J. G. 2001, PhD Thesis, University of Washington, USA
Suetsugu, R., Tanaka, H., Kobayashi, H., & Genda, H. 2018, Icarus, 314, 121
Sugiura, K., Kobayashi, H., & Inutsuka, S. 2018, A&A, 620, A167
Takeda, T., & Ohtsuki, K. 2007, Icarus, 189, 256
Takeda, T., & Ohtsuki, K. 2009, Icarus, 202, 514
Tillotson, J. H. 1962, General Atomic Report, GA-3216
Vernazza, P., Brož, M., Drouard, A., et al. 2018, A&A, 618, A154
Vinogradova, T. A. 2019, MNRAS, 484, 3755
Wickham-Eade, J. E., Burchell, M. J., Price, M. C., & Harriss, K. H. 2018, Icarus, 311, 52

Appendix A: Handling particle overlaps

Since we treat particles as solid spheres during the reaccumulation phase, particle overlaps are unavoidable and need to be handled by our N-body integrator. There are two main reasons why particle overlaps occur.

First, the spheres overlap initially after the hand-off (Eq. (18)). In SPH, the particles naturally overlap as they describe a continuum rather than point masses. After converting them to solid spheres, particles belonging to the same body will necessarily overlap, unless their radius is decreased significantly.

Second, overlaps occur when particles are being merged. When two spherical particles collide, they merge into a larger particle with volume equal to the sum of volumes of the colliders. This merging is an atomic operation, particles are converted into the merger in an instant rather than over several timesteps, so any other particles located close to the colliders potentially overlap the particle merger.

Our code allows for several options to resolve overlaps. One straightforward solution is to always merge the overlapping particles. While this is a simple and robust solution, it can potentially create unphysical, supercritically rotating bodies. Alternatively, we can repel the overlapping particles, so that they are in contact rather than overlap. However, this causes an "inflation" of the largest remnant after the hand-off. Even worse, the angular momentum is no longer conserved.

Another option is to abandon the 1:1 conversion of spheres and instead construct a new set of spheres inside the alpha-shape of the largest remnant (Ballouz et al. 2018). Such an approach allows the placement of spheres onto a regular grid and to thus avoid overlaps by construction. However, it is more suitable when collided particles form rigid aggregates instead of mergers. As spheres never fill the entire volume (a filling factor of hexagonal close packing is about 0.74) and the merging conserves volume, fragments would shrink considerably.

We decided to merge particles only if the spin rate of the would-be merger is lower than the critical spin rate, otherwise we allow particles to pass through each other. Of course, such handling is only applied to resolve overlaps; particles that collide are always treated as solid.

Appendix B: Comparison of inertial and co-rotating reference frames

We can choose two different approaches to implementing the rotation of the target:

1. rotate the particles around the center of the target, and
2. perform the simulation in the coordinate system co-rotating with the target.

From a numerical point of view, the second approach is easier to handle, as the particles of the target initially have zero velocities and we thus avoid numerical problems with the bulk rotation outlined in Sect. 2.1. The rotation is taken into account by introducing inertial accelerations, meaning the last two terms of Eq. (2).

However, it only solves the issue partially. Even though the target is stationary (in the co-rotating frame) before the impact, the projectile can spin up the target and the impact can also eject rotating fragments. To properly handle rotating bodies in SPH, it is necessary to introduce the correction tensor in Eq. (5). This allows us to perform simulations in the inertial frame, which is a natural choice.

Ideally, these two approaches should produce identical results. To test it, we ran two simulations with $D_{\mathrm{pb}} = 200\,\mathrm{km}$ parent bodies rotating critically. The results are plotted in Fig. B.1. We observe some stochastic differences, but the spatial distribution of the ejected fragments is similar in both simulations. This test confirms the consistency of both approaches.

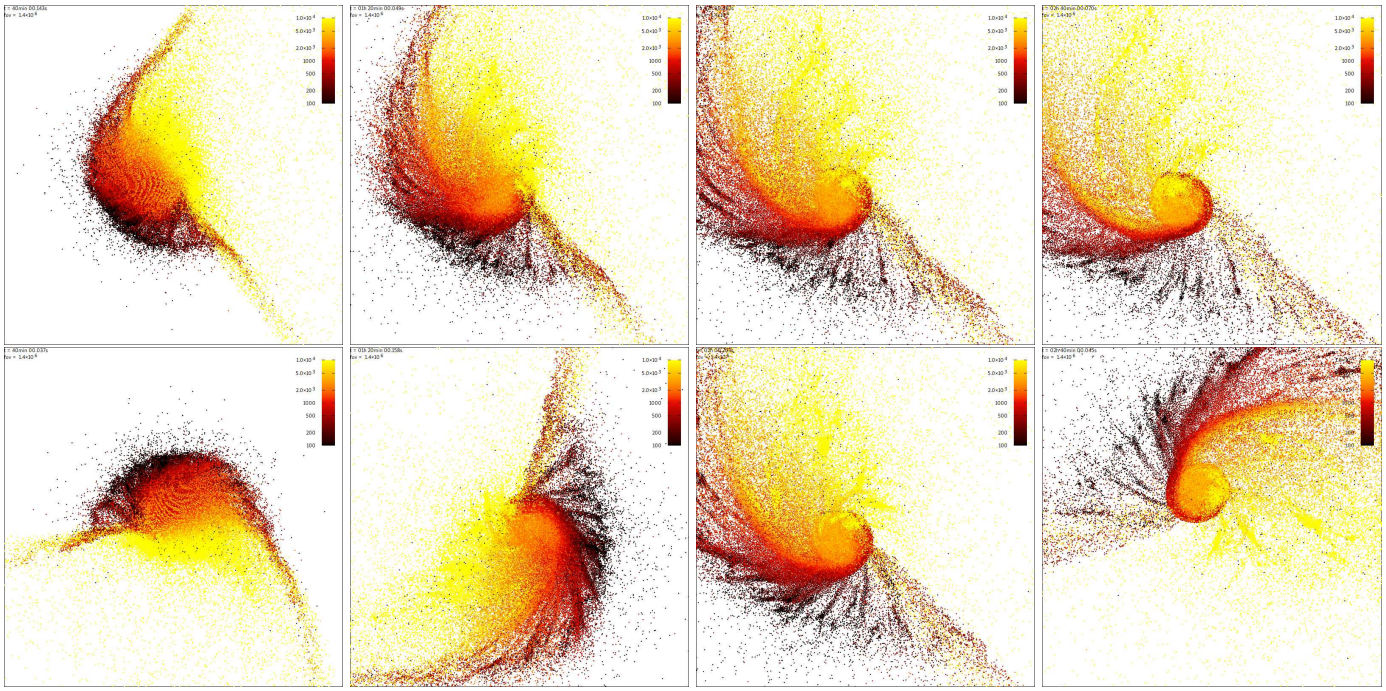

Fig. B.1. Impact into $D_{\mathrm{pb}} = 200\,\mathrm{km}$ target. This was computed with a rotating target (*upper row*) and with a rotating coordinate frame in which the target is stationary (*lower row*), and plotted at times $t = 40, 80, 120,$ and 160 min after the impact. The color scale represents the specific energy of the particles (in SI units).

Appendix C: Implementation notes

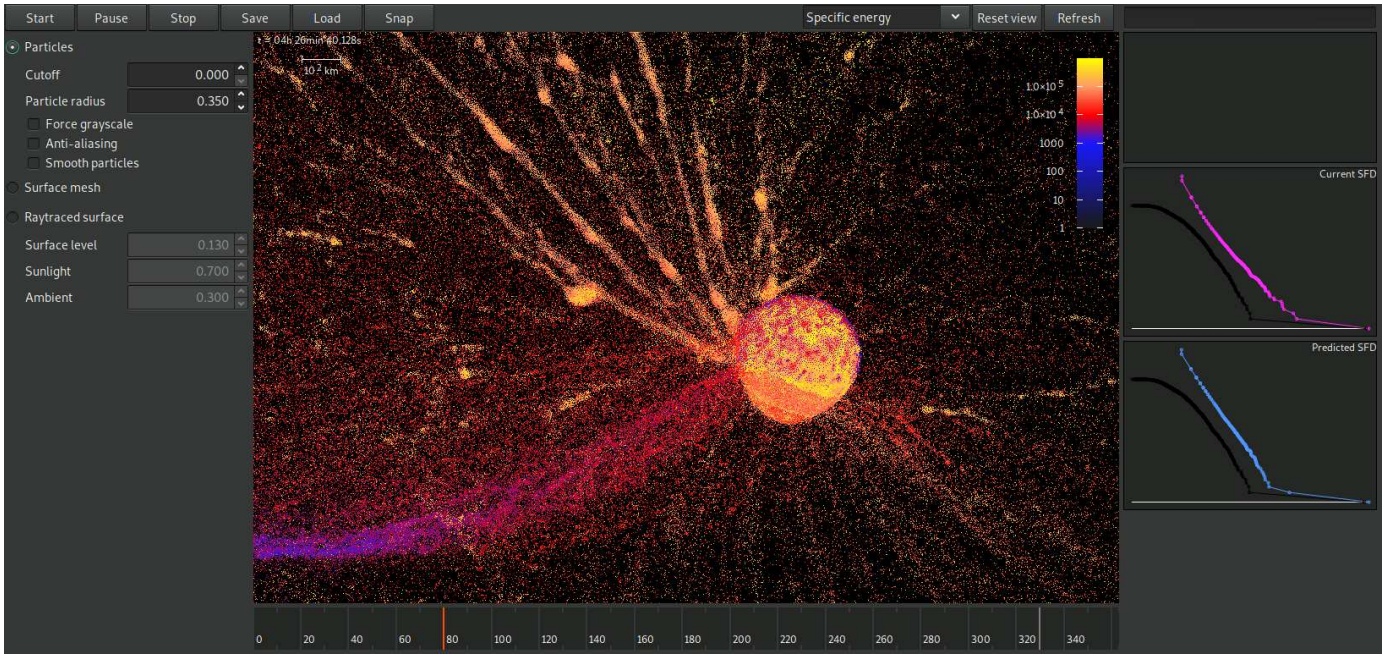

Fig. C.1. Screenshot of graphic interface of our code.

The code `OpenSPH` used throughout this work is open-source, available under MIT license. As of August 7, 2019, it can be downloaded[1]. It includes a helpful graphic interface, allowing the user to interactively visualize the simulation (see Fig. C.1). It is also a stand-alone viewer of `OpenSPH` output files and potentially files generated by other particle-based codes, provided their file formats are implemented.

Our code can be used as both an SPH solver and an N-body integrator, as we separated computations of SPH derivatives and gravitational accelerations. In each time step, accelerations due to hydrodynamics and gravity are computed independently and summed up. Even though we miss some optimization possibilities with this approach, it allows us to use the same code for both the fragmentation and the reaccumulation phase; the hand-off is thus only an internal change of a solver, replacing SPH hydrodynamics with a collision detection.

We used the Barnes–Hut algorithm to evaluate gravitational accelerations (Barnes & Hut 1986). The code uses the same functionality in SPH and N-body solver. It only differs in the softening kernel ϕ; in SPH, it is defined by Eq. (14), while for N-body it corresponds to a homogeneous sphere. Our implementation uses a k-d tree, which is also used to find particle neighbors.

In the fragmentation phase, we found that the time step criterion that uses stress tensor derivatives (see Eq. (16)) is often unnecessarily restricting, as the stress tensor changes rapidly inside the projectile. However, as we are not very interested in remnants of projectiles, simulations can be thus be sped up by applying the criterion only for particles of the target. No such optimization is applied for CFL criterion, as it determines stability of the method and it is thus essential for all particles.

In the reaccumulation phase, collided particles are merged, provided their relative velocity does not exceed the escape velocity v_{esc} (as in Eq. (19)) and the spin rate does not exceed the critical spin rate ω_{crit} (as in Eq. (20)). In practice, both v_{esc} and ω_{crit} are multiplied by user-defined factors (i.e., a merging limit). It may be useful to tune it in such a way that a simplified N-body model of reaccumulation matches a full SPH simulation (in terms of resulting SFDs).

The total computation time needed depends on a type of simulation. Generally, catastrophic impacts take longer to compute than cratering impacts (quantities change more rapidly, hence smaller time steps are needed). For smaller targets, SPH particles are also smaller, which in turn implies smaller time steps due to the CFL criterion. The computation time is thus longer. The code is parallelized using a custom thread pool, utilizing the native C++11 threads, or optionally using the Intel Thread Building Blocks library. For $D_{\mathrm{km}} = 10\,\mathrm{km}$ target and $N = 500\,000$ particles, a single simulation takes about ten hours on a AMD Ryzen Threadripper 1950X 16-Core processor.

[1] https://gitlab.com/sevecekp/sph

— Chapter vi —

impact forming the Hygiea family

It has only recently become possible to obtain disk-resolved observations of large Main-belt asteroids using ground-based instruments. The second-generation adaptive-optics (AO) instruments can now acquire images with the angular resolution of 3.6 mas/pixel [Schmid et al., 2017], allowing to analyze the shapes of asteroids and resolve impact craters and other topographic features with only a few kilometers in size. Formerly, detailed images of asteroid surfaces and other small bodies were taken exclusively by *in situ* measurements during space missions.

For bodies visited by a spacecraft, it was possible to derive a detailed shape model using either photogrammetric structure-from-motion [Hirata et al., 2020] or photoclinometric shape-from-shading [Gaskell et al., 2008] techniques. The shapes of other asteroids were only constrained using lightcurve inversion [Ďurech et al., 2010], stellar occultations [Buie et al., 2015] or radar images [Ostro et al., 2000]. Adaptive optics now allows to reconstruct an accurate shape of a number of large asteroids, yielding valuable insights to their collisional histories, and it also resolves the albedo–shape ambiguity.

In light of these new research possibilities, I decided to move on from generic studies of normative targets and focus on interpretations of observational data. As a number of the observed asteroids are associated with a collisional family, numerical simulations can be used to compute the expected size of the crater from which the family originated. This can be directly compared with the images of the surface. In this chapter, I focus on the asteroid (10) Hygiea and its family.

6.1 Observational constraints

Asteroid (10) Hygiea is the fourth-largest body in the Main Belt, after (1) Ceres, (2) Pallas and (4) Vesta. It has been discovered on the 12th of April 1849 by Annibale De Gasparis and was named after Hygiea (or Hygieia), the Greek goddess of health and hygiene. The asteroid is located in the outer Main Belt, having the proper semi-major axis $a_{\mathrm{p}} = 3.14\,\mathrm{au}$. Prior to the AO observations, it was estimated that the asteroid has a diameter of $D = 443\,\mathrm{km}$ [Bowell et al.,

1979], the mass of $M = (5.57 \pm 0.70) \times 10^{-11}\,\mathrm{M}_\odot$ [Michalak, 2001], and the rotational period of $P \simeq 27.6\,\mathrm{h}$ [Michalowski et al., 1991]. Due to its low albedo and carbonaceous surface, Hygiea is a C-type asteroid [Mothé-Diniz et al., 2001] with a composition similar to (1) Ceres [Vernazza et al., 2017].

6.1.1 Hygiea family

There is a known asteroid family associated with (10) Hygiea, first identified by Zappalà et al. [1995]. It currently consists of approximately 7000 observed members. Hygiea itself lies in the center of the respective region of the proper elements a_p, e_p and I_p, as seen in Fig. 6.1. It is bounded by the mean-motion resonance J2:1 at $a = 3.28$ au and crossed by several weaker mean-motion resonances as well as secular resonances, such as $\nu_6 = g - g_6$. The volume-equivalent diameter of all fragments is $D_\mathrm{eq} = 110\,\mathrm{km}$, well below the diameter of Hygiea itself, suggesting the family was created by a cratering event. This shall be revised in the light of our work.

The largest asteroids in the region are (538) Friederike with a diameter of $D = 70\,\mathrm{km}$, (1109) Tata with $D = 62\,\mathrm{km}$, and (1599) Giomus with $D = 46\,\mathrm{km}$. However, the spectra of both Friederike and Tata are distinct from the spectrum of Hygiea, hinting these bodies are likely interlopers. Asteroids Friederike and Giomus were also recognized as dynamical interlopers by Carruba et al. [2014], however, the spectrum of Giomus is compatible with Hygiea, suggesting it is actually a family member [Vernazza et al., 2020].

Most of the family members are C-type asteroids and are taxonomically similar to Hygiea [Carruba et al., 2014]. The family also contains several X-type and B-type asteroids. Furthermore, there are few asteroids of different spectral types in the region (D-type, K-type, ...), although these are probable interlopers. Using Monte Carlo simulations, Carruba et al. [2014] estimated the age of the family $T = 3200^{+380}_{-120}\,\mathrm{Myr}$, suggesting very old and dynamically evolved family.

6.1.2 Adaptive-optics observations of (10) Hygiea

Hygiea was selected as one of the asteroids of interest for the imaging survey [Vernazza et al., 2018] using ESO VLT[1], located at the Paranal Observatory. The images were acquired using the adaptive-optics SPHERE[2]/ZIMPOL[3] camera between June 2017 and September 2018. The raw images were deconvolved using MISTRAL[4] algorithm [Fusco et al., 2003] to obtain sharp images of the asteroids. The deconvolved images together with disk-integrated data were then used to reconstruct the surface shape of Hygiea using `ADAM`[5] code [Viikinkoski et al., 2015].

The images revealed a smooth spherical surface. By finding an optimal fit to an ellipsoid, Vernazza et al. [2020] determined semi-axes $a = 225\,\mathrm{km}$, $b = 215\,\mathrm{km}$, $c = 212\,\mathrm{km}$. While these are indeed comparable, they do not indicate how spherical the body actually is. A better measure

[1] Very Large Telescope
[2] Spectro-Polarimetric High-contrast Exoplanet REsearch
[3] Zurich IMaging POLarimeter
[4] Myopic Iterative STep Preserving ALgorithm
[5] All-Data Asteroid Modeling

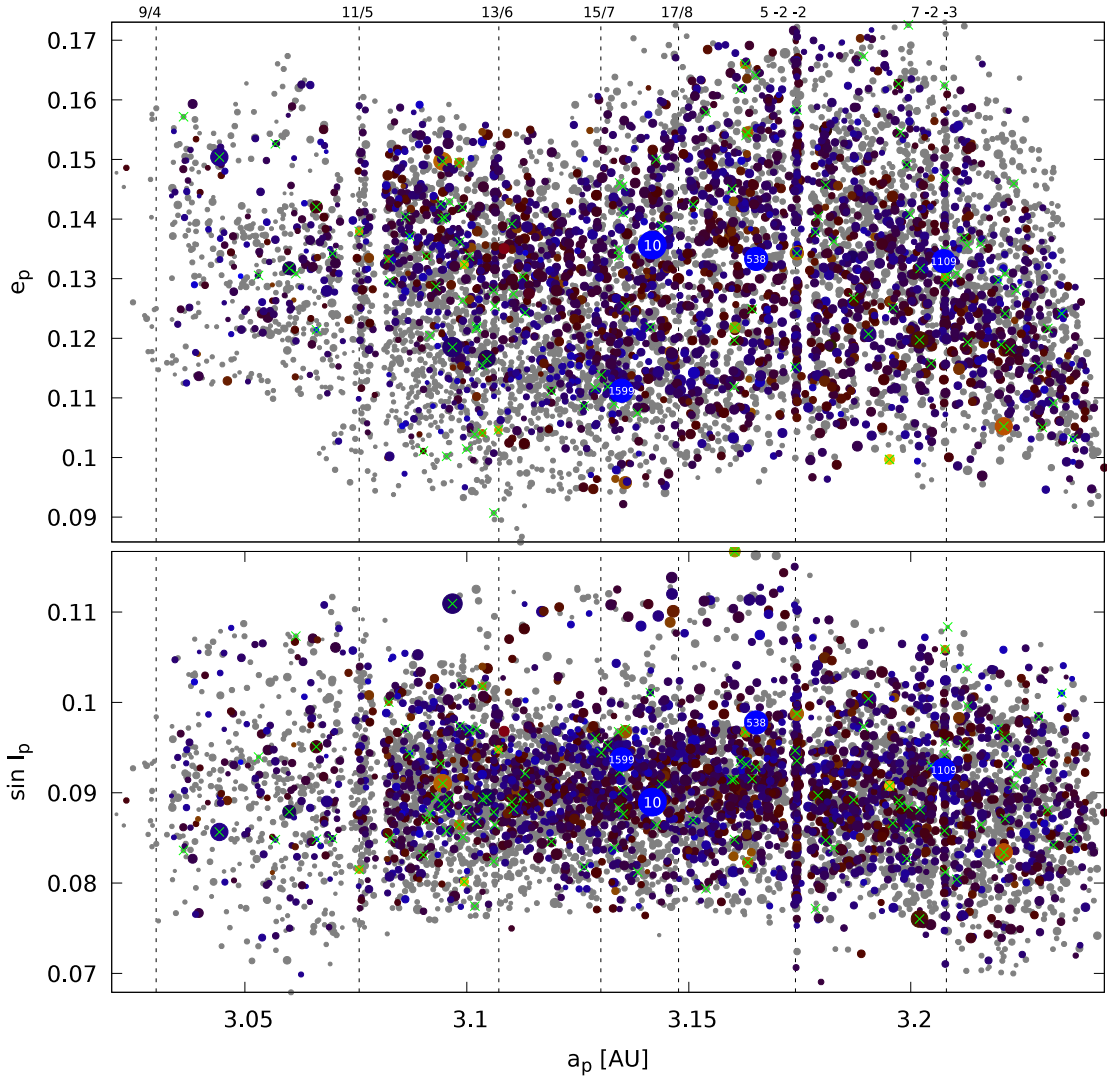

Figure 6.1: Hygiea family in the space of proper orbital elements $(a_\mathrm{p}, e_\mathrm{p})$ and $(a_\mathrm{p}, \sin I_\mathrm{p})$ [Knežević and Milani, 2003]. It is located close to the 2:1 mean-motion resonance with Jupiter at $a = 3.28$ au. The family has been identified using the HCM [Zappalà et al., 1995] using cutoff velocity $v_\mathrm{cutoff} = 60\,\mathrm{m/s}$. We observe a family core with diffuse surroundings and a smooth transition to the background population. Colors correspond to WISE albedos p_V, sizes of dots are related to body sizes. Green crosses show the potential interlopers. (10) Hygiea itself and the largest asteroids in the vicinity are marked by their respective numbers.

for the surface roundness is Wadell's sphericity [Wadell, 1935]. It is defined as the surface area of a sphere with equal volume V and the surface area A of the body:

$$\psi = \frac{\pi^{\frac{1}{3}}(6V)^{\frac{2}{3}}}{A}. \tag{6.1}$$

However, small-scale topographical features can substantially enlarge the total surface area and thus decrease the sphericity ψ. In fact, a higher resolution will always add some complexity to the surface and therefore decrease the sphericity; it is a two-dimensional equivalent of the coastline paradox. To get a resolution-independent measure of sphericity which can be used to compare Hygiea with other asteroids, the surface shape was first approximated using spherical harmonics up to the tenth order and only then the sphericity was evaluated.

Using this definition, the sphericity of Hygiea is $\psi \simeq 0.9975$, quite comparable to the sphericity of Ceres $\psi \simeq 0.9988$. The other asteroids larger than Hygiea, Vesta and Pallas, are considerably less spherical, having sphericities of $\psi \simeq 0.985$ and $\psi \simeq 0.991$, respectively.

Vernazza et al. [2020] further revised the rotational period of Hygiea and derived a value of $P = 13.83\,\mathrm{h}$, half of the value reported previously. Due to its extremely spherical shape, the lightcurves have been formerly misread and the period was incorrectly computed as twice the real value.

Hence, we faced seemingly contradictory facts. On one hand, we observe a numerous family with Hygiea its center. The family matches Hygiea spectroscopically, making it likely the largest remnant. On the other hand, the deconvolved images revealed a smooth surface of the asteroid with a lack of large-scale topographic features. Only two impact craters have been identified, neither of which could be a progenitor of the family due to their small diameters ($D = 180\,\mathrm{km}$ and 97 km). A large impact basin has been expected, similar to the one seen on (4) Vesta, but no such feature has been found. These findings were quite puzzling and we thus performed hydrodynamical simulations of the impact in an attempt to interpret these observational data.

6.2 Methods and aims

We simulated the impact using our code `OpenSPH`, which was developed and tested during the previous years. The diameter of the target was $D = 428\,\mathrm{km}$, other parameters of the impact were varied to obtain the optimal fit to the observed SFD. We ran simulations with various impact speeds v_{imp}, impact angles ϕ_{imp}, impactor diameters d_{imp}, and initial rotational periods P of the target.

Contrary to the previous work, we employed both the standard von Mises rheological model as well as the more complex Drucker-Prager model (see Sec. 2.8.2). As the shape of Hygiea was one of our observational constraints, it was important to choose such rheology that results in a shape of the largest remnant which is compatible with the given shape model. The main difference between the two is the behavior of fully damaged material; while the von Mises material is completely strengthless when damaged and thus the largest remnant always takes on a spherical shape, the Drucker-Prager material has non-negligible dry friction even if damaged and the resulting shape may be significantly different.

To reconstruct the final shape of the largest remnant in the simulation and to avoid any possible numerical artifacts from the hand-off to an N-body integrator, we performed a significant fraction of the reaccumulation phase in the SPH framework. Instead of the $t_{\mathrm{handoff}} = 30\,\mathrm{min}$ used previously, we prolonged the run time of SPH simulations to $t_{\mathrm{handoff}} = 24\,\mathrm{hours}$. This time was sufficient to separate individual fragments in space and attenuate any further changes of their shapes. The following reaccumulation phase ran for $t_{\mathrm{reac}} = 10\,\mathrm{days}$ in order to merge the particles and obtain the final synthetic SFD which can be compared with the observed SFD.

Such a long integration time of SPH simulation was viable for two reasons. First, Hygiea is a much larger body than targets studied in previous works, allowing us to use larger time steps; the same run time would require about forty times the computation time if used for $D = 10\,\mathrm{km}$ targets. Second, the total number of performed simulations is significantly lower; in the previous works, we thoroughly explored the parameter space, here we only focused on one particular impact regime.

The initial density of the target was set to $\rho_0 = 2000\,\mathrm{kg/m^3}$ to approximately match the derived density $\rho \simeq 1944\,\mathrm{kg/m^3}$ of Hygiea. Other material parameters were equal to the parameters of basalt, assuming a monolithic internal structure of the target. As Hygiea is one of the largest bodies in the Main belt, it was likely a primordial body with low macroporosity [Morbidelli et al., 2009] and the monolithic material model is thus viable. The number of particles was $N = 4 \times 10^5$ in all simulations.

The main goal of our work was to find the parameters of the target and impactor that simultaneously produce SFD matching the observed family and the shape of the largest remnant with semi-axes and sphericity similar to the present-day asteroid (10) Hygiea.

6.3 Major results

We ran a number of hybrid SPH/N-body simulations from which we selected a few that match the observed SFD most closely. Snapshots of one representative simulation can be seen in Fig. 6.2.

6.3.1 Matching SFD

SFDs of selected simulations are shown in Fig. 6.3. In these simulations, the von Mises rheology is used for both the target and the impactor. Some simulations intentionally overestimated or underestimated the total ejected mass to get an idea of how big the error bars are for the studied impact parameters. Using these results, we inferred that a SFD with the same ratio of the largest remnant to the largest fragment can be obtained by an impactor with a diameter between 75 km and 150 km, depending on the impact angle. The best match can be achieved with the impactor diameter $d_{\mathrm{imp}} \simeq 100\,\mathrm{km}$.

Given such a large impactor, this event belongs among the most energetic impacts in the Main-belt history. For comparison, the family associated with asteroid (221) Eos was likely created by a $d_{\mathrm{imp}} \approx 200\,\mathrm{km}$ impactor. For (24) Themis, the probable impactor diameter is $d_{\mathrm{imp}} \approx 160\,\mathrm{km}$, for (15) Eunomia it is $d_{\mathrm{imp}} \approx 90\,\mathrm{km}$, and for (4) Vesta $d_{\mathrm{imp}} \approx 65\,\mathrm{km}$ [Durda et al., 2007].

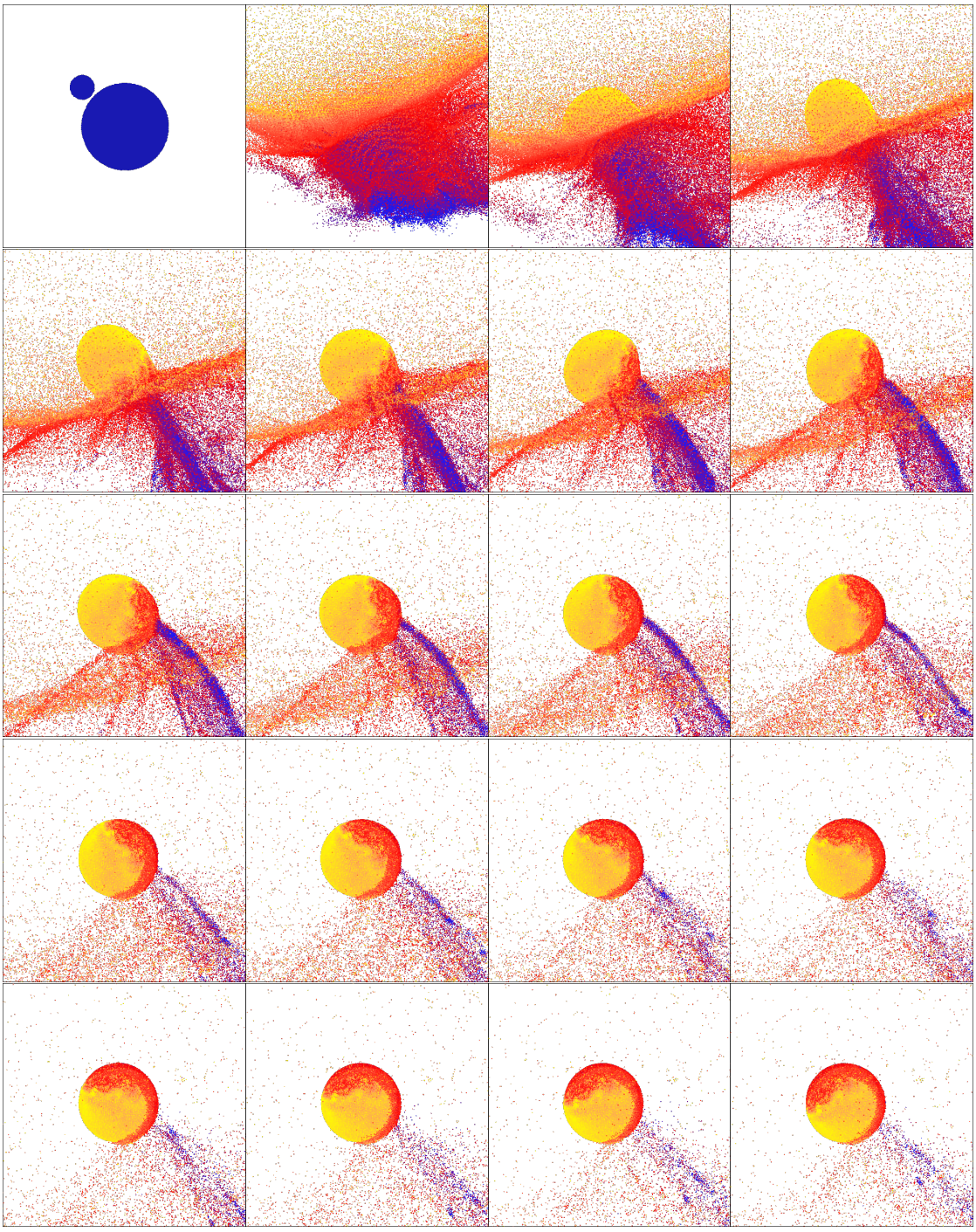

Figure 6.2: Snapshots of one of the performed impact simulations. The impactor diameter was $d_{\mathrm{imp}} = 120\,\mathrm{km}$ and the impact angle $\phi_{\mathrm{imp}} = 45^{\circ}$. The color of particles corresponds to the specific internal energy, time elapsed between consecutive images is 30 min. The impact clearly cannot be classified as a cratering event; the entire target disintegrated and the largest remnant, despite being similar in size to the parent body, gained its mass only after substantial reaccumulation.

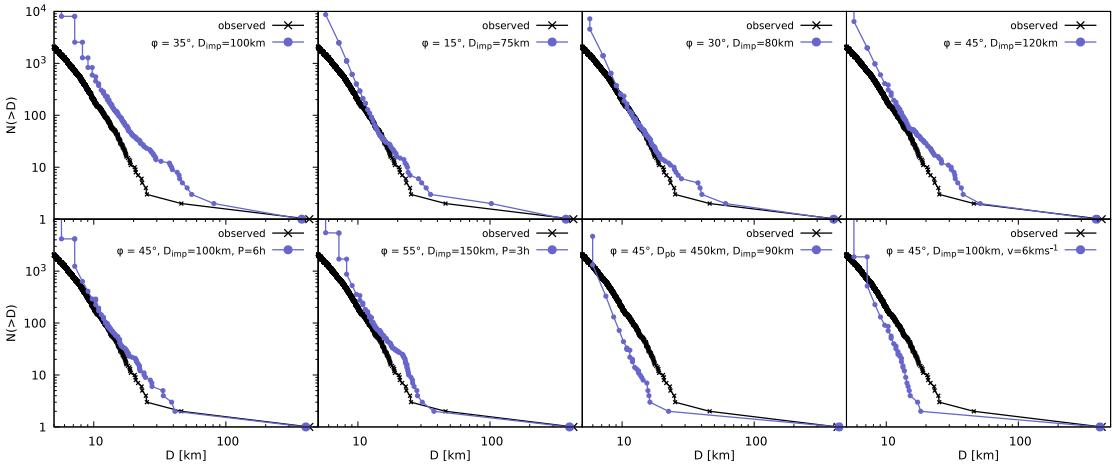

Figure 6.3: Selected synthetic SFDs compared with the observed SFD of the Hygiea family. Probable interlopers have been removed from the observed SFD.

For the studied impact on Hygiea, the relative impact energy was $Q/Q^{\star}_{\mathrm{D}} \approx 0.25$, assuming the scaling law $Q^{\star}_{\mathrm{D}} = Q^{\star}_{\mathrm{D}}(D)$ of Benz and Asphaug [1994]. As the impact energy is substantially lower than 1, this impact falls to the cratering regime. Indeed, most of the mass is stored in the largest remnant; the largest fragment with a diameter of $d_{\mathrm{lf}} \simeq 40$ is ten times smaller than Hygiea itself. However, Fig. 6.2 clearly shows that the whole target has been disintegrated and later reaccumulated due to self-gravitation. The parent body was fully damaged by the impact and the pre-impact topography was completely erased, meaning any craters found on the present-day Hygiea are necessarily younger than the family. It shows that the established nomenclature does not fit this particular impact well, as the role of self-gravity is much more important for the $D_{\mathrm{pb}} = 428\,\mathrm{km}$ parent body, compared to the $D_{\mathrm{pb}} = 100\,\mathrm{km}$ asteroids. This impact is evidently not a "cratering" event, perhaps a "reaccumulative" event is a more suitable term.

Although both the head-on and oblique impacts can produce the observed a SFD with a power-law slope similar to the observed value, we noticed the head-on impacts consistently produce intermediate-sized fragments, while no such fragments were observed in SFDs of the oblique impacts. These intermediate-sized bodies have diameters in the range $40\,\mathrm{km} < D < 100\,\mathrm{km}$ and they always originate from the antipode, see Fig. 6.4. As these fragments do not fit to the canonical SFDs, where only the largest remnant and a power-law of smaller fragments are expected, the intermediate-sized bodies are often discarded as interlopers.

The intermediate-sized bodies are particularly interesting in the case of the Hygiea family. Although the two largest bodies in the region have been removed as interlopers, there still remains an intermediate-sized asteroid, (1599) Giomus with diameter of $d \simeq 41\,\mathrm{km}$. Its reflection spectrum seems to be similar to the spectrum Hygiea; see the Supplementary Information of Vernazza et al. [2020]. We thus hypothesized that Giomus is indeed a family member that has been ejected from the antipode of the parent body during the impact. This helps us to constrain the impact geometry. It likely was a head-on or low-angle impact, as there is no significant

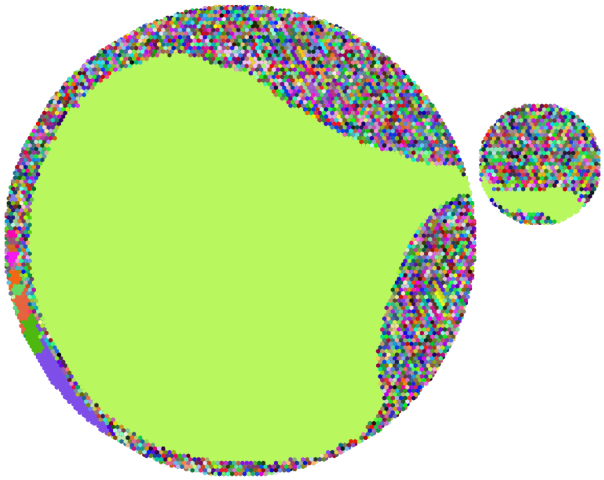

Figure 6.4: Original positions of particles that end up in the same fragment. Each fragment is rendered with a unique color. As $Q/Q^{\star}_{\mathrm{D}} \approx 0.25$, most of the particles form the largest remnant (lime color). Several of the largest fragments are ejected from the impact antipode.

fragment ejection from antipode in case of oblique impacts. Furthermore, one could estimate the direction from which the impactor arrived.

Finally, we see two major sources of fragments in our simulations. The first group of fragments originate from the antipode and generally contains larger bodies, as mentioned above. The second group is ejected from the point of the impact and contains smaller fragments, often underresolved in our simulations (i.e. single-particle fragments). This group lies close to the impact plane, perpendicular to the normal at the impact point. Both groups differ in the specific internal energies of fragments. The antipodal fragments are mostly ejected by the shock wave (reflection from free surface) and therefore their internal energy is quite low. On the other hand, the impact-point fragments are significantly heated by the compression and their peak internal energy is higher by one or two orders of magnitude. This distinction may potentially influence the taxonomical classes of both groups.

6.3.2 Constraining dry friction

In the simulations computed with the von Mises material, a fully damaged body will always end up as a Maclaurin spheroid due to its self-gravity. However, a body made of granular material always has non-zero shear strength, hence the largest remnant as well as fragments generally have non-trivial shapes, often significantly different from spheroids. To analyze the shape of synthetic largest remnant, we further ran a set of simulations with the Drucker-Prager material model with various values of the coefficient μ_{d} of dry friction. Several of the simulations are summarized in Fig. 6.5.

We compared these results to the shape of present-day Hygiea. The spherical shape without large-scale topographical features is a natural outcome of an energetic impact event, considering the largest remnant was created by reaccumulation of smaller fragments. However, we found

μ_d	0	0.05	0.2	0.6
c/b	0.988	0.937	0.906	0.913
b/a	0.999	0.987	0.911	0.943
surface	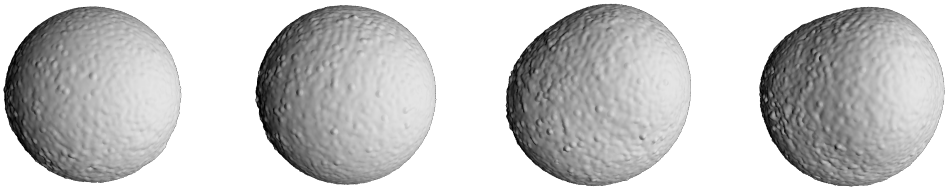			

Figure 6.5: The shape of the largest remnant is shown for increasing values of the coefficient μ_d of dry friction. Columns show μ_d together with the resulting ratios of semi-axes c/b and b/a. To obtain a shape consistent with the observed one for (10) Hygiea, the friction coefficient needs to be as low as 0.1. This substantial weakening of the material can be attributed to acoustic fluidization.

that Hygiea is actually *too* spherical. Assuming realistic values[6] of μ_d, the largest remnants in our simulations were much more deformed; for reference, the ratii of semiaxes of (10) Hygiea are $c/b = 0.989$ and $b/a = 0.955$. The coefficient of dry friction has to be extremely low to obtain a shape consistent with the observational data. Counter-intuitively, the simulations with the von Mises rheology give better predictions than the more physically accurate Drucker-Prager model.

We attribute this discrepancy to fluidization of material during the impact. The material strength must have been significantly weakened by the impact, thus allowing the material to flow almost like a fluid during a short transient period after the impact, before the material strength was regained. This material weakening is commonly explained as the acoustic fluidization, as briefly discussed in Sec.2.8.3.

To better understand the fluidization, we looked at the evolution of the shape of the largest remnant during the simulations with the von Mises material. We observed macroscopic oscillations of the body with the Keplerian period, as seen on Fig. 6.6. Naturally, the oscillations are eventually attenuated due to the lack of friction and we end up with a body that is much more spherical than Hygiea; nevertheless, the ratii of semi-axes often seem to match the observed values at some point during the simulations, usually around $t_\mathrm{match} = 4\,\mathrm{h}$. If the von Mises model was used as a "proxy" for the fluidized material and the dry friction was only added at time t_match to solidify the material, the shapes of the synthetic largest remnants would be much closer to the observed shape, compared to the simulations with the Drucker-Prager material.

This can be modeled more realistically by weakening the material in the presence of acoustic waves and using an exponential decay for the fluidization magnitude, as explained in Sec. 2.8.3. However, the time scale of such decay is still a free parameter, which is difficult to constrain independently, it is thus infeasible to make any predictions based on the model alone. The

[6]The coefficient μ_d of dry friction is between 0.4 and 1 for most materials.

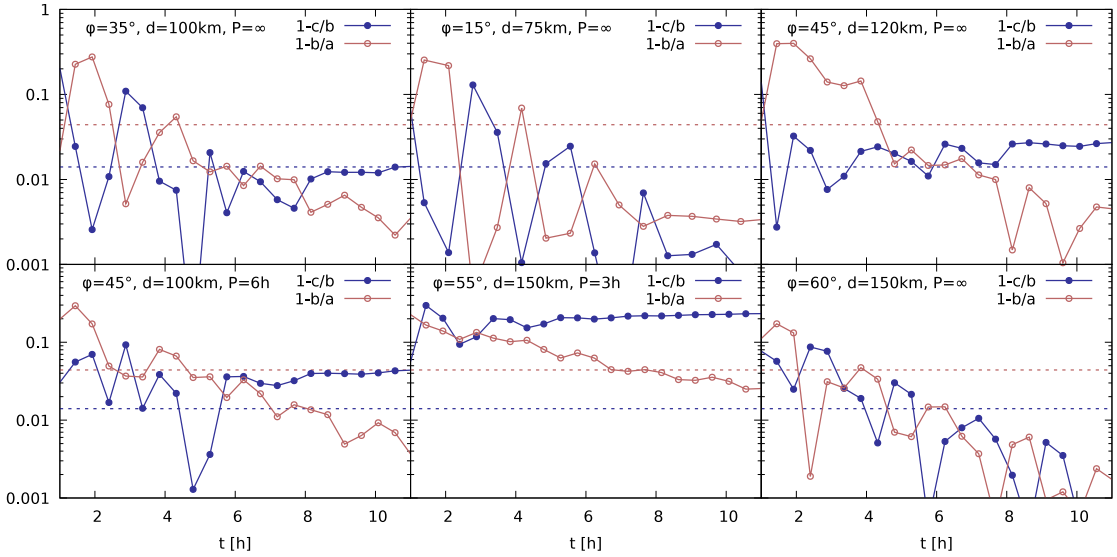

Figure 6.6: Global oscillations of the largest remnant in SPH simulations. Temporal evolution of the axis ratios $1 - c/b$ (blue) and $1 - b/a$ (red) is shown, along with the present-day observed values (dashed lines). In most simulations (5 out of 6), it is possible to find an agreement, typically around (4 ± 1) hours, which may be regarded as the acoustic fluidization time span. When acoustic oscillations stop, the body suddenly regains its strength and the shape freezes. The impact angle, projectile size and initial rotation period are indicated on top.

respective time scale certainly depends on the size of bodies. For Earth-sized planets, acoustic waves will travel away from the impact point, while for Hygiea-sized asteroids, they will reflect multiple times from the free surface.

In any case, the acoustic fluidization has been employed in several other contexts to interpret observational data, hence the Hygiea case study is very useful to examine weakening of materials due to high-energy impacts and constrain the time scale of such fluidization.

6.4 Reprint

See pages 149 to 154.

nature astronomy

LETTERS

https://doi.org/10.1038/s41550-019-0915-8

A basin-free spherical shape as an outcome of a giant impact on asteroid Hygiea

P. Vernazza[1*], L. Jorda[1], P. Ševeček[2], M. Brož[2], M. Viikinkoski[3], J. Hanuš[2], B. Carry[4], A. Drouard[1], M. Ferrais[5], M. Marsset[6], F. Marchis[1,7], M. Birlan[8], E. Podlewska-Gaca[9,10], E. Jehin[5], P. Bartczak[9], G. Dudzinski[9], J. Berthier[8], J. Castillo-Rogez[11], F. Cipriani[12], F. Colas[8], F. DeMeo[6], C. Dumas[13], J. Durech[2], R. Fetick[1,14], T. Fusco[1,14], J. Grice[4,15], M. Kaasalainen[3], A. Kryszczynska[9], P. Lamy[1], H. Le Coroller[1], A. Marciniak[9], T. Michalowski[9], P. Michel[4], N. Rambaux[8], T. Santana-Ros[16,17], P. Tanga[4], F. Vachier[8], A. Vigan[1], O. Witasse[12], B. Yang[18], M. Gillon[5], Z. Benkhaldoun[19], R. Szakats[20], R. Hirsch[9], R. Duffard[21], A. Chapman[22] and J. L. Maestre[23]

(10) Hygiea is the fourth largest main belt asteroid and the only known asteroid whose surface composition appears similar to that of the dwarf planet (1) Ceres[1,2], suggesting a similar origin for these two objects. Hygiea suffered a giant impact more than 2 Gyr ago[3] that is at the origin of one of the largest asteroid families. However, Hygeia has never been observed with sufficiently high resolution to resolve the details of its surface or to constrain its size and shape. Here, we report high-angular-resolution imaging observations of Hygiea with the VLT/SPHERE instrument (~20 mas at 600 nm) that reveal a basin-free nearly spherical shape with a volume-equivalent radius of 217 ± 7 km, implying a density of $1{,}944 \pm 250$ kg m^{-3} to 1σ. In addition, we have determined a new rotation period for Hygiea of ~13.8 h, which is half the currently accepted value. Numerical simulations of the family-forming event show that Hygiea's spherical shape and family can be explained by a collision with a large projectile (diameter ~75–150 km). By comparing Hygiea's sphericity with that of other Solar System objects, it appears that Hygiea is nearly as spherical as Ceres, opening up the possibility for this object to be reclassified as a dwarf planet.

Although it is an easy target for ground-based observations owing to its large angular diameter, Hygiea is the least studied of the four asteroids with diameters greater than 400 km (Ceres, (2) Pallas, (4) Vesta and Hygiea; Fig. 1), whose large sizes may have allowed them to reach hydrostatic equilibrium early in their history. It follows that a number of its basic physical properties, such as its shape and spin state, have not yet been reliably constrained.

To constrain these physical properties, we performed—as part of our European Southern Observatory large programme[4]—high-angular-resolution imaging observations of Hygiea with the SPHERE (Spectro-Polarimetric High-contrast Exoplanet REsearch) instrument on the VLT (Very Large Telescope) at 12 different epochs in 2017 and 2018. We used the new-generation visible adaptive optics ZIMPOL (Zurich IMaging POLarimeter)[5] in narrow-band imaging mode (N_R filter; central wavelength 645.9 nm). To restore the optimal angular resolution of each reduced image, we used the MISTRAL (Myopic Iterative STep Preserving ALgorithm) myopic deconvolution algorithm[6] along with a parametric point spread function[7]. We then applied the All-Data Asteroid Modeling (ADAM)[8] algorithm to our set of deconvolved images to reconstruct the three-dimensional (3D) shape model and the spin of Hygiea. The shape reconstruction was complicated by discernible albedo variegation apparent in the images (see Methods). To take into account such phenomena, the relative brightness of each facet with respect to the surrounding ones was treated as a free parameter (we allowed a maximum variegation of ±30%), and we further defined a smoothing operator as a regularization term to prevent large deviations between neighbouring facets. The comparison between the 12 adaptive optics epochs and the corresponding shape model projections is shown in Fig. 2.

Our best fits yielded semi-axes of 225 ± 5 km, 215 ± 5 km and 212 ± 10 km and a volume-equivalent radius of 217 ± 7 km. We found a rotational pole of right ascension $319 \pm 3°$, declination $-46 \pm 3°$ and a rotation period of 13.82559 ± 0.00005 h, which is half the previously reported and widely accepted value[9]. Our rotation period is compatible both with all light curves acquired so far for Hygiea, including the ones acquired with the Transiting Planets and Planetesimals Small Telescopes (TRAPPIST) in parallel with

[1]LAM (Laboratoire d'Astrophysique de Marseille) UMR 7326, Aix Marseille Université, CNRS, Marseille, France. [2]Institute of Astronomy, Charles University, Prague, Czech Republic. [3]Mathematics and Statistics, Tampere University, Tampere, Finland. [4]Laboratoire Lagrange, Université Côte d'Azur, Observatoire de la Côte d'Azur, CNRS, Nice, France. [5]Space Sciences, Technologies and Astrophysics Research Institute, Université de Liège, Liège, Belgium. [6]Department of Earth, Atmospheric and Planetary Sciences, MIT, Cambridge, MA, USA. [7]SETI Institute, Carl Sagan Center, Mountain View, CA, USA. [8]IMCCE, Observatoire de Paris, Paris, France. [9]Astronomical Observatory Institute, Faculty of Physics, Adam Mickiewicz University, Poznań, Poland. [10]Institute of Physics, University of Szczecin, Szczecin, Poland. [11]Jet Propulsion Laboratory, California Institute of Technology, Pasadena, CA, USA. [12]European Space Agency, ESTEC - Scientific Support Office, Noordwijk, the Netherlands. [13]TMT Observatory, Pasadena, CA, USA. [14]ONERA, The French Aerospace Lab, Chatillon, France. [15]School of Physical Sciences, The Open University, Milton Keynes, UK. [16]Departamento de Física, Ingeniería de Sistemas y Teoría de la Señal, Universidad de Alicante, Alicante, Spain. [17]Institut de Ciències del Cosmos, Universitat de Barcelona, Barcelona, Spain. [18]European Southern Observatory (ESO), Santiago, Chile. [19]Oukaimeden Observatory, High Energy Physics and Astrophysics Laboratory, Cadi Ayyad University, Marrakesh, Morocco. [20]Konkoly Observatory, Research Centre for Astronomy and Earth Sciences, Hungarian Academy of Sciences, Budapest, Hungary. [21]Instituto de Astrofísica de Andalucía (CSIC), Glorieta de la Astronomía, Granada, Spain. [22]Observatorio de Buenos Aires, Buenos Aires, Argentina. [23]Observatorio de Albox, Albox, Spain. *e-mail: pierre.vernazza@lam.fr

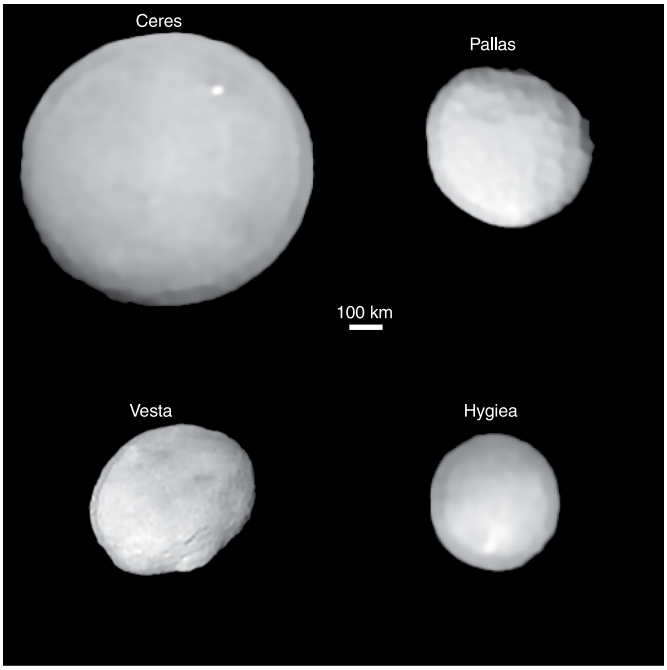

Fig. 1 | VLT/SPHERE deconvolved images of the four largest main belt objects. The relative sizes are respected, and the scale is indicated on the plot.

our SPHERE observations (Supplementary Fig. 1), and the SPHERE images. The axial ratios, including their uncertainties, appear compatible with the equilibrium Maclaurin spheroid. The specific angular momentum $L_{norm} = L/\sqrt{GM^3R}$, where L denotes the actual angular momentum of the body, G the gravitational constant, M the mass and R the mean radius, is equal to 0.070 ± 0.002, which is lower than the bifurcation point (0.304) where the equilibrium figure becomes a triaxial Jacobi ellipsoid[10].

Our shape and our best estimate of Hygiea's mass ($(8.32 \pm 0.80) \times 10^{19}$ kg; Supplementary Fig. 2 and Supplementary Table 3) yield a density of 1,944 ± 250 kg m^{-3}. Such density is compatible, within errors, with Ceres's density[11] (2,161.6 ± 2.5 kg m^{-3}). Note that the reaccumulation process following the giant impact at the origin of the family may have triggered some level of macroporosity, and the original density of Hygiea may be even closer to that of Ceres. The high water fraction inferred in both cases, along with their similar spectral properties[1,2], imply a formation location beyond the snowline for these two bodies.

We observed Hygiea with sub-Earth latitudes near 50° S (first epoch) and 24° S (second epoch) so that the visible surface extended from 66° N to 90° S, leading to ~95% surface coverage. Surprisingly, none of our images and their associated contours (Supplementary Fig. 3) revealed the large impact basin expected from the large size of the Hygiea family[3,12] (volume-equivalent diameter (D_{eq}) of the family members ~100 km; see Methods). In comparison, Vesta possesses a large impact basin that is clearly observable from the ground[7,13] (Fig. 1), although its family is smaller in volume than Hygiea's family by a factor of ~8 ($D_{eq} \approx 50$ km)[12]. To quantify the overall absence of a large basin on Hygiea, we fit Hygiea's 3D shape model with an ellipsoid and, subsequently, measured the radial difference between the two shapes. We also calculated the volume fraction of excavated material as $|V_{body} - V_{ellipsoid}|/V_{body}$. We performed the same calculations for Ceres and Vesta. Our calculations show that the large-scale topography of Hygiea is similar to that of Ceres, implying a global lack of large impact basins across its surface. They also reveal that—similar to Ceres—Hygiea's shape is very close to that of an ellipsoid. In the case of Vesta, the existence of a large depression is clearly observed in the histogram (Supplementary Fig. 4).

To investigate the origin of Hygiea's nearly spherical shape, as well as the absence of a large impact basin, we used a smoothed-particle hydrodynamics (SPH) code[14–16] to simulate the family-forming event. Our code is well adapted to simulate collisions of rotating and self-gravitating asteroids. We assumed monolithic basaltic material, the Tillotson equation of state[17], the von Mises yield criterion[18] to account for plastic deformations and the Grady–Kipp model[19] for fragmentation. The self-gravity has been implemented using the Barnes–Hut algorithm[20]. All input parameters are listed in Supplementary Table 5. Before running the simulations, our code was tested against previous studies[14], and we carefully verified the stability of rotating objects, as well as the validity of the gravity approximation by comparing it with the 'brute force' approach.

We performed a large number of simulations testing various projectile diameters (D_{imp} range: 70–150 km), impact angles (ϕ_{imp} range: 15–60°) and initial rotation periods for the target (P_{pb} range: 3–∞ h, where the subscript 'pb' denotes the parent body). Large values for the projectile diameter were required to match the large size of the Hygiea family. We further used a range of impact speeds from 5 km s^{-1} to 7 km s^{-1}. Both fragmentation and reaccumulation phases were computed by the SPH algorithm to resolve the shape of the largest remnant (that is, Hygiea). For the final reaccumulation only, we switched to a more efficient N-body algorithm, using hard-sphere and perfect-merging approximations, to obtain a synthetic family and its size-frequency distribution (SFD). The numerical model is described in detail in Methods.

A first outcome of our simulations is that Hygiea's final shape is highly spherical, regardless of the diameter of the impactor (in the 75–150 km size range) and the impact angle (Fig. 3). In particular, all pre-existing surface features have been erased, implying that the observed absence of a large impact basin on Hygiea is a natural outcome of the family-forming impact. We further used the SFD of the observed family to better constrain the parameters of the giant collision. It appears that the observed SFD can be matched either by head-on (0–30°) $D_{imp} = 75$ km impacts or, alternatively, oblique (30–60°) $D_{imp} = 150$ km impacts, although only the head-on impacts form one or a few intermediate-sized (40 km < D < 100 km, where D is the diameter) fragments; no such fragments are formed for impact angles greater than 45°. Given that the second largest body of the family ((1599) Giomus; see Methods) is indeed an intermediate-sized fragment, the head-on impact is more plausible. It follows that the impactor probably had $D_{imp} \approx 100$ km. Our simulations imply that the impact fully damaged the parent body and resulted in substantial reaccumulation[21]. When Hygiea formed, macroscopic oscillations drove the material to behave as a fluid[22], naturally resulting in the formation of a nearly spherical object in rotational equilibrium (Fig. 3). Accordingly, the effective friction of the damaged material had to be negligible for Hygiea (see Methods). Some departures from a rotational equilibrium can occur only if the material regains its strength, for example when acoustic fluidization is stopped[23,24]. Indeed, we detect global oscillations of the shape in our simulations (see Supplementary Fig. 5), which logically occur on the Keplerian timescale, that is, 2.4 h. Using a, b and c for semi-axes of a dynamically equivalent ellipsoid, we can explain the observed b/a and c/b ratios provided the fluidization stopped after approximately 4 h. In contrast to Hygiea, the Rheasilvia basin on Vesta resulted from an impact by a $D \approx 65$ km-sized projectile[25]. In this case, we suppose that, as Vesta is around three times more massive than Hygeia, the impact energy was not sufficient to completely shatter it, and the collision ended up being an excavation event.

The nearly spherical shape of Hygiea led us to evaluate the possibility of classifying this object as a dwarf planet. Any main belt asteroid immediately satisfies three of the four characteristics required for an object being labelled a dwarf planet, namely, a celestial

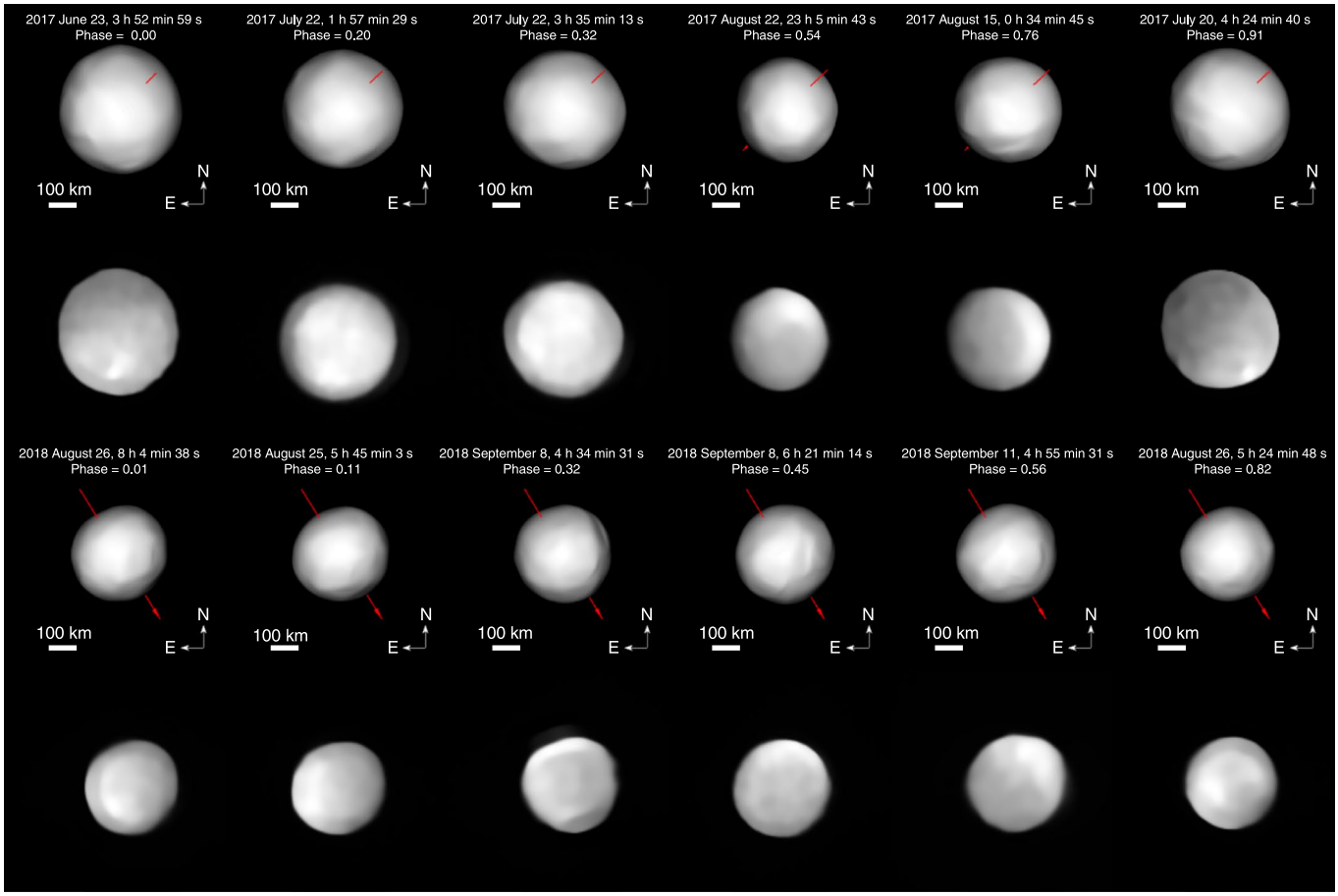

Fig. 2 | Comparison between the deconvolved images of Hygiea and the corresponding shape model projections. Bottom rows: Hygiea. Top rows: the corresponding shape model projections. Hygiea's spin axis (red) is also shown.

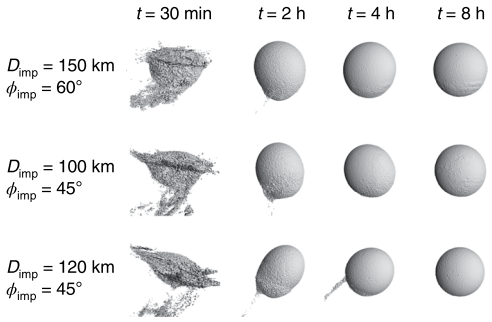

Fig. 3 | SPH simulations reveal a nearly spherical shape for Hygiea following post-impact reaccumulation. SPH simulations were ran to simulate the giant collision at the origin of the prominent Hygiea family, with a focus on the post-impact shape of the largest remnant, namely, Hygiea. For an accurate representation of the surface, we generated it as an isosurface of the density, using the ray-marching algorithm, rather than rendering individual SPH particles. At time $t = 30$ min, Hygiea is fully fragmented and notably deformed. Shortly after, most of the ejected material reaccumulates on Hygiea. Finally, macroscopic oscillations are suppressed, and Hygiea reaches a nearly spherical equilibrium shape. No large crater has been preserved.

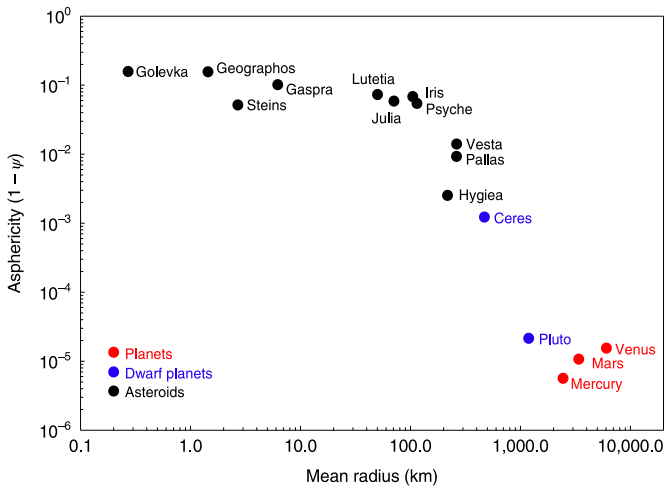

Fig. 4 | Asphericity of Solar System objects as a function of their mean radius. The parameter ψ corresponds to the sphericity index[26] applied to spherical harmonics developments of the 3D shape models of each object. Hygiea appears nearly as spherical as the dwarf planet Ceres.

body that (1) is in orbit around the Sun, (2) has not cleared the neighbourhood around its orbit and (3) is not a satellite. The fourth requirement is to have sufficient mass for its self-gravity to overcome rigid body forces so that it assumes a hydrostatic equilibrium nearly round shape. To properly quantify this last and essentially main criterion, we measured the sphericity[26], ψ, of Hygiea (see Methods) for comparison with that of the terrestrial planets, the two dwarf planets (134340) Pluto and Ceres and a few asteroids (Fig. 4).

It appears that Hygiea is nearly as spherical as Ceres ($\psi_{\mathrm{Hygiea}} \approx 0.9975$; $\psi_{\mathrm{Ceres}} \approx 0.9988$). Hygiea could thus be classified as a dwarf planet, so far the smallest in the Solar System. We anticipate the discovery of several new dwarf planet candidates when 3D shape models become available for $D > 400$ km trans-Neptunian objects.

Methods

Revision of Hygiea's rotation period. As part of our European Southern Observatory large programme[4] (199.C-0074; principal investigator: P.V.), we acquire complementary light curves when the pole solution of our target is not well constrained and/or when we are not able to reconstruct its 3D shape with ADAM[8], possibly indicating a wrong estimate of its pole solution or of its rotation period. This is exactly the case for Hygiea. Since 1991[9], multiple authors have all reported a rotation period of 27.6 h for Hygiea[27], but there has always been a lack of densely sampled phased light curves for this object.

We therefore planned our observations assuming a 27.6 h rotation period, and we observed Hygiea with TRAPPIST-North and -South[28] over a time frame of ~40 nights. The phased light curve started to show an ordinary double-sinusoidal shape as our observations were going on. However, the light curve appeared to be perfectly symmetrical, which is very unlikely. We then phased the data using the half period of ~13.8 h, which produced a very convincing fit with a single peak light curve (Supplementary Fig. 1). Assuming this new rotation period, we were able to reconstruct Hygiea's 3D shape model and to constrain its spin. In addition, the phasing of our VLT/SPHERE images acquired at several epochs were correct with this new rotation period, which was not the case with the old one.

How round is Hygiea?. *Contour extraction.* We used a first approach, namely, contour extraction[7], to highlight the sphericity of Hygiea. In Supplementary Fig. 3, we compare the contours of our Hygiea images with those of a sphere, revealing—on average—a minimal difference between the two. It is important to stress that the contours obtained with VLT/SPHERE are precise at the pixel level[7].

Calculation of the sphericity. To constrain Hygiea's sphericity and compare it with that of other Solar System bodies, including planets and minor bodies (asteroids, comets), we applied a sphericity formula[26] to our 3D shape model. Following this formula, the sphericity is a function of the surface area and of the volume. However, the surface area is very sensitive to the surface topography and the resolution of the 3D shape model. Therefore, performing a direct comparison of the sphericity of various objects having very different 3D shape model resolutions and/or topographies would lead to incorrect results. To overcome this problem and to perform a self-consistent comparison, we computed the real spherical harmonic expansion coefficients (tenth order) of the 3D shape model for each object[4,29–40]. By doing so, we produced 3D shape models that reproduce well the overall shape of our objects, ignoring the small-scale topographic variations. An example of the procedure is highlighted in Supplementary Fig. 6. As a final step, we applied the formula of the sphericity to these spherical harmonics models.

Hygiea's reflectance map. The best-quality SPHERE images were combined into a cylindrical-projection map to study the main geological features of Hygiea. We call it a reflectance map because it contains both albedo and shadow information. Indeed, the limited number of observed geometries and the resolution of the images do not allow us to accurately correct for illumination of local topography. As a consequence, we cannot always separate albedo information from shadowing effects.

The quality of each sequence of observations was evaluated according to three criteria: (1) the angular size of Hygiea at the time of the observation, (2) the presence, or not, of deconvolution artefacts in the images and (3) the consistency of the location of the main albedo features on the surface of Hygiea across the full sequence of images. According to these criteria, the first two epochs of observations, 2017 June 23 and 2017 July 20, were found to provide the highest image quality. The images for these two epochs also exhibit the highest variability in reflectance seen across the surface of Hygiea, and include most of its main albedo features. We therefore chose to use only these images to maximize the resolution and reliability of our map, despite the fact that they sample only about one-third of the total surface covered by our complete set of observations.

A photometric correction was applied to each image to correct the overall illumination gradient[7]. The asteroid-centric longitude and latitude of each pixel were measured using the ADAM shape model, and the values were projected using an equidistant cylindrical projection. The individual maps built from the complete set of selected images were then combined, using their overlapping regions to adjust their brightness level[7]. The combined map was finally normalized to the average geometric albedo of Hygiea of 7.2%.

The resulting reflectance map is shown in Supplementary Fig. 7. It exhibits a wide range of values, with more than 20% variability with respect to the average, although shadowed regions enhance this variability. Several bright spots are clearly identifiable, the brightest one, located near longitude $\lambda = 290°$, latitude $\phi = -30°$, showing a 10% brightness enhancement with respect to the average reflectance. The large dark region at $\lambda = 60°$, $\phi = 0°$ is most probably a shadowed region, as it is located near the asteroid limb on the second sequence of images.

For comparison, we further show a reflectance map of Ceres (Supplementary Fig. 7), built from our SPHERE observations following the same method as described above for Hygiea. Ceres was observed at one epoch as the benchmark target for our observing programme, with the NASA Dawn mission providing us with the ground truth for that object. Similarly to Hygiea, we used only the best-quality image acquired for that object when building its map. This image contains Ceres's main albedo feature, the bright spot located in the Occator crater. Ceres is slightly brighter than Hygiea in average albedo ($p_{\mathrm{V}} = 0.09$ versus $p_{\mathrm{V}} = 0.07$, where p_{V} is geometric albedo in the visual (V) band). The range of reflectance values revealed by our observations for these two bodies is very similar, with about 20% variability. Ceres's bright spot in the Occator crater, located around $\lambda = 240°$, $\phi = 20°$, shows a 20% brightness enhancement with respect to Ceres's average. To conclude, like the density and the spectral properties, the reflectance/albedo properties of Hygiea and Ceres are highly similar.

Cratering on Hygiea. From our set of images, we could identify only two unambiguous craters, with respective diameters of 180 ± 15 km and 97 ± 10 km (Supplementary Fig. 8). This low number of identified craters contrasts with the large number of craters recognized at the surface of Pallas (Fig. 1) and that of Vesta[7] and (7) Iris[41]. Although this may be understood as Hygiea's surface being younger than that of the above-mentioned bodies, it is unlikely to be the only explanation, given that Hygiea's surface age (estimated formation time of the family) is estimated to be at least 3 Gyr (ref. [3]). Both the crater morphology and, to a lesser extent, the reflectance properties of the surface play an important role in the contrast between the crater rim and crater floor. Whereas bowl-shaped craters will be easily identifiable from the ground, leading to a clear contrast between the crater floor/walls and the crater rim, the same will not be true in the case of complex craters with a flat floor. Most probably, our observations imply a paucity of large ($D > 30$ km, which corresponds to our detection limit) bowl-shaped craters in the case of Hygiea. This is an additional common feature between Hygiea and Ceres. In the case of Ceres, the Dawn mission has unambiguously revealed a heavily cratered surface[42], where most $D > 10$–15 km craters are not bowl shaped, but flat floored. By analogy with Ceres, this strongly supports the presence of water ice in the subsurface of Hygiea. The presence of water ice in the subsurface would also favour the relaxation of the surface topography as observed on Ceres[43], thus rendering the remote-sensing identification of craters on Hygiea more difficult.

Identifying the members of the Hygiea family. Before running the SPH simulations, we carefully identified the Hygiea family members using the proper elements[44] and the hierarchical clustering method[45], with the cut-off relative velocity $v_{\mathrm{cut}} = 60\ \mathrm{m\,s^{-1}}$. We further used physical data to remove interlopers with incompatible spectra (Supplementary Fig. 9 and Supplementary Table 4), colour (using Sloan Digital Sky Survey data[46]) or albedo (using Wide-field Infrared Survey Explorer[47] and AKARI[48] data). We found 6,857 family members and constructed their SFD. Besides the usual largest remnant (Hygiea), there is one intermediate-sized asteroid, namely Giomus, with $D = 46$ km, whose near-infrared spectrum is compatible with that of Hygiea (Supplementary Fig. 9). By summing the masses of fragments, we estimate that the mass ejected during the collision is at least 1.7% of the mass of Hygiea. In comparison, the ejected mass of the Vesta family makes up only 0.5% of Vesta, suggesting that the Hygiea-forming impact was substantially more energetic.

Numerical model. Impact simulations have been carried out using our SPH/*N*-body code OpenSPH. The code can perform both SPH and *N*-body simulations. It thus allows us to run a whole simulation, from an initial fragmentation to a final reaccumulation. In all simulations presented here, the duration of the SPH simulation is $t_{\mathrm{SPH}} = 24$ h, which is sufficient for the largest remnant (as well as for the largest fragments) to gain a well-defined shape and damp any macroscopic oscillations. We then follow up with the *N*-body simulation for another $t_{N\text{-body}} = 10$ d to obtain the final SFD of the synthetic family. The hand-off between the SPH and *N*-body parts is done by simply changing the solver and modifying the particle radii, $R_i = [3M_i/(4\pi\rho)]^{1/3}$, where M_i and R_i are respectively the mass and the radius of the ith particle, and ρ is the material density of the particle, to convert smoothed particles into hard spheres while preserving their masses and volumes.

The SPH solver computes particle accelerations due to the stress tensor and self-gravity, shock heating, material yielding and fragmentation. It further includes the artificial viscosity term for proper treatment of shocks, the artificial stress to suppress tensile instabilities and the correction tensor for consistent bulk rotation[49]. The code can use either a frictionless rheology (von Mises criterion) or a more complex Drucker–Prager rheology[15,50], which includes both internal friction for intact material and dry friction for damaged material. Motivated by the observed round shape of Hygiea, we used the simpler frictionless model, as the friction clearly did not play a major role in the Hygiea-forming impact. For comparison, we also ran simulations with various friction coefficients.

During *N*-body simulations, we searched for particle collisions, performing either an inelastic bounce or a merging of collided particles, depending on their relative velocities and the spin rate of the merger. When particles merged, the

resulting volume, velocity and spin rate of the merger were determined, to conserve the total volume, momentum and angular momentum. Overlapping particles were treated the same way as collided particles; as we performed a late hand-off when the relative velocities of particles inside individual fragments were already small, the respective particles underwent a quick merging, and a precise handling of overlaps was not needed. Although merging erased the shape information, here, we are interested only in fragment sizes, and merging is thus a viable option.

Rheology in SPH simulations. In the simulations presented in the main text, we use the von Mises criterion. The yield stress is computed using $Y=(1-d)Y_m$, where Y_m is a material-specific, but pressure-independent, constant and d is the scalar damage. In this model, fully damaged material experiences no friction and essentially behaves as a fluid.

To model friction of granular material (which would be especially important for asteroids and impacts much smaller than in Hygiea's case), we also implemented the Drucker–Prager rheology[15,50] in our code. It defines the yield strength of intact material as

$$Y_i = Y_0 + \frac{\mu_i p}{1+\mu_i p/(Y_{vM}-Y_0)}$$

where μ_i is the coefficient of internal friction, Y_0 is the cohesion (yield strength at zero pressure), Y_m is the von Mises elasticity limit and p is the pressure. For fully damaged rock, the yield strength, Y_d, is proportional to the pressure as $Y_d=\mu_d p$, where μ_d is the coefficient of dry friction, which is related to the angle of repose. In the intermediate state where $0<d<1$, the yield strength is given by a linear interpolation, $Y=(1-d)Y_i+dY_d$.

The final shape of the largest remnant is affected by the coefficient of dry friction. However, using the model with non-negligible friction, $\mu_d>0.1$, yields a very poor match to the observed round shape of Hygiea (see Supplementary Fig. 10). This issue has been previously recognized by studies of cratering events[24,25] and is commonly explained by introducing the acoustic fluidization. In the block model of acoustic fluidization, yield strength is further modified as $Y_{vib}=\mu_d(p-p_{vib})+\eta_l\rho\dot{\epsilon}$, where p_{vib} is the vibrational pressure, calculated from the maximum vibrational particle velocity[51], η_l is the effective viscosity of fluidized material and $\dot{\epsilon}$ is the strain rate. The vibrational velocity is exponentially attenuated after the impact; however, the timescale of this process is a free parameter. Instead of using the block model directly, we prefer the von Mises model, with a similar free parameter, that is, the timescale of acoustic fluidization after which the body regains its strength. This model matches the observed shape very well (see Fig. 3 and Supplementary Fig. 10).

Parameters of the SPH simulations. We considered both the target and the impactor to be monolithic bodies with an initial density of the material $\rho_0=2{,}000\,\mathrm{kg\,m^{-3}}$, corresponding to the present-day density of Hygiea. We assumed material properties of basalt[14,16]. The pressure and the sound speed were determined using the Tillotson equation of state, assuming bulk modulus $A=2.67\times10^{10}$ Pa, and specific energies for incipient and complete vaporization $u_{iv}=4.72\times10^6\,\mathrm{J\,kg^{-1}}$ and $u_{cv}=1.82\times10^7\,\mathrm{J\,kg^{-1}}$, respectively. The strength model used the von Mises yield criterion with shear modulus $\mu=2.27\times10^{10}$ Pa, elasticity limit $Y_m=3.5\times10^9$ Pa and specific melting energy $u_{melt}=3.4\times10^6\,\mathrm{J\,kg^{-1}}$. To account for material fragmentation, we used the Grady–Kipp model with Weibull coefficient $k=4\times10^{29}$ and Weibull exponent $m=9$. In our simulations, the target had $N\approx4\times10^5$ particles, the spatial resolution therefore being ~6 km, which is sufficient to resolve hundreds of the family members. The number of particles for the impactor was chosen so as to obtain the same particle density as the target. The equations were integrated using a predictor–corrector method, the time step of which was limited by the Courant–Friedrichs–Lewy criterion with Courant number $C=0.2$. A subset of our simulations and the parameters used are displayed in Supplementary Fig. 5. Finally, the cumulative SFDs of synthetic families are compared with the SFD of the observed Hygiea family in Supplementary Fig. 11.

Data availability

As soon as papers for our large programme are accepted for publication, we will make the corresponding reduced and deconvolved adaptive optics images and 3D shape models publicly available at http://observations.lam.fr/astero/.

Code availability

The code used to generate the 3D shape is freely available at https://github.com/matvii/ADAM. The code used to perform the SPH simulations is freely available at https://gitlab.com/sevecekp/sph.

Received: 8 April 2019; Accepted: 13 September 2019;
Published online: 28 October 2019

References

1. Takir, D. & Emery, J. P. Outer main belt asteroids: identification and distribution of four 3-μm spectral groups. *Icarus* **219**, 641–654 (2012).
2. Vernazza, P. et al. Different origins or different evolutions? Decoding the spectral diversity among C-type asteroids. *Astron. J.* **153**, 72 (2017).
3. Carruba, V., Domingos, R. C., Huaman, M. E., dos Santos, C. R. & Souami, D. Dynamical evolution and chronology of the Hygiea asteroid family. *Mon. Not. R. Astron. Soc.* **437**, 2279–2290 (2014).
4. Vernazza, P. et al. The impact crater at the origin of the Julia family detected with VLT/SPHERE? *Astron. Astrophys.* **618**, A154 (2018).
5. Thalmann, C. et al. SPHERE ZIMPOL: overview and performance simulation. *Proc. SPIE* **7014**, 70143F (2008).
6. Fusco, T. et al. Deconvolution of astronomical images obtained from ground-based telescopes with adaptive optics. *Proc. SPIE* **4839**, 1065–1075 (2003).
7. Fetick, R. et al. Closing the gap between Earth-based and interplanetary mission observations: Vesta seen by VLT/SPHERE. *Astron. Astrophys.* **623**, A6 (2019).
8. Viikinkoski, M., Kaasalainen, M. & Durech, J. ADAM: a general method for using various data types in asteroid reconstruction. *Astron. Astrophys.* **576**, A8 (2015).
9. Michalowski, T. et al. The spin vector of asteroid 10 Hygiea. *Astron. Astrophys. Suppl. Ser.* **91**, 53–59 (1991).
10. Chandrasekhar, R. *Ellipsoidal Figures of Equilibrium* (Dover Publications, 1987).
11. Park, R. S. et al. High-resolution shape model of Ceres from stereophotoclinometry using Dawn imaging data. *Icarus* **319**, 812–827 (2019).
12. Nesvorný, D., Brož, M. & Carruba, V. in *Asteroids IV* (eds Michel, P. et al.) 297–321 (Univ. Arizona Press, 2015).
13. Thomas, P. C. et al. Impact excavation on asteroid 4 Vesta: Hubble Space Telescope results. *Science* **277**, 1492–1495 (1997).
14. Benz, W. & Asphaug, E. Impact simulations with fracture. I. Method and tests. *Icarus* **107**, 98–116 (1994).
15. Jutzi, M., Holsapple, K., Wünneman, K. & Michel, P. in *Asteroids IV* (eds Michel, P. et al.) 679–699 (Univ. Arizona Press, 2015).
16. Ševeček, P. et al. SPH/*N*-body simulations of small ($D=10$ km) asteroidal breakups and improved parametric relations for Monte-Carlo collisional models. *Icarus* **296**, 239–256 (2017).
17. Tillotson, J. H. *Metallic Equations of State for Hypervelocity Impact* General Atomic Report GA-3216 (General Dynamics, 1962).
18. von Mises, R. Mechanik der festen Körper in plastisch-deformablen Zustand. *Nachr. d. Kgl. Ges. Wiss. Göttingen, Math.-phys. Klasse* **4**, 582–592 (1913).
19. Grady, D. & Kipp, M. Continuum modelling of explosive fracture in oil shale. *Int. J. Rock Mech. Min. Sci.* **17**, 147–157 (1980).
20. Barnes, J. & Hut, P. A hierarchical O(*N* log *N*) force-calculation algorithm. *Nature* **324**, 446–449 (1986).
21. Michel, P., Benz, W., Tanga, P. & Richardson, D. C. Collisions and gravitational reaccumulation: forming asteroid families and satellites. *Science* **294**, 1696–1700 (2001).
22. Tanga, P., Hestroffer, D., Delbo, M. & Richardson, D. C. Asteroid rotation and shapes from numerical simulations of gravitational re-accumulation. *Planet. Space Sci.* **57**, 193–200 (2009).
23. Melosh, H. J. & Ivanov, B. A. Impact crater collapse. *Ann. Rev. Earth Planet. Sci.* **27**, 385–415 (1999).
24. Riller, U. et al. Rock fluidization during peak-ring formation of large impact structures. *Nature* **562**, 511–518 (2018).
25. Jutzi, M., Asphaug, E., Gillet, P., Barrat, J.-A. & Benz, W. The structure of the asteroid 4 Vesta as revealed by models of planet-scale collisions. *Nature* **494**, 207–210 (2013).
26. Wadell, H. Volume, shape and roundness of quartz particles. *J. Geol.* **43**, 250–280 (1935).
27. Warner, B. D., Harris, A. W. & Pravec, P. The asteroid lightcurve database. *Icarus* **202**, 134–146 (2009).
28. Jehin, E. et al. TRAPPIST: TRAnsiting Planets and PlanetesImals Small Telescope. *Messenger* **145**, 2–6 (2011).
29. Pettengill, G. H., Ford, P. G., Johnson, W. T. K., Raney, R. K. & Soderblom, L. A. Magellan: radar performance and data products. *Science* **252**, 260–265 (1991).
30. Thomas, P. C. et al. The shape of Gaspra. *Icarus* **107**, 23–36 (1994).
31. Hudson, R. S. et al. *Asteroid Radar Shape Models, 6489 Golevka* PDS ID EAR-A-5-DDR-RADARSHAPE-MODELS-V1.1:RSHAPES-6489GOLEVKA-200006 (NASA PDS, 2000).
32. Ostro, S. J. et al. *Asteroid Radar Shape Models, 1620 Geographos* PDS ID EAR-A-5-DDR-RADARSHAPE-MODELS-V1.1:RSHAPES-1620GEOGRAPHOS-200006 (NASA PDS, 2000).
33. Smith, D. E. et al. Mars Orbiter Laser Altimeter: experiment summary after the first year of global mapping of Mars. *J. Geophys. Res.* **106**, 23689–23722 (2001).
34. Jorda, L. et al. Asteroid (2867) Steins: shape, topography and global physical properties from OSIRIS observations. *Icarus* **221**, 1089–1100 (2012).

35. Preusker, F. et al. Stereo-photogrammetrically derived topography of asteroid (4) Vesta. *Proc. American Geophysical Union, Meeting Number 93* abstr. P43E-05 (2012).
36. Jaumann, R. et al. Vesta's shape and morphology. *Science* **336**, 687–690 (2012).
37. Farnham, T. L. *Shape Model of Asteroid 21 Lutetia* PDS ID RO-A-OSINAC/OSIWAC-5-LUTETIA-SHAPE-V1.0 (NASA PDS, 2013).
38. Preusker, F. et al. Topography of Mercury: a global model from MESSENGER orbital stereo mapping. *Proc. Ninth Conference European Planetary Science Congress* Vol. 9 abstr. EPSC2014-709 (2014).
39. Preusker, F. et al. Dawn at Ceres—shape model and rotational state. *Proc. 47th Lunar and Planetary Science Conference* 1954 (LPI, 2016).
40. Viikinkoski, M. et al. (16) Psyche: a mesosiderite-like asteroid? *Astron. Astrophys.* **619**, L3 (2018).
41. Hanuš, J. et al. The shape of (7) Iris as evidence of an ancient large impact? *Astron. Astrophys.* **624**, A121 (2019).
42. Hiesinger, H. et al. Cratering on Ceres: implications for its crust and evolution. *Science* **353**, aaf4759 (2016).
43. Bland, M. T. et al. Composition and structure of the shallow subsurface of Ceres revealed by crater morphology. *Nat. Geosci.* **9**, 538–542 (2016).
44. Knezevic, Z. & Milani, A. Proper element catalogs and asteroid families. *Astron. Astrophys.* **403**, 1165–1173 (2003).
45. Zappala, V., Cellino, A., Farinella, P. & Milani, A. Asteroid families. II. Extension to unnumbered multiopposition asteroids. *Astron. J.* **107**, 772–801 (1994).
46. Ivezic, Ž. et al. Solar System objects observed in the Sloan Digital Sky Survey commissioning data. *Astron. J.* **122**, 2749–2784 (2001).
47. Nugent, C. R. et al. NEOWISE Reactivation Mission Year One: preliminary asteroid diameters and albedos. *Astrophys. J.* **814**, 117 (2015).
48. Usui, F. et al. Asteroid catalog using AKARI: AKARI/IRC Mid-infrared Asteroid Survey. *Pub. Astron. Soc. Jpn* **63**, 1117–1138 (2011).
49. Schäfer, C. et al. A smooth particle hydrodynamics code to model collisions between solid, self-gravitating objects. *Astron. Astrophys.* **590**, A19 (2016).
50. Collins, G. S., Melosh, H. J. & Ivanov, B. A. Modeling damage and deformation in impact simulations. *Met. Planet. Sci.* **39**, 217–231 (2004).
51. Silber, E. A., Osinski, G. R., Johnson, B. C. & Grieve, R. A. F. Effect of impact velocity and acoustic fluidization on the simple-to-complex transition of lunar craters. *J. Geophys. Res. Planets* **122**, 800–821 (2017).

Acknowledgements

P.V., A.D. and B.C. were supported by CNRS/INSU/PNP. M.Brož was supported by grant 18-04514J of the Czech Science Foundation. J.H. and J.D. were supported by grant 18-09470S of the Czech Science Foundation and by the Charles University Research Programme no. UNCE/SCI/023. This project has received funding from the European Union's Horizon 2020 research and innovation programmes under grant agreement nos 730890 and 687378. This material reflects only the authors' views, and the European Commission is not liable for any use that may be made of the information contained herein. TRAPPIST-North is a project funded by the University of Liège, in collaboration with Cadi Ayyad University of Marrakech (Morocco). TRAPPIST-South is a project funded by the Belgian Fonds (National) de la Recherche Scientifique (F.R.S.-FNRS) under grant FRFC 2.5.594.09.F. E.J. and M.G. are F.R.S.-FNRS Senior Research Associates.

Author contributions

P.V. designed the research. P.V., M.M., R.F. and T.F. reduced and deconvolved the SPHERE images. M.V. and J.H. reconstructed the 3D shape of Hygiea. L.J. and P.V. performed the analysis of Hygiea's shape. P.Š. and M.Brož ran the SPH simulations. M.F. and E.J. acquired and reduced the TRAPPIST data. M.M. and L.J. produced the albedo map. P.V. and F.D. served as principal investigators to acquire the near-infrared spectral data. B.C. provided the mass estimate. P.V., L.J., P.Š. and M.Brož worked jointly to write the manuscript. All authors discussed the results and commented on the manuscript.

Competing interests

The authors declare no competing interests.

Additional information

Supplementary information is available for this paper at https://doi.org/10.1038/s41550-019-0915-8.

Correspondence and requests for materials should be addressed to P.V.

Peer review information *Nature Astronomy* thanks Derek Richardson and the other, anonymous, reviewer(s) for their contribution to the peer review of this work.

Reprints and permissions information is available at www.nature.com/reprints.

Publisher's note Springer Nature remains neutral with regard to jurisdictional claims in published maps and institutional affiliations.

© The Author(s), under exclusive licence to Springer Nature Limited 2019

— Chapter vii —

CONCLUSIONS

In this thesis, we explored collisions of asteroids, their fragmentation and reaccumulation and formation of families. These processes were modeled using a hybrid approach, combining a state-of-the-art SPH solver with an N-body integrator.

7.1 Code development

To perform these simulations, we developed a new code named `OpenSPH`. The code includes both an SPH solver and an N-body solver and it can thus compute the entire hybrid simulation of a family-forming event, from the set-up of the initial conditions to the final fragment distribution. Combined with handy analysis and visualization utilities that allow to view the particle quantities while the simulation is running, the code greatly simplifies studies of collisions. We also utilized the visualization of the impact on the parent body of the Hygiea family, which was included in the ESO press release[1] and which met with success.

The code is robust and capable of simulating bodies or arbitrary sizes, allowing to compute collisions of planet-sized objects as well as small $D \sim 100$ m bodies. The only limitation is the time step, which effectively prohibits computing reaccumulative events of such small bodies. However, it is feasible to assume a lower bulk modulus of the material and thus substantially increase the time step. A similar trick was already done by Jutzi and Asphaug [2015] or Sugiura et al. [2019]. This opens up possibilities to study impacts and reaccumulations of small bodies which are less strengthened by gravity, or even bodies in the strength regime of the scaling law.

7.2 Simulations of D = 10 km and 100 km targets

At first, we focused on simulations that explore the parametric space of collisions, with no reference to a specific asteroid family. We studied the disruption of small $D_{\text{pb}} = 10$ km monolithic

[1] See `https://www.eso.org/public/news/eso1918/` (as of August 2021).

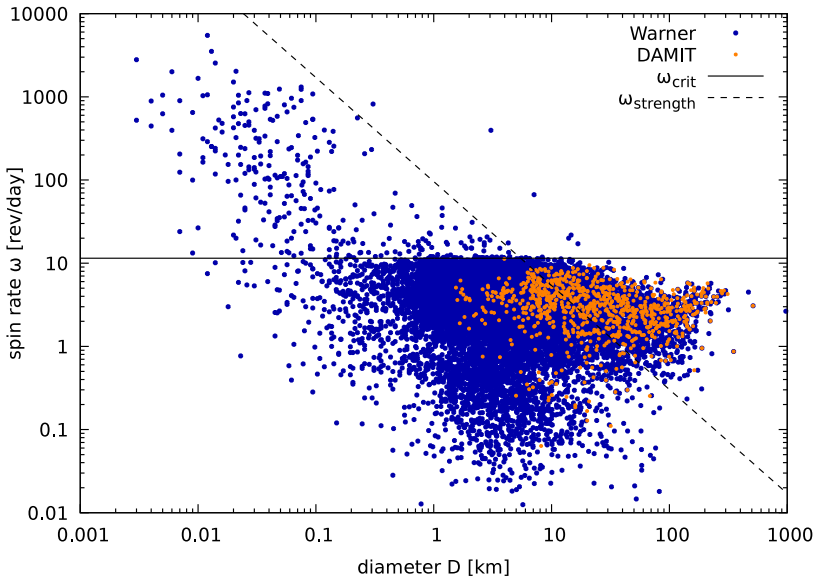

Figure 7.1: Scatter plot of asteroid diameters and their respective spin rates. The dashed line shows the limit spin rate ω_{strength} in the strength regime, as derived by Holsapple [2007]. Data from Warner et al. [2009]; Ďurech et al. [2010].

targets and compared the resulting SFDs with the corresponding SFDs of $D_{\text{pb}} = 100\,\text{km}$ targets from the dataset of Durda et al. [2007]. Using these synthetic SFDs, we assessed their scaling with the diameter D_{pb} of the parent body and estimated an error introduced by using simulations with fixed-sized targets to determine the size of a parent body of observed families.

The simulations showed that the corresponding $D_{\text{pb}} = 10\,\text{km}$ and $D_{\text{pb}} = 100\,\text{km}$ targets differ significantly in a large part of parametric space. The differences are most pronounced in the weak cratering regime ($Q/Q^{\star}_{\text{D}} \ll 1$) and in the supercatastrophic regime ($Q/Q^{\star}_{\text{D}} \gg 1$). We further see substantial differences in oblique impact angles, which we identified to be a geometrical effect.

We analyzed velocities of ejected fragments and constructed speed histograms as well as angular histograms of velocity directions. These velocity fields can be used as initial conditions of an N-body simulation of a synthetic family, allowing to constrain ages of observed families, as in e.g. Yang et al. [2020a].

The synthetic SFDs were used to construct parametric relations that can be utilized in Monte Carlo models of the Main Belt. For small $D \sim 10\,\text{km}$ bodies, these relations provide more accurate predictions for the mass M_{lr} of the largest remnant, the mass M_{lf} of the largest fragment and the slope q of the size-frequency distribution, compared to the parametric relations derived using $D_{\text{pb}} = 100\,\text{km}$ targets.

The second part of the thesis was focused on rotating asteroids. We mainly studied asteroids close to the spin barrier ω_{crit}. Considering a large fraction of observed asteroids have high spin rates (see Fig. 7.1), such bodies are an important case study. We assumed the target retains its spherical shape despite fast rotation due to shear strength, which is then released on impact.

The material rheology is thus more pronounced and studies of (almost) critically rotating asteroids are very valuable.

The fast rotation increases the ejected mass considerably. Compared to the static target, the mass ejection is larger by up to five times. When averaged over impact angles, the ejection is still increased by up to 100 %. We observed the biggest differences for large $D_{\mathrm{pb}} = 100\,\mathrm{km}$ targets, cratering events ($Q \ll Q^{\star}_{\mathrm{D}}$) and oblique impact angles.

We further studied the impact-induced change of the angular momentum of the target. The simulations showed that sub-catastrophic impacts mostly cause acceleration at prograde impact angles and deceleration at retrograde impact angles. However, the statistically average impact tends to decelerate the target. An asteroid encountering a number of successive cratering impacts will thus be slowed down over time. This angular momentum draining contrasts with the normal YORP effect which can cause both a spin-up and spin-down [Čapek and Vokrouhlický, 2004; Hanuš et al., 2011] and the tangential YORP effect which always accelerates the rotation [Golubov et al., 2014; Ševeček et al., 2015].

All impacts took place in the equatorial plane. Due to reflection symmetry, collisions mostly affected spin rates of targets, rotational axes remained unchanged. A similar analysis could be performed for general impact directions in order to study impact-induced rotational excitations, as in Henych and Pravec [2013].

7.3 (10) Hygiea

Lastly, we focused on impact simulations of selected observed families. For the Hygiea family with C-type members, we ran a number of simulations to determine impact parameters that produce a SFD matching the observed SFD. We assumed either the frictionless von Mises rheology or the Drucker-Prager rheology that takes into account dry friction of damaged material. Surprisingly, the frictionless model gave a better match of the observed shape of the largest remnant. There are two conceivable explanations:

1. Hygiea formed as an aspherical irregular body after the impact, but it became more round over time due to long-term relaxation of the surface (or subsurface layers).

2. The impact induced temporary weakening of the material, which allowed the material to flow as if it was frictionless. We hypothesized that such weakening could have been caused by acoustic fluidization.

Since Hygiea formed more than 2 Gyr ago [Carruba et al., 2014], a slow surface relaxation seems feasible. However, we found that the asteroid (31) Euphrosyne is a similar case [Yang et al., 2020b]. It is also a C-type asteroid, created by an energetic impact that disintegrated the parent body and formed a spherical largest remnant. Unlike Hygiea, its age is only $t \simeq 280\,\mathrm{Myr}$ [Yang et al., 2020a]. We thus prefer the acoustic fluidization as the likely cause of the observed sphericity of C-type asteroids.

7.4 Future work

While our SPH code was mainly developed for collision simulations, it is designed as a generic particle-based code and can be utilized for other applications. For example, it allows to set up arbitrary initial conditions, it can be straightforwardly extended by more sophisticated equations of state, material rheologies, acceleration terms, heat sources, cooling mechanisms, etc. We believe the code can be a useful tool for other researchers.

There is a number of possible directions for future research. The code can be used to study shapes of largest remnants [as in Sugiura et al., 2018] as well as the shapes of smaller fragments. With extensive databases of observed shapes obtained by light curve inversion [Ďurech et al., 2010] and numerous members of asteroid families, e.g. Eos, Themis and Flora [Hanuš et al., 2013], collisional models can be used to constrain rheology of real asteroidal materials. Following Michel et al. [2020], SPH simulations can be used to explain the formation of top-shaped asteroids, e.g. (162173) Ryugu, or even changes to local topography due to small craterings. The cratering events are particularly interesting because of recently acquired *in situ* data from the artificial impact experiment and formation of a crater on Ryugu [Arakawa et al., 2020]. Furthermore, the planned DART mission [Maindl and Schäfer, 2019; Raducan and Jutzi, 2021] will obtain additional valuable information in the near future.

The code allows to easily set up bodies of arbitrary shapes and various materials, hence it is suitable for simulations of differentiated bodies. Together with "geodetic" observations of asteroid satellites [Johnston, 2018], one can address key questions of Solar System science about the internal structure of asteroids. Regarding larger bodies, one can study hit-and-run impacts and the stripping of Mercury's mantle [as Asphaug and Reufer, 2014] or relevant collisions of gas giants to explain Jupiter's diluted core [Liu et al., 2020]. The code can be generalized for simulations in a gas disk and employed for collisions of protoplanets [Chrenko et al., 2017; Brož et al., 2018]. Another option is to study collisions of moons of Jupiter or Saturn and formation of rings [Dubinski, 2019]; the code already provides an easy way to set up tidal forces.

Of course, we do not need to limit ourselves to the Solar System. The discovery of 1I/'Oumuamua opens up the possibility to study interstellar objects, which is especially intriguing given its extraordinary "cigar" shape. Apart from already tested formation scenarios, e.g. low-speed collisions [Sugiura et al., 2019] or tidal fragmentation [Zhang and Lin, 2020], we are sure there is something to be discovered…

— Chapter viii —

LIST OF PUBLICATIONS

Journal articles:

Yang, B., Hanuš, J., Brož, M., Chrenko, O., Willman, M., **Ševeček, P.**, Masiero, J., and Kaluna, H. (2020a). Physical and dynamical characterization of the Euphrosyne asteroid family. *A&A*, 643:A38.

Yang, B., Hanuš, J., Carry, B., Vernazza, P., Brož, M., Vachier, F., Rambaux, N., Marsset, M., Chrenko, O., **Ševeček, P.**, Viikinkoski, M., Jehin, E., Ferrais, M., Podlewska-Gaca, E., Drouard, A., Marchis, F., Birlan, M., Benkhaldoun, Z., Berthier, J., Bartczak, P., Dumas, C., Dudziński, G., Ďurech, J., Castillo-Rogez, J., Cipriani, F., Colas, F., Fetick, R., Fusco, T., Grice, J., Jorda, L., Kaasalainen, M., Kryszczynska, A., Lamy, P., Marciniak, A., Michalowski, T., Michel, P., Pajuelo, M., Santana-Ros, T., Tanga, P., Vigan, A., and Witasse, O. (2020b). Binary asteroid (31) Euphrosyne: ice-rich and nearly spherical. *A&A*, 641:A80.

Vernazza, P., Jorda, L., **Ševeček, P.**, Brož, M., Viikinkoski, M., Hanuš, J., Carry, B., Drouard, A., Ferrais, M., Marsset, M., Marchis, F., Birlan, M., Podlewska-Gaca, E., Jehin, E., Bartczak, P., Dudzinski, G., Berthier, J., Castillo-Rogez, J., Cipriani, F., Colas, F., DeMeo, F., Dumas, C., Ďurech, J., Fetick, R., Fusco, T., Grice, J., Kaasalainen, M., Kryszczynska, A., Lamy, P., Le Coroller, H., Marciniak, A., Michalowski, T., Michel, P., Rambaux, N., Santana-Ros, T., Tanga, P., Vachier, F., Vigan, A., Witasse, O., Yang, B., Gillon, M., Benkhaldoun, Z., Szakats, R., Hirsch, R., Duffard, R., Chapman, A., and Maestre, J. L. (2020). A basin-free spherical shape as an outcome of a giant impact on asteroid Hygiea. *Nature Astronomy*, 4:136–141.

Marsset, M., Brož, M., Vernazza, P., Drouard, A., Castillo-Rogez, J., Hanuš, J., Viikinkoski, M., Rambaux, N., Carry, B., Jorda, L., **Ševeček, P.**, Birlan, M., Marchis, F., Podlewska-Gaca, E., Asphaug, E., Bartczak, P., Berthier, J., Cipriani, F., Colas, F., Dudziński, G., Dumas, C., Ďurech, J., Ferrais, M., Fétick, R., Fusco, T., Jehin, E., Kaasalainen, M., Kryszczynska, A., Lamy, P., Le Coroller, H., Marciniak, A., Michalowski, T., Michel, P., Richardson, D. C., Santana-Ros, T., Tanga, P., Vachier, F., Vigan, A., Witasse, O., and Yang, B. (2020). The violent collisional history of aqueously evolved (2) Pallas. *Nature Astronomy*, 4:569–576.

Ševeček, P., Brož, M., and Jutzi, M. (2019). Impacts into rotating targets: angular momentum draining and efficient formation of synthetic families. *A&A*, 629:A122.

Vernazza, P., Brož, M., Drouard, A., Hanuš, J., Viikinkoski, M., Marsset, M., Jorda, L., Fetick, R., Carry, B., Marchis, F., Birlan, M., Fusco, T., Santana-Ros, T., Podlewska-Gaca, E., Jehin, E., Ferrais, M., Bartczak, P., Dudziński, G., Berthier, J., Castillo-Rogez, J., Cipriani, F., Colas, F., Dumas, C., Ďurech, J., Kaasalainen, M., Kryszczynska, A., Lamy, P., Le Coroller, H., Marciniak, A., Michalowski, T., Michel, P., Pajuelo, M., Tanga, P., Vachier, F., Vigan, A., Warner, B., Witasse, O., Yang, B., Asphaug, E., Richardson, D. C., **Ševeček, P.**, Gillon, M., and Benkhaldoun, Z. (2018). The impact crater at the origin of the Julia family detected with VLT/SPHERE? *A&A*, 618:A154.

Ševeček, P., Brož, M., Nesvorný, D., Enke, B., Durda, D., Walsh, K., and Richardson, D. C. (2017). SPH/N-Body simulations of small (D = 10km) asteroidal breakups and improved parametric relations for Monte-Carlo collisional models. *Icarus*, 296:239–256.

Ševeček, P., Golubov, O., Scheeres, D. J., and Krugly, Y. N. (2016). Obliquity dependence of the tangential YORP. *A&A*, 592:A115.

Ševeček, P., Brož, M., Čapek, D., and Ďurech, J. (2015). The thermal emission from boulders on (25143) Itokawa and general implications for the YORP effect. *MNRAS*, 450(2):2104–2115.

Conference contributions:

Golubov, O., Myhrvold, N., **Ševeček, Pavel**, Özen, C., and Sivam, D. (2019). Sensitivity of Tangential YORP Effect to Shapes and Arrangement of Boulders. EPSC-DPS Joint Meeting. September 2019.

Brož, M., **Ševeček, Pavel**, Vernazza, P., Jorda, L., Hanuš, J., Marsset, M., Drouard, A., Viikinkoski, M., Carry, B., Marchis, F., Fetick, R., Fusco, T., and Birlan, M. (2019). Main Belt evolution in the context of adaptive-optics observations of large asteroids. EPSC-DPS Joint Meeting. September 2019.

Ševeček, Pavel and Brož, M. (2019). Numerical simulations of the impact formingthe Hygiea family. The Main Belt: A Gateway to the Formation and Early Evolution of the Solar System Workshop. June 2019.

Ševeček, Pavel and Brož, M. (2018). Impact simulations with rotating targets - draining vs. embedding of the angular momentum. AAS/Division for Planetary Sciences Meeting #50. October 2018.

Ševeček, Pavel and Brož, M. (2017). Collisional disruptions of rotating targets. AAS/Division for Planetary Sciences Meeting #49. October 2017.

Ševeček, Pavel, Brož, M., Nesvorný, D., Durda, D. D., Asphaug, E., Walsh, K. J., and Richardson, D. C. (2016). SPH/N-body simulations of small (D = 10 km) monolithic

asteroidal breakups and improved parametric relations for Monte-Carlo collisional models. AAS/Division for Planetary Sciences Meeting #48. October 2016.

Ševeček, Pavel, Brož, M., Čapek, D., and Ďurech, J. (2014). Three-dimensional heat diffusion in boulders and the influence on the YORP effect. Thermal Models for Planetary Sciences II. June 2014.

Entries in the ASCL database:

Ševeček, Pavel (2019). OpenSPH: Astrophysical SPH and N-body simulations and interactive visualization tools.

— Chapter ix —

REFERENCES

Arakawa, M., Saiki, T., Wada, K., Ogawa, K., Kadono, T., Shirai, K., Sawada, H., Ishibashi, K., Honda, R., Sakatani, N., Iijima, Y., Okamoto, C., Yano, H., Takagi, Y., Hayakawa, M., Michel, P., Jutzi, M., Shimaki, Y., Kimura, S., Mimasu, Y., Toda, T., Imamura, H., Nakazawa, S., Hayakawa, H., Sugita, S., Morota, T., Kameda, S., Tatsumi, E., Cho, Y., Yoshioka, K., Yokota, Y., Matsuoka, M., Yamada, M., Kouyama, T., Honda, C., Tsuda, Y., Watanabe, S., Yoshikawa, M., Tanaka, S., Terui, F., Kikuchi, S., Yamaguchi, T., Ogawa, N., Ono, G., Yoshikawa, K., Takahashi, T., Takei, Y., Fujii, A., Takeuchi, H., Yamamoto, Y., Okada, T., Hirose, C., Hosoda, S., Mori, O., Shimada, T., Soldini, S., Tsukizaki, R., Iwata, T., Ozaki, M., Abe, M., Namiki, N., Kitazato, K., Tachibana, S., Ikeda, H., Hirata, N., Hirata, N., Noguchi, R., and Miura, A. (2020). An artificial impact on the asteroid (162173) Ryugu formed a crater in the gravity-dominated regime. *Science*, 368(6486):67–71.

Asphaug, E. and Reufer, A. (2014). Mercury and other iron-rich planetary bodies as relics of inefficient accretion. *Nature Geoscience*, 7(8):564–568.

Asphaug, E. I. (1993). Dynamic fragmentation in the solar system: Applications of fracture mechanics and hydrodynamics to questions of planetary evolution. PhD thesis, The University Of Arizona.

Avdellidou, C., Price, M. C., Delbo, M., and Cole, M. J. (2017). Survival of the impactor during hypervelocity collisions - II. An analogue for high-porosity targets. *MNRAS*, 464(1):734–738.

Avdellidou, C., Price, M. C., Delbo, M., Ioannidis, P., and Cole, M. J. (2016). Survival of the impactor during hypervelocity collisions - I. An analogue for low porosity targets. *MNRAS*, 456(3):2957–2965.

Bagatin, A., Petit, J.-M., and Farinella, P. (2001). How many rubble piles are in the asteroid belt? *Icarus*, 149(1):198–209.

Bagatin, A. C. and Petit, J.-M. (2001). Effects of the geometric constraints on the size distributions of debris in asteroidal fragmentation. *Icarus*, 149(1):210–221.

Ballouz, R.-L., Richardson, D. C., Michel, P., and Schwartz, S. R. (2014). Rotation-dependent catastrophic disruption of gravitational aggregates. *The Astrophysical Journal*, 789(2):158.

Ballouz, R.-L., Richardson, D. C., Michel, P., Schwartz, S. R., and Yu, Y. (2015). Numerical simulations of collisional disruption of rotating gravitational aggregates: Dependence on material properties. *Planet. Space Sci.*, 107:29–35.

Balsara, D. S. (1995). Von Neumann stability analysis of smoothed particle hydrodynamics—suggestions for optimal algorithms. *Journal of Computational Physics*, 121:357–372.

Barai, P., Proga, D., and Nagamine, K. (2011). Smoothed particle hydrodynamics simulations of black hole accretion: a step to model black hole feedback in galaxies. *MNRAS*, 418(1):591–611.

Barnes, J. and Hut, P. (1986). A hierarchical $\mathcal{O}(N \log N)$ force-calculation algorithm. *Nature*, 324:446–449.

Beck, A. M., Murante, G., Arth, A., Remus, R.-S., Teklu, A. F., Donnert, J. M. F., Planelles, S., Beck, M. C., Förster, P., Imgrund, M., Dolag, K., and Borgani, S. (2015). An improved SPH scheme for cosmological simulations. *Monthly Notices of the Royal Astronomical Society*, 455(2):2110–2130.

Benavidez, P. G., Durda, D. D., Enke, B., Campo Bagatin, A., Richardson, D. C., Asphaug, E., and Bottke, W. F. (2018). Impact simulation in the gravity regime: Exploring the effects of parent body size and internal structure. *Icarus*, 304:143–161.

Benavidez, P. G., Durda, D. D., Enke, B. L., Bottke, W. F., Nesvorný, D., Richardson, D. C., Asphaug, E., and Merline, W. J. (2012). A comparison between rubble-pile and monolithic targets in impact simulations: Application to asteroid satellites and family size distributions. *Icarus*, 219:57–76.

Bennett, B. I., Johnson, J. D., Kerley, G. I., and Rood, G. T. (1978). Recent developments in the sesame equation-of-state library. *Los Alamos Scientific Lab. Technical Report*.

Bentley, J. L. (1975). Multidimensional binary search trees used for associative searching. *Commun. ACM*, 18(9):509–517.

Benz, W. and Asphaug, E. (1994). Impact simulations with fracture. I — Method and tests. *Icarus*, 107:98.

Benz, W. and Asphaug, E. (1995). Simulations of brittle solids using smooth particle hydrodynamics. *Computer Physics Communications*, 87:253–265.

Benz, W. and Asphaug, E. (1999). Catastrophic disruptions revisited. *Icarus*, 142(1):5–20.

Blinn, J. F. (1982). A generalization of algebraic surface drawing. *ACM Trans. Graph.*, 1(3):235–256.

Bonet, J. and Lok, T.-S. (1999). Variational and momentum preservation aspects of smooth particle hydrodynamic formulations. *Computer Methods in Applied Mechanics and Engineering*, 180(1):97–115.

Bottke, W. F., Nesvorný, D., Vokrouhlický, D., and Morbidelli, A. (2010). The irregular satellites: The most collisionally evolved populations in the solar system. *AJ*, 139(3):994–1014.

Bowell, E., Gehrels, T., and Zellner, B. (1979). Magnitudes, colors, types and adopted diameters of the asteroids. *Asteroids*, pages 1108–1129.

Bray, V. J., Collins, G. S., Morgan, J. V., Melosh, H. J., and Schenk, P. M. (2014). Hydrocode simulation of Ganymede and Europa cratering trends – How thick is Europa's crust? *Icarus*, 231:394–406.

Brookshaw, L. (1985). A method of calculating radiative heat diffusion in particle simulations. *Proceedings of the Astronomical Society of Australia*, 6:207–210.

Brož, M., Morbidelli, A., Bottke, W. F., Rozehnal, J., Vokrouhlický, D., and Nesvorný, D. (2013). Constraining the cometary flux through the asteroid belt during the late heavy bombardment. *A&A*, 551:A117.

Brož, M., Chrenko, O., Nesvorný, D., and Lambrechts, M. (2018). Dynamics of multiple protoplanets embedded in gas and pebble discs and its dependence on Σ and ν parameters. *A&A*, 620:A157.

Brož, M., Marchis, F., Jorda, L., Hanuš, J., Vernazza, P., Ferrais, M., Vachier, F., Rambaux, N., Marsset, M., Viikinkoski, M., Jehin, E., Benseguane, S., Podlewska-Gaca, E., Carry, B., Drouard, A., Fauvaud, S., Birlan, M., Berthier, J., Bartczak, P., Dumas, C., Dudziński, G., Ďurech, J., Castillo-Rogez, J., Cipriani, F., Colas, F., Fetick, R., Fusco, T., Grice, J., Kryszczynska, A., Lamy, P., Marciniak, A., Michalowski, T., Michel, P., Pajuelo, M., Santana-Ros, T., Tanga, P., Vigan, A., Vokrouhlický, D., Witasse, O., and Yang, B. (2021). An advanced multipole model for (216) Kleopatra triple system. *arXiv e-prints*, page arXiv:2105.09134.

Brož, M. and Morbidelli, A. (2019). A study of 3-dimensional shapes of asteroid families with an application to Eos. *Icarus*, 317:434–441.

Buie, M., Olkin, C., Merline, W., Walsh, K., Levison, H., Timerson, B., Herald, D., Jr, W., Abramson, H., Abramson, K., Breit, D., Caton, D., Conard, S., Croom, M., Dunford, R., Dunford, J., Dunham, D., Ellington, C., Liu, Y., and Venable, R. (2015). Size and shape from stellar occultation observations of the double Jupiter Trojan Patroclus and Menoetius. *The Astronomical Journal*, 149:113.

Canup, R. M. (2005). A giant impact origin of Pluto-Charon. *Science*, 307:546–550.

Canup, R. M. (2008). Lunar-forming collisions with pre-impact rotation. *Icarus*, 196:518–538.

Carruba, V., Domingos, R. C., Huaman, M. E., Santos, C. R. d., and Souami, D. (2014). Dynamical evolution and chronology of the Hygiea asteroid family. *MNRAS*, 437(3):2279–2290.

Čapek, D. and Vokrouhlický, D. (2004). The YORP effect with finite thermal conductivity. *Icarus*, 172(2):526–536.

Chrenko, O., Brož, M., and Lambrechts, M. (2017). Eccentricity excitation and merging of planetary embryos heated by pebble accretion. *A&A*, 606:A114.

Christou, A. A., Borisov, G., Dell'Oro, A., Cellino, A., and Bagnulo, S. (2017). Is the Eureka cluster a collisional family of Mars Trojan asteroids? *Icarus*, 293:243–258.

Cibulková, H., Brož, M., and Benavidez, P. G. (2014). A six-part collisional model of the main asteroid belt. *Icarus*, 241:358–372.

Colagrossi, A., Antuono, M., and Le Touzé, D. (2009). Theoretical considerations on the free-surface role in the smoothed-particle-hydrodynamics model. *Phys. Rev. E*, 79(5):056701.

Collins, G. S., Melosh, H. J., and Ivanov, B. A. (2004). Modeling damage and deformation in impact simulations. *Meteoritics and Planetary Science*, 39:217–231.

Cossins, P. J. (2010). *The Gravitational Instability and its Role in the Evolution of Protostellar and Protoplanetary Discs*. PhD thesis, University of Leicester.

Ćuk, M. and Burns, J. A. (2005). Effects of thermal radiation on the dynamics of binary NEAs. *Icarus*, 176(2):418–431.

Cullen, L. and Dehnen, W. (2010). Inviscid smoothed particle hydrodynamics. *MNRAS*, 408:669–683.

Dahlgren, M. (1998). A study of Hilda asteroids. III. Collision velocities and collision frequencies of Hilda asteroids. *A&A*, 336:1056–1064.

Dehnen, W. and Aly, H. (2012). Improving convergence in smoothed particle hydrodynamics simulations without pairing instability. *Monthly Notices of the Royal Astronomical Society*, 425:1068–1082.

Dell'Oro, A. and Paolicchi, P. (1997). A new way to estimate the distribution of encounter velocity among the asteroids. *Planet. Space Sci.*, 45(7):779–784.

Demura, H., Kobayashi, S., Nemoto, E., Matsumoto, N., Furuya, M., Yukishita, A., Muranaka, N., Morita, H., Shirakawa, K., Maruya, M., Ohyama, H., Uo, M., Kubota, T., Hashimoto, T., Kawaguchi, J., Fujiwara, A., Saito, J., Sasaki, S., Miyamoto, H., and Hirata, N. (2006). Pole and global shape of 25143 Itokawa. *Science*, 312(5778):1347–1349.

Diehl, S., Rockefeller, G., Fryer, C., Riethmiller, D., and Statler, T. (2015). Generating optimal initial conditions for smoothed particle hydrodynamics simulations. *Publications of the Astronomical Society of Australia*, 32:e048.

Dilts, G. A. (1999). Moving-least-squares-particle hydrodynamics—I. Consistency and stability. *International Journal for Numerical Methods in Engineering*, 44(8):1115–1155.

Dobrovolskis, A. R. and Burns, J. A. (1984). Angular momentum drain - A mechanism for despinning asteroids. *Icarus*, 57:464–476.

Dolag, K., Vazza, F., Brunetti, G., and Tormen, G. (2005). Turbulent gas motions in galaxy cluster simulations: the role of smoothed particle hydrodynamics viscosity. *MNRAS*, 364:753–772.

Domínguez, J., Crespo, A., Gómez-Gesteira, M., and Rogers, B. (2013). Simulating more than 1 billion SPH particles using GPU hardware acceleration. In *Proceedings of the 8th International SPHERIC Workshop*, pages 249–254.

Dubinski, J. (2019). A recent origin for Saturn's rings from the collisional disruption of an icy moon. *Icarus*, 321:291–306.

Durda, D. D., Bottke, W. F., Nesvorný, D., Enke, B. L., Merline, W. J., Asphaug, E., and Richardson, D. C. (2007). Size-frequency distributions of fragments from SPH/N-body simulations of asteroid impacts: Comparison with observed asteroid families. *Icarus*, 186:498–516.

Ďurech, J., Sidorin, V., and Kaasalainen, M. (2010). DAMIT: a database of asteroid models. *A&A*, 513:A46.

Emsenhuber, A., Jutzi, M., and Benz, W. (2018). SPH calculations of Mars-scale collisions: The role of the equation of state, material rheologies, and numerical effects. *Icarus*, 301:247–257.

Español, P. and Revenga, M. (2003). Smoothed dissipative particle dynamics. *Phys. Rev. E*, 67:026705.

Ferrais, M., Vernazza, P., Jorda, L., Rambaux, N., Hanuš, J., Carry, B., Marchis, F., Marsset, M., Viikinkoski, M., Brož, M., Fetick, R., Drouard, A., Fusco, T., Birlan, M., Podlewska-Gaca, E., Jehin, E., Bartczak, P., Berthier, J., Castillo-Rogez, J., Cipriani, F., Colas, F., Dudziński, G., Dumas, C., Ďurech, J., Kaasalainen, M., Kryszczynska, A., Lamy, P., Le Coroller, H., Marciniak, A., Michalowski, T., Michel, P., Santana-Ros, T., Tanga, P., Vachier, F., Vigan, A., Witasse, O., and Yang, B. (2020). Asteroid (16) Psyche's primordial shape: A possible Jacobi ellipsoid. *A&A*, 638:L15.

Frontiere, N., Raskin, C. D., and Owen, J. M. (2017). CRKSPH – A conservative reproducing kernel smoothed particle hydrodynamics scheme. *Journal of Computational Physics*, 332:160–209.

Fujiwara, A., Kawaguchi, J., Yeomans, D. K., Abe, M., Mukai, T., Okada, T., Saito, J., Yano, H., Yoshikawa, M., Scheeres, D. J., Barnouin-Jha, O., Cheng, A. F., Demura, H., Gaskell, R. W., Hirata, N., Ikeda, H., Kominato, T., Miyamoto, H., Nakamura, A. M., Nakamura, R., Sasaki, S., and Uesugi, K. (2006). The rubble-pile asteroid Itokawa as observed by Hayabusa. *Science*, 312(5778):1330–1334.

Fusco, T., Mugnier, L. M., Conan, J.-M., Marchis, F., Chauvin, G., Rousset, G., Lagrange, A.-M., Mouillet, D., and Roddier, F. J. (2003). Deconvolution of astronomical images obtained from ground-based telescopes with adaptive optics. In Wizinowich, P. L. and Bonaccini, D., editors, *Adaptive Optical System Technologies II*, volume 4839 of *Society of Photo-Optical Instrumentation Engineers (SPIE) Conference Series*, pages 1065–1075.

García-Senz, D. and Bravo, E. (2005). Type Ia Supernova models arising from different distributions of igniting points. *A&A*, 430:585–602.

Gaskell, R., Saito, J., Ishiguro, M., Kubota, T., Hashimoto, T., Hirata, N., Abe, S., Barnouin-Jha, O., and Scheeres, D. (2008). Gaskell Itokawa Shape Model V1.0.

Genda, H., Kokubo, E., and Ida, S. (2012). Merging criteria for giant impacts of protoplanets. *ApJ*, 744(2):137.

Gingold, R. A. and Monaghan, J. J. (1977). Smoothed particle hydrodynamics — Theory and application to non-spherical stars. *MNRAS*, 181:375–389.

Golubov, O., Scheeres, D. J., and Krugly, Y. N. (2014). A Three-dimensional Model of Tangential YORP. *ApJ*, 794(1):22.

Goswami, P. and Pajarola, R. (2011). Time Adaptive Approximate SPH. In Bender, J., Erleben, K., and Galin, E., editors, *Workshop in Virtual Reality Interactions and Physical Simulation "VRIPHYS" (2011)*. The Eurographics Association.

Grady, D. and Kipp, M. (1980). Continuum modelling of explosive fracture in oil shale. *International Journal of Rock Mechanics and Mining Sciences & Geomechanics Abstracts*, 17(3):147–157.

Gray, J. (2001). SPH elastic dynamics. *Computer Methods in Applied Mechanics and Engineering*, 190(49-50):6641–6662.

Halton, J. H. (1964). Algorithm 247: Radical-inverse quasi-random point sequence. *Commun. ACM*, 7(12):701–702.

Hanuš, J., Brož, M., Ďurech, J., Warner, B. D., Brinsfield, J., Durkee, R., Higgins, D., Koff, R. A., Oey, J., Pilcher, F., Stephens, R., Strabla, L. P., Ulisse, Q., and Girelli, R. (2013). An anisotropic distribution of spin vectors in asteroid families. *A&A*, 559:A134.

Hanuš, J., Marsset, M., Vernazza, P., Viikinkoski, M., Drouard, A., Brož, M., Carry, B., Fetick, R., Marchis, F., Jorda, L., Fusco, T., Birlan, M., Santana-Ros, T., Podlewska-Gaca, E., Jehin, E., Ferrais, M., Grice, J., Bartczak, P., Berthier, J., Castillo-Rogez, J., Cipriani, F., Colas, F., Dudzi ."0301nski, G., Dumas, C., Ďurech, J., Kaasalainen, M., Kryszczynska, A., Lamy, P., Le Coroller, H., Marciniak, A., Michalowski, T., Michel, P., Pajuelo, M., Tanga, P., Vachier, F., Vigan, A., Witasse, O., and Yang, B. (2019). The shape of (7) Iris as evidence of an ancient large impact? *A&A*, 624:A121.

Hanuš, J., Ďurech, J., Brož, M., Warner, B. D., Pilcher, F., Stephens, R., Oey, J., Bernasconi, L., Casulli, S., Behrend, R., Polishook, D., Henych, T., Lehký, M., Yoshida, F., and Ito, T. (2011). A study of asteroid pole-latitude distribution based on an extended set of shape models derived by the lightcurve inversion method. *A&A*, 530:A134.

Hanuš, J., Vernazza, P., Viikinkoski, M., Ferrais, M., Rambaux, N., Podlewska-Gaca, E., Drouard, A., Jorda, L., Jehin, E., Carry, B., Marsset, M., Marchis, F., Warner, B., Behrend, R., Asenjo, V., Berger, N., Bronikowska, M., Brothers, T., Charbonnel, S., Colazo, C., Coliac, J. F., Duffard, R.,

Jones, A., Leroy, A., Marciniak, A., Melia, R., Molina, D., Nadolny, J., Person, M., Pejcha, O., Riemis, H., Shappee, B., Sobkowiak, K., Soldán, F., Suys, D., Szakats, R., Vantomme, J., Birlan, M., Berthier, J., Bartczak, P., Dumas, C., Dudziński, G., Ďurech, J., Castillo-Rogez, J., Cipriani, F., Fetick, R., Fusco, T., Grice, J., Kaasalainen, M., Kryszczynska, A., Lamy, P., Michalowski, T., Michel, P., Santana-Ros, T., Tanga, P., Vachier, F., Vigan, A., Witasse, O., and Yang, B. (2020). (704) Interamnia: a transitional object between a dwarf planet and a typical irregular-shaped minor body. *A&A*, 633:A65.

Hay, H. C. F. C., Collins, G. S., and Davison, T. M. (2014). Complex crater collapse: A comparison of the block and Melosh models of acoustic fluidization. In *Lunar and Planetary Science Conference Proceedings*, page 1938.

Henych, T. and Pravec, P. (2013). Asteroid rotation excitation by subcatastrophic impacts. *MNRAS*, 432(2):1623–1631.

Herant, M. (1994). Dirty tricks for SPH (Invited paper). *Mem. Soc. Astron. Italiana*, 65:1013–1022.

Hergenrother, C. W. and Whiteley, R. J. (2011). A survey of small fast rotating asteroids among the near-Earth asteroid population. *Icarus*, 214(1):194–209.

Hiesinger, H., Marchi, S., Schmedemann, N., Schenk, P., Pasckert, J. H., Neesemann, A., O'Brien, D. P., Kneissl, T., Ermakov, A. I., Fu, R. R., Bland, M. T., Nathues, A., Platz, T., Williams, D. A., Jaumann, R., Castillo-Rogez, J. C., Ruesch, O., Schmidt, B., Park, R. S., Preusker, F., Buczkowski, D. L., Russell, C. T., and Raymond, C. A. (2016). Cratering on Ceres: Implications for its crust and evolution. *Science*, 353(6303):1003–1011.

Hillier, J. K., Bauer, J. M., and Buratti, B. J. (2011). Photometric modeling of asteroid 5535 Annefrank from Stardust observations. *Icarus*, 211(1):546–552.

Hirabayashi, M. and Scheeres, D. J. (2014). Analysis of asteroid (216) Kleopatra using dynamical and structural constraints. *ApJ*, 780:160.

Hirata, N., Sugiyama, T., Hirata, N., Tanaka, S., Nishikawa, N., Noguchi, R., Shimaki, Y., Gaskell, R., Palmer, E., Matsumoto, K., Senshu, H., Yamamoto, Y., Murakami, S., Ishihara, Y., Sugita, S., Morota, T., Honda, R., Arakawa, M., Ogawa, K., Tsuda, Y., and Watanabe, S. (2020). Shape reconstruction of the asteroid Ryugu with structure-from-motion method. In *Lunar and Planetary Science Conference Proceedings*, page 2015.

Hirayama, K. (1918). Groups of asteroids probably of common origin. *AJ*, 31:185–188.

Holsapple, K. A. (2007). Spin limits of Solar System bodies: From the small fast-rotators to 2003 EL61. *Icarus*, 187(2):500–509.

Holsapple, K. A. (2009). On the "strength" of the small bodies of the solar system: A review of strength theories and their implementation for analyses of impact disruptions. *Planetary and Space Science*, 57(2):127–141.

Hrennikoff, A. (1941). Solution of problems of elasticity by the framework method. *J. Appl. Mech.*

Ihmsen, M., Orthmann, J., Solenthaler, B., Kolb, A., and Teschner, M. (2014). SPH fluids in computer graphics. In Lefebvre, S. and Spagnuolo, M., editors, *Eurographics 2014 - State of the Art Reports*. The Eurographics Association.

Ivanov, B. (2019). Acoustic fluidization during impact crater's formation. In Kocharyan, G. and Lyakhov, A., editors, *Trigger Effects in Geosystems*, pages 497–505, Cham. Springer International Publishing.

Ivanov, B. A., Kocharyan, G. G., Kostuchenko, V. N., Kirjakov, A. F., and Pevzner, L. A. (1996). Puchezh-Katunki impact crater: Preliminary data on recovered core block structure. In *Lunar and Planetary Science Conference Proceedings*, page 589.

Ji, J., Jiang, Y., Zhao, Y., Wang, S., and Yu, L. (2016). Chang'e-2 spacecraft observations of asteroid 4179 Toutatis. In Chesley, S. R., Morbidelli, A., Jedicke, R., and Farnocchia, D., editors, *Asteroids: New Observations, New Models*, volume 318, pages 144–152.

Jiang, M., Zhou, Y., Wang, R., Southern, R., and jun Zhang, J. (2015). Blue noise sampling using an SPH-based method. *ACM Trans. Graph.*, 34:211:1–211:11.

Johnson, G. R. and Beissel, S. R. (1996). Normalized smoothing functions for SPH impact computations. *International Journal for Numerical Methods in Engineering*, 39(16):2725–2741.

Johnston, W. R. (2018). Binary Minor Planets Compilation V2.0. *NASA Planetary Data System*.

Jutzi, M. and Asphaug, E. (2015). The shape and structure of cometary nuclei as a result of low-velocity accretion. *Science*, 348(6241):1355–1358.

Jutzi, M., Asphaug, E., Gillet, P., Barrat, J.-A., and Benz, W. (2013). The structure of the asteroid 4 Vesta as revealed by models of planet-scale collisions. *Nature*, 494:207–210.

Jutzi, M. and Benz, W. (2017). Formation of bi-lobed shapes by sub-catastrophic collisions. A late origin of comet 67P's structure. *A&A*, 597:A62.

Jutzi, M., Benz, W., and Michel, P. (2008). Numerical simulations of impacts involving porous bodies. I. Implementing sub-resolution porosity in a 3D SPH hydrocode. *Icarus*, 198(1):242–255.

Jutzi, M., Holsapple, K., Wünneman, K., and Michel, P. (2015). Modeling asteroid collisions and impact processes. *Asteroids IV*.

Jutzi, M., Michel, P., and Richardson, D. C. (2019). Fragment properties from large-scale asteroid collisions: I: Results from SPH/N-body simulations using porous parent bodies and improved material models. *Icarus*, 317:215–228.

Kaasalainen, M., Torppa, J., and Muinonen, K. (2001). Optimization methods for asteroid lightcurve inversion. II. The complete inverse problem. *Icarus*, 153(1):37–51.

Kadono, T., Sakaiya, T., Hironaka, Y., Otani, K., Sano, T., Fujiwara, T., Mochiyama, T., Kurosawa, K., Sugita, S., Sekine, Y., Matsui, T., Ohno, S., Shiroshita, A., Miyanishi, K., Ozaki, N., Kodama, R., Nakamura, A. M., Arakawa, M., Fujioka, S., and Shigemori, K. (2009). Impact experiments with projectiles at velocities higher than 10 km/s. In Elert, M., Furnish, M. D., Anderson, W. W., Proud, W. G., and Butler, W. T., editors, *Shock Compression of Condensed Matter*, volume 1195 of *American Institute of Physics Conference Series*, pages 875–877.

Kegerreis, J. A., Eke, V. R., Gonnet, P., Korycansky, D. G., Massey, R. J., Schaller, M., and Teodoro, L. F. A. (2019). Planetary giant impacts: convergence of high-resolution simulations using efficient spherical initial conditions and swift. *Monthly Notices of the Royal Astronomical Society*, 487(4):5029–5040.

Kipfer, P. and Westermann, R. (2006). Realistic and interactive simulation of rivers. In *Proceedings of Graphics Interface 2006*, GI '06, page 41–48, CAN. Canadian Information Processing Society.

Knežević, Z. and Milani, A. (2003). Proper element catalogs and asteroid families. *A&A*, 403:1165–1173.

Koschier, D., Bender, J., Solenthaler, B., and Teschner, M. (2019). Smoothed particle hydrodynamics techniques for the physics based simulation of fluids and solids. In *Eurographics 2019*. The Eurographics Association.

Krongauz, Y. and Belytschko, T. (1997). Consistent pseudo-derivatives in meshless methods. *Computer Methods in Applied Mechanics and Engineering*, 146(3):371–386.

Lajeunesse, E., Monnier, J. B., and Homsy, G. M. (2005). Granular slumping on a horizontal surface. *Physics of Fluids*, 17(10):103302.

Landau, L. D. and Lifshitz, E. M. (1987). *Fluid Mechanics*, volume 6. Pergamon.

Landshoff, R. (1955). A numerical method for treating fluid flow in the presence of shocks. *Los Alamos National Laboratory Report*.

Lastiwka, M., Basa, M., and Quinlan, N. J. (2009). Permeable and non-reflecting boundary conditions in SPH. *International Journal for Numerical Methods in Fluids*, 61(7):709–724.

Lattanzio, J. C., Monaghan, J. J., Pongracic, H., and Schwarz, M. P. (1985). Interstellar cloud collisions. *MNRAS*, 215:125–147.

Lauretta, D. S. (2012). An overview of the OSIRIS-REx asteroid sample return mission. In *Lunar and Planetary Science Conference Proceedings*, page 2491.

Lawn, B. R. and Wilshaw, T. R. (1975). *Fracture of brittle solids*. Cambridge University Press Cambridge.

Lefebvre, S. and Hoppe, H. (2006). Perfect spatial hashing. *ACM Trans. Graph.*, 25(3):579–588.

Leinhardt, Z. M. and Stewart, S. T. (2012). Collisions between gravity-dominated bodies. I. Outcome regimes and scaling laws. *ApJ*, 745(1):79.

Libersky, L. D. and Petschek, A. (1991). Smooth particle hydrodynamics with strength of materials. In *Advances in the free-Lagrange method including contributions on adaptive gridding and the smooth particle hydrodynamics method*, pages 248–257. Springer.

Libersky, L. D., Randles, P. W., Carney, T. C., and Dickinson, D. L. (1997). Recent improvements in SPH modeling of hypervelocity impact. *International Journal of Impact Engineering*, 20(6):525–532. Hypervelocity Impact.

Liu, G. and Liu, M. (2003). *Smoothed Particle Hydrodynamics: A Meshfree Particle Method*. World Scientific.

Liu, S., Hori, Y., Müller, S., Zheng, X., Helled, R., Lin, D., and Isella, A. (2020). The formation of Jupiter's diluted core by a giant impact. In *American Astronomical Society Meeting Abstracts #235*, volume 235 of *American Astronomical Society Meeting Abstracts*, page 226.08.

Lorensen, W. E. and Cline, H. E. (1987). Marching cubes: A high resolution 3D surface construction algorithm. In *Proceedings of the 14th Annual Conference on Computer Graphics and Interactive Techniques*, SIGGRAPH '87, page 163–169, New York, NY, USA. Association for Computing Machinery.

Love, S. G. and Ahrens, T. J. (1997). Origin of asteroid rotation rates in catastrophic impacts. *Nature*, 386(6621):154–156.

Lubarda, V. and Krajcinovic, D. (1993). Damage tensors and the crack density distribution. *International Journal of Solids and Structures*, 30(20):2859–2877.

Lucy, L. B. (1977). A numerical approach to the testing of the fission hypothesis. *AJ*, 82:1013–1024.

Maindl, T. I. and Schäfer, C. M. (2019). Momentum enhancement for the DART kinetic impactor. In *EPSC-DPS Joint Meeting 2019*.

Marrone, S., Antuono, M., Colagrossi, A., Colicchio, G., Touzé, D. L., and Graziani, G. (2011). δ-SPH model for simulating violent impact flows. *Computer Methods in Applied Mechanics and Engineering*, 200(13):1526–1542.

Marsset, M., Brož, M., Vernazza, P., Drouard, A., Castillo-Rogez, J., Hanuš, J., Viikinkoski, M., Rambaux, N., Carry, B., Jorda, L., Ševeček, P., Birlan, M., Marchis, F., Podlewska-Gaca, E., Asphaug, E., Bartczak, P., Berthier, J., Cipriani, F., Colas, F., Dudziński, G., Dumas, C., Ďurech, J., Ferrais, M., Fétick, R., Fusco, T., Jehin, E., Kaasalainen, M., Kryszczynska, A., Lamy, P., Le Coroller, H., Marciniak, A., Michalowski, T., Michel, P., Richardson, D. C., Santana-Ros, T., Tanga, P., Vachier, F., Vigan, A., Witasse, O., and Yang, B. (2020). The violent collisional history of aqueously evolved (2) Pallas. *Nature Astronomy*, 4:569–576.

Masiero, J., Mainzer, A., Grav, T., Delbó, M., Mueller, M., and WISE Team (2010). The WISE survey of the albedo distribution of main belt asteroids. In *Lunar and Planetary Science Conference Proceedings*, page 1283.

McHardy, J. D. (2018). An introduction to the theory and use of SESAME equations of state. *Los Alamos National Laboratory Report*, LA-14503.

Melosh, H. J. (1996). Dynamical weakening of faults by acoustic fluidization. *Nature*, 379(6566):601–606.

Melosh, H. J. (2000). A new and improved equation of state for impact computations. In *Lunar and Planetary Science Conference Proceedings*.

Melosh, J. and Ivanov, B. (1999). Impact crater collapse. *Annual Review of Earth and Planetary Sciences*, 27.

Meltzer, M. (2007). Mission to Jupiter: A history of the Galileo project. NASA STI/Recon Technical Report.

Michalak, G. (2001). Determination of asteroid masses. II. (6) Hebe, (10) Hygiea, (15) Eunomia, (52) Europa, (88) Thisbe, (444) Gyptis, (511) Davida and (704) Interamnia. *A&A*, 374:703–711.

Michalowski, T., Velichko, F. P., Lindgren, M., Oja, T., Lagerkvist, C. I., and Magnusson, P. (1991). The spin vector of asteriod 10 Hygiea. *A&AS*, 91(1):53–59.

Michel, P., Ballouz, R. L., Barnouin, O. S., Jutzi, M., Walsh, K. J., May, B. H., Manzoni, C., Richardson, D. C., Schwartz, S. R., Sugita, S., Watanabe, S., Miyamoto, H., Hirabayashi, M., Bottke, W. F., Connolly, H. C., Yoshikawa, M., and Lauretta, D. S. (2020). Collisional formation of top-shaped asteroids and implications for the origins of Ryugu and Bennu. *Nature Communications*, 11:2655.

Michel, P., Benz, W., Paolo, T., and Richardson, D. C. (2001). Collisions and gravitational reaccumulation: Forming asteroid families and satellites. *Science*, 294(5547):1696–1700.

Michel, P., Benz, W., and Richardson, D. C. (2003). Disruption of fragmented parent bodies as the origin of asteroid families. *Nature*, 421:608–611.

Michel, P., Benz, W., and Richardson, D. C. (2004). Catastrophic disruption of pre-shattered parent bodies. *Icarus*, 168:420–432.

Michel, P., Richardson, D. C., Durda, D. D., Jutzi, M., and Asphaug, E. (2015). Collisional formation and modeling of asteroid families. In Michel, P., DeMeo, F. E., and Bottke, W. F., editors, *Asteroids IV*, pages 341–354. The University of Arizona Press.

Michel, P., Tanga, P., Benz, W., and Richardson, D. C. (2002). Formation of asteroid families by catastrophic disruption: simulations with fragmentation and gravitational reaccumulation. *Icarus*, 160(1):10–23.

Monaghan, J. (1989). On the problem of penetration in particle methods. *Journal of Computational Physics*, 82(1):1–15.

Monaghan, J. (2000). SPH without a tensile instability. *Journal of Computational Physics*, 159(2):290–311.

Monaghan, J. J. (1992). Smoothed particle hydrodynamics. *ARA&A*, 30:543–574.

Monaghan, J. J. (1997). SPH and Riemann Solvers. *Journal of Computational Physics*, 136:298–307.

Morbidelli, A., Bottke, W. F., Nesvorný, D., and Levison, H. F. (2009). Asteroids were born big. *Icarus*, 204:558–573.

Morris, A. J. W. and Burchell, M. J. (2017). Laboratory tests of catastrophic disruption of rotating bodies. *Icarus*, 296:91–98.

Morris, J. P. and Monaghan, J. J. (1997). A switch to reduce SPH viscosity. *J. Comput. Phys.*, 136(1):41–50.

Mothé-Diniz, T., Martino, M. D., Bendjoya, P., Doressoundiram, A., and Migliorini, F. (2001). Rotationally resolved spectra of 10 Hygiea and a spectroscopic study of the Hygiea family. *Icarus*, 152(1):117–126.

Mottola, S., Sears, W. D., Erikson, A., Harris, A. W., Young, J. W., Hahn, G., Dahlgren, M., Mueller, B. E., Owen, B., Ricardo, G.-H., Licandro, J., Barucci, M., Angeli, C., Neukum, G., Lagerkvist, C.-I., and Felix Lahulla, J. (1995). The slow rotation of 253 Mathilde. *Planetary and Space Science*, 43(12):1609–1613.

Müller, M., Charypar, D., and Gross, M. (2003). Particle-based fluid simulation for interactive applications. In *Proceedings of the 2003 ACM SIGGRAPH/Eurographics Symposium on Computer Animation*, SCA '03, page 154–159, Goslar, DEU. Eurographics Association.

Nakamura, A. and Fujiwara, A. (1991). Velocity distribution of fragments formed in a simulated collisional disruption. *Icarus*, 92:132–146.

Nesvorný, D., Bottke, William F., J., Dones, L., and Levison, H. F. (2002). The recent breakup of an asteroid in the main-belt region. *Nature*, 417(6890):720–771.

Nesvorný, D., Bottke, W. F., Levison, H. F., and Dones, L. (2003). Recent origin of the solar system dust bands. *ApJ*, 591(1):486–497.

Nesvorný, D., Brož, M., and Carruba, V. (2015). Identification and dynamical properties of asteroid families. *Asteroids IV*, pages 297–321.

Nesvorný, D., Enke, B. L., Bottke, W. F., Durda, D. D., Asphaug, E., and Richardson, D. C. (2006). Karin cluster formation by asteroid impact. *Icarus*, 183:296–311.

Nesvorný, D., Jedicke, R., Whiteley, R. J., and Ivezić, Ž. (2005). Evidence for asteroid space weathering from the sloan digital sky survey. *Icarus*, 173(1):132–152. Hapke Symposium.

von Mises, R. (1913). Mechanik der festen Körper im plastisch—deformablen Zustand. *Nachrichten von der Gesellschaft der Wissenschaften zu Göttingen, Mathematisch-Physikalische Klasse*, 1913:582–592.

Ševeček, P., Brož, M., Čapek, D., and Ďurech, J. (2015). The thermal emission from boulders on (25143) Itokawa and general implications for the YORP effect. *MNRAS*, 450(2):2104–2115.

Nugent, C. R., Mainzer, A., Masiero, J., Bauer, J., Cutri, R. M., Grav, T., Kramer, E., Sonnett, S., Stevenson, R., and Wright, E. L. (2015). NEOWISE reactivation mission year one: Preliminary asteroid diameters and albedos. *ApJ*, 814(2):117.

Ogawa, R., Nakamura, A. M., Suzuki, A. I., and Hasegawa, S. (2021). Crater shape as a possible record of the impact environment of metallic bodies: Effects of temperature, impact velocity and impactor density. *Icarus*, 362:114410.

Onderik, J. and Ďurikovič, R. (2008). Efficient neighbor search for particle-based fluids. *Journal of the Applied Mathematics, Statistics and Informatics 4*, 4:29–43.

Ostro, S. J., Hudson, R. S., Nolan, M. C., Margot, J.-L., Scheeres, D. J., Campbell, D. B., Magri, C., Giorgini, J. D., and Yeomans, D. K. (2000). Radar observations of asteroid 216 Kleopatra. *Science*, 288(5467):836–839.

Owen, J. M. (2010). ASPH modeling of material damage and failure. In *Proceedings of the 5th international SPHERIC workshop*. Lawrence Livermore National Laboratory.

Owen, J. M. (2014). A compatibly differenced total energy conserving form of SPH. *International Journal for Numerical Methods in Fluids*, 75:749–774.

Owen, J. M., Villumsen, J. V., Shapiro, P. R., and Martel, H. (1998). Adaptive smoothed particle hydrodynamics: Methodology. II. *ApJS*, 116:155–209.

Pakmor, R., Kromer, M., Taubenberger, S., Sim, S. A., Röpke, F. K., and Hillebrandt, W. (2012). Normal type Ia supernovae from violent mergers of white dwarf binaries. *ApJ*, 747(1):L10.

Parker, A., Ivezić, Ž., Jurić, M., Lupton, R., Sekora, M. D., and Kowalski, A. (2008). The size distributions of asteroid families in the SDSS Moving Object Catalog 4. *Icarus*, 198:138–155.

Peer, A., Gissler, C., Band, S., and Teschner, M. (2017). An implicit SPH formulation for incompressible linearly elastic solids: Implicit elastic SPH solids. *Computer Graphics Forum*, 37.

Penrose, R. (1955). A generalized inverse for matrices. *Mathematical Proceedings of the Cambridge Philosophical Society*, 51(3):406–413.

Pheatt, C. (2008). Intel® Threading Building Blocks. *J. Comput. Sci. Coll.*, 23(4):298.

Pravec, P. and Harris, A. W. (2000). Fast and slow rotation of asteroids. *Icarus*, 148(1):12–20.

Pravec, P., Vokrouhlický, D., Polishook, D., Scheeres, D. J., Harris, A. W., Galád, A., Vaduvescu, O., Pozo, F., Barr, A., Longa, P., Vachier, F., Colas, F., Pray, D. P., Pollock, J., Reichart, D., Ivarsen, K., Haislip, J., Lacluyze, A., Kušnirák, P., Henych, T., Marchis, F., Macomber, B., Jacobson, S. A., Krugly, Y. N., Sergeev, A. V., and Leroy, A. (2010). Formation of asteroid pairs by rotational fission. *Nature*, 466(7310):1085–1088.

Price, D. J. (2008). Modelling discontinuities and Kelvin Helmholtz instabilities in SPH. *Journal of Computational Physics*, 227:10040–10057.

Price, D. J. (2012). Smoothed particle hydrodynamics and magnetohydrodynamics. *Journal of Computational Physics*, 231:759–794.

Radović, V. (2017). Limitations of backward integration method for asteroid family age estimation. *MNRAS*, 471(2):1321–1329.

Raducan, S. D. and Jutzi, M. (2021). Global scale deformations caused by the DART impact: Insights to the collisional evolution of small asteroids. In *Lunar and Planetary Science Conference Proceedings*, page 1900.

Raskin, C. and Owen, J. M. (2016). Rapid optimal SPH particle distributions in spherical geometries for creating astrophysical initial conditions. *ApJ*, 820(2):102.

Read, J. I., Hayfield, T., and Agertz, O. (2010). Resolving mixing in smoothed particle hydrodynamics. *MNRAS*, 405(3):1513–1530.

Reinhardt, C. and Stadel, J. (2017). Numerical aspects of giant impact simulations. *MNRAS*, 467:4252–4263.

Richardson, D. C., Quinn, T., Stadel, J., and Lake, G. (2000). Direct large-scale N-body simulations of planetesimal dynamics. *Icarus*, 143:45–59.

Riller, U., Poelchau, M., Rae, A., Schulte, F., Collins, G., Melosh, J., Grieve, R., Morgan, J., Gulick, S., Lofi, J., Diaw, A., McCall, N., and Kring, D. (2018). Rock fluidization during peak-ring formation of large impact structures. *Nature*, 562.

Robertson, B. E., Kravtsov, A. V., Gnedin, N. Y., Abel, T., and Rudd, D. H. (2010). Computational Eulerian hydrodynamics and Galilean invariance. *Monthly Notices of the Royal Astronomical Society*, 401(4):2463–2476.

Rosswog, S. (2009). Astrophysical smooth particle hydrodynamics. *New A. Rev.*, 53:78–104.

Rosswog, S., Davies, M. B., Thielemann, F.-K., and Piran, T. (2000). Merging neutron stars: asymmetric systems. *A&A*, 360:171–184.

Rubincam, D. P. (2000). Radiative spin-up and spin-down of small asteroids. *Icarus*, 148(1):2–11.

Russell, C. T., McSween, H. Y., Jaumann, R., and Raymond, C. A. (2015). *The Dawn mission to Vesta and Ceres*, pages 419–432. University of Arizona Press.

Russell, C. T., Raymond, C. A., Ammannito, E., Buczkowski, D. L., De Sanctis, M. C., Hiesinger, H., Jaumann, R., Konopliv, A. S., McSween, H. Y., Nathues, A., Park, R. S., Pieters, C. M., Prettyman, T. H., McCord, T. B., McFadden, L. A., Mottola, S., Zuber, M. T., Joy, S. P., Polanskey, C., Rayman, M. D., Castillo-Rogez, J. C., Chi, P. J., Combe, J. P., Ermakov, A., Fu, R. R., Hoffmann, M., Jia, Y. D., King, S. D., Lawrence, D. J., Li, J. Y., Marchi, S., Preusker, F., Roatsch, T., Ruesch, O., Schenk, P., Villarreal, M. N., and Yamashita, N. (2016). Dawn arrives at Ceres: Exploration of a small, volatile-rich world. *Science*, 353(6303):1008–1010.

Saff, E. B. and Kuijlaars, A. B. J. (1997). Distributing many points on a sphere. *The Mathematical Intelligencer*, 19(1):5–11.

Saito, J., Miyamoto, H., Nakamura, R., Ishiguro, M., Michikami, T., Nakamura, A. M., Demura, H., Sasaki, S., Hirata, N., Honda, C., Yamamoto, A., Yokota, Y., Fuse, T., Yoshida, F., Tholen, D. J., Gaskell, R. W., Hashimoto, T., Kubota, T., Higuchi, Y., Nakamura, T., Smith, P., Hiraoka, K., Honda, T., Kobayashi, S., Furuya, M., Matsumoto, N., Nemoto, E., Yukishita, A., Kitazato, K., Dermawan, B., Sogame, A., Terazono, J., Shinohara, C., and Akiyama, H. (2006). Detailed Images of Asteroid 25143 Itokawa from Hayabusa. *Science*, 312(5778):1341–1344.

Saitoh, T. R. and Makino, J. (2013). A density-independent formulation of smoothed particle hydrodynamics. *ApJ*, 768(1):44.

Samet, H. (1990). *The Design and Analysis of Spatial Data Structures*. Addison-Wesley Longman Publishing Co., Inc., USA.

Schäfer, C., Riecker, S., Maindl, T. I., Speith, R., Scherrer, S., and Kley, W. (2016). A smooth particle hydrodynamics code to model collisions between solid, self-gravitating objects. *A&A*, 590:A19.

Schäfer, C., Speith, R., and Kley, W. (2007). Collisions between equal-sized ice grain agglomerates. *A&A*, 470(2):733–739.

Schenk, P., Singer, K. N., Beyer, R., Beddingfield, C., Robbins, S. J., McKinnon, W. B., Lauer, T. R., Verbiscer, A. J., Keane, J. T., Dhingra, R. D., Moore, J., Parker, J. W., Olkin, C., Spencer, J., Weaver, H., and Stern, S. A. (2021). Origins of pits and troughs and degradation on a small primitive planetesimal in the Kuiper Belt: high-resolution topography of (486958) Arrokoth (aka 2014 MU69) from New Horizons. *Icarus*, 356:113834.

Schiavi, R., Capuzzo-Dolcetta, R., Arca-Sedda, M., and Spera, M. (2020). Future merger of the Milky Way with the Andromeda galaxy and the fate of their supermassive black holes. *A&A*, 642:A30.

Schlichting, H. E. and Sari, R. (2009). The creation of Haumea's collisional family. *ApJ*, 700(2):1242–1246.

Schmid, H. M., Bazzon, A., Milli, J., Roelfsema, R., Engler, N., Mouillet, D., Lagadec, E., Sissa, E., Sauvage, J. F., Ginski, C., Baruffolo, A., Beuzit, J. L., Boccaletti, A., Bohn, A. J., Claudi, R., Costille, A., Desidera, S., Dohlen, K., Dominik, C., Feldt, M., Fusco, T., Gisler, D., Girard, J. H., Gratton, R., Henning, T., Hubin, N., Joos, F., Kasper, M., Langlois, M., Pavlov, A., Pragt, J., Puget, P., Quanz, S. P., Salasnich, B., Siebenmorgen, R., Stute, M., Suarez, M., Szulágyi, J., Thalmann, C., Turatto, M., Udry, S., Vigan, A., and Wildi, F. (2017). SPHERE/ZIMPOL observations of the symbiotic system R Aquarii. I. Imaging of the stellar binary and the innermost jet clouds. *A&A*, 602:A53.

Schoenberg, I. J. (1946). Contributions to the problem of approximation of equidistant data by analytic functions. Part A — On the problem of smoothing or graduation. A first class of analytic approximation formulae. *Quarterly of Applied Mathematics*, IV(1):45–99.

Sedov, L. I. (1959). *Similarity and Dimensional Methods in Mechanics*. Academic Press.

Ševeček, P., Brož, M., and Jutzi, M. (2019). Impacts into rotating targets: angular momentum draining and efficient formation of synthetic families. *A&A*, 629:A122.

Ševeček, P., Brož, M., Nesvorný, D., Enke, B., Durda, D., Walsh, K., and Richardson, D. C. (2017). SPH/N-Body simulations of small (D = 10km) asteroidal breakups and improved parametric relations for Monte-Carlo collisional models. *Icarus*, 296:239–256.

Shepard, M. K., Timerson, B., Scheeres, D. J., Benner, L. A. M., Giorgini, J. D., Howell, E. S., Magri, C., Nolan, M. C., Springmann, A., Taylor, P. A., and Virkki, A. (2018). A revised shape model of asteroid (216) Kleopatra. *Icarus*, 311:197–209.

Silber, E., Osinski, G., Johnson, B., and Grieve, R. (2017). Effect of impact velocity and acoustic fluidization on the simple-to-complex transition of lunar craters. *The Journal of Geophysical Research Planets*, 122.

Sod, G. A. (1978). A survey of several finite difference methods for systems of nonlinear hyperbolic conservation laws. *Journal of Computational Physics*, 27(1):1–31.

Soderblom, L. A., Boice, D. C., Britt, D., Brown, R. H., Buratti, B. J., Hicks, J., Hillier, M., Lee, R., Meier, R., Nelson, J., Oberst, T., Owen, A., Rivkin, W., Sandel, A., Stern, N., Thomas, R., Yelle, and v., R. (1999). Deep Space 1 MICAS observations of 9969 Braille. In *Bulletin of the American Astronomical Society*, volume 31, page 1127.

Spoto, F., Tanga, P., Milani, A., Carry, B., and Knežević, Zoran (2018). The impact of the ESA Gaia mission in our knowledge of collisional families. In *42nd COSPAR Scientific Assembly*, volume 42, pages B1.1–35–18.

Springel, V. (2010). Smoothed particle hydrodynamics in astrophysics. *Annual Review of Astronomy and Astrophysics*, 48(1):391–430.

Stadel, J. G. (2001). *Cosmological N-body simulations and their analysis*. PhD thesis, University of Washington.

Sugiura, K., Kobayashi, H., and Inutsuka, S.-i. (2018). Toward understanding the origin of asteroid geometries. Variety in shapes produced by equal-mass impacts. *A&A*, 620:A167.

Sugiura, K., Kobayashi, H., and Inutsuka, S.-i. (2019). Collisional elongation: Possible origin of extremely elongated shape of 1I/'Oumuamua. *Icarus*, 328:14–22.

Swegle, J., Attaway, S., Heinstein, M., Mello, F., and Hicks, D. (1994). An analysis of smoothed particle hydrodynamics. *NASA STI/Recon Technical Report*, 95:17439.

Swegle, J., Hicks, D., and Attaway, S. (1995). Smoothed particle hydrodynamics stability analysis. *Journal of Computational Physics*, 116(1):123–134.

Takeda, T. and Ohtsuki, K. (2007). Mass dispersal and angular momentum transfer during collisions between rubble-pile asteroids. *Icarus*, 189(1):256–273.

Takeda, T. and Ohtsuki, K. (2009). Mass dispersal and angular momentum transfer during collisions between rubble-pile asteroids. II. Effects of initial rotation and spin-down through disruptive collisions. *Icarus*, 202(2):514–524.

Tanga, P., Cellino, A., Michel, P., Zappalà, V., Paolicchi, P., and Dell'Oro, A. (1999). On the size distribution of asteroid families: The role of geometry. *Icarus*, 141:65–78.

Tasker, E. J., Brunino, R., Mitchell, N. L., Michielsen, D., Hopton, S., Pearce, F. R., Bryan, G. L., and Theuns, T. (2008). A test suite for quantitative comparison of hydrodynamic codes in astrophysics. *Monthly Notices of the Royal Astronomical Society*, 390(3):1267–1281.

Teschner, M., Heidelberger, B., Müller, M., Pomeranets, D., and Gross, M. (2003). Optimized spatial hashing for collision detection of deformable objects. *VMV'03: Proceedings of the Vision, Modeling, Visualization*, 3.

Thomas, P. and Couchman, H. (1992). Simulating the formation of a cluster of galaxies. *Monthly Notices of the Royal Astronomical Society*, 257:11–31.

Thomas, P. C., Veverka, J., Simonelli, D., Helfenstein, P., Carcich, B., Belton, M. J. S., Davies, M. E., and Chapman, C. (1994). The shape of Gaspra. *Icarus*, 107(1):23–36.

Thompson, S. and Lauson, H. (1974). Improvements in the CHART D radiation-hydrodynamic code III: Revised analytic equations of state. *Material Science Report*, SC-RR–71-0714.

Tillotson, J. H. (1962). Metallic equations of state for hypervelocity impact. *General Atomic Report*, GA-3216.

Toro, E. (2009). *Riemann Solvers and Numerical Methods for Fluid Dynamics: A Practical Introduction*. Springer Berlin Heidelberg.

Turk, G. and Levoy, M. (1994). Zippered polygon meshes from range images. In *Proceedings of the 21st Annual Conference on Computer Graphics and Interactive Techniques*, SIGGRAPH '94, page 311–318, New York, NY, USA. Association for Computing Machinery.

Usui, F., Kuroda, D., Müller, T. G., Hasegawa, S., Ishiguro, M., Ootsubo, T., Ishihara, D., Kataza, H., Takita, S., Oyabu, S., Ueno, M., Matsuhara, H., and Onaka, T. (2011). Asteroid catalog using Akari: AKARI/IRC mid-infrared asteroid survey. *PASJ*, 63:1117–1138.

Valcke, S., De Rijcke, S., Rödiger, E., and Dejonghe, H. (2010). Kelvin–Helmholtz instabilities in smoothed particle hydrodynamics. *Monthly Notices of the Royal Astronomical Society*, 408(1):71–86.

Valdarnini, R. (2012). Hydrodynamic capabilities of an SPH code incorporating an artificial conductivity term with a gravity-based signal velocity. *A&A*, 546:A45.

Vernazza, P., Brož, M., Drouard, A., Hanuš, J., Viikinkoski, M., Marsset, M., Jorda, L., Fetick, R., Carry, B., Marchis, F., Birlan, M., Fusco, T., Santana-Ros, T., Podlewska-Gaca, E., Jehin, E., Ferrais, M., Bartczak, P., Dudzi ."0301nski, G., Berthier, J., Castillo-Rogez, J., Cipriani, F.,

Colas, F., Dumas, C., Ďurech, J., Kaasalainen, M., Kryszczynska, A., Lamy, P., Le Coroller, H., Marciniak, A., Michalowski, T., Michel, P., Pajuelo, M., Tanga, P., Vachier, F., Vigan, A., Warner, B., Witasse, O., Yang, B., Asphaug, E., Richardson, D. C., Ševeček, P., Gillon, M., and Benkhaldoun, Z. (2018). The impact crater at the origin of the julia family detected with vlt/sphere? *A&A*, 618:A154.

Vernazza, P., Castillo-Rogez, J., Beck, P., Emery, J., Brunetto, R., Delbo, M., Marsset, M., Marchis, F., Groussin, O., Zanda, B., Lamy, P., Jorda, L., Mousis, O., Delsanti, A., Djouadi, Z., Dionnet, Z., Borondics, F., and Carry, B. (2017). Different origins or different evolutions? Decoding the spectral diversity among C-type asteroids. *AJ*, 153(2):72.

Vernazza, P., Jorda, L., Ševeček, P., Brož, M., Viikinkoski, M., Hanuš, J., Carry, B., Drouard, A., Ferrais, M., Marsset, M., Marchis, F., Birlan, M., Podlewska-Gaca, E., Jehin, E., Bartczak, P., Dudzinski, G., Berthier, J., Castillo-Rogez, J., Cipriani, F., Colas, F., DeMeo, F., Dumas, C., Ďurech, J., Fetick, R., Fusco, T., Grice, J., Kaasalainen, M., Kryszczynska, A., Lamy, P., Le Coroller, H., Marciniak, A., Michalowski, T., Michel, P., Rambaux, N., Santana-Ros, T., Tanga, P., Vachier, F., Vigan, A., Witasse, O., Yang, B., Gillon, M., Benkhaldoun, Z., Szakats, R., Hirsch, R., Duffard, R., Chapman, A., and Maestre, J. L. (2020). A basin-free spherical shape as an outcome of a giant impact on asteroid Hygiea. *Nature Astronomy*, 4:136–141.

Veverka, J., Thomas, P., Harch, A., Clark, B., Bell, J. F., I., Carcich, B., Joseph, J., Chapman, C., Merline, W., Robinson, M., Malin, M., McFadden, L. A., Murchie, S., Hawkins, S. E., I., Farquhar, R., Izenberg, N., and Cheng, A. (1997). NEAR's flyby of 253 Mathilde: Images of a C asteroid. *Science*, 278:2109.

Viikinkoski, M., Kaasalainen, M., and Ďurech, J. (2015). ADAM: a general method for using various data types in asteroid reconstruction. *A&A*, 576:A8.

Vinogradova, T. A. (2015). Identification of asteroid families in Trojans and Hildas. *MNRAS*, 454(3):2436–2440.

Vokrouhlický, D., Brož, M., Bottke, W. F., Nesvorný, D., and Morbidelli, A. (2006). Yarkovsky/YORP chronology of asteroid families. *Icarus*, 182(1):118–142.

Vokrouhlický, D., J., Ďurech,., Michalowski, T., Krugly, Yu. N., Gaftonyuk, N. M., Kryszczyńska, A., Colas, F., Lecacheux, J., Molotov, I., Slyusarev, I., Polińska, M., Nesvorný, D., and Beshore, E. (2009). Datura family: the 2009 update*. *A&A*, 507(1):495–504.

VonNeumann, J. and Richtmyer, R. D. (1950). A method for the numerical calculation of hydrodynamic shocks. *Journal of Applied Physics*, 21(3):232–237.

Wadell, H. (1935). Volume, shape, and roundness of quartz particles. *Journal of Geology*, 43(3):250–280.

Wadsley, J. W., Veeravalli, G., and Couchman, H. M. P. (2008). On the treatment of entropy mixing in numerical cosmology. *Monthly Notices of the Royal Astronomical Society*, 387(1):427–438.

Warner, B. D., Harris, A. W., and Pravec, P. (2009). The asteroid lightcurve database. *Icarus*, 202(1):134–146.

Watanabe, S., Hirabayashi, M., Hirata, N., Hirata, N., Noguchi, R., Shimaki, Y., Ikeda, H., Tatsumi, E., Yoshikawa, M., Kikuchi, S., Yabuta, H., Nakamura, T., Tachibana, S., Ishihara, Y., Morota, T., Kitazato, K., Sakatani, N., Matsumoto, K., Wada, K., Senshu, H., Honda, C., Michikami, T., Takeuchi, H., Kouyama, T., Honda, R., Kameda, S., Fuse, T., Miyamoto, H., Komatsu, G., Sugita, S., Okada, T., Namiki, N., Arakawa, M., Ishiguro, M., Abe, M., Gaskell, R., Palmer, E., Barnouin, O. S., Michel, P., French, A. S., McMahon, J. W., Scheeres, D. J., Abell, P. A., Yamamoto, Y., Tanaka, S., Shirai, K., Matsuoka, M., Yamada, M., Yokota, Y., Suzuki, H., Yoshioka, K., Cho, Y., Tanaka, S., Nishikawa, N., Sugiyama, T., Kikuchi, H., Hemmi, R., Yamaguchi, T., Ogawa, N., Ono, G., Mimasu, Y., Yoshikawa, K., Takahashi, T., Takei, Y., Fujii, A., Hirose, C., Iwata, T., Hayakawa, M., Hosoda, S., Mori, O., Sawada, H., Shimada, T., Soldini, S., Yano, H., Tsukizaki, R., Ozaki, M., Iijima, Y., Ogawa, K., Fujimoto, M., Ho, T. M., Moussi, A., Jaumann, R., Bibring, J. P., Krause, C., Terui, F., Saiki, T., Nakazawa, S., and Tsuda, Y. (2019). Hayabusa2 arrives at the carbonaceous asteroid 162173 Ryugu—A spinning top-shaped rubble pile. *Science*, 364(6437):268–272.

Weibull, W. (1939). *A Statistical Theory of the Strength of Materials*. Ingeniörsvetenskapsakademiens handlingar. Generalstabens litografiska anstalts förlag.

Wendland, H. (1995). Piecewise polynomial, positive definite and compactly supported radial functions of minimal degree. *Advances in Computational Mathematics*, 4(1):389–396.

Yan, D., Guo, J., Wang, B., Zhang, X., and Wonka, P. (2015). A survey of blue-noise sampling and its applications. *Journal of Computer Science and Technology*, 30:439–452.

Yang, B., Hanuš, J., Brož, M., Chrenko, O., Willman, M., Ševeček, P., Masiero, J., and Kaluna, H. (2020a). Physical and dynamical characterization of the Euphrosyne asteroid family. *A&A*, 643:A38.

Yang, B., Hanuš, J., Carry, B., Vernazza, P., Brož, M., Vachier, F., Rambaux, N., Marsset, M., Chrenko, O., Ševeček, P., Viikinkoski, M., Jehin, E., Ferrais, M., Podlewska-Gaca, E., Drouard, A., Marchis, F., Birlan, M., Benkhaldoun, Z., Berthier, J., Bartczak, P., Dumas, C., Dudziński, G., Ďurech, J., Castillo-Rogez, J., Cipriani, F., Colas, F., Fetick, R., Fusco, T., Grice, J., Jorda, L., Kaasalainen, M., Kryszczynska, A., Lamy, P., Marciniak, A., Michalowski, T., Michel, P., Pajuelo, M., Santana-Ros, T., Tanga, P., Vigan, A., and Witasse, O. (2020b). Binary asteroid (31) Euphrosyne: ice-rich and nearly spherical. *A&A*, 641:A80.

Yu, J. and Turk, G. (2013). Reconstructing surfaces of particle-based fluids using anisotropic kernels. *ACM Trans. Graph.*, 32(1).

Zappalà, V., Bendjoya, P., Cellino, A., Farinella, P., and Froeschlé, C. (1995). Asteroid families: Search of a 12,487-asteroid sample using two different clustering techniques. *Icarus*, 116(2):291–314.

Zhang, Y. and Lin, D. N. C. (2020). Tidal fragmentation as the origin of 1I/2017 U1 (‘Oumuamua). *Nature Astronomy*, 4:852–860.